UC Berkeley
UC Berkeley Electronic Theses and Dissertations

Title
Nanophotonic Devices Based on Indium Phosphide Nanopillars Grown Directly on Silicon

Permalink
https://escholarship.org/uc/item/6r24c7cb

Author
Bhattacharya, Indrasen

Publication Date
2017

Peer reviewed|Thesis/dissertation

eScholarship.org Powered by the California Digital Library
University of California

Nanophotonic Devices Based on Indium Phosphide Nanopillars Grown Directly on Silicon

by

Indrasen Bhattacharya

A dissertation submitted in partial satisfaction of the
requirements for the degree of
Doctor of Philosophy

in

Applied Science and Technology
and the Designated Emphasis
in
Nanoscale Science and Engineering

in the

Graduate Division

of the

University of California, Berkeley

Committee in charge:

Professor Connie Chang-Hasnain, Chair
Professor Eli Yablonovitch
Professor Liwei Lin

Fall 2017

Nanophotonic Devices Based on Indium Phosphide Nanopillars Grown Directly on Silicon

Copyright 2017
by
Indrasen Bhattacharya

Abstract

Nanophotonic Devices Based on Indium Phosphide Nanopillars Grown Directly on Silicon

by

Indrasen Bhattacharya

Doctor of Philosophy in Applied Science and Technology
and the Designated Emphasis
in
Nanoscale Science and Engineering

University of California, Berkeley

Professor Connie Chang-Hasnain, Chair

III-V optoelectronic device integration in a CMOS post-process compatible manner is important for the intimate integration of silicon-based electronic and photonic integrated circuits. The low temperature, self-catalyzed growth of high crystalline quality Wurtzite-phase InP nanopillars directly on silicon presents a viable approach to integrate high performance nano-optoelectronic devices.

For the optical transmitter side of the photonic link, InGaAs quantum wells have been grown in a core-shell manner within InP nanopillars. Position-controlled growth with varying pitch is used to systematically control emission wavelength across the same growth substrate. These nanopillars have been fabricated into electrically-injected quantum well in nanopillar LEDs operating within the silicon transparent 1400-1550 nm spectral window and efficiently emitting micro-watts of power. A high quality factor ($Q \sim 1000$) undercut cavity quantum well nanolaser is demonstrated, operating in the silicon-transparent wavelength range up to room temperature under optical excitation.

We also demonstrate an InP nanopillar phototransistor as a sensitive, low-capacitance photoreceiver for the energy-efficient operation of a complete optical link. Efficient absorption in a compact single nanopillar InP photo-BJT leads to a simultaneously high responsivity of 9.5 A/W and high 3dB-bandwidth of 7 GHz.

For photovoltaic energy harvesting, a sparsely packed InP nanopillar array can absorb 90% of the incident light because of the large absorption cross section of these near-wavelength nanopillars. Experimental data based on wavelength and angle resolved integrating sphere measurements will be presented to discuss the nearly omnidirectional absorption properties of these nanopillar arrays.

To Mammai, Babbai, Bantu and your fondest memory, Kaku

“We have watered the trees that blossom in the summer-time. Now let’s sprinkle those whose flowering-time is past.”
- Abhijñānaśakuntalā, Kālidāsa

Contents

Contents **ii**

List of Figures **iv**

List of Tables **xvi**

1 Introduction **1**
- 1.1 Optical Processes in Semiconductors 4
- 1.2 Photonic Integration 8
- 1.3 Monolithic Integration Techniques 12
- 1.4 III/V nanowire/nanopillar growth on Silicon 17
- 1.5 Organization of thesis 20

2 Nanopillar Solar Cells **23**
- 2.1 Quantitative Photoluminescence from Nanopillars 25
- 2.2 Doped Nanopillars: Electrical Characterization 41
- 2.3 Regrown Nanopillar Solar Cell 45
- 2.4 Position Controlled Nanopillar Solar Cells 51

3 Omnidirectional Light Harvesting with Nanopillars **58**
- 3.1 Detailed Balance Efficiency Limit for LED Energy Harvesting 59
- 3.2 Angle Insensitive Single Nanopillar Solar Cell 69
- 3.3 Absorption in Sparse Nanopillar Arrays 72
- 3.4 Nanopillar Array Absorption Measurement 75
- 3.5 Nanopillar Antireflection 77

4 Nanopillar Phototransistors **82**
- 4.1 Photoreceiver Scaling Reduces Link Energy 84
- 4.2 Regrown Nanopillar Bipolar Phototransistor 89
- 4.3 Phototransistor Operation 91
- 4.4 Device Characteristics 95
- 4.5 Responsivity-Bandwidth Tradeoff 100
- 4.6 Prospects for Silicon Photonics Integration 103

5 InP-based Nanopillar Lasers on Silicon **104**
5.1 Transparency Condition in Nanopillar with Quantum Well 106
5.2 Hakki-Paoli Gain Measurement 110
5.3 Undercut Cavity Laser 115
5.4 Thermal Resistance 118
5.5 Silicon Photonics Integration 120
5.6 Regrown Nanocavity Laser 126
5.7 Resonant Second Harmonic Generation in Nanopillar Lasers 127

6 Position Controlled 1.5 μm Nanopillar LEDs **139**
6.1 Growth of Position Controlled Nanopillar Devices 140
6.2 Optical Characterization 142
6.3 Pitch-defined Wavelength in Nanopillar Arrays 148
6.4 Scalable Fabrication of Position Controlled Nanopillar Devices 151
6.5 Bright Silicon Transparent Electroluminescence 154

7 Conclusion and Outlook **159**

References **162**

List of Figures

1.1 The main optical processes in a direct gap semiconductor 5
1.2 This chart provides a qualitative comparison of photonic integration technologies, with a focus on the eventual goal of monolithic integration with silicon photonics. This infographic is based on the author's opinion, derived from the published literature and should be interpreted as such. It can be noticed that while Indium Phosphide photonic integration provides the most capabilities and functionalities on the same platform, it is the least compatible with silicon-based CMOS electronics, that are fabricated under stringent conditions on a silicon substrate. On the other hand, group IV based optoelectronic materials as of yet have poor performance due to the indirect bandgap and unavailability of bandgap engineering with heterostructures. III/V nanopillars grown on silicon can potentially help to bridge the two worlds. Some of the steps required to improve the technology readiness of the nanopillars towards the top right corner of CMOS compatibility and performance are highlighted. 18

2.1 Quantitative μPL measurement: (top) Calibration of the photon collection efficiency of the setup, measured at the photoluminescence wavelength. The calibration needs to be carried out at the PL wavelength (875 nm for Wurtzite InP, 1400-1550 nm for quantum wels) (bottom) The actual PL measurement was then made by exciting the active region with photons that are efficiently absorbed, and at comparable intensity to what is expected under AM1.5G solar illumination. This figure illustrates the case of 980 nm excitation and 1550 nm PL, and can be extended to other relevant cases. 26
2.2 Photoluminescence yield in two different situations: (left) In material with high surface recombination or defective material, the generated excess charge carrier density is comparatively low, since the generation of carriers is balanced by rapid non radiative recombination. (right) If the non-radiative recombination is slow, the charge carrier density can be higher, leading to a higher quasi Fermi level split, and hence a higher implied open circuit voltage. 27

2.3 Normalized PL spectra: (left) Log scale PL spectra from Wurtzite InP nanopillars, showing the characteristic high and low energy tails in the spectrum. (right) Linear scale spectra showing PL characteristics of doped and nominally undoped nanopillars. 28
2.4 Modeling internal luminescence yield: (left) Each curve depicts the carrier injection level dependence of the internal luminescence yield. Note the typical trend that the luminescence yield rises with increasing carrier concentration at lower levels of carrier concentration as radiative recombination starts to become competitive with the SRH process. This can be further helped by simply increasing the doping level, as shown for N_d from $10^{14} cm^{-3}$ to $10^{17} cm^{-3}$. However, as the carrier injection level increases beyond $10^{18} cm^{-3}$, or the doping level exceeds the same value, the Auger process starts to dominate the radiative process, and the luminescence yield suffers. There exists an optimal doping level (as explained in the text), for which the luminescence yield can have its maximal value over a large range of carrier injection levels. This maximal luminescence yield value depends on the A, B and C coefficients (see equation 2.13) and was slightly shy of 30% for the chosen parameter values. (right) Given that B and C are mostly material dependent parameters, it is typically the SRH coefficient A that determines the maximum possible luminescence yield. As explained in the text, in pristine semiconductors, the SRH non-radiative process largely depends on surface (or interface) recombination. Hence, the luminescence yield can be plotted as a function of heterostructure width and interface recombination velocity. . . . 35
2.5 Fermi level split measurement for multiple N-doped nanopillars. There is some doping variation in the pillars, that leads to PL peak variation through the Burstein Moss effect. Some part of this bandgap variation also contributes to the Fermi level split variation. 39
2.6 Contactless I-V: (left) The Fermi level slit (X-axis) as a funcion of the excitation intensity in suns (Y-axis), as measured for differently doped pillars. (right) Fermi level split measured for exemplary p-doped pillars as a function of excitation intensity. 40
2.7 Device fabrication process: While the devices in this section were resistors used to test the doping level, the same fabrication process is also applied to p-i-n doped nanopillar devices. See main text for details. 42
2.8 Nanopillar Resistors: (left) Schematics showing the structure of fabricated p and n doped nanopillar devices. Note that the different contacts used to study the behavior of these nanopillars will also influence electrical characteristics. (right) Electrical I-V characteristics from n-doped nanopillars and microscope images of fabricated devices. Each characteristic corresponds to an individual single nanopillar device. The characteristics are largely Ohmic, with some Schottky like behavior near zero bias. 44

2.9 Four point probe: (left) Schematic showing the measurement principle and SEM image of a device. (right) Electrical characteristics from the 4 point measurement, allowing a calculation of the resistance. The obtained value of series resistance with the linear fit in orange is $0.72 M\Omega$. 45
2.10 Nanopillar regrowth: (a) Direct core-shell device showing the presence of a shunt path, (b) I-V characteristic showing orders of magnitude improvement in dark current after regrowth, (c) SEM image of the same nanopillar before and after regrowth, (d) Schematic showing nanopillar and layer structure before and after regrowth 47
2.11 Nanopillar device schematic: (a) Comparison of active region exposure for core-shell vs. axial geometry, (b) Nanopillar device SEM, (c) Schematic illustrating corresponding structure 48
2.12 Nanopillar solar cell I-v: (a) linear scale I-V for an exemplary nanopillar device in dark and under AM1.5G illumination (b) Log scale for the same 49
2.13 Nanopillar solar cell temperature dependence: open circuit voltage dependence for two exemplary devices 50
2.14 (a) Tilt-view low magnification SEM images of arrays of site-controlled InP nanopillars grown at $460°C$. The scale bar in all images corresponds to 10 m and the growth periods (pitch) are 1 m, 4 and 40 m, respectively. (b) Nanopillars grown under the same nominal V/III ratio, for 15 min at $460, 455,$ and $450C$, exhibit different taper angles. The scale bar in all figures is 1 m. (c) HAADF-STEM image of a cross-section of an InP nanopillar nucleating on Si, with a schematic representation in the inset 53
2.15 Comparison of S-shape I-V characteristic in p-core and n-core devices: (a) p-core isotype nanopillar device showing light response and s-shaped characteristic on increasing light intensity, (b) Type-II heterojunction alignment showing the impediment to hole transport, (c) S-shaped characteristics were eliminated in n-core nanopillars, and the open circuit voltage increases with excitation intensity 55
2.16 Gold etching for better optical access: (a) to (e) - see main text for details, (f) scanning electron microscope image of nanopillars with gold etched from tip for optical access 56

3.1 Detailed balance limit: (left) geometry showing light harvesting from LED at some distance to a PV cell PV-cell bandgap dependent. The annotated quantities are described in the main text. The efficiency limit will depend on the solid angle subtended by the LED at the PV cell. (right) Detailed balance efficiency limit for LED to PV energy conversion for a fixed LED spectral irradiance (warm white) shown in orange and PV cell bandgap dependent power conversion efficiency (blue curves). The two efficiency curves are for different external luminescence efficiencies. 60
3.2 Two terminal dual junction: Efficiency contours for a two terminal dual junction solar cell. The overall efficiency suffers if the currents are not matched, leading to a narrow optimal range for the bandgaps. 67

3.3 Four terminal dual junction: Efficiency contours for a dual junction solar cell with separate contacts. The are optically stacked and are assumed to have perfect anti reflection for this calculation. Note that the cells do not need to be current matched: one of the cells can absorb all the light, leading to an efficiency close to the single junction efficiency limit. The configuration is described in detail in the main text. 68
3.4 Spectrally resolved IPCE: The ratio of incident photons to collected electrons (IPCE), resolved along photon energy is higher than unity for a significant portion of the spectrum. IPCE and EQE are used interchangeably to describe the quantum efficiency at short circuit. 69
3.5 Enhanced absorption cross section: (left) Schematic showing light absorption enhancement due to the nanopillar geometry. (right) Photocurrent scanning reveals that the light absorption spot is a couple of microns in size, and the silicon substrate does not contribute to photocurrent generation. The scan was carried out using a diffraction limited spot of 660 nm light. 70
3.6 Angle-independent performance: Polar plots showing experimentally determined (a) open circuit voltage, (b) short circuit current and (c) external quantum efficiency (or equivalently, short circuit current density normalized to projected physical cross section). In particular, in (b) we note that for top down incidence ($\theta = 0$) the short circuit current is anomalously high compared to what we would expect from the small projected physical cross section. This is decribed in greater detail in the main text. 71
3.7 Nanopillar optical simulation: Simulated angular response of a single nanopillar solar cell and simulated absorption from a nanopillar array. (a) Simulated short circuit current I_{sc} (red) also shows angle insensitive response that scales slowly compared to the change in the capture area of the solar cell (blue). (b) Simulated short circuit current density J_{sc} confirms the directional antenna enhancement effect compensating for the change in capture cross-section as the illumination angle is changed, along with ultra-high external quantum efficienc for on-axis illumination. (c) Simulated absorption spectra of two nanopillar arrays showing greater than 90% absorption despite having only 17% volume fill ratio. The red curve shows the absorption spectrum of an array of 510 nm wide non-tapered nanopillars that are spaced 1 μm apart. The blue curve shows the absorption spectrum of a nanopillar array with tapered sidewalls. The array with tapered nanopillars is able to absorb 95% of the light, compared to 90% for the non-tapered nanopillars. To keep the volume fill ratio the same at 17%, the tapered nanopillars have upper and lower diameters of 325 nm and 650 nm, respectively, and are 6 μm tall. Micro/nanopillars of this dimension can be easily achieved by scaling growth time. The tapered nanopillars in this array are also spaced 1 μm apart. 73

3.8 Nanopillar absorber: One particular special case of the gradient index texture is when the nanopillar itself absorbs light. The left panel shows the normalized carrier generation rate at two different wavelengths (660 nm, 800 nm), two different anges of incidence ($\theta = 0°, 40°$) and both s, p polarizations. It can be noted that most of the light is absorbed in the InP nanopillar, with little penetrating down to the substrate. The right figure compares the simulated absorption spectra of the nanopillar array at different angles of incidence, along with comparable equivalent thin films of InP and siicon. 74

3.9 Nanopillar array SEM: (left) 85 degree tilt view SEM image of the nanopillar array and close up (right) showing high pillar density. Scale bars: left - 30 μm, right - 3 μm 76

3.10 Absorption measurement: (right, top) Schematic showing the integrating sphere measurement setup, (right, bottom) optical microscope image of the dense nanopillar array, (left) Measured reflectivity spectra of the nanopillar array, compared with the thick silicon substrate. 77

3.11 Gradient index anti reflection: Schematic illustrating the nanopillar AR coating principle. AR coatings are based on wave effects and typically only work well for a particular incidence angle. In this case, the gradient index structure has the effect of bending even the glancing incidence rays such that the angle of incidence at the AR coating is close to the normal. With incidence angle closer to the normal, the AR coating functions better and leads to improved anti-reflectivity. 78

3.12 Nanopillar anti-reflection (AR) coating: Schematic describing the use of a transparent textured AR coating in order to allow omnidirectional anti-reflection for a III/V based solar cell. The pillar dimensions and spacing have been chosen to index match the underlying quarter-wave AR coating, which is the same material as the nanopillars (silicon nitride). The case when the nanopillar and AR coating are the same material as the underlying substrate is also possible. 79

3.13 Angle dependent reflectivity: (a) Calculated angle-dependent reflectivity using an effective medium model for the nanopillar anti-reflective coating. In the case where only the quarter-wave coating is used, we have good anti-reflection for normal incidence. However this degrades beyond 60 degrees incidence angle. When a gradient index is used, the reflectivity improves significantly at higher angles. However, the effective medium approach becomes incorrect when the gradient index layer thickness is finite. In order to account for this, we use a rigorous Maxwell solver to obtain better estimates for the reflectivity spectrum, as shown in (b). Each of the curves is explained in detail in the main text. . . . 81

4.1 Total link energy consumption as a function of link power (in photons/bit). As the number of photons is reduced, the receiver needs to work harder to amplify the photocurrent to the swing voltage. On the other hand, higher photons/bit leads to increasing transmitter power consumption. The optimum is when the receiver and transmitter consume the same power. The minimal link energy consumption can be reduced by shrinking the photoreceiver capacitance, as shown for the family of curves. 88
4.2 Bipolar phototransistor: (a) Scanning electron microscope image of an exemplary device, (b) Schematic labeling the corresponding parts, (c) Cross section showing p-n-p regrown layers. 90
4.3 Regrowth process: (a) P-core nanopillar, (b) amorphous silicon coating, followed by MOCVD precursor flow, (c) Regrown p-n-p junction, (d) Fabricated device with one side exposed for light access, (e) comparison of structure with regrowth and shunted core-shell structure, (f) I-V characteristics of regrowth vs. shunt . . 92
4.4 Bipolar gain and illumination conditions: this experiment shows how the bipolar gain mechanism can be discerned from the excitation wavelength. (a) 660 nm optical bias and (b) corresponding device characteristics, (c) 780 nm optical bias and (d) 780 nm I-V characteristics showing photoBJT gain. See main text for further details. 94
4.5 Comparison of device characteristics for axial (left) and core-shell (right) nanopillars. Note that the axial device has a tradeoff between transit time and absorption that the core-shell device can overcome. 96
4.6 DC responsivity characteristics of the nanopillar: (a) Transfer characteristics of an exemplary photo-BJT showing dark current below 25 pA at 0.5 V bias, and a high responsivity of 25 A/W. (b) Responsivity as a function of input power at a few different collector biases. (c) Responsivity as a function of collector bias and (d) measured external quantum efficiency for a p-i-n device of the same dimensions, showing approximately 30-40 % quantum efficiency without BJT gain 98
4.7 Removal of pad parasitics: (a) Reactive component of measured impedance, showing a clear fit to a capacitive load, (b) Comparison of S12 characteristic of an open pad (red) and the p-n-p photo-BJT, showing the effect of the pad parasitic on the device. 99
4.8 De-embedded high speed characteristics of nanopillar phototransistor: (a) Impulse response measured under pulsed optical excitation shows a somewhat large 120 picosecond full width at half maximum due to the pad parasitics, (b) Circuit showing device and pad capacitance, (c) High speed characteristic showing a 3dB frequency of 7 GHz after de-embedding pad parasitics. 101
4.9 Tradeoff between responsivity and bandwidth: (a) high external quantum efficiency of the nanopillar diode without gain shows that the intrinsic light absorption efficiency of the structure is quite good, (b) Tradeoff empirically observed in reported phototransistor devices due to the competing requirements of low transit time against high light absorption efficiency 102

5.1 Electron microscope images of nanopillars with QWs: (a) 85° tilt view scanning electron microscope (SEM) image of nanopillars containing 5 QWs (pillars are aligned to four degenerate [111] directions), (b) Cross sectional transmission electron microscope (TEM) image of a nanopillar containing a single QW (highlighted in yellow), (c) Close-up SEM image of an exemplary single nanopillar, (d) Cross sectional TEM of a nanopillar with 5 core-shell conformally grown QWs, with an inset showing the individual QWs, (e) cross sectional TEM of a nanopillar with 2 conformal QWs, with inset (f) showing a high resolution TEM image where individual atoms can be seen. The continuity of the crystal lattice across InP and InGaAs is clearly visible. Scale bars: (a) 5 μm, (b) 100 nm, (c) 1 μm, (d) 100 nm (inset: 20 nm), (e) 100 nm, and (f) 2 nm 107
5.2 QW luminescence and transparency condition: (a) Schematic showing indirect excitation of QWs using rapid capture of electrons and holes from the InP cladding layer, (b) Photoluminescence (PL) spectra for indirect excitation of a QW, showing minimal cladding luminescence, (c) Quantitative Fermi level split, inferred from luminescence intensity. It is found that the difference $\Delta F - h\nu$ is significantly higher (and exceeds 0 i.e. transparency) for the QW as compared to the 'bulk' InP nanopillar. (d) Quantum size effect showing wavelength tuning over 200 nm in the silicon transparent window by simply changing the quantum well thickness. 109
5.3 Internal Quantum Efficiency (IQE) of nanopillars: The IQE was measured by dividing room temperature total PL counts by low temperature total PL counts, and was found to be significantly higher for the QW active region at low pump excitation (note log scale in y-axis). The bulk InP nanopillar IQE is significantly poorer at low excitation intensity and improves as the radiative process becomes more competitive at higher injection level. However, due to the super-injection effect in the QWs, we have high carrier densities in the QW even at low pump excitation levels. 111
5.4 Transferred Nanopillar Laser: (a) PL spectra of a transferred nanopillar laser below and above threshold (inset shows laser structure schematic - QWs condensed together for clarity), (b) PL intensity and full width-at-half-maximum (FWHM) of the lasing mode at $\sim 1.3\mu m$ as a function of pump pulse fluence. The inset is the near field image of nanopillar emission above lasing threshold. 112
5.5 Hakki-Paoli method: (a) Microscope image of a transferred nanopillar showing amplified spontaneous emission (ASE), (b) ASE spectra of the nanopillars at different CW pump excitation intensities. The peak to valley modulation in the spectrum can be used to infer the gain at each wavelength, as shown in (c) . . . 114

5.6 Undercut cavity structure: (a) SEM image of a nanopillar with selectie silicon etch using the SF_6+O_2 plasma. The inset below shows how the pillar is left unaffected, while etching away the silicon in an isotropic manner. The process is self aligned, with the nanopillar providing an etch mask. (b) Simulated (FDTD) quality factor of an exemplary TM_{52} mode in a nanopillar shows significant improvement in quality factor as the undercut dimension δ is increased above 150 nm. Scale bars: 1 μm 116

5.7 Undercut cavity lasing upto room temperature: (a) Pulsed optical excitation leads to lasing from 5K up to room temperature, (b) The lasing light-light curves show a characteristic S-shape all the way up to room temperature and can be fit with a rate equation model, (c) Continuous wave low temperature (5K) luminescence spectra showing linewidth narrowing with increasing pump power, (d) to $\sim$ 0.8 nm linewidth at the onset of lasing 117

5.8 Thermal dissipation in nanopillars: (a) Schematic showing temperature gradients in a nanopillar under high current injection. The two main paths for heat conduction are the metal (gold) layer and long InP nanopillar body. The metal contact is a significantly more effective heat conductor, as discussed in the text. (b) A situation in which there is no insulating oxide is better for heat dissipation, but would lead to higher optical loss. (c) An oxide coating would add a significant series resistance in the thermal conduction path, but allows for a higher cavity quality factor. 121

5.9 Thermal resistance measurement in fabricated nanopillars: (a) Schematic of the fabricated device and current conduction path, with details of the fabrication process in chapter 2. (b) I-V characteristics of the single nanopillar resistor, showing close to Ohmic characteristics. (c) Photoluminescence peak wavelength red shift with increasing power dissipation, note that the wavelength under no heat dissipation is blue shifted compared to the InP Wurtzite bandgap due to the Burstein-Moss blue shift that arises from heavy doping. (d) Inferred nanopillar temperature from the graph in (c) and using the Varshni coefficients for InP. A linear fit to this curve allows us to extract the thermal resistance of the device. . 122

5.10 Nanopillar lasers on silicon photonics structures: (a) Lasing spectra under low temperature pulsed excitation for the structure shown in the inset. This proves that the fabrication process is robust and preserves material quality. (b) light-light curve of the nanopillar laser on silicon-photonics. Microscope images of the excited nanopillar both below (c) and above (d) threshold are also shown for comparison. 124

5.11 Waveguide coupling: These images show waveguide coupling of silicon transparent emission in the nanopillars. (a) Scanning electron microscope (SEM) image of an upright nanopillar with aligned waveguide crossing fabricated post-growth. (b) Photoluminescence (PL) microscope image captured with an InGaAs camera, showing PL emission around 1300 nm from the ends of the waveguides. (c) top view SEM image of a slanted nanopillar again showing PL coupling into waveguides in the camera image of (d). (e) PL intensity map captured by raster scanning a 980 nm excitation laser, showing how a small portion of the laser light is actually coupled into the waveguides and delivered to the nanopillars. 125

5.12 Regrown nanocavity laser: (a) Scanning electron microscope image of a regrown laser, without removing the oxide+amorphous silicon regrowth coating. The shelf due to secondary growth on the top portion of the nanopillar is clearly visible. (b) Schematic of the cross section of a regrown nanopillar, showing spatially where the high quality factor mode is expected to be supported. (c) Room temperature pulsed excitation lasing spectra from an exemplary single regrown nanopillar. We note that the lasing threshold pulse energy is an order of magnitude lower than that required for similar InP nanopillars grown directly on silicon. (d) Light-light curve from the data in (c) shows a clear S-shape behavior. The saturation in peak PL counts at high pump excitation power is due to pulse broadening, as observed in (c). 128

5.13 Second harmonic measurement setup: This setup was used to measure direct second harmonic generation of the excitation laser. Half wave plates were used to control both the illumination and output polarization, as explained in the text. 132

5.14 SHG from pump: (left) light-light curve of 420 nm output as a function of pump pulse fluence at 840 nm showing a quadratic dependence, (right) spectrum of second harmonic generation from the 840 nm femtosecond laser 133

5.15 Second harmonic polarization: These polar plots were obtained by varying the excitation laser polarization for a fixed output polarization, using the setup depicted in figure 5.13. (a) SHG output is analyzed at a polarization parallel to the pillar, while the excitation polarization is rotated using a half wave plate. The polar plot angle is with respect to the growth axis of the pillar. The data very closely follows what is theoretically expected from the Wurtzite second harmonic tensor. Note that measuring over 180 degrees is sufficient, but a few more measurements were carried out for consistency. (b) Here, the SHG output is analyzed in an orientation perpendicular to the growth axis of the pillar. (c) and (d) Similar measurements on an upright pillar, for the orientation shown below each. 134

5.16 Resonant SHG from QW nanopillar: Experimental data for undercut laser showing resonance enhanced second harmonic from the lasing wavelength of the pillar (a) Lasing and SHG spectra from an exemplary undercut nanopillar. (b) light-light curve of the SHG output counts vs. the lasing counts shows a quadratic dependence. (c) Polarization analysis of the lasing mode (top panel) and second harmonic light (bottom panel) shows that the former is azimuthally polarized whereas the latter is radially polarized. 136
5.17 Resonant SHG from regrown nanopillars: (a) Plot of resonant second harmonic wavelength against fundamental lasing wavelength for multiple individual regrown nanopillars exhibiting internal SHG (all at room temperature and under pulsed excitation), (b) Lasing spectrum (top) and resulting SHG spectrum (bottom) from an exemplary regrown nanopillar showing resonant second harmonic generation. 137

6.1 Selective area growth of nanopillars: (left) schematic showing growth process, starting with lithographically defined nucleation positions. (right) Scanning electron microscope image of position controlled array of nanopillars, showing the regular placement of the pillars. The inset shows a closeup of a few individual nanopillars from the array. 141
6.2 TEM image showing the interface of the silicon and oxide: the crystal lattice is shown in the high resolution TEM image in the inset, with the transition from the amorphous oxide to crystalline InP clearly visible. 142
6.3 PL from InP position controlled nanopillars: (a) Excitation power dependent spectral series for an individual InP nanopillar, showing expected Wurtzite peak at 1.42 eV and exponential tails in the PL spectrum, (b) Comparison of PL spectral lineshape of randomly nucleated and selectively grown nanopillars, showing similarity. (c) Time resolved photoluminescence from an exemplary individual undoped InP nanopillar showing a good minority carrier lifetime on the order of 3-4 nanoseconds, (d) Room temperature pulsed lasing characteristic of an exemplary individual InP nanopillar, showing clear lasing transition below and above threshold. 144
6.4 RT, pulsed lasing of SAG nanopillar: (left) Excitation pulse energy dependent lasing spectral series showing that the nanopillar laser exhibits a clear transition at about 1.5 mJ/cm^2. (right) Lasing S-curve (log-log scale L-L curve) showing a sudden increase in peak counts above lasing threshold. 145
6.5 Absolute Luminescence counts: it is important to compare the absolute brightness of the selectively grown nanopillars with that of the randomly nucleated nanopillars. This shows that the Fermi level split for the selectively grown and randomly nucleated pillars is somewhat comparable, although the selectively grown pillars were typically slightly larger than the randomly nucleated nanopillars. 146

6.6 Optical characterization of nanopillars containing QWs: (a) excitation dependent PL spectra of InGaAs QWs in InP nanopillars, showing exponential tails and peak around 0.83 eV, approximately 1490 nm. (b) PL lineshape comparison of a commercial epi thin film (blue) with an ensemble of nanopillars, showing comparable exponential tails in the PL spectrum and attesting to the low inhomogeneous broadening. (c) Time resolved PL from the InGaAs QW showing a good minority carrier lifetime of 3-4 ns in the quantum wells. (d) Temperature dependent normalized PL spectra showing a typical Varshni dependence in the quantum well energ, which is displayed in top inset of (e). The temperature dependence of the Urbach energy can also be determined from these spectra (bottom inset, (e)). . 147
6.7 Pitch dependence of pillar dimensions: this schematic shows how the nanopillar dimensions vary systematically as a function of the pillar pitch. Due to precursor competition, pillars grown at a smaller pitch,(a) tend to be smaller and have thinner quantum wells than those at a larger pitch (b). This leads to a pitch-dependent systematic variation in the QW PL. 149
6.8 Pitch dependence of QW PL: (a) PL spectral dependence on pillar pitch, showing substantial blue shift as the pitch is reduced. The different amounts of inhomogeneous broadening reflect the number of pillars captured within the excitation laser spot. (b) The dependence can be captured using a simple finite quantum well model with a pitch dependent quantum well width. 150
6.9 Scalable fabrication of SAG nanopillars: (a) The full nanopillar core-shell stack is grown in a position-controlled manner on the silicon substrate, (b) isolation oxide deposited, (c) photoresist etch back mask followed by an oxide etch allows only the top of the oxide to be removed, (d) the gold pads are defined using patterning (aligned to markers on the growth substrate), followed by liftoff. A back contact is also deposited on the n-silicon substrate. (e) The pillars are then ready for electrical characterization. 152
6.10 Single pillar after fabrication: (left) Scanning electron microscope image of an individual nanopillar after gold deposition and liftoff, (right) matching schematic showing the different materials, starting from the outermost gold to the InP nanopillar within. 153
6.11 Microscope image of fabricated chip containing hundreds of devices. The chip has been organized to grow ensemble nanopillar devices (with some pitch variation) as well as single nanopillar devices. The dense black squares seen in the microscope image are the ensemble devices. They have L-shaped pads for providing electrical contact. Through the middle of the field of view, there is a line of single pillar devices with the inset showing one such device, with a small circular pad contacting the nanopillar. This pad has a nanopillar-shaped shadow on it from the line of sight gold evaporation. 153

6.12 Active region band diagram: the band offsets from core to shell for the nanopillar device are shown. Electrical contact is directly through the silicon substrate, with the type II band alignment aiding rather than impeding the preferred direction of current flow in the n-core, p-shell device. Note that a p-InGaAs contact layer is used in order to reduce contact resistance. 155
6.13 Measurement setup schematic: the single nanopillar device is electrically swept using a parameter analyzer, while simultaneously, the power is measured using a calibrated germanium photodiode. The photodiode is placed directly behind the objective, which has a high numerical aperture of 0.7. 156
6.14 Nanopillar LEDs with silicon transparent emission: (a) 3D-schematic of a single nanopillar device showing the active region cross section and device geometry. (b) Absolute measured light output from the nanopillar LED, as a function of current. The light output in 100s of nanoWatts was measured using the setup described in figure 6.13. The light output is quite linear with current (except at very low current injection), indicating high internal quantum efficiency. (c) Normalized electroluminescence spectra measured as a function of current injected. The small device can sustain a current as high as 2 mA, with blue shift due to band filling at the high current levels (showing that the Fermi level split exceeds bandgap qualitatively). (d) Calibrated electroluminescence counts can be directly converted to Fermi level splits, demonstrating that indeed the brightness exceeds what would be expected at transparency. 157
6.15 Photodetection of silicon transparent light: (left) I-V characteristics of multiple devices. (b) The QW p-i-n devices also show pronounced photodetection of 1310 nm illumination light, which is important for on-chip silicon photonics. 158

List of Tables

1.1 Band structure parameters for some commonly used III/V semiconductors. . . . 4
1.2 Survey of III/V lasers monolithically integrated on silicon, acronyms used in table: SLS: strained layer superlattice, DWELL: dots in a well, QDs: quantum dots, DFB: distributed feedback 16

2.1 Ideality factor dependence on recombination mechanism and injection level. Note that low level injection implies a doped semiconductor, in which the excess carrier concentration is much smaller than the doping level. High level injection refers to the case when the excess carrier concentration is much higher than the background doping level, typical for the undoped active region in a semiconductor p-i-n junction. 31

3.1 Calculated peak efficiencies for monochromatic LED sources and PV cells with corresponding optimized bandgaps. Note that the LED bias was chosen to be 50 mV below the bandgap, and the two different cases are chosen to contrast the effect of the solid angle penalty. 65

4.1 Table showing the effect of photoreceiver scaling on reducing the link energy consumption. The first line is the device presented in paper [39]. The rest have been optimized to minimize link energy. The last two rows show the effect of shrinking the photoreceiver size, and hence improving f_T and reducing capacitance. This would have to be done in a manner so as to avoid reducing light absorption. The calculations are based on equation 4.12 87

Acknowledgments

First and foremost, I would like to thank my research adviser Prof. Connie Chang-Hasnain for her mentorship. From her, I have not only learned the art of conducting research and communicating with my peers, but also the lifelong virtue of perceiving a holistic vision even in the most mundane task I might undertake. I am also grateful to my dissertation readers and qualifying committee members Prof. Eli Yablonovitch, Prof. Ming Wu and Prof. Liwei Lin for their insightful comments and suggestions. I would like to thank my department faculty academic advisor Prof. David Attwood for being incredibly approachable and sharing his thoughts on a variety of topics.

The research described here would not have been possible without funding and access to resources. Firstly, I thank the Berkeley Graduate Division Fellowship through the Anselmo J. Macchi fund for graduate students: for granting me the freedom to explore in my initial days in the PhD program. I also acknowledge the following funded research programs: E3S NSF award (0939514, 1335609), NRF Singapore (NRF-CRP14-2014-03), Tsinghua-Berkeley Shenzhen Institute and US DOE Sunshot (DE-EE0005316). All the fabrication and processing described in this thesis has been carried out at the Marvell Nanofabrication Lab at Berkeley, and I am grateful for the support provided by Bill Flounders, Kim Chan, Richelieu Hemphill and many other staff members. I also acknowledge the support of the National Center for Electron Microscopy at LBNL.

This work was highly collaborative, and I particularly want to acknowledge the material growth, substrate preparation and MOCVD maintenance efforts of Wilson Ko, Kar Wei Ng, Fanglu Lu, Fan Ren, Saniya Deshpande, Emil Kolev, Daria Skuridina and Jiaxing Wang. To Wilson, from whom I learned a great deal about being a good engineer and paying careful attention to detail. To Thai Tran, Linda Kun Li (my first mentor) and April Hao Sun for their guidance on working at an optical bench and interpreting experimental data. To the undergraduates and younger PhD students I have had the opportunity to mentor and who have helped me on significant portions of this work: Eric McShane, Willi Mantei and Jonas Kapraun. To Gilliard Malheiros-Silveira, for all the discussions and nanophotonics insights. To the many folks in CCHG and the other Optoelectronic groups for the excellent collaborative environment at Berkeley (and beyond): Roger Chen, James Ferrara, Vidya Ganapati, Christopher Keraly, Ryan Going, Adair Gerke, Patrick Xiao, Greggory Scranton, Seth Fortuna and Phillip Sandborn.

To my incredible friends in grad school for looking out for my emotional and physical well being, commiserating when things were looking challenging and celebrating when those challenges could be overcome. To Nishant Totla, for asking me how much I have written nearly every single day. To my family, for helping me cultivate scientific temper, perseverance and my core beliefs that have sustained me and made this undertaking possible.

Chapter 1

Introduction

Our ability to generate, manipulate and detect photons has been instrumental in humanity's technological progress. As a concrete example that captures a large cross section of photonics and optoelectronics, let us consider telecommunication. Telecommunication or communication over long distances has been enabled by diode lasers that can produce spatially and temporally coherent light. The light then carries information over anywhere between 10's of meters to 1000's of kms, through high capacity and low loss optical fiber. Depending on the length scale involved, the information is imprinted using direct electrical modulation of the laser, or through electro-optic modulators operating at 10s of Gb/s. On the receiver side, the photons are detected and converted to electrical signals using efficient, high speed photodetectors. As these advanced optoelectronic devices become more energy efficient, the argument for replacing electrical wires with optical links is becoming more and more compelling at shorter and shorter length scales, leading to an outpouring of work in the field of *nanophotonics*. Note that the key to these remarkable advances are the basic building blocks: high performance optoelectronic devices based on direct bandgap III-V materials that serve as an ideal interface betweeen light and matter.

Before we take a closer look at what makes III-V materials particularly suitable for optoelectronics, it is worth examining some other ubiquitous applications of optoelectronic devices:

1. **Photovoltaics**: The vast amount of solar energy that the Earth receives is sufficient to meet global energy requirements many times over. A practical estimate of the annual potential of solar energy is 50,000 exaJoules (1 exaJoule = 10^{18} Joules) per year, which is an order of magnitude higher than the $\sim$1000 exaJoule annual demand. Currently, the world record for single and dual junction photovoltaic (PV) cells is held by Gallium Arsenide based solar cells. It turns out that the quantum efficiency of light emission is fundamentally related to the efficiency of photovoltaic energy conversion. No surprise then that the most efficient solar cells are based on III-V materials related to GaAs. In applications such as space vehicles and satellites where efficiency is the most important metric, advanced multijunction photovoltaic cells with efficiency around 30-40% are

utilized for solar energy harvesting. III-V materials may also be particularly useful for harvesting energy from indoor illumination sources to power the multitude of devices that will soon be connected to the Internet of Everything.

2. **Lighting**: The nobel prize in physics in 2014 was awarded for the invention of highly efficient and bright light emitting diodes (LEDs) based on the Gallium Nitride ((In,Al)GaN) material system. Incandescent light bulbs are particularly inefficient and light generation is merely incidental to heat generation. Compact fluorescent lights also typically have an efficiency of 7-10%, along with adverse health and environmental impacts due to mercury content. Light emitting diodes have a 50-100% external quantum efficiency, leading to dramatic energy savings. The current challenge in nitride based materials is to extend solid state lighting to green wavelengths (the green gap) and opening up new spectral windows in the near infrared and ultraviolet.

3. **3D scanning**: Optoelectronic devices are also important for sensing, ranging, non-destructive testing and 3D scanning. Laser scanners are particularly useful for inferring the 3D shape of an object. Time of flight sensing at optical wavelengths is extremely pertinent to the explosion of self driven cars that we are currently witnessing. Advanced signal processing and scanning techniques can be used to determine the range of various objects and create a 3D point cloud of the surrounding environment. Highly directed, coherent laser sources, along with highly sensitive photodetectors, are important for extending the range of such 3D scanning techniques known as LiDAR (Light detection and ranging). Further, in the consumer space, the explosion of mixed reality devices has relied on advanced 3D sensing techniques. It is essential to accurately measure the orientation and position of the head mounted display in order to project the correct 2-dimensional images to the user: making the difference between a jittery, nausea-inducing experience and 'true presence' where the user is convinced into thinking that she is in a virtual reality. This is a rapidly developing area, and the most advanced virtual reality headsets (eg: HTC vive) rely on multiple lasers, LEDs and infrared photodetectors on both the headset as well as external 'lighthouses' for accurate pose and position estimation.

4. **Datacom and Telecom**: The physical layer of the internet consists of optical fibers that carry data at Terabits per second. This is enabled by complex photonic integrated circuits that both transmit and receive data. Coherent light is generated by lasers based on III/V semiconductor active materials. Each wavelength in the telecom band is directly modulated at 30-50 Gb/s using electro-absorption modulators. On the receiver side, with the advent of coherent communication, we have a local oscillator that allows for advanced modulation schemes such as quadrature phase shift keying. The information embedded in the optical domain is converted into electrical data using high speed and highly sensitive III/V based photodetectors. Given the explosion of information bandwidth (driven by consumer demand), it has recently made sense to move to photonic integrated circuits, where many hundreds of components are fab-

ricated on the same chip. A similar integration argument is also starting to make sense for higher volume *datacom* applications for optical communication in data centers, which is currently dominated by vertical cavity surface emitting lasers that are not integrated on chip. Silicon photonics may present some advantages given the high volume of datacom. However, the laser is still a key requirement and in the foreseeable future will be based on III/V compound semiconductor materials.

5. **Chemical sensing**: A tremendous advantage of III/V compound semiconductors is the ability to engineer electronic states using precise control of the bandgaps and layer thicknesses. Hundreds of periods of crystal lattice matched heterostructures can be grown into *quantum cascade lasers* (QCLs) with precisely engineered electronic levels. These QCLs exploit intersubband transitions that allow lasing operation within mid infrared and even terahertz regimes. These spectra are very interesting for chemical and material sensing due to the presence of material spectral signatures and are currently being implemented for the detection of explosives and illicit substances.

6. **Infrared imaging**: While silicon based CMOS image sensors are excellent in the visible range, their usefulness rapidly diminishes for wavelengths beyond 1000 nm due to the bandgap of silicon at 1.1 eV. In particular, there are several important application spaces for near and mid-wave infrared imaging that would require 2D detector arrays. The thermal radiation emitted by warm blooded animals is also in the mid-wave infrared region (typically few microns wavelength) as are some spectral windows of importance in security and defence applications. Astronomy, LIDAR and specific microscopy applications would also benefit from inexpensive large scale focal plane detector arrays. Further, bandgap engineering allows for the design of quantum dot and quantum well infrared photodetectors with excellent sensitivity tuned within the mid-IR wavelengths of interest. However, due to the expensive III-V substrate and large pixel arrays required, these image sensors continue to remain rather expensive and are limited to niche applications thus far.

These examples illlustrate some of the ways in which III-V based optoelectronic devices have had a significant impact on the technologies that enable the Internet, solid state lighting, bar code readers and scanners at airport security. Several other applications such as water purification, photoelectrochemical water splitting, quantum key distribution, mid-IR array detectors and non-linear comb generation for advanced spectroscopy continue to emerge. Given the plethora of applications enabled by III/V active optoelectronic devices, it is important to take a closer look at the fundamental processes through which light interacts with matter in these compound semiconductor materials.

1.1 Optical Processes in Semiconductors

Electronic states in a semiconductor crystal can be described in terms of their reciprocal lattice dispersion. In equilibrium, the lowest energy states above the Fermi level constitute the conduction band. The conduction band is analogous to the lowest unoccupied molecular orbital (LUMO) for a molecule. Due to the tail of the Fermi distribution, the lowest states in the conduction band are occupied at room temperature. Typically, it is sufficient to describe the $E(k)$ dispersion of these states with respect to the reciprocal lattice k using a simple parabolic effective mass model $E = \frac{k^2\hbar^2}{2m_c}$ where k is the reciprocal lattice vector, m_c is the conduction band effective mass and $\hbar$ is the reduced Planck's constant. Similarly, the highest states below the Fermi level are unoccupied and constitute the valence band, similar to the highest occupied molecular orbital (HOMO). The dispersion relation for these states can be conveniently described by an inverted parabolic dispersion, $E = -E_g - \frac{\hbar^2(k-k_o)^2}{2m_v}$, also parametrized by a valence band effective mass m_v. The energy gap E_g is the difference between the peak of the valence band and the minimum of the conduction band. In case the reciprocal lattice vector for the minimum of the conduction band and the maximum of the valence band are the same we have $k_o = 0$. Semiconductors of interest for optoelectronics satisfy this condition and are known as *direct bandgap semiconductors*. Typically, several semiconductors formed by alloying group III and group V elements of the periodic table satisfy this condition. Some of these parameters for III-V semiconductor alloys of interest are indicated in the table below.

Semiconductor	Direct?	E_g	m_c
GaAs	yes	1.42 eV	$0.063m_e$
InP	yes	1.34 eV	$0.08m_e$
$In_{0.53}Ga_{0.47}As$	yes	0.74 eV	$0.041m_e$
AlAs	no	2.4 eV	$0.71m_e$
$Al_{0.3}Ga_{0.7}As$	yes	1.8 eV	$0.088m_e$

Table 1.1: Band structure parameters for some commonly used III/V semiconductors.

In direct bandgap semiconductor crystals, the minimum of the $E(k)$ dispersion in the conduction band lines up with the maximum of the valence band. This is important because of the dual requirements for conserving energy as well as momentum in light matter interaction. Photons carry sufficient energy to be of interest for interactions involving typical semiconductor bandgaps. However, the momentum carried by photons is negligible compared to the crystal momentum of electrons. Therefore, electronic states need to have the same k-vector value for strong light interaction. More quantitatively, a photon with energy of 1 eV has a wavelength of 1.24 μm, which corresponds to the excess crystal momentum that an electron would have merely 12 μ eV above the band edge. An electron that is 25

meV (the thermal energy) above the band edge has excess crystal momentum the same as that of a high energy photon with an extremely small wavelength of picometers. Therefore, optical transition probabilities in indirect bandgap semiconductors are typically quite small and require interactions with phonons or defect levels to ensure momentum conservation. This lies at the heart of the utility of direct bandgap semiconductors.

Given this background, we are now in a position to examine the optical processes in III/V compound semiconductos. There are three important ways through which photons interact with electronic states in a semiconductor crystal: spontaneous emission, absorption and stimulated emission. These are the main linear processes and can reach very high efficiencies in direct gap semiconductors. We will later see that this thesis is organized along the lines of these fundamental processes. Chapters 2, 3 and 4 are closely related to absorption; Chapter 5 to stimulated emission and Chapter 6 to spontaneous emission. There are some other useful optical nonlinearities such as second harmonic generation and four wave mixing that are also useful. The main linear optical processes and their rates are summarized below:

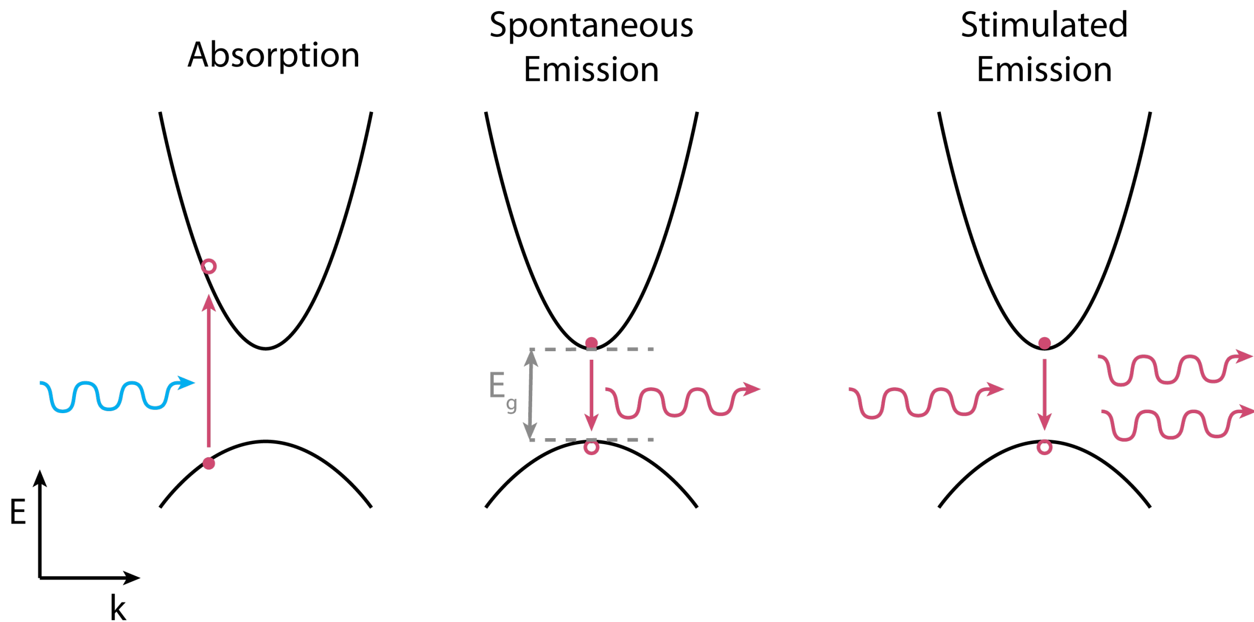

Figure 1.1: The main optical processes in a direct gap semiconductor

1. **Absorption**: When a photon with energy above the direct bandgap is incident, it can cause an electron to transition from the valence band (VB) to the conduction band (CB). This process requires both energy and momentum to be conserved and the absorption rate (equivalently electron-hole generation rate) can be calculated using Fermi's golden rule using time dependent perturbation theory. On integrating over k-space and applying energy conservation, the absorption rate per unit volume can be described for interband transitions as follows:

$$R_{abs}(\hbar\omega) = \frac{2\pi}{\hbar}|H'_{ba}|^2\rho_r(\hbar\omega - E_g)f_v(1 - f_c) \quad (1.1)$$

where $\hbar\omega$ is the photon energy, $\hbar$ is the reduced Planck's constant, $|H'_{ba}|$ is the optical matrix element derived from time dependent perturbation theory and is proportional to the intensity of the electric field. The energy and momentum conservation requirement allows for transitions only between CB and VB states separated by exactly the photon energy and vertically at the same reciprocal lattice vector. This requirement integrates the permitted states into a reduced density of states for the transition given by $\rho_r(\hbar\omega - E_g)$ which has the same form as the density of states for a parabolic band, but with a reduced effective mass. Further, the transition depends not only on the existence of the states, but also the probability that a valence band state is occupied and that the corresponding conduction band state is unoccupied. These are given by f_v and $1 - f_c$ from the Fermi-Dirac distribution of the form $f_c = 1/(1 + e^{\frac{E-F_c}{k_BT}})$, assuming quasi Fermi levels F_c and F_v for the CB and VB states. The term $|H'_{ba}|^2$ is proportional to the electric field squared, and hence the number of photons incident. Then, a simpler expression can be written for the absorption rate:

$$R_{abs}(\hbar\omega) = Bn_{ph}(\hbar\omega)f_v(1 - f_c) \quad (1.2)$$

where the constant B is termed the Einstein B-coefficient and n_{ph} is the local photon density. The absorption of photons can also be described in terms of an absorption coefficient that causes optical intensity to attenuate exponentially through the propagation distance. This coefficient is typically around $10^4 cm^{-1}$ for direct band gap semiconductors and can lead to highly efficient photodetectors and photovoltaics using only a thin absorbing layer. The amount of light absorbed in a few microns of III/V direct gap material is usually comparable to 50-100 microns of silicon. This particularly has advantages for high speed photodetectors, where the transit time can be much lower for a thin absorbing layer.

2. **Stimulated Emission**: Stimulated emission is the dominant optical process in a laser above lasing threshold. When a photon encounters an electron in the CB, it could stimulate the electron to transition from the CB to the VB and emit a photon. The second photon emitted is exactly identical to the incident photon: the transition energy has to therefore match that of the incident photon, and the transition needs to be direct in reciprocal space. This is exactly the inverse of the absorption process, where instead of unoccupied CB states, we require occupied CB states and empty VB states:

$$R_{st}(\hbar\omega) = Bn_{ph}(\hbar\omega)(1 - f_v)f_c \quad (1.3)$$

where B is identical to the constant in 1.2, due to the symmetry of the process. The main difference is in the population terms. We require unoccupied states in the valence band and occupied states in the conduction band for the stimulated emission process to occur. This requires a quasi-Fermi level split, where the CB and VB are not in equilibrium. If we subtract equations 1.2 from 1.3, this tells us the rate of generation of photons due to excitation of the semiconductor, or equivalently the gain:

$$g(\hbar\omega) \propto (R_{stim} - R_{abs})/n_{ph}(\hbar\omega) = B(f_c - f_v) \tag{1.4}$$

which is proportional to the *Fermi inversion factor* $f_c - f_v$ corresponding to the difference of occupied states in the CB and VB across the energy gap for optically permitted transitions. The requirement for gain is then that the Fermi inversion factor is positive. On simplifying this expression further, if we have that the CB and VB Quasi Fermi levels are at F_c and F_v respectively, and if the optical transition is from state with energy E_2 in the the CB into state E_1 in the VB, then the condition for gain is:

$$F_c - F_v > E_2 - E_1 \tag{1.5}$$

Therefore, to see any gain at all, we require that the Fermi level split exceeds the bandgap (minimum possible value of $E_2 - E_1$). This is known as the Bernard-Duraffourg condition. As the Quasi Fermi level split increases, we notice that more and more states can provide optical gain, and all photons with energy less than the Fermi level split $F_c - F_v$ will experience optical gain. When we have a low loss optical resonator along with optical gain, there is a possibility of photons to be amplified as fast as they are lost from the cavity. This situation allows for stimulated emission in a single cavity mode to become the dominant optical process, which is known as lasing. Lasers are highly desirable due to the high intensity, coherence and fast modulation speed available.

3. **S**pontaneous Emission An electron in the CB can transition to an unoccupied VB state spontaneously and emit a photon corresponding to the energy difference. A full description of the process requires a quantum optics treattment based on ground state fluctuations. However, we can arrive at some understanding based on detailed balance of these optical process. We can describe the rate of the spontaneous emission process based on the same population statistics as stimulated emission, while recognizing that the rate is independent of light intensity (or equivalently, photon density):

$$R_{spon}(\hbar\omega) = A(1 - f_v)f_c \tag{1.6}$$

where the constant A is known as the Einstein A coefficient. If we consider steady state, where the rate of generation of photons matches the rate of absorption, we have the following relationship:

$$R_{stim} + R_{spon} = R_{abs} \rightarrow n_{ph} = \frac{A}{B}\frac{f_c(1-f_v)}{f_v - f_c} \tag{1.7}$$

This expression can be further simplified to describe the photoluminescence intensity from a semiconductor surface. We will consider this and detailed quantitative photoluminescence experiments in **chapter 2**. However, it is worth mentioning that spontaneous emission underlies the large solid state lighting industry. High brightness emission with high external quantum efficiency can be obtained from InGaN quantum well heterostructures in a GaN-based LED structure. This is expected to lead to tremendous energy savings.

Having described the main linear optical processes in semiconductors, it is worth pausing to consider a few non-linear optical processes of interest too. Nonlinearities could involve second order effects such as sum and difference frequency generation from photons. This is commonly used in the green laser pointer, where photons at wavelength 1064 nm can combine to generate coherent light at 532 nm in a cavity enhanced condition. Terahertz generation using the same nonlinearity is also possible with sufficiently intense light. III/V semiconductors are particularly interesting for second harmonic generation because they lack inversion symmetry (as opposed to silicon). Non-centrosymmetry is a requirement for second harmonic generation, based on symmetry arguments. Having summarized some of these important optical processes and the utility of III/V semiconductors, it is important to consider what we can learn from the silicon CMOS manufacturing ecosystem to truly make this technology ubiquitous and successful in the same manner as microelectronics.

1.2 Photonic Integration

Silicon based integrated circuits are manufactured using precisely controlled nanofabrication processes that have been developed over decades. These integrated circuits are packaged as microprocessors and permeate our lives through our smartphones, laptops, sensors (and other *Internet of Things* devices). The size of the semiconductor industry has grown to be $335 billion in the year 2015. The sheer volume of these devices justifies the kind of economic investment that is necessary for building and maintaining such advanced billion-dollar fabrication facilities and clean rooms. There exist entire industries based purely on manufacturing capital equipment for semiconductor giants such as Intel and TMSC. The message in all these details is that any new technology that can leverage the silicon based semiconductor manufacturing ecosystem will have a tremendous advantage brought about from decades of learning.

Integration however does not need to be on a silicon-based platform. Indium Phosphide based photonic integrated circuits have become extremely important in telecommunication applications. All the optical components required for high data rate communication: including lasers, modulators, photodetectors, and various passive components can be integrated

on the same monolithic semiconductor chip. There are several advantages to this approach in terms of scaling up functionality and bandwidth on the same platform. Additionally, the volume for such telecommunication products is low and does not merit the scale of the silicon manufacturing ecosystem. However, there exist certain applications which would benefit tremendously from CMOS integration. We will consider two of these silicon photonics integration areas: optical interconnects and image sensor arrays.

On-chip Optical Interconnects

Transistor scaling and the explosion of data throughput in integrated circuits has far outstripped our capability to communicate information on chip. Signaling between different parts of a microprocessor is achieved through metal interconnects that can be modeled as transmission lines carrying electromagnetic waves with a phase velocity close to that of light. However, in contrast with an optical fiber or waveguide based link, the energy consumption to transmit information is determined by the distance traversed. More specifically, in the case of a resistive-capacitive transmission line, if the CMOS line voltage is V and the total capacitance of the line is C, we would require a total energy of CV^2 to charge the line. This is the energy consumed per bit of information transmitted and is split equally between capacitive charging and resistive dissipation.

Further, the charging time is limited by the RC time constant of the transmission line, which is proportional to the aspect ratio: length-squared divided by cross-sectional area of the wires. Signal attenuation due to the RC delay can be somewhat mitigated by using logic buffers called repeaters that amplify the signal and allow longer wire lengths. However, this is at the expense of the power consumed by the repeater. Additionally, the repeater also adds some time delay. Hence, to transmit information over longer distances, we require thicker metal wires that maintain a certain aspect ratio of area divided by length-squared. This simple physical problem has led to a complex set of design considerations in large scale integrated circuits, where there are currently more than 10 layers of metal interconnects, with the short and thin metal being closest to the device layer and the longer global interconnects being on higher layers of the *interconnect stack*. Further, due to the increased complexity of integrated circuits, the wire length has been progressively increasing, along with a concomitant increase in the power consumption of the metal interconnects. The capacitance of metal interconnects is determined most strongly by the length and scales approximately as $200aF/\mu m$. For a 1 V CMOS line voltage and total interconnect length of roughly 1 m, this leads to a power consumption of 20 nJ/bit. If we assume a clock frequency of roughy 3 GHz, this is a total power dissipation of 60 W. The power budget for the entire chip is around 150 W. Scaling only exacerbates this problem as the total wire length continues to increase (as per calculations based on Rent's rule [1]) while capacitance per unit length stays constant, and we end up with more than 80% of the power consumption in a microprocessor chip being attributed to the interconnects. This famous probem has been described as the *interconnect bottleneck*.

The same problem was also encountered at longer distances and the solution there has been achieved by using optics for communication. Optical fibers have extremely low loss and the energy consumption of an *optical link* depends primarily on the efficiency of the transmitter and receiver. The transmitter is typically a laser and the receiver is a photodetector connected to a transimpendance amplifier. Miller has commented on some of the requirements for making these devices efficient enough to replace short distance electrical wires with optical links [2]. One metric is to suggest that we would like the optical link to consume 10x less energy compared to the electrical link at the same length scale. Using the capacitance as described above, this energy metric is approximately 2 pJ/bit/cm, or equivalently 2 mW/GHz/cm. Thus, for a compelling optical link on chip (centimeter scale), we would need to have energy consumption around 200 fJ/bit or less. In **chapter 4** we describe how this could be possible by considering the transmitter and receiver energy consumption, as well as a sensitivity requirement based on voltage swing. It is most likely that an optical link on chip will be used for the longest global interconnections, and for distributing the clock signal without electronic interference.

In order to consider a slightly more detailed picture, we can take inspiration from the way telecommunication systems are organized. Typically, a single mode optical fiber or integrated nanophotonic waveguide can transmit multiple different laser wavelengths within specific communication bands. For telecommunication over optical fiber, the C-band between 1530-1565 nm has been standardized since these wavelengths can be amplified using erbium doped fiber amplifiers. Multiple wavelengths in this band are coupled to the same single mode fiber using a passive wavelength multiplexing device. These fibers can often be on the order of 1000 kilometers in length and traverse between continents. On the receiver side, the wavelengths are separated into individual channels using a demultiplexer. These individual wavelength channels are terminated by a photodetector followed by a receiver circuit that outputs an electrical signal. This scheme was transformative due to its scalability and is known as *Wavelength Division Multiplexing*. Given the extremely large and rapidly increase data throughput across chips, it is worth understanding how optical links can scale their communication bandwidth density: and WDM seems like a logical progression to optical interconnection. Currently however, the shortest distance optical links in data centers are dominated by vertical cavity surface emitting lasers that couple to multi mode fiber. These VCSELs are typically separate components that are packaged as a transmit optical subassembly (TOSA). As the component volume and bandwidth density requirements scale, the argument for *silicon photonics* becomes more encouraging, where the multiple different wavelengths are generated and modulated on the same silicon-based photonics chip and connected over short distances to other parts of the data center. For this approach, and also for on-chip optical interconnects, it is important that the laser light can be routed using silicon-based waveguides and needs to be within the silicon transparent wavelength range: typically $1.2\mu m$ and higher. In **chapter 6** we describe how we can achieve silicon transparent light emitting diodes and high quality active material. Additionally, in **chapter 5** we describe how we have demonstrated an optically pumped laser directly grown on silicon as well as some initial qualitative demonstrations on coupling emission into silicon based waveguides.

Electronic-photonic integration for imaging, sensing and mixed reality

In the previous section we have stressed on the ability of photons to transport information. Here, we consider photons as an effective way to image, characterize the world around us as well as help us interact with information in a three dimensional manner, as we are used to interacting with the real world (as opposed to interacting with screens).

Firstly, we consider an imaging application: the development of novel cameras that provide information richer than current frame based sensors. This application is particularly well suited for integration due to the requirement for combining a large number of pixels in order to produce a spatial array of sensor pixels. Such a sensor array could be placed at the focal plane of an imaging lens, and would then be known as a focal plane array. One direct application for the integration of III/V materials would be our ability to sense new wavelength ranges on a silicon based platform. Current InGaAs based focal plane arrays need to be fabricated on an expensive InP substrate. Integrating III/V materials to detect in the shortwave infrared (using direct gap photodetectors) as well as into the mid infrared (using quantum well infrared photodetectors) would significantly help the penetration of such cameras into new applications. There continues to be great interest in extending the detection wavelength range of CMOS sensors, and progress on photoconductive broadband sensor arrays with 2-dimensional materials such as graphene has been demonstrated[3]. However, a high frame rate III/V based sensor array on silicon with sufficient absorption and heterostructure based bandgap engineering would be a major development and would likely lead to cost effective multi-spectral and hyper-spectral image sensors.

Further, currently ubiquitous CMOS image sensors are highly uniform pixel based quantitative light sensors and tend to collect vast amounts of redundant data. For a simple contrast, the human eye and visual perception system are dramatically different from CMOS-based sensor arrays. The human retina has a spatially varying resolution, with the best angular resolution around the *fovea*. The visual system is also more sensitive to changes or variations in the scene rather than the scene itself. Additionally, the human eye has a remarkable dynamic range: capable of seeing in the brightest sunlight as well as extremely dark rooms. These characteristics are partially encoded at the hardware level in terms of the firing of the rods and cones, and partially in the visual cortex of the brain. One interesting new camera design is the *event camera*, in which every pixel has a detection circuit built in that sends out electrical data only when the pixel detects a change in light intensity. This vastly reduces the data throughput through the camera and allows for microsecond changes to be detected[4]. Similarly encoding more functionality at the hardware level, perhaps using novel materials, would allow for better system design and improved tradeoffs in the system design.

Lastly, creating a true hologram that presents realistic 3-dimensional visual cues would be extremely desirable for applications in mixed or augmented reality. Mixed reality is particularly important because it may impact how we interact with richer 3-dimensional information and how we communicate. To present realistic depth cues, we need to make sure that both the angular and spatial distribution of light rays is reproduced correctly compared

to what we would expect from the same 3D object. Initial progress has been made on this kind of an integrated *lightfield display* using multi-directional backlighting[5] based on diffraction gratings, as well as a nanophotonic phased array[6]. Both these approaches rely on silicon photonics foundry processes. In the nanophotonic phased array, light from a laser is distributed between a large number of dielectric antennas with precisely tuned delays. The ability to precisely control the phase delay for each of the dielectric antennas allows for wavefront control. Leveraging these techniques while introducing III-V active materials would be incredibly beneficial because of the added advantage of having the light source directly on chip.

Given these examples, it becomes clear that monolithically integrating optically active material with silicon-based integrated circuits would have tremendous implications. We now focus on the technological challenge of monolithic integration.

1.3 Monolithic Integration Techniques

The main challenge with silicon based photonic integration (as opposed to InP based) is that the light source can not be fabricated using silicon. As discussed in section 1.1, silicon does not have a direct bandgap and light emission processes tend to be extremely inefficient since they typically require some other process to make up for the momentum mismatch in the indirect gap transition. Another CMOS process compatible semiconductor is Germanium. The situation with Germanium is slightly better, the direct gap is only 140 meV above the indirect gap. Using strain, doping and other forms of bandgap engineering such as alloying with Tin, it is possible to improve the efficiency of optical processes. In particular, a monolithic electrically pumped Germanium laser was produced by engineering an extremely high doping level, producing a small gain of 50 cm^{-1} [7], [8]. The threshold current density of this laser was however two orders of magnitude higher than that of conventional III/V based lasers, making it impractical for sustained operation. More recent progress has been reported on alloying with Tin, where it has been claimed that a true direct bandgap has been achieved using purely group IV semiconductors and optically pumped lasing has been demonstrated[9]. At a tin alloy concentration of 9%, the GeSn alloy transitions from indirect to direct bandgap. However, the indirect gap still remains energetically close to the direct gap. At 13% tin, the indirect gap is only 30 meV above the direct, and thermally assisted non-radiative recombination processes remain a major issue. Optically pumped pulsed lasing has been demonstrated up to 90 K, and further work is necessary before this becomes comparable to the quality of III/V materials.

The most significant challenges of integrating III/V materials in a monolithic fashion are the large lattice mismatch with the silicon substrate and the high temperature required for growth. GaAs has a lattice constant 4% larger than that of silicon. InP is even worse, with an 8% lattice mismatch, that rules out the possibility of high quality thin film epitaxy due to the low critical thickness permitted by this level of strain[10]. GaP, with lattice constant closer to silicon is unfortunately indirect bandgap. Further, the high temperature

of organometallic vapor phase epitaxy is incompatible with CMOS back end integration processing requirements. Back end integration refers to the processes that are performed after the main transistor device layer is fabricated. Such processes include the fabrication of multi-layer metal interconnects, assembly, testing and packaging. The typical temperature budget is limited to $400 - 450°$, along with some time constraints dependent on the temperature. This is to ensure that the carefully controlled dopant distribution profiles are not affected due to the thermal stress. However, typical III/V epitaxial growth temperature is on the order of $600-700°$, which violates this thermal budget. Further, the considerable mechanical stress that builds up due to the different thermal expansion coefficients is also an issue. We will also shortly examine some of the ways this can be mitigated, even for thin film epitaxy, however it remains a considerable challenge.

One of the ways to circumvent challenges related to monolithic integration is to integrate material in a heterogeneous manner, typically through approaches such as wafer or chip scale bonding. This is currently the approach being pursued for integrating laser sources on silicon photonics[11]. While it is challenging to integrate the pre-fabricated laser dies onto silicon waveguides for optical coupling, the approach followed by Fang *et al.* uses evanescent coupling of the light from a silicon based cavity into the electrical pumped III/V gain region. Although the modal gain is low for such an evanescent coupling approach, it is sufficient to produce high performance electrically injected lasers. The alignment is less critical since the III/V is not patterned. It remains to be noted if this approach can scale and use the full benefits of integration. One known challenge in the heterogeneous bonding approach is the requirement for a thin and uniform bonding layer through which the field is evanescently coupled. Firstly, the thermal resistance of this layer leads to issues with laser performance and reliability. Secondly, the size and cost of the III/V growth substrate leads to poorer economies of scale compared to direct growth on silicon.

Hence, there is tremendous interest in growing high quality III/V gain material directly on silicon. In the following, we will summarize some of the approaches for monolithic integration on silicon, with specific details presented in Table 1.2.

Wave-length	Substrate	Buffer	Active Region	Growth Tempera-ture	Laser structure	Lasing conditions	Refer-ence
1.3 μm	GaAs on off-cut Ge virtual substrate	none	InAs/ In-GaAs/ GaAs DWELL	510-680°C	Broad area, edge emitting	RT CW electrical	[12]
1.27 μm	GaAs off-cut Si virtual substrate	InAlAs/ GaAs SLS	InAs/ GaAs QDs	510-610°C	Broad area, edge emitting	RT pulsed electrical	[13]

1.31 μm	GaAs on off-cut Si virtual substrate	InGaAs/ GaAs SLS	InAs/ GaAs QDs	340-610°C	Broad area, edge emitting	120°C CW electrical	[14]
1.3 μm	GaAs on exact [001] Si virtual substrate	InGaAs/ GaAs SLS	InAs/ In-GaAs/ GaAs DWELL	600-700°C	Broad area, edge emitting	RT CW electrical	[15]
1.3 μm	Ge on off-cut Si virtual substrate	none	InAs/ In-GaAs/ GaAs DWELL	∼600°C	Ridge waveguide	RT CW electrical	[16]
1.3 μm	GaAs on V-grooved exact [001] Si	none	InAs/ In-GaAs/ GaAs DWELL	∼600°C	4 μm diameter micro-disk laser	RT CW optical pump	[17]
1.2 μm	GaAs on V-grooved exact [001] Si	none	InAs/ In-GaAs/ GaAs DWELL	∼600°C	1 μm diameter micro-disk laser	10 K CW optical	[18]
1.3 μm	GaAs on V-grooved exact [001] Si	none	InAs/ In-GaAs/ GaAs DWELL	∼600°C	50 μm diameter micro-disk laser	100°C CW electrical	[19]
1.55 μm	InP on GaAs buffer on exact [001] Si	AlGaAs/ GaAs SLS	InAs/ In-GaAs/ InAl-GaAs DWELL	not reported	1.5 μm diameter micro-disk laser	60°C pulsed optical	[20]

1.55 μm	InP on GaAs buffer on exact [001] Si	InAs/ InAlGaAs dislocation filter	InAs/ InAlGaAs QDs	430-630°C	4 μm diameter micro-disk laser	LT CW optical	**Shi2017a**
1.25-1.27 μm	GaAs on V-grooved exact [001] Si	none	InAs/ InGaAs/ GaAs DWELL	490-800°C	Ridge waveguide	RT CW electrical	[21]
0.93 μm	InP on V-grooved exact [001] Si	none	bulk InP	$\sim$ 550°C	DFB laser (45 μm length)	RT pulsed optical	[22]
1.32-1.36 μm	InP on V-grooved exact [001] Si	none	bulk InGaAs (60 nm DH) on InP	$\sim$ 550°C	DFB laser (100 μm length)	RT pulsed optical	[23]
0.95 μm	[111] Si	none	bulk InGaAs DH	∼450°C	650 nm diameter Nanopillar	RT pulsed optical	[24]
0.97 μm	exact [001] Si, with MOSFETS	none	bulk InGaAs DH	$\sim$ 410°C	850 nm diameter Nanopillar	RT pulsed optical	[25]
0.91 μm	[111] Si	none	bulk InP	∼450°C	800 nm diameter InP Nanopillar	RT pulsed optical	[26]
1.28 μm	[111] SOI	none	InGaAs/ InP QW	∼450°C	950 nm diameter InP Nanopillar	LT pulsed optical	[27]

1.22 μm	[111] Si	none	InGaAs/ InP QW	∼450°C	950 nm diameter InP Nanopillar with silicon undercut	RT pulsed optical	[27]
1.22 μm	[111] Si	none	InGaAs/ InP QW	∼450°C	950 nm diameter InP Nanopillar with silicon undercut	LT CW optical	[27]

Table 1.2: Survey of III/V lasers monolithically integrated on silicon, acronyms used in table: SLS: strained layer superlattice, DWELL: dots in a well, QDs: quantum dots, DFB: distributed feedback

One of the major challenges that needs to be addressed for monolithic integration is the presence of crystal defects due to lattice relaxation. These defects can be classified on the basis of their direction of propagation and the specific crystal configuration associated with each kind of defect. The challenge is that these defects typically act as non-radiative recombination centers and quench electroluminescence. These defects are detrimental to device operation, and typically lead to reliability issues over long periods of operation. The approach followed by *Liu et al.* in [12] is to firstly use a Germanium virtual substrate grown on silicon. This substrate is first grown on the silicon, and then used for the growth of GaAs, which has a reduced threading dislocation density due to the low lattice mismatch between Germanium and GaAs ($\sim 0.08\%$). Further, anti-phase boundaries (common in the case of III/V growth on group IV substrate irrespective of lattice mismatch) are mitigated using a 6° off-cut substrate and a Gallium pre-layer for nucleation. A 5 layer dots-in-a-well gain region was used to obtain optical gain, leading to a 1.3 μm electrically injected laser. Another approach followed for the same material system by Wan *et al.* proposes to completely eliminate both the Germanium virtual substrate as well as the off-cut required for hetero-epitaxy. This method has been termed the GaAs on V-grooved silicon approach (GoVS). GaAs is grown on a silicon substrate patterned with V-shaped grooves that serve to trap threading dislocations and prevent them from propagating into the active region. This approach has shown promise, with a reduction of dislocation density to $\sim 10^8$ cm^{-2}. This defect density is typically too high for quantum well gain, however a dots in a well structure is more resistant to defect formation due to the low density of quantum dots. Even if a defect passes through the active region, it ends up affecting only a few dots, and the detrimental

effects are expected to be spatially localized. Several lasers, both optical and electrical have been demonstrated using this approach [17], [18], [19], [21].

A similar approach as GaAs on V-grooved silicon has also been applied to the InP material system by Wang *et al.*[22]. V-grooves have been formed on silicon using the wet chemical etchant tetramethyl ammonium hydroxide, following which high quality InP with lattice mismatch of 8% has been grown. Initial promising results with optical pumping of a DFB laser have been demonstrated.

1.4 III/V nanowire/nanopillar growth on Silicon

All the aforementioned methods for heteroepitaxial III/V growth on silicon have used a high growth temperature of about 600°C. Further, the demonstrated quantum dot based lasers typically require a very high quality factor cavity in order to compensate for the low material gain possible with a quantum dot active region. This translates into either a large device size, or challenging cavity design in the case of a high-Q whispering gallery mode laser. Real estate on a CMOS chip is extremely precious, as are thermal budget restrictions for back end integration[28]. Due to the large device size and high growth temperature, these III/V growth methods are unsuitable for integration with CMOS electronics.

There is a need for a method to grow high quality III/V material while meeting all the requirements for CMOS back-end integration. One of the methods to grow high quality III/V nanowires is vapor liquid solid growth (VLS). This method can be used to grow whisker-like nanowires on lattice mismatched substrates, and the growth temperature is typically around 400-450°C, which potentially allows a thermal budget low enough for back-end integration. An additional requirement for nanophotonic devices such as a nanocavity laser is the diameter of the nanowires. In case the nanowire diameter is smaller than a few hundred nanometers, it becomes challenging to effectively confine the mode and obtain sufficient modal gain for lasing. The dimensions of a typical silicon photonic waveguide are roughly 200 nm by 400 nm, which allows for effective confinement and long propagation distance. It is not desirable to scale the nanocavity lateral dimension significantly beyond this. In light of this, Chuang *et al.* have investigated the critical diameter for growth of high quality III/V nanowires using gold-catalyzed VLS growth[29]. The critical diameter, beyond which crystal quality deteriorated, was found to be inversely proportional to the lattice mismatch between the growth substrate and nanowire material. The critical diameter for InP growth on silicon was found to be merely 50 nm, due to the high lattice mismatch of 8%. This is insufficient for a nanolaser cavity. Further, another disadvantage of the VLS growth mode is its reliance on a gold catalyst for nucleation. Gold is typically not permitted in a CMOS foundry, since it is a deep level impurity in silicon.

The discovery of a catalyst-free, low-temperature method for high quality III/V growth on silicon is therefore of tremendous interest. High quality III/V nanopillars were serendipitously found to grow on silicon after mechanically roughening the growth substrate. The growth method does not rely on a gold catalyst, and could be extended to various differ-

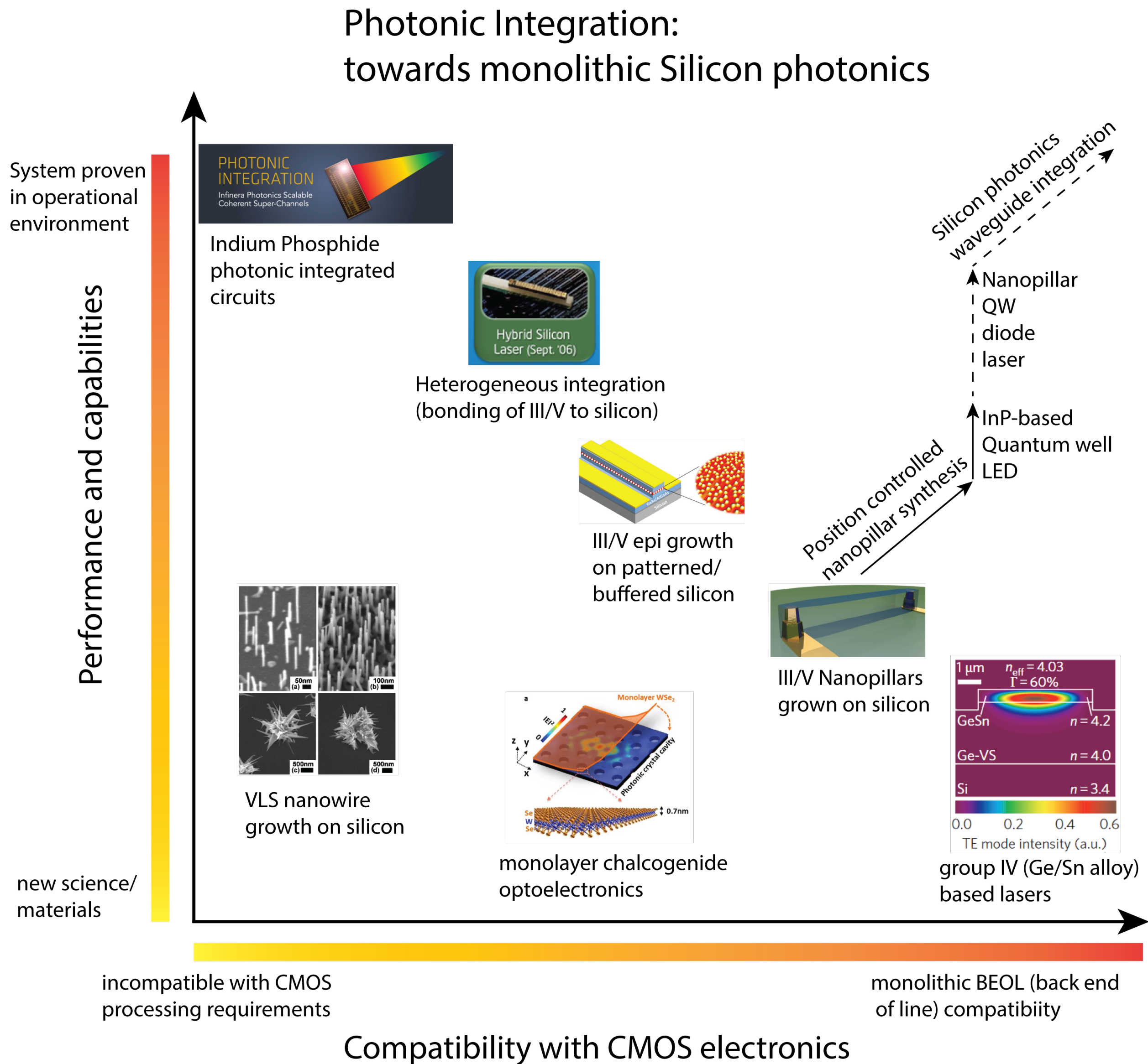

Figure 1.2: This chart provides a qualitative comparison of photonic integration technologies, with a focus on the eventual goal of monolithic integration with silicon photonics. This infographic is based on the author's opinion, derived from the published literature and should be interpreted as such. It can be noticed that while Indium Phosphide photonic integration provides the most capabilities and functionalities on the same platform, it is the least compatible with silicon-based CMOS electronics, that are fabricated under stringent conditions on a silicon substrate. On the other hand, group IV based optoelectronic materials as of yet have poor performance due to the indirect bandgap and unavailability of bandgap engineering with heterostructures. III/V nanopillars grown on silicon can potentially help to bridge the two worlds. Some of the steps required to improve the technology readiness of the nanopillars towards the top right corner of CMOS compatibility and performance are highlighted.

ent lattice mismatched substrates such as sapphire and poly-silicon. The initial discovery and demonstrations were based on the InGaAs/GaAs material system. The GaAs-based *nanoneedles* were found to be pure Wurtzite phase, and free of defects and dislocations in the main body of the pillar[30],[31]. The pillars grow in a core-shell manner, similar to the layers of an onion, which allows for interface passivation of a double heterostructure gain medium. The small lattice mismatch of the pillar with the silicon substrate allows for optical feedback of helicalaly propagating modes. This was used to demonstrate a nanolaser grown on silicon, operating at room temperature under pulsed optical pump (see table 1.2) [24]. As further evidence of CMOS post-process compatibility, the pillars were grown on an exact [100] silicon substrate with transistors fabricated. The transistors were able to tolerate the low thermal budget of the nanopillar growth, and continued to function as expected [25]. Continuing to build on demonstrations of optical pumping, the GaAs-based nanolasers have also been fabricated into light emitting diodes (showing amplified spontaneous emission), avalanche photodiodes and solar cells [32],[33].

However, a couple of challenges continue to persist with the InGaAs/GaAs based nanopillars. Firstly, there is a thin layer of polycrystalline InGaAs deposited across the growth substrate, simultaneously with the nanopillar growth. This makes it challenging to access the silicon substrate for processing, and also creates shunt leakage paths in the core-shell nanopillar device. Additionally, the InGaAs active region was found to show composition inhomogeneity, leading to the precipitation of indium rich segments within the nanopillar body[34]. One possible cause of this could be the high alloy strain. This kind of inhomogeneity is detrimental for laser gain and leads to inhomogeneous broadening, as well spatially localized modal gain.

Further, in nanoscale structures with a high surface to volume ratio, non-radiative recombination at the surface becomes a limitation on the luminescence efficiency. The non-radiative surface recombination rate increases as the surface to volume ratio of the nanopillar, as well as a material parameter described as the surface recombination velocity. It turns out that the surface recombination velocity for (In)GaAs is two orders of magnitude higher than that of InP. This makes the GaAs based nanopillars particularly susceptible to surface recombination and diminishes the luminescence quantum efficiency, particularly at low excitation. Hence, the nanopillar growth mode was also investigated for the Indium Phosphide material system. Sun *et al.* demonstrated a significant improvement in internal luminescence efficiency and minority carrier lifetime in InGaAs-based pillars that were passivated with an InGaP window layer. This was attributed to the heterostructure surface passivation provided by the high bandgap layer[35]. Ren *et al.* demonstrated the growth of high quality InP nanopillars directly on silicon at a low temperature[36]. Pure Wurtzite phase InP nanopillars were obtained, growing in a core-shell mode upto one micrometer in diameter, which makes this interesting as an optical cavity. Further, Li, Ng *et al.* confirmed that the defects in the nanopillar cavity are terminated at the base, with one in every twelve periodic lattice spacings forming a threading dislocation[37]. One in twelve corresponds to the approximately 8% lattice mismatch between InP and silicon, and allows the body of the pillar to be completely relaxed and pristine Wurtzite phase. Additionally, it was also confirmed

that the minority carrier lifetime of the pillars was as high as 10 ns, corresponding to a low surface recombination velocity. The long minority carrier lifetime is comparable to radiative lifetimes at reasonable carrier concentration. Further, Tran *et al.* developed a method to quantify the absolute luminescence counts from a nanopillar and hence the external quantum efficiency of photoluminescence. This was used to infer a material dependent limit on the open circuit voltage of nanopillar-based solar cells, which turned out to be as high as 1 V under light intensity equivalent to one sun. The high minority carrier lifetime and bright external luminescence are highly encouraging for optoelectronic devices based on these InP nanopillars.

1.5 Organization of thesis

This thesis builds upon techniques developed for fabricating and studying InGaAs based nanopillar devices as well as material studies of the InP based nanopillars. The main outcome of the thesis is in demonstrating how excellent material properties have been translated to device performance for fabricated nano-optoelectronic devices. The thesis is organized as below (following this introductory chapter):

- **C**hapter 2, Nanopillar Solar Cells: P-I-N doped single nanopillar solar cells have been fabricated using a novel regrowth technique that eliminates shunt paths to the silicon substrate. We describe detailed characterization of the photovoltaic properties of the nanopillar solar cells, including temperature dependence and spectrally resolved external quantum efficiency[38]. We extend the luminescence-based material characterization technique to doped nanopillars, and also characterize these isotype InP nanopillars using electrical methods such as 4-point probe. Finally, we move to position controlled nanopillars that were grown at lithographically defined locations on silicon. We use the doping level characterization to fabricate a better electrical design that allows higher injection current. We demonstrate a nanopillar PV that reaches 0.9 V of open circuit voltage under high power excitation, enabled by the improved electrical design. Future work on eliminating defects and shunt paths in the position controlled nanopillars will enable high efficiency PV under low excitation.

- **C**hapter 3, Omnidirectional Light Harvesting with Nanopillars: We describe measurements on the single nanopillar PV to demonstrate angle insensitive light harvesting, an order of magnitude higher at normal incidence than expected from the physical cross section. These angle insensitive properties are validated with 3D finite difference simulations. This has also been extended to the case of nanopillar arrays, where it is found that a mere 5% volume fill factor of nanopillar forest (equivalent epi-layer thickness of 300 nm) was sufficient to absorb more than 90% of the incident light. This was validated with angle and spectrum resolved measurements of light absorption on a 50μm size nanopillar array. These results bode very well for indoor light harvesting based photovoltaics to power internet of things devices. Lastly, we also calculate the

detailed balance efficiency limit for photovoltaic energy conversion from indoor LED light. Due to the narrower spectral distribution of solid state lighting, the efficiency limit is found to be significantly higher than single junction solar. The limit is 54% for a white LED and higher than 80% for light from a blue LED.

- **C**hapter 4, Nanopillar Phototransistor: Here we extend the regrown InP nanopillar phototransistors to fabricate a p-n-p bipolar (homo)junction transistor. The rationale for this is described in detail, but the essential argument is that integrating the transimpedance amplifier gain directly at the photodetection device significantly reduces the total photoreceiver capacitance. This allows the optical link to operate with low total energy consumption, potentially enabling shot-noise limited on-chip communication. The low dark current and high quality homojunction device allows high current gain to be achieved at a low optical power and at voltage bias close to the CMOS line voltage. Using this, we have demonstrated a single nanopillar bipolar junction phototransistor with a high current gain β of 53.6, bandwidth of 7 GHz and responsivity of 9.5 A/W for the same sub-micron footprint device[39]. The key to the simultaneously high responsivity and bandwidth is the high absorptivity of the III/V material.

- **C**hapter 5, InP-based Nanopillar Lasers on Silicon: In this section, we firstly extend the quantitative photoluminescence technique developed by Tran *et al.* [40] to the case of a quantum well heterostructure, and measure the power required for the quantum wells embedded within the nanopillars to reach transparency. Further, we use the Hakki-Paoli technique on mechanical transferred nanopillars to measure the modal gain as a function of excitation intensity. Having demonstrated the excellent material quality of the nanopillars, the next step is to build a nanopillar optical cavity to allow high quality factor optical resonances and lasing oscillation. Two different gain media are demonstrated for lasing. Firstly, lasing is demonstrated for an InGaAs/InP based five quantum well active region which is interesting for silicon photonics[27]. Silicon transparent pulsed lasing operation upto room temperature is demonstrated with an undercut cavity laser, as well as continuous wave lasing at low temperature. The high quality factor allows for a high optical power density to build up in a small volume cavity, thus leading to a resonance enhanced second harmonic generation from the lasing wavelength. Using the quantum well nanopillars, we also demonstrate how silicon transparent spontaneous emission is coupled into monolithic silicon waveguides[41]. The second gain medium demonstrated is in the short wavelength IR range, used for data center optical links. Pure InP nanopillars are optically excitated at room temperature to show pulsed lasing. Lasing is demonstrated for two different cavities: a silicon undercut cavity, and a regrown cavity. The regrown cavity shows a reduced lasing threshold, as well as second harmonic generation from the lasing wavelength.

- **C**hapter 6, Position Controlled 1.5μm Nanopillar LEDs: Here we discuss how nanopillars containing multiple quantum wells have been grown in a position controlled manner. Nanopillar nucleation is restricted to holes defined in an oxide mask deposited

on the silicon substrate. Nanopillars containing quantum wells show systematic variations in photoluminescence wavelength based on the pitch of the nanopillar array. The controlled variation is due to a combination of the quantum size effect as well as alloy composition variation, arising from group III precursor competition. This allows for lithographically defined gain control on the same growth substrate. Further, the nanopillars could be doped to produce an electrically injected p-i-n junction light emitting diode with bright electroluminescence and luminescence ideality factor of unity, as expected for radiative-dominant carrier recombination[42]. The injection current density could be increased up to several kA/cm^2, allowing for band filling of the quantum well emission and electrically injected gain. This was inferred from the bright electroluminescence counts and the spectral blue shift observed at high current density.

- **C**hapter 7, Conclusion: We conclude by discussing some of the bright future prospects for nanopillar based devices on silicon. These considerations are based on the need to monolithically integrate nanopillar based III/V optoelectronic devices with silicon photonics waveguides, while retaining the possibility to also integrate with CMOS integrated circuits in an intimate manner. Future potential for omnidirectional photovoltaics using nanopillar arrays is also highlighted. This section is inherently somewhat speculative, as the factors driving future technological interest are uncertain. However, it is informed by the understanding and lessons learned from the work in this thesis.

Chapter 2

Nanopillar Solar Cells

The key metric for the adoption of any new form of power generation is the levelized cost of energy (LCOE). Typically, the metric is defined as a ratio of lifetime costs over the total energy generated, and has the units of cents/kiloWatt-hour (c/kWh). This figure of merit is calculated from the combined costs of installation, maintenance, operation and other lifetime expenditures. This number is then divided by the total energy delivered by the generation source over the course of its lifetime. This combined levelized metric can then be used to compare utility scale and distributed sources of energy (such as photovoltaics):

$$LCOE = \frac{\text{total cost over lifetime}}{\text{energy generated over lifetime}} \text{ in c/kWh} \tag{2.1}$$

Note that the lifetime cost of a solar installation is a somewhat difficult parameter to capture in terms of a single metric. Typically, an argument is made that photovoltaic (PV) modules that are inexpensive have greater potential for deployment. However, beyond a certain point, the costs related to installation, financing and other non-hardware costs (soft costs) tend to dominate the overall lifetime cost of the photovoltaic installation rather than the cost of the module itself. In this case, reducing the module cost by using poorer quality material, while suffering a penalty in efficiency, is not the best approach for improving the LCOE, and leads to a smaller improvement than the overall improvement provided by a commensurate change in the denominator (power conversion efficiency). This then leads to the argument that *efficiency is the more important parameter for evaluating photovoltaic technology, as opposed to the module cost.*

With this viewpoint, it is then reasonable to use material that will lead to the best photovoltaic power conversion efficiency. Miller *et al.* have discussed that a high photoluminescence quantum efficiency (both externally and internally) is required to reach the Shockley-Queisser limit [43]. In fact, if the external quantum efficiency is imperfect, the voltage penalty suffered by a solar cell is given by:

$$\delta V = \frac{k_B T}{q} ln(EQE_{PL}) \tag{2.2}$$

where k_B is the Boltzmann constant, T is the solar cell temperature, q is the electron charge and EQE_{PL} is the external quantum efficiency of photoluminescence, a number less than or equal to unity. For no voltage penalty, we require that every absorbed photon leads to the re-emission of a photon at the bandgap of the absorber material. With indirect bandgap materials, the energy from absorbed photons is mostly converted to heat. However, with well passivated materials and careful optical design, the external quantum efficiency can be as high as 70% for direct bandgap compound semiconductor materials[44]. The rationale for using nanopillars is then two fold:

1. III/V compound semiconductor material based nanopillars are direct bandgap and accordingly, the photoluminescence efficiency is much higher compared to silicon. This is particularly the case for Indium Phosphide based nanopillars, where the low surface recombination velocity prevents minority carriers from recombining non-radiatively at the surface and ensures a high photoluminescence internal quantum efficiency (IQE).

2. The tapered nanopillar shape allows for both high absorption efficiency (without using an additional anti-reflective coating), and also omnidirectional absorption. This allows for diffuse and angled sunlight to be absorbed and has implications for harvesting ambient light energy. Further, the sub-wavelength size near the tip of the nanopillar allows for efficient extraction of generated photons - leading to a high EQE_{PL}.

Due to these reasons, it becomes compelling to consider the potential of Indium Phospide based nanopillars for photovoltaics. Additionally, the III-V nanopillars have been grown at a relatively low temperature of 450°C on an inexpensive and scalable silicon substrate. This also has favorable implications for the module cost, since III/V substrates continue to remain infeasible, in spite of some promising attempts to recycle the III/V substrate[45].

The first demonstration of InP nanopillars directly grown on a silicon substrate was accomplished by Ren *et al.* [36]. The nanopillars grow in the metastable Wurtzite phase in a core-shell mode at low growth temperature of 450°C, and scale up in diameter upto a micrometer, depending on the growth duration. Further, the growth of the lattice matched InGaAs/InP heterostructure was also demonstrated, additionally helping to confirm the core-shell growth and allowing for heterostructure surface passivation. There was some variation in the height and tip structure of the nanopillars, which continues to be under investigation[46]. In order to examine the material properties, Li and Ng *et al.* have performed detailed time resolved photoluminescence (TRPL) studies as well as high resolution transmission electron microscope (HRTEM) measurements of the nanopillars[37]. They have used a simple method to isolate the non radiative surface recombination rate coefficient, and estimated the surface recombination velocity to be two orders of magnitude lower than what is typical of InGaAs based nanopillars. The HRTEM studies not only confirmed the pristine Wurtzite crystal phase in the body of the pillar, but also indicated that the lattice mismatch is completely relaxed by dislocations running parallel to the interface with silicon. The dislocation density is exactly what would be expected to completely relax the 12% lattice mismatch between InP and silicon. The low dislocation density in the bulk of the

nanopillar was confirmed by the long minority carrier lifetime of 5-10 nanoseconds, a record parameter for such nanoscale structures. Other groups have also confirmed the long minority carrier lifetime of Indium Phosphide based nanopillars, using detailed TRPL measurements **Gao2014a** In the following sections, we continue to validate the material properties of the InP nanopillars and proceed towards impurity doping for electrical device synthesis.

2.1 Quantitative Photoluminescence from Nanopillars

We emphasize that metrics of performance for photovoltaics can be inferred from the photoluminescence (PL) yield of these nanopillars. As explained above, the voltage penalty from the detailed balance open circuit voltage is related to the photoluminescence yield at open circuit2.2. This leads to a 'contactless-IV' measurement, where the maximum possible short circuit current is directly related to the electron-hole generation rate and the limit for the electrical open circuit voltage is simply equal to the quasi Fermi level split of the electrons and holes. In fact, PL measurements such as PL-imaging, suns-Voc and implied-Voc have been used as a contacless method of determining electrical data, such as open circuit voltage, I-V characteristics, saturation current densities and series resistances [47], [48], [49]. Tran *et al.* have described in detail how the Fermi level split can be calculated from the total external photoluminescence counts, and have demonstrated that a quasi Fermi level split greater than 1 eV can be obtained for Indium Phosphide nanopillars grown directly on silicon[40]. In the following sections, we will describe the measurement technique and in particular, the characterization of doped nanopillars, with the goal of fabricating a p-i-n doped nanopillar solar cell.

Note that Tran *et al.* have interpreted the Fermi level split measurement technique as 'contactless-IV', and use it to provide an indication of the excitation power dependent open circuit voltage in the solar cell[40]. However, it must be emphasized that the Fermi level split measured using the quantitative photoluminescence technique is best interpreted as an upper limit or maximum on the electrical open circuit voltage. The reason for this is that *selective electrical contacts* are also extremely important for the Fermi level split (ΔF) in the active region to be converted to a measured electrical open circuit voltage. Series losses in voltage due to improperly chosen bandgap alignments will degrade the measured open circuit voltage from what is suggested by the Fermi level split.

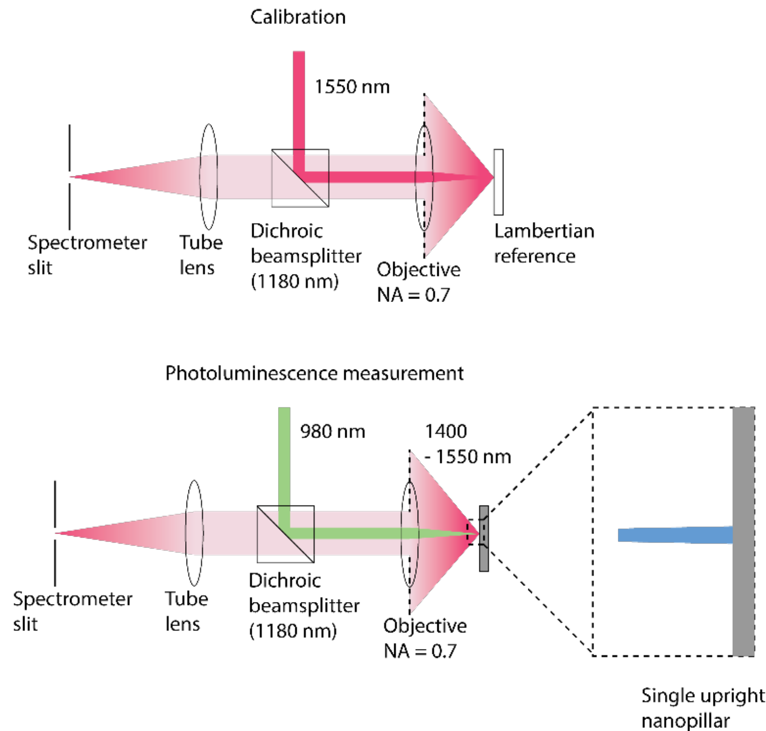

Figure 2.1: Quantitative μPL measurement: (top) Calibration of the photon collection efficiency of the setup, measured at the photoluminescence wavelength. The calibration needs to be carried out at the PL wavelength (875 nm for Wurtzite InP, 1400-1550 nm for quantum wels) (bottom) The actual PL measurement was then made by exciting the active region with photons that are efficiently absorbed, and at comparable intensity to what is expected under AM1.5G solar illumination. This figure illustrates the case of 980 nm excitation and 1550 nm PL, and can be extended to other relevant cases.

With the above caveat in mind, we pay attention to the photoluminescence counts and radiative quantum yield as these are necessary prerequisites for high efficiency PV. Defective PV material with poor minority carrier lifetime and low Fermi level split ΔF will not be able to provide high power conversion efficiency, no matter how selective and conducting the electrical contacts are designed to be. As described in figure 2.2, the Fermi level split is related to the excess carrier concentration in a semiconductor volume under optical excitation. If the material is defective or has exposed surfaces, the non-radiative carrier recombination rate is very high, and only a small excess carrier concentration can be sustained. However, if the material is good and minority carrier lifetimes are long, a large Fermi level split can be sustained, leading to a large open circuit voltage V_{oc} and good PV performance.

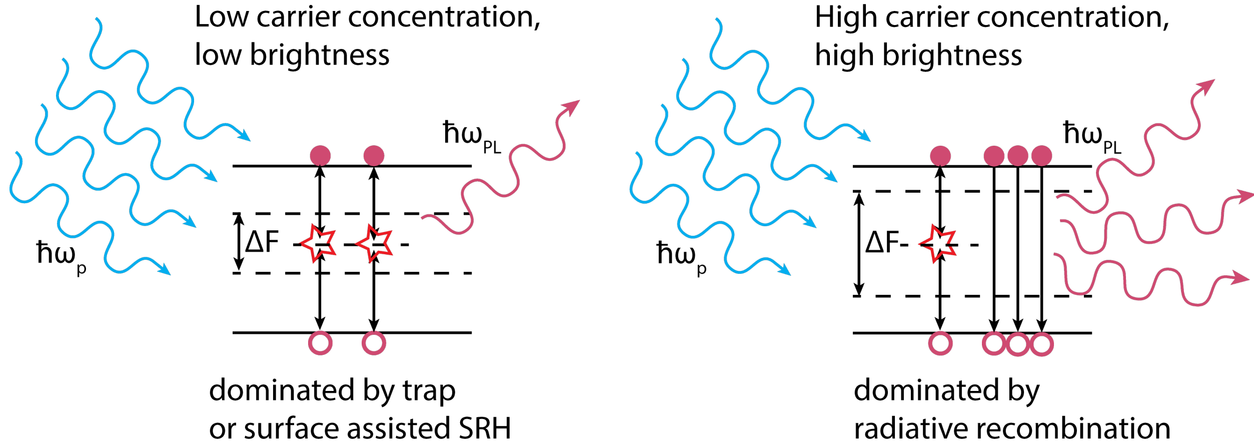

Figure 2.2: Photoluminescence yield in two different situations: (left) In material with high surface recombination or defective material, the generated excess charge carrier density is comparatively low, since the generation of carriers is balanced by rapid non radiative recombination. (right) If the non-radiative recombination is slow, the charge carrier density can be higher, leading to a higher quasi Fermi level split, and hence a higher implied open circuit voltage.

We first consider the uncalibrated photoluminescence measurement and highlight the information that can be gained already from a simple light out vs. light in curve. Note that the light-light curve is obtained from a micro-photoluminescence (μPL) measurement on a single nanopillar as shown in figure 2.1. A single nanopillar is measured by using a high numerical aperture objective, focused at the position of the nanopillar on the silicon substrate. The spot diameter is $2.4\mu m$, as measured using a scanning knife edge method[50]. A smaller (diffraction limited) spot size could be obtained by spatially filtering the beam if necessary. Finally, the excited photoluminescence is collected using a long-pass optical filter to discard any reflected pump light. For the PV material, Indium Phosphide nanopillars with photoluminescence at 870 nm were measured. The excitation wavelength was a 660 nm wavelength laser, with pump excitation intensity varying from 0.5 sun (60 mW/cm^2 at 660 nm), up to 10^6 suns. Wavelength resolved spectra were obtained at each excitation intensity by dispersing the collected light with a spectrometer and measuring with a CCD array. Normalized PL spectra for Wurtzite phase InP nanopillars are shown in figure 2.3. Note that for good quality material, as depicted in the figure, the high energy tail of the PL spectrum is determined by the Boltzmann distribution:

$$PL(\hbar\omega) \sim e^{\frac{-\hbar\omega}{k_B T}} \tag{2.3}$$

where $\hbar\omega$ is the photon energy at which the PL spectrum is being measured, k_B is the Boltzmann constant and T is the carrier temperature (= lattice temperature). Similarly, the low energy tail of the spectrum is determined by a product of the exponential tail of the absorptivity at the band edge (Urbach tail) as well as the decaying Boltzmann distribution:

$$PL(\hbar\omega) \sim e^{\frac{\hbar\omega}{U_E}} \times e^{\frac{-\hbar\omega}{k_B T}} \tag{2.4}$$

where the constant U_E denotes the Urbach energy[51], which is typically less than 9 meV for semiconductor material with low alloy disorder and $k_B T$ is the thermal energy, roughly 26 meV for room temperature. The combination of these leads to a rising exponential on the low energy side of the spectrum, rising by a decade every 30-35 meV of photon energy as show in fig. 2.3. The high energy tail of the spectrum decays by a decade every 60 meV of photon energy, as consistent with the Boltzmann distribution. The peak of the spectrum is at 1.42 eV (around 873 nm), slightly higher in energy compared to the Zinc Blende phase of InP, which has a band gap around 1.33 eV. Note that the Wurtzite phase InP bandgap is serendipitously the optimal band gap for single junction PV for the AM1.5 solar spectrum.

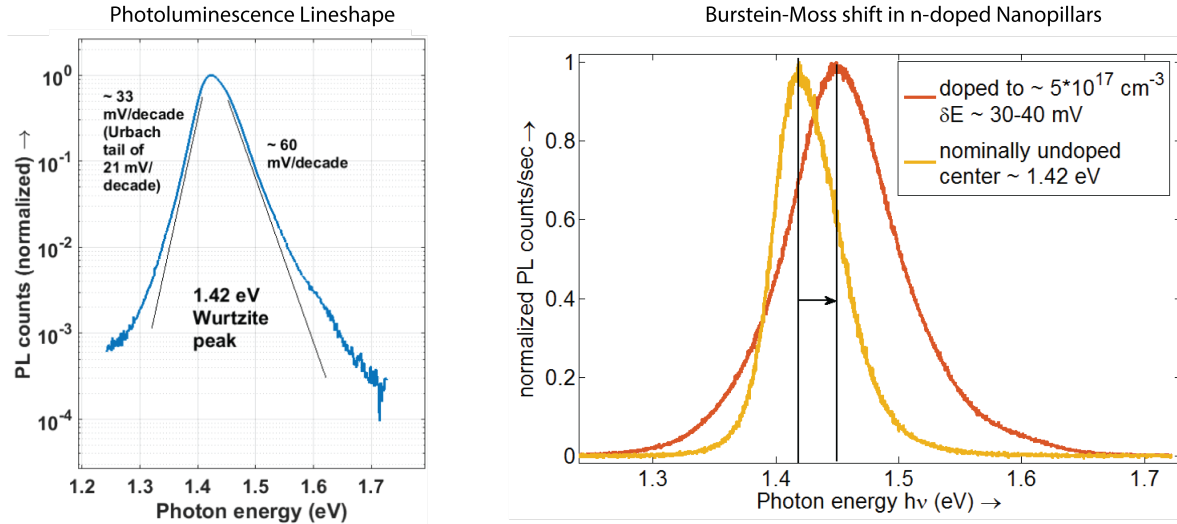

Figure 2.3: Normalized PL spectra: (left) Log scale PL spectra from Wurtzite InP nanopillars, showing the characteristic high and low energy tails in the spectrum. (right) Linear scale spectra showing PL characteristics of doped and nominally undoped nanopillars.

The cumulative PL output is obtained by integrating the PL spectrum over energy. As a first step, we attempt to glean as much information as possible from the uncalibrated light-light curve obtained from the μPL measurement. The input light power (P_{in}), measured in μW, is related to the volumetric generation rate G of electrons and holes in the nanopillar,

which then recombine through three different pathways: Shockley-Read-Hall(SRH) recombination (An), radiative recombination (Bnp) and Auger recombination (Cnp^2). The output light power (P_{out}) is related to the volumetric radiative recombination rate and is typically orders of magnitude lower in intensity compared to P_{in} (nW vs. μW):

$$P_{in}(\mu W) \times a(\hbar\omega_p) = \hbar\omega_p(eV) \times G(/cm^3/s) \times V_{tot}(cm^3) \tag{2.5}$$

$$P_{out}(nW) = \eta_{ext} \times \hbar\omega(eV) \times Bnp(/cm^3/s) \times V_{tot}(cm^3) \tag{2.6}$$

where a is the light absorption efficiency at the pump wavelength, $\hbar\omega$ is the photon energy, V_{tot} is the active region volume, Bnp is the radiative recombination rate, determined by the radiative recombination coefficient B, η_{ext} is the extraction efficiency of internally generated photoluminescence and EQE_{PL} is the external quantum efficiency of photoluminescence. Note that the P_{in} can also be related to the absorption cross section of the pillar in cm^2 and the incident power density in mW/cm^2, measured using the scanning knife-edge technique[50].

Given the three different recombination mechanisms (SRH, radiative and Auger), we can write down an equation for steady state for electron minority carriers in a p-doped region, under low level injection:

$$\frac{dn}{dt} = G - R = G - (An + Bnp + Cnp^2) = 0 \tag{2.7}$$

where, as above, G refers to the volumetric carrier generation rate (from absorbed photons), and the other three A, B, C terms represent the three main carrier recombination processes. The term 'low level injection' refers to the situation when the number of minority carriers in steady state is much less compared to the acceptor doping level ($n \ll p = N_a$).

Another situation is 'high level injection', in which the injected carrier density greatly exceeds the background doping level ($n \sim p \gg N_a$) and the steady state equation can be written as:

$$\frac{dn}{dt} = G - R = G - (An + Bn^2 + Cn^3) \tag{2.8}$$

More generally, we can use the law of mass action to determine the excess carrier concentration:

$$np = n_i^2 e^{\frac{\Delta F}{k_B T}} \tag{2.9}$$

where n and p are the absolute electron and hole concentrations, and n_i refers to the intrinsic carrier concentration, defined by the density of states of the semiconductor. ΔF refers to the quasi Fermi level split of the electrons and holes, which is zero under steady state (no excitation). Typically, the minority carrier concentration under solar illumination is many orders of magnitude higher than the intrinsic carrier concentration.

Our goal is to determine the absolute emitted photoluminescence counts as a function of the input power. To start with, we examine the dependence of the volumetric radiative emission rate as a function of the volumetric generation rate, under different injection levels. Considering a situation of low level injection (minority carrier concentration much less than doping level), and SRH dominated recombination, we have:

$$\begin{aligned} G(=R) &= An \\ np = n_i^2 e^{\frac{\Delta F}{k_B T}} &\rightarrow n \sim \frac{n_i^2}{N_a} e^{\frac{\Delta F}{k_B T}} \\ \rightarrow G &= A \times \frac{n_i^2}{N_a} e^{\frac{\Delta F}{k_B T}} \\ \rightarrow \Delta F &= k_B T log \left(\frac{G}{A \frac{n_i^2}{N_a}} \right) \end{aligned}$$

which shows that the Fermi level split grows logarithmically as the volumetric generation rate, and hence the incident photon intensity. Similarly, for high level injection (carrier density greatly exceeds doping level):

$$\begin{aligned} n = p &\gg N_a \\ np = n_i^2 e^{\frac{\Delta F}{k_B T}} &\rightarrow n \sim p \sim n_i e^{\frac{\Delta F}{2 k_B T}} \\ \rightarrow G &= A \times n_i e^{\frac{\Delta F}{2 k_B T}} \\ \rightarrow \Delta F &= 2 k_B T log \left(\frac{G}{A n_i^2} \right) \end{aligned}$$

Here we notice the factor of 2 in the dependence of the Fermi level split on the logarithm. This factor is related to the ideality factor in a conventional diode I-V characteristic. The analogy to a current-voltage characteristic can be made by viewing the incident photon current as the maximum possible short circuit current in the solar cell, ignoring shunt paths. Similarly, the Fermi level split can be viewed as the maximum possible open circuit voltage, not including series resistance or contact losses. For a solar cell under illumination:

$$\begin{aligned} I(V) &= I_d \times (e^{\frac{qV}{n k_B T}} - 1) - I_{sc} \\ \rightarrow V_{oc} &= \frac{n k_B T}{q} ln \left(\frac{I_{sc}}{I_d} + 1 \right) \end{aligned}$$

where $I(V)$ is the bias dependent current, I_d is the 'dark' or saturation current, I_{sc} is the short circuit current, V is the voltage bias, and n is the diode ideality factor. We can simplify this to obtain the open circuit voltage V_{oc} as a function of the short circuit current,

as expressed in the second line above. Note the similarity with equation 2.15 above, where V_{oc} has been replaced by $\frac{\Delta F}{q}$ and the generation rate has been replaced by terms proportional to the ideality factor. The ideality factor n is related to the recombination mechanism and the injected minority carrier concentration. The dependence for all the three A, B, C mechanisms at different injection levels can be derived (as show for the SRH case above):

Injection level	SRH (A)	Radiative (B)	Auger (C)
High	$n = 2$	$n = 1$	$n = 2/3$
Low	$n = 1$	$n = 1$	$n = 1$

Table 2.1: Ideality factor dependence on recombination mechanism and injection level. Note that low level injection implies a doped semiconductor, in which the excess carrier concentration is much smaller than the doping level. High level injection refers to the case when the excess carrier concentration is much higher than the background doping level, typical for the undoped active region in a semiconductor p-i-n junction.

Typically, the variation in pump excitation level is over several orders of magnitude, and the deviation from the low and high injection level approximations as presented in table 2.1 is only significant when the carrier concentration is close to the doping level. In that case, the charge conservation ($n + N_a = p$) can be used to exactly determine the individual carrier concentrations as a function of pump excitation level.

Finally, we can obtain the internal photoluminescence yield from the A, B, C model. The internal luminescence yield is given by the ratio of the radiative recombination rate to the total carrier generation rate (sum of all recombination processes):

$$\eta_{int} \text{ (low level injection)} = \frac{Bnp}{G} = \frac{Bnp}{An + BnN_a + CnN_a^2} \tag{2.10}$$

$$\eta_{int} \text{ (high level injection)} = \frac{Bn^2}{An + Bn^2 + Cn^3} \tag{2.11}$$

where, in the two equations above, η_{int} refers to the internal efficiency of photoluminescence, and the two equations refer to the two separate cases of high level injection and low level injection. Note that the transition from low level injection to high level injection can be analytically modeled using the charge conservation and mass action laws. This has been shown in figure 2.4. When the doping level is low, or the structure is undoped, we have a high level injection situation and the internal quantum efficiency (IQE) shows a pronounced variation with the carrier injection level. We note that equations 2.10 and 2.11 predict that there is an optimal carrier injection level at which the IQE is maximized. In an undoped semiconductor at very low carrier concentration, the most dominant recombination process is the non-radiative SRH process. As carrier concentration increases, the radiative process becomes more dominant and the IQE continues to increase up to a maximum value. Beyond this optimal carrier concentration, the Auger recombination process starts to pick up and

leads to a reduction in IQE. A similar phenomenon is expected when we vary doping level. The advantage of doping is that it provides a boost to the radiative process and helps achieve high IQE even when the excess carrier concentration is low. However, excessive doping leads to the Auger process dominating. Equations 2.10 and 2.11 lead to the conclusion that the optimal doping level for maximum IQE under low level injection is equal to the optimal carrier injection level under high level injection. The formula for the optimal doping level is given below and the corresponding maximum IQE is given by equation 2.13.

$$N_d^{opt} = \sqrt{\frac{C}{A}} \tag{2.12}$$

$$\eta_{int}^{max} = \frac{B}{B + 2\sqrt{AC}} \tag{2.13}$$

We note that this simple model suggests limitations to how much we can engineer the internal luminescence yield, given by non radiative processes. Essentially, if $\sqrt{(AC)}$ is significantly smaller than the radiative coefficient B, we have the possibility of engineering a system with internal quantum efficiency approaching unity. In the case of InP and InGaAs (lattice matched to InP), the radiative coefficient is approximately $1 \times 10^{-10} cm^3/s$. For InP, the Auger coefficient C is $9 \times 10^{-31} cm^6/s$. In order to obtain an IQE of 99%, we would require an A coefficient of $2.8 \times 10^5/s$, or equivalently an SRH minority carrier lifetime of $3.6\mu s$. Similarly, for InGaAs with an Auger coefficient of $7 \times 10^{-29} cm^6/s$, we require an SRH minority carrier lifetime as high as $280\mu s$.

It is worth examining the main factors that determine the SRH minority carrier lifetime. Generation and recombination of electrons and holes can take place at interstitial defects, lattice dislocations, substitutional impurities and defects at surfaces and interfaces. The formula for the SRH lifetime can be derived based on the detailed balance of four processes that are mediated via recombination centers: electron capture, electron emission, hole capture and hole emission. The recombination rate for non-equilibrium, but steady state conditions can be written as follows [52]:

$$R = \frac{(np - n_i^2)}{[(n + n_1)\tau_{p0} + (p + p_1)\tau_{n0}]} \tag{2.14}$$

where R is the SRH recombination rate (number/time/volume), n and p are the electron and hole concentrations respectively, n_1 (p_1) is the electron(hole) concentration when the quasi Fermi level is at the same energy as that of the trap state and $\tau_{n0}(\tau_{p0})$ is the electron(hole) minority carrier lifetime. Typically, this can be integrated over energy, for all the traps present in the energy range of the semiconductor bandgap, although the most dominant trap centers are typically at mid-gap. The formula can be simplified for the case of low minority carrier (electron) injection in a p doped semiconductor with mid-gap traps as ($np \gg n_i^2;\ n_1, p_1 \sim n_i \ll N_a$):

$$R_{LLI} = \frac{n}{\tau_{n0}} \tag{2.15}$$

Similarly, for high level injection, we have ($n \sim p \gg N_a, np \gg n_i^2$):

$$R_{HLI} = \frac{n}{\tau_{n0}} \tag{2.16}$$

Which shows that the simple SRH formula for a single minority carrier lifetime works well for a broad range of injection level. Note that minority carrier lifetime can be expressed as:

$$\tau_{n0} = \frac{1}{v_{th} N_T \sigma_{n0}} \tag{2.17}$$

where v_{th} is the thermal velocity, N_T is the volume density of trap states (typically found by integrating density of states of traps over energy) and σ_{n0} is the trap capture cross section (in units of area). For recombination due to surface defects, it is natural to use a surface density of trap states $N_{T,surf}$ (found by integrating a surface density of states for traps with units $cm^{-2}eV^{-1}$), and we obtain a recombination rate as:

$$R_{surf} = v_{th} N_{T,surf} \sigma_{n0} \times n \times A \tag{2.18}$$

where R_{surf} is the recombination rate integrated over the volume (units of s^{-1}), A is the total interface area and the pre-factor has units of velocity rather than lifetime. This is defined as the surface recombination velocity:

$$S = v_{th} N_{T,surf} \sigma_{n0} \tag{2.19}$$

An SRH recombination equation combining the effects of bulk and surface recombination can then be written, and integrated over volume. If we consider a double heterostructure of width d (typically few nanometers for a quantum well, upto several microns as desirable), then the total rate of change of carriers (number of carriers/s) in the heterostructure can be written as:

$$\begin{aligned} \frac{dN_{tot}}{dt} &= G(Ad) - \frac{n}{\tau_{nB}}(Ad) - S_{front} n(A) - S_{back} n(A) \\ \rightarrow \frac{1}{Ad}\frac{dN_{tot}}{dt} &= G - \frac{n}{\tau_{nB}} - \frac{S_{front} + S_{back}}{d} n \sim G - \frac{n}{\tau_{nB}} - \frac{2S}{d} n \end{aligned}$$

where N_{tot} is the volume integrated carrier concentration, τ_{nB} is the contribution to minority carrier recombination from bulk defects, S_{front} and S_{back} refer to the surface recombination velocities at front and back interfaces (assumed to be equal). Here we note that the effective surface recombination lifetime is $\frac{d}{2S}$ in the particular case of this geometry. More generally, it can easily be shown that the surface recombination rate (units of s^{-1}) is given by:

$$\frac{1}{\tau_{surf}} = S \times \frac{A}{V} \tag{2.20}$$

where A is the total exposed surface area, and V is the volume enclosed. The surface to volume ratio has units of inverse length and is given by $\frac{2}{d}$ for the simple case of a double heterostructure. For the case of a cylinder of radius r, the side surface to volume ratio is $\frac{2}{r}$ while for a nanoneedle with height 10x the radius ($h \sim 10 \times r$), the ratio is $\sim \frac{3}{r}$. Clearly, in the case of smaller dimensions, we have aggravated surface recombination, unless this is addressed by passivating naked surfaces in some manner. We consider the case of a double heterostructure in order to provide some estimates of the maximum IQE, as expected from equation 2.13. Note that surface recombination velocities, particularly at the silicon-silicon dioxide interface, have been under detailed investigation [53], [54]. Li *et al.* have also measured the surface recombination velocity of naked InP nanopillars and found it to be three orders of magnitude lower than that of GaAs [37]. This is also reflected in the bright PL counts observed from these nanopillars [40]. In figure 2.4, we present the effect of doping and carrier injection on the IQE. It is shown that an optimal doping level exists, for which the IQE can be at its maximum value for a large range of carrier injection levels, until Auger recombination starts to dominate. For the left figure, we perform the estimate for an InGaAs quantum well double heterostructure having a width of 5 nm, and interface recombination velocity of 80 cm/s. This leads to a maximum IQE of 25% according to an SRH lifetime of $3.1ns$ as calculated from equation 2.13, as was experimentally observed [27]. The optimal doping level required to achieve this for a broad injection range is fairly high at $2.1 \times 10^{18} cm^{-3}$. Similarly, for an InP nanopillar with radius 500 nm and surface recombination velocity of 1000 cm/s, we expect a minority carrier lifetime as high as 25 ns and a maximum IQE of 90%. In practice, a minority carrier lifetime of 10 ns is observed, possibly due to surface depletion effects.

In order to experimentally measure the IQE, we use temperature dependent measurements of the photoluminescence intensity. At sufficiently low temperature (30 K and below), the thermal velocity becomes low enough to completely eliminate the non radiative recombination, and the PL intensity corresponds to unity internal luminescence yield. At room temperature, we observe a diminished radiative output, and the internal luminescence yield can be obtained as:

$$\eta_{int} = \frac{PL_{tot}(300K)}{PL_{tot}(5K)} \tag{2.21}$$

where η_{int} refers to the internal luminescence yield (IQE), $PL_{tot}(300K)$ refers to the total PL output at room temperature and $PL_{tot}(5K)$ refers to the total PL output at low temperature. Using this technique, we have measured an internal yield close to 25-30 % in InGaAs quantum wells, and an injection-level dependent IQE as high as 30% in InP nanopillars [27], [37]. It is important to note that this technique strictly measures the ratio of external luminescence at the two different temperatures. If we agree that the extraction efficiency is not temperature dependent, we can extend this to the internal luminescence yield. This will be violated in case the band edge photons are absorbed and re-emitted. However, this is not a concern for the micro and nanoscale structures that we are investigating. A more detailed

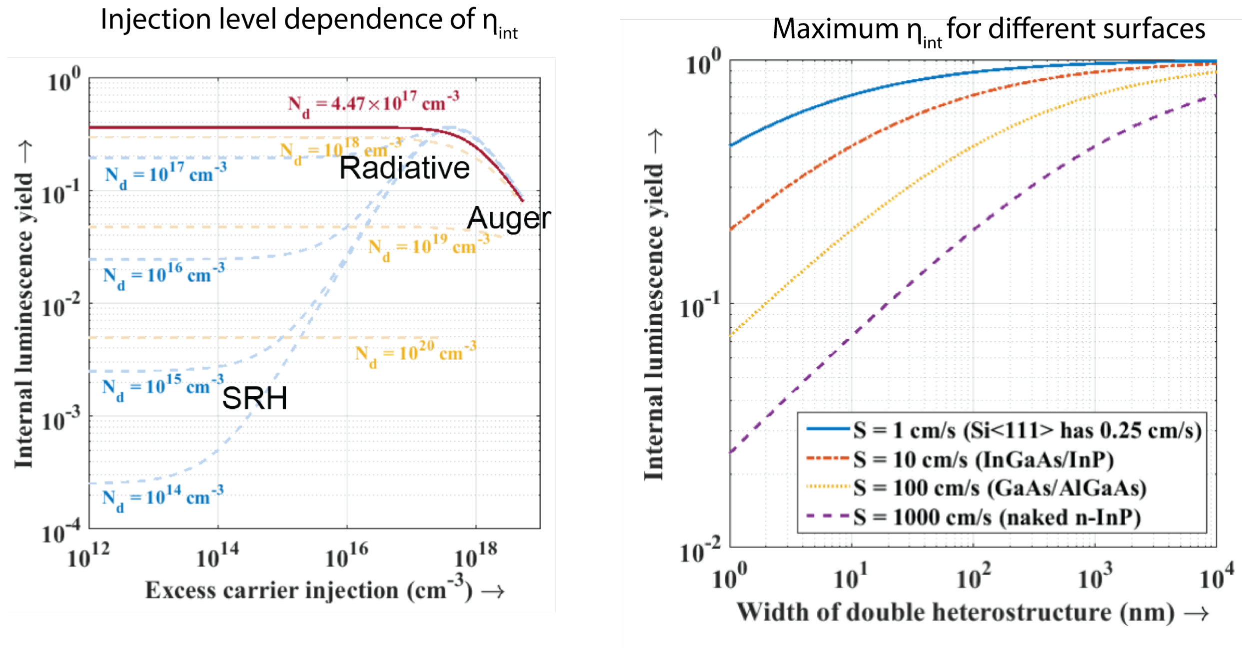

Figure 2.4: Modeling internal luminescence yield: (left) Each curve depicts the carrier injection level dependence of the internal luminescence yield. Note the typical trend that the luminescence yield rises with increasing carrier concentration at lower levels of carrier concentration as radiative recombination starts to become competitive with the SRH process. This can be further helped by simply increasing the doping level, as shown for N_d from $10^{14}cm^{-3}$ to $10^{17}cm^{-3}$. However, as the carrier injection level increases beyond $10^{18}cm^{-3}$, or the doping level exceeds the same value, the Auger process starts to dominate the radiative process, and the luminescence yield suffers. There exists an optimal doping level (as explained in the text), for which the luminescence yield can have its maximal value over a large range of carrier injection levels. This maximal luminescence yield value depends on the A, B and C coefficients (see equation 2.13) and was slightly shy of 30% for the chosen parameter values. (right) Given that B and C are mostly material dependent parameters, it is typically the SRH coefficient A that determines the maximum possible luminescence yield. As explained in the text, in pristine semiconductors, the SRH non-radiative process largely depends on surface (or interface) recombination. Hence, the luminescence yield can be plotted as a function of heterostructure width and interface recombination velocity.

discussion of these measurements is presented in **chapter 5**, when we study the quantum well heterostructure.

The Fermi level split is of particular interest for photovoltaic applications. As described in figure 2.2, internal photoluminescence is tied directly to the carrier concentration. However, as Miller *et al.* and Wuerfel have noted, it is the total external luminescence that is directly related to the Fermi level split [43], [55]. In order to obtain the Fermi level split as a function of the incident light intensity, we would like to quantitatively determine both the excitation power as well as the output photoluminescence power. Determining the exact output power P_{out} is a little more involved compared to determining the excitation power. The excitation source is a spatially coherent laser, with carefully controlled single transverse mode leading to a circular gaussian beam distribution at the nanopillar position, which can be measured. However, the output PL is much less directed, and is best modelled as a Lambertian irradiance function, with uniform energy distributed across the entire solid angle of emission. In order to emulate this irradiance function, the nanopillar is replaced with a high reflectivity Lambertian surface (Spectralon). The total power reflected P_{ref} from the Lambertian surface can be measured using a photodetector placed at the sample position, behind the objective. Then, the total power measured by the CCD array placed behind the monochromator slit can also be measured (P_{coll}). The collection efficiency is obtained from:

$$\eta_{coll} = 0.5 \times \frac{P_{coll}}{P_{ref}} \tag{2.22}$$

where the collection efficiency for Lambertian emission from the nanopillar η_{coll} is typically around 1% or lower. Note that the factor of 0.5 in 2.22 is due to the fact that reflection from the Lambertian surface is only over the hemisphere, whereas the PL emission is over the entire 4π steradians. Since the Lambertian surface doesn't transmit light, $\frac{P_{coll}}{P_{ref}}$ is an underestimate by a factor of two. The major collection efficiency is quite low due to the following factors:

- The collection cone of the $NA \sim 0.7$ objective is only a 45-degree half angle cone, out of the total 4π steradian emission of the nanopillar. This implies that only about 14% of the Lambertian emission is collected, and the vast majority of emitted PL is outside the collection cone of the objective. A large fraction of it is also funneled into the high index silicon substrate and can not be collected.

- There are several losses along the optical path, particularly at the spectrometer slit, and due to the limited etendue accepted by the spectrometer optics. For instance, the numerical aperture accepted by a standard monochromator is on the order of 0.1 (which corresponds to a solid angle of 0.03 steradians), as opposed to the NA of 0.7 for (1.84 steradians: 58 times that of the monochromator) accepted by the 100x objective. By conservation of etendue, the area of the sample from which light is collected will be 58 times lower than the area of the beam at the slit. A sufficiently small slit is required to obtain a reasonable wavelength resolution at the spectrometer. Hence, a portion of

the PL is cut out of the spectrometer at the slit. Along with reflection losses, CCD efficiency and losses in the optics, this could easily amount to 10-20%. One way to mitigate the etendue mismatch is to use a more dispersive spectrometer, so that an extremely small slit width is not required.

Finally, having measured the collection efficiency, we are in a position to obtain the true PL counts in photons/s at the position of the nanopillar, by simply dividing the measured counts with η_{coll}. This can then be converted to spectral irradiance, in photons/s/cm^2/eV, by normalizing with respect to the nanopillar emission cross section (projected perpendicular to the optical axis) and the energy spread (full width at half maximum) of the PL emission spectrum. This spectral irradiance of spontaneous emission r_{sp} can be related to the Fermi level split of the electrons and hole as described in equation 2.23.

The quasi Fermi level split ΔF of electrons and holes at steady state in a semiconductor is equal to the chemical potential μ of emitted photons. The chemical potential of the photons determines the photon population statistics and hence the quantitative PL intensity from the nanopillar (through a density of states times population statistics calculation):

$$r_{sp}(\hbar\omega,\mu) = \frac{2\pi(\hbar\omega)^2)}{h^3c^2} \times a(\hbar\omega,\Delta F) \times \frac{1}{e^{\frac{\hbar\omega-\mu}{k_BT}}-1} \tag{2.23}$$

where r_{sp} is the energy-resolved photoluminescence spectral irradiance counts in $photons/s/cm^2/eV$, $\hbar\omega$ is the photon energy, h is Plancks constant, c is the speed of light, k_B is the Boltzmann constant, T is the lattice temperature and $a(\hbar\omega,\mu)$ is the dimensionless absorptivity (or equivalently emissivity) of the single nanopillar. The absorptivity depends on the photon energy through the quantum well bandgap and quantization energy, as well as on the chemical potential (= quasi Fermi level split) through the Fermi inversion factor at any given excitation level. For the PV case, the excitation intensity is on the order of mW/cm^2, which is too low to cause population inversion. Note that this absorptivity is different from the per unit length absorption. The absorptivity incorporates several optical effects, and the best way to measure it is using an integrating sphere. We will examine the absorption measurement in detail in **chapter 3**.

The above expression for r_{sp} has been integrated over solid angle, assuming Lambertian emission from the effective cross section of the nanopillar. The effective nanopillar cross section is quite small since the nanopillar side walls are oriented almost perpendicular to the optical axis and only a small fraction of the PL is collected[40]. Using the projected cross section from the SEM-measured hexagonal cross section of the nanopillar and the collection efficiency η_{coll} we are able to calculate the photoluminescence intensity r_{sp} from the total counts measured by the spectrometer CCD. The PL experiments were performed by optimizing the position of the nanopillar for maximum PL counts, so as to make sure the nanopillar is at the peak intensity position in the beam. Using the measured collection efficiency from the 99% reflective Lambertian reference and the numerical aperture of the objective, the quantitative photoluminescence intensity r_{sp} can be determined and hence the chemical potential of the photons μ at every photon energy ($\hbar\omega$):

$$\mu(\hbar\omega) = \hbar\omega + k_B T ln\left(\frac{r_{sp}(\hbar\omega) \times h^3 c^2}{2\pi(\hbar\omega)^2 \times a(\hbar\omega)}\right) \tag{2.24}$$

Note that since the PL photons are all in equilibrium with the same electron-hole distribution, the measured chemical potential of the photons will be independent of the photon energy. Tran *et al.* indeed found that the chemical potential was not a function of the photon energy, since all the photons arise from the same Fermi level split (ΔF) [40]. However, it was found that the calculated chemical potential for photon energies below the bandgap was inaccurate. This could be corrected by incorporating the energy dependence of the absorptivity $a(\hbar\omega)$, which shows a steep fall off at the band-edge. To measure the chemical potential (hence Fermi level split) accurately, it is important to measure the absorptivity of the nanopillar structure.

The Fermi level split has been measured at one sun intensity for several nanopillars on the same n-doped growth run. The doping was performed by in-situ flow of diethyl Tellurium precursor, leading to n-doping. Note that the n-doping of InP is achieved quite easily, to the extent of leading to degenerate doping. Once the doping level becomes close to the conduction band density of states, the quasi Fermi level starts moving into the conduction band. This leads to a blue shift and broadening of the photoluminescence peak, known as the Burstein-Moss effect. The blue shift can be related quantitatively to the doping level, and provides a convenient measurement technique:

$$N(cm^{-3}) = \frac{\Delta E(meV) m_{eff}}{16.9 m_0} \times 1.5 \times 10^{19} \tag{2.25}$$

where ΔE is the blue shift in photoluminescence, m_{eff} and m_0 are the conduction band effective mass and electron mass respectively. Using this for the spectrum presented in figure 2.3, we note that the doping is on the order of $5 \times 10^{17} cm^{-3}$, which is reasonably high for solar cell applications. Using the calibraed photoluminescence technique, we can measure the Fermi level splits for multiple nanopillars.

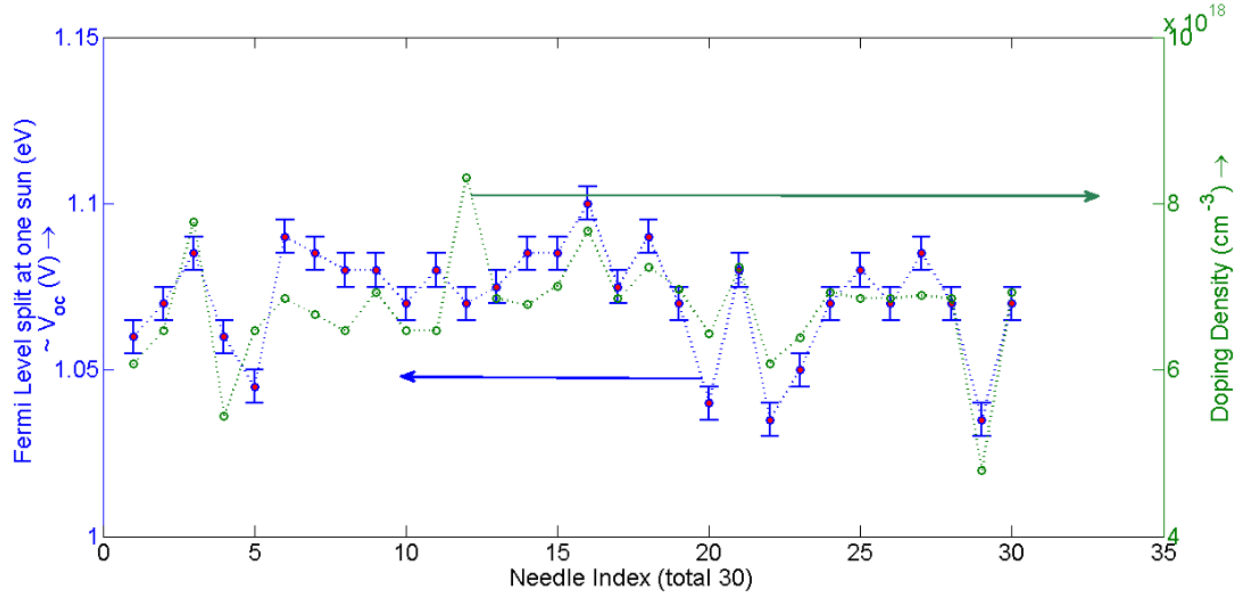

Figure 2.5: Fermi level split measurement for multiple N-doped nanopillars. There is some doping variation in the pillars, that leads to PL peak variation through the Burstein Moss effect. Some part of this bandgap variation also contributes to the Fermi level split variation.

Note that the PL brightness is related to the difference of the Fermi level split from the bandgap, rather than the absolute Fermi level split. Hence, the Burstein-Moss shifts in bandgap due to doping level variation are also observed as variations in the Fermi level split. The interesting aspect is to note that the pillars are very bright and the Fermi level split under one sun typically exceeds 1 eV for these n-doped nanopillars. A more detailed excitation-dependent PL measurement was performed on exemplary nanopillars from several different samples. The samples were: undoped (non intentially doped), intentionally n-doped (Tellurium impurity doping), intentionally p-doped (Zinc impurity doping) and core-shell p-i-n doped nanopillars. The excitation dependent photoluminescence counts also reveal the ideality factor as described in table 2.1.

In the left inset of figure 2.6, we note that illumination intensity dependent Fermi level splits show significant dependence on the kind of doping in the structure. Note that the X-axis is Fermi level split (equivalent to implied open circuit voltage), and Y-axis is the illumination intensity in suns (equivalent to short circuit current). The Fermi level split, or equivalently implied V_{oc}, is inferred from the photoluminescence(PL) counts, with brighter PL corresponding to higher Fermi level(FL) split. It can be noted that the n-doped pillar has the brightest PL, with FL split exceeding 1 eV at 1 sun illumination intensity (also see fig. 2.5) and an ideality factor of 1 (corresponding to 60 mV/decade). Two pillars that are respectively undoped and lightly p-doped have similar Fermi level splits, with Fermi level splitting around 0.9 eV under 1 sun illumination intensity. The regrown case is explained in the section below, and has similar PL intensity as the non regrown case. However, the p-i-n

junction with regrowth shows a markedly reduced PL intensity, with extrapolated 1 sun FL split less than 0.7 eV. This may be due to the separation of carriers at the p-i-n junction due to the built-in electric field. The carriers then non-radiatively recombine at the contacts due to poor selectivity of the contacts. One of the contacts is the heterojunction between silicon and p-doped InP. This contact will be investigated in detail in the sections below on the optoelectronic design and characterization of a nanopillar photovoltaic design.

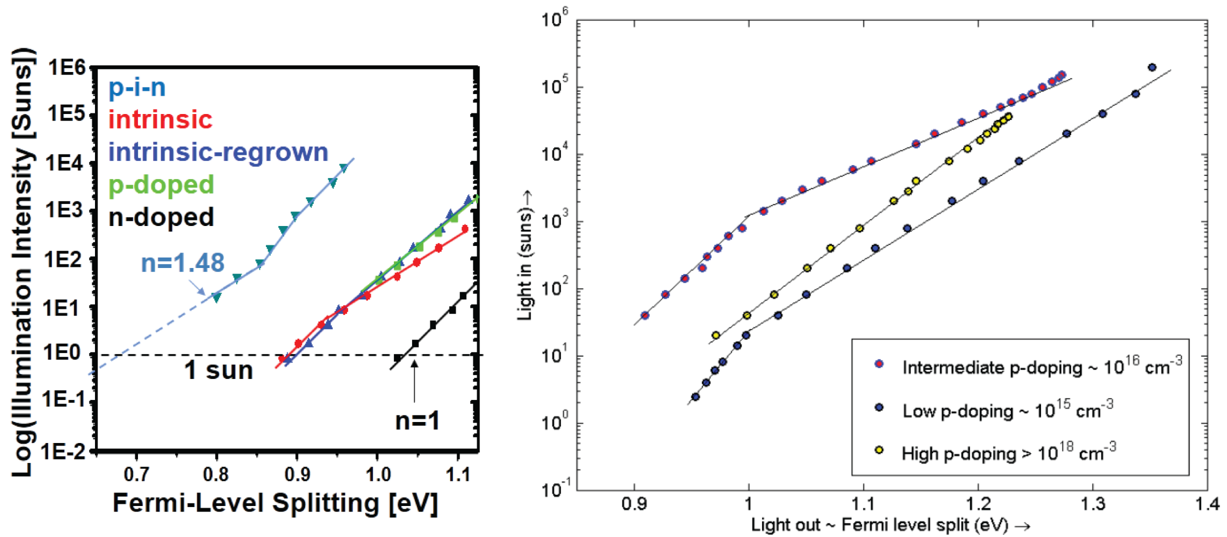

Figure 2.6: Contactless I-V: (left) The Fermi level slit (X-axis) as a funcion of the excitation intensity in suns (Y-axis), as measured for differently doped pillars. (right) Fermi level split measured for exemplary p-doped pillars as a function of excitation intensity.

Before concluding this section, it is worthwhile to examine the PL characteristics of the p-doped isotype nanopillars. It was earlier noted that the n-doped InP nanopillars show a marked blue shift due to the Burstein-Moss effect, and the doping density can be inferred using equation 2.25. Further, the n-doped pillars are brighter since increased carrier concentration favors radiative recombination. In the right inset of figure 2.6, we see three different exemplary nanopillars measured on three different p-doped growth runs. Note that the X-axis is a proxy for PL brightness. The PL spectrum for the p-doped pillars does not show any blue shift, since the hole effective mass is rather high for band filling to become important. Further, the dopant activation energy of the Zn impurity is somewhat high, so the activated dopant concentration is generally quite low for InP. The three different cases in the figure show three different precursor flows. The low p-doping case corresponds to a practically undoped situation, and the brightness is quite similar to the intrinsic case. The intermediate p-doping case is significantly dimmer, but also shows a change in ideality factor from n=1 at low injection level to higher ideality factor at high injection. This is the expected behavior for non-radiative Shockley-Read-Hall dominated recombination. The 'highly' p-doped structure has moderate PL intensity, and shows an intermediate ideality

factor. It is likely the case that the interpretation of PL ideality factor is complicated by the effect of surface band bending and it's injection level dependence. For this reason, and to obtain a more direct measurement of impurity doping levels, we have investigated electrical characterization of the doping of these InP nanopillars.

2.2 Doped Nanopillars: Electrical Characterization

While the optical method for doping characterization provides useful short-loop feedback, it is more meaningful to fabricate electrical contacts on isotype devices and make direct electrical measurements. Several different doping characterization techniques are available. The simplest method is to fabricate single nanopillar resistors and measure I-V characteristics. For this method to provide meaningful information, we require that the metal contact is Ohmic with low specific resistance, and not Schottky-like. Keeping this caveat in mind, we proceed to fabricate single nanopillar n- and p-doped devices.

The isotype nanopillars are grown on similarly doped silicon substrates. The n-doped nanopillars were grown directly on an n-doped silicon substrate oriented along the [1 1 1] crystal axis. The substrate was chemically roughened using a tetramethyl ammonium hydroxide etch, and carefully controlled group III and group V precursor flows were used to nucleate and grow the devices. The detailed substrate preparation procedure, growth recipe, temperature and precursor flows are described elsewhere [38]. The N-dopant precursor used was diethyl tellurium (DeTe), and P-doping was achieved using diethyl zinc (DeZn). As-grown isotype pillars were then fabricated into single nanopillar resistors using the process summarized in figure 2.7. Note that this process has been described for a regrown p-i-n junction nanopillar as described in section 2.3. However, the identical process also applies for isotype doped pillars as well as core-shell devices.

The process is summarized as follows (see figure 2.7 for schematics):

a **a**s-grown pillar: The as-grown isotype pillar is subject to an organic clean before continuing the rest of the process. Note that the pillars are fabricated directly on the silicon substrate, without transferring to another substrate. For the pillar schematic shown in figure 2.7, the lower half is covered by an oxide coating due to the regrowth process. This is absent in the case of the isotype nanopillar.

b **o**xide isolation: A blanket oxide deposition is performed which later serves as an insulator to electrically isolate the top contact from the silicon substrate, as well as to isolate individual devices. The deposition is performed using a low temperature plasma enhanced chemical vapor deposition (PECVD) process, using silane and oxygen precursors. The oxide layer thickness is 150-200 nm depending on PECVD chamber conditions.

c **p**hotoresist (PR) spin: A 2 micron thick photoresist layer is spun on. This will be used as a temporary etch mask to open the top contact to the nanopillar. The photoresist

used was standard g-line, although other photoresists can also be used.

d **o**xide etch and PR strip: A short buffered hydrofluoric acid etch is used to chemically etch away the exposed oxide, so as to allow contact to the top, while allowing isolation at the base. The photoresist etch mask is then stripped using a photoresist remover bath (PG remover), followed by an oxygen plasma to completely eliminate residues.

e **c**ontact definition: The metal contacts are defined using liftoff, with electron beam lithography used to pattern the contacts. This step is somewhat lengthy, but is fairly standard for the lift-off procedure. A bilayer lift-off resists consisting of methyl methacrylate followed by polymethyl methacrylate is spun on to the nanopillar sample. This is followed by electron beam writing of contacts, which are aligned to registered positions of the pillars. The positive resist is then developed away, leaving the contact pads open for deposition. Finally, metal deposition is performed using an electron beam evaporator at a slow rate of less than 0.2 nm/s. The contact metal used for the n-contact was Ni-Ge-Au and that for the p-contact was Ti-Au. The ideal choice of a Zn-Au contact for the p-doped pillars was not available at the time of fabricating these test structures.

Note that this is a summary of the fabrication process, and full details can be obtained in [38]. It is important to emphasize that the spontaneous nucleated pillars need to be registered using SEM imaging before they can be fabricated. For the registration process, alignment markers were patterned using e-beam lithography, and the positions of the pillars was manually defined with respect to the position of the alignment markers.

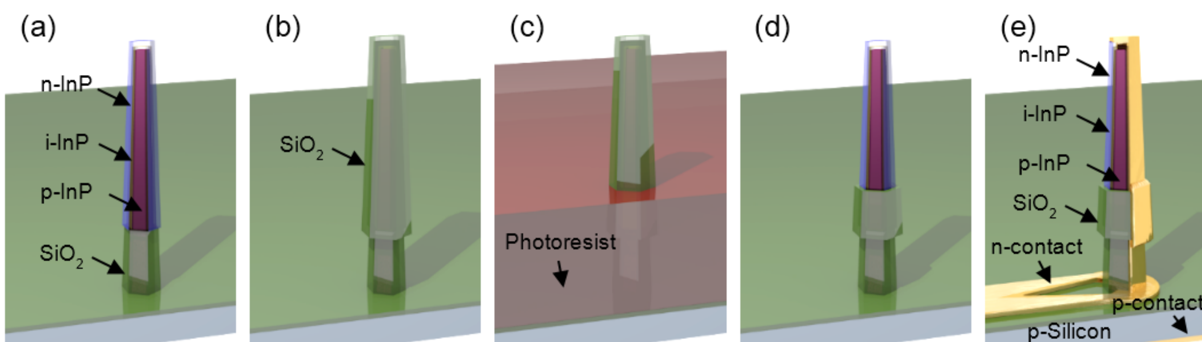

Figure 2.7: Device fabrication process: While the devices in this section were resistors used to test the doping level, the same fabrication process is also applied to p-i-n doped nanopillar devices. See main text for details.

Figure 2.8 shows schematics and measured I-V characteristics of single nanopillar n-doped resistors. Note that current conduction was directly through the nanopillar-silicon interface, with a back contact to the silicon substrate. The doping level for the n-doped pillars

measured from the Burstein-Moss shift was aproximately $5 \times 10^{17} cm^{-3}$. This was confirmed from measurements on multiple single nanopillar resistors as shown in the I-V characteristic in Fig. 2.8. The reduced slope near the origin indicates some Schottky like character to the contact, and the maximum resistance is around $1-2k\Omega$. Using a simplistic model of current transport through 2 microns of height (oxide sleeve) of nanopillar, this corresponds to a resistivity of $8 \times 10^{-4} \Omega m$. Assuming an electron mobility of $5000 cm^2 V^{-1} s^{-1}$, this leads to an inferred dopant concentration of $\sim 1.6 \times 10^{16} cm^{-3}$. This somewhat lower than the value inferred from the photoluminescence blue shift. However, if we use the slope at higher bias (Ohmic part of characteristic), this leads to an inferred doping level of $\sim 1.6 \times 10^{17} cm^{-3}$, which is the same order of magnitude as expected from the Burstein-Moss shift. Further, we note that there are some contact resistances and spreading resistances that will lead to an increment in the measured resistance value, so this inferred doping level is a lower estimate. Another important aspect is that the typical current density through the nanopillar active region under electrical injection for electroluminescence testing is expected to be less than $10k\Omega/cm^2$. If we note that the area of the active region is on the order $10\mu m^2$, this will lead to a voltage drop of roughly 1 V. It would be desirable to reduce this resistive drop further by annealing the contact or using a highly doped contact layer, but this conductance is more than satisfactory for the low current density expected for photovoltaic applications.

The results for fabricated p-doped InP nanopillars on a p-doped silicon substrate were somewhat less conclusive. The current conducted was rather low, at approximately $1\mu A$ under 1 V bias. More importantly, the I-V characteristics were Schottky-like, with a pronounced asymmetry in current conduction. This is shown in figure 2.15 and discussed in greater detail. Another interesting aspect is the pronounced photoresponse and photovoltage, which will be expected for a III/V-metal Schottky junction. Note that this was not observed for the n-doped pillars. There could be several reasons for the Schottky character: non-Ohmic metal contact due to Ti/Au metal, poor contact due to low doping and the effect of the heterojunction barrier. The heterojunction barrier is expected to impede conductance in the forward direction, noting that the positive direction for current flow is chosen to be silicon to InP (same for voltage bias). Therefore, it is more likely that in this case, the Schottky character is due to the metal contact and poor doping. An appropriate contact metal for p-InP is Zn/Au, which additionally requires some annealing to produce Ohmic characteristics. Alternatively, a highly p-doped InGaAs layer can be used to reduce contact resistance. The latter approach may be preferable since Zn atoms tend to diffuse easily and lead to leakage.

However, it is important to obtain an estimate of the activated dopant density in the nominally p-InP nanopillars. Optical characterization of p doping using the Burstein-Moss effect is challenging since the valence band effective mass is significantly higher than the conduction band effective mass. In order to obtain an estimate of the doping level, the 4 point probe method has been used to isolate the electrical characteristics from the effect of contacts and obtain the true p-doping level for some exemplary p-doped nanopillars. A 4 point probe structure was characterized and the voltage drop across the two inner terminals was obtained as a function of the current across the two outer terminals. Since no current

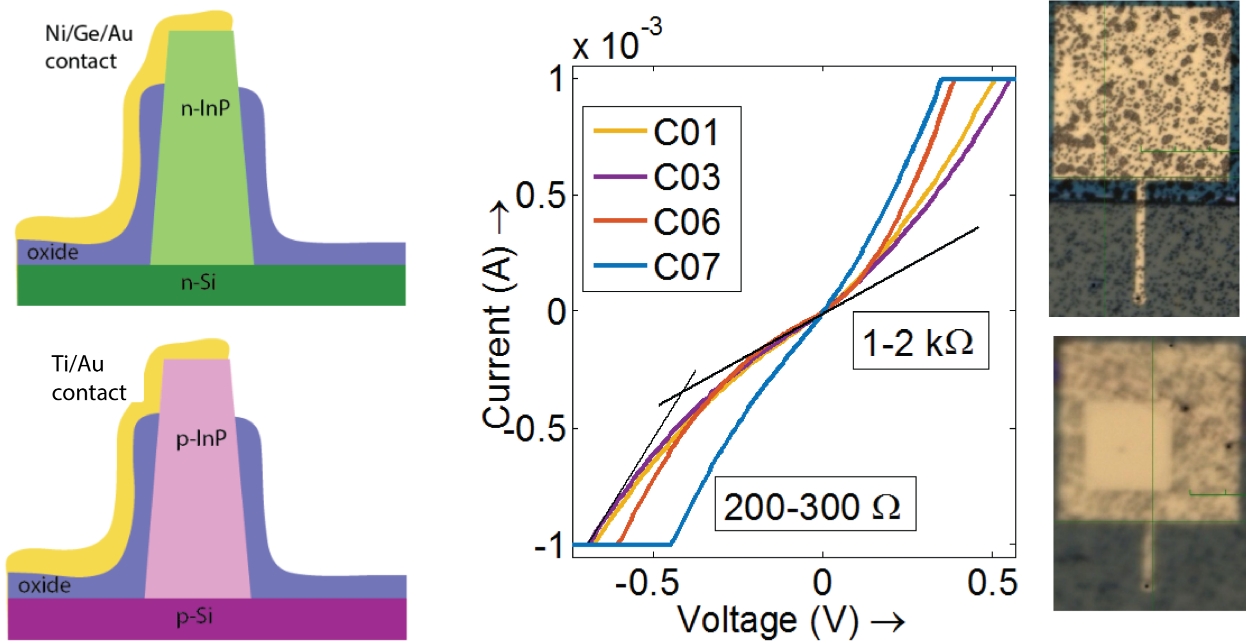

Figure 2.8: Nanopillar Resistors: (left) Schematics showing the structure of fabricated p and n doped nanopillar devices. Note that the different contacts used to study the behavior of these nanopillars will also influence electrical characteristics. (right) Electrical I-V characteristics from n-doped nanopillars and microscope images of fabricated devices. Each characteristic corresponds to an individual single nanopillar device. The characteristics are largely Ohmic, with some Schottky like behavior near zero bias.

flows through the inner two terminals across which the voltage drop is measured (see Fig. 2.9), the contact resistance does not add to the measured voltage drop.

Four point probe structures were fabricated for isotype p-doped nanopillars, doped insitu with Zinc and then mechanically transferred to an insulating silicon dioxide substrate. It was found that the resistance of the nanopillar was $0.72M\Omega$. This leads us to infer a rather low dopant density of $N_a = 5 \times 10^{15} cm^{-3}$. The doping density was calculated with a measured nanopillar diameter of 900 nm and length of 10 m. The hole mobility was assumed to be $200cm^2V^{-1})s^{-1}$. The built in p-i-n junction voltage corresponding to this p-doping density and n-doping density of $N_d = 5 \times 10^{17} cm^{-3}$ is:

$$V_{bi} = \frac{k_B T}{q} ln \left(\frac{N_a N_d}{n_i^2} \right) \sim 1.15 \text{ V} \tag{2.26}$$

which is close to the theoretical maximum possible open circuit voltage expected from the detailed balance limit. However, it would be desirable to have a slightly higher p-doping level in order to obtain better current conduction. In the case of electrical injection devices, it also makes sense to have a higher doping so that the resistive voltage drop at higher

current densities is not excessive. Ways to mitigate the effect of low p-doping concentration and contact resistance will be discussed in **chapter 6** for the nanopillar light emitting diode.

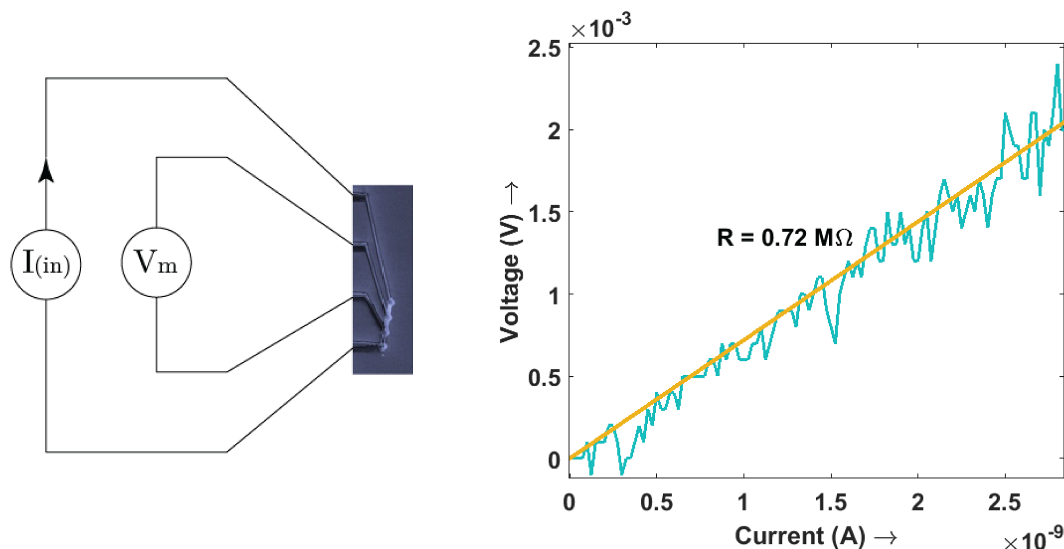

Figure 2.9: Four point probe: (left) Schematic showing the measurement principle and SEM image of a device. (right) Electrical characteristics from the 4 point measurement, allowing a calculation of the resistance. The obtained value of series resistance with the linear fit in orange is $0.72 M\Omega$.

2.3 Regrown Nanopillar Solar Cell

The efficiency of a solar cell depends strongly on its open circuit voltage, V_{oc}, which by detailed balance depends on the ratio of short circuit current I_{sc} to dark current I_d. The former depends on the product of optical absorption efficiency (converting photons to electronhole pairs) and the collection efficiency of electrons and holes at the contacts as current. On the other hand, the dark current is proportional to defect density and surface recombination rate. Here, excellent material quality using a regrown coreshell p-i-n junction leads to a drastically increased I_{sc}/I_d and consequently higher V_{oc}. The fabrication of the solar cell begins with the catalyst-free synthesis of wurtzite phase InP nanopillars via metalorganic chemical vapor deposition (MOCVD) on a [111] silicon substrate at a low growth temperature of $450°C$ [36], [37]. The nanopillars grow in a unique coreshell growth mode, allowing us to demonstrate the growth of single crystalline phase, high quality material with size scalable to microns without being subjected to the nanowire critical diameter limit[29]. As the growth is in coreshell mode, a radial p-i-n junction is easily formed by flowing dopants during the growth sequence. The surface recombination rate for different p-i-n junction geometries on the same material system can be compared via the ratios of exposed surface to

absorption volume for these structures. Surface exposure of the depletion region in a p-i-n junction is particularly unfavorable in terms of nonradiative recombination and leads to a dark recombination current of with an ideality factor of 2 (under high level injection). In this regard, the reduced surface exposure of the intrinsic part of the core-shell p-i-n junction is particulary advantageous compared to the axial p-i-n junction, and has orders of magnitude lower surface to volume ratio (see figure 2.11, (a)). This, and other advantages of the core-shell p-i-n junction structure will be discussed in the phototransistor chapter.

However, in spite of the low surface exposure of the core-shell p-i-n junction active region, we note that there is a prominent electrical shunt path that allows current to circumvent the active region and flow from the n-doped shell to the p-doped silicon substrate. This situation is depicted in figure 2.10, inset (a). This leads to a leakage currrent on the order of several hunder nanoAmperes, too high for any photovoltage to be observed under solar illumination. The leakage current due to the shunt path is shown in figure 2.10, (b) in red.

To circumvent this problem, we performed a secondary growth (i.e., regrowth) to place the p-i-n junction on the top portion of a p-doped nanopillar and, hence, eliminating the shunt path. A p-doped core was chosen because the regrowth on the n-doped nanopillar was not successful on a first attempt, although this is most likely due to issues with MOCVD chamber cleanliness. This regrowth process is schematically shown in Figure 2.10, (d). Regrowth was done by masking the bottom portion of an already grown p-type nanopillar with thin layers of silicon dioxide (SiO2) and amorphous silicon prior to regrowth. Amorphous silicon was found to be critical to the regrowth process as it shortens the diffusion lengths of the growth precursor adatoms on the growth mask to aid thin film like deposition on the nanopillar sidewalls. More details on the preparation steps can be found in [39] and [38]. We point out that the shunt isolation is provided because the adatoms diffuse to the exposed top of the InP nanopillar and contribute to further core-shell growth only at the top. With regrowth, the size and location of the p-i-n junction can be controlled precisely along the length of the nanopillar. This added control and the elimination of shunt current path allow us to dramatically improve the device dark current characteristic by 6 orders of magnitude, as shown by the blue trace in figure 2.10, (b). Figure 2.10 (c), shows the before and after regrowth scanning electron micrographs, showing the smooth sidewalls of a regrown nanopillar as a sign of excellent regrowth material quality. Indeed, when examined under a high-resolution transmission electron microscope (HRTEM) (Figure 2d), the regrown junction exhibits high crystal quality over large examined sections along the length of the nanopillar, suggesting that the regrown material is virtually free of stacking dislocations [38]. When the regrowth process is completed, a typical nanopillar has a natural vertically tapered shape with an upper and lower diameter of 650 and 900 nm, respectively, and a junction length of $5.5\mu m$. This natural nanopillar shape produces a unique dielectric antenna effect that is further enhanced by the tapered sidewalls, facilitating enhanced absorption over a broad spectrum and large range of incidence angles. The absorption properties are discussed in the next chapter.

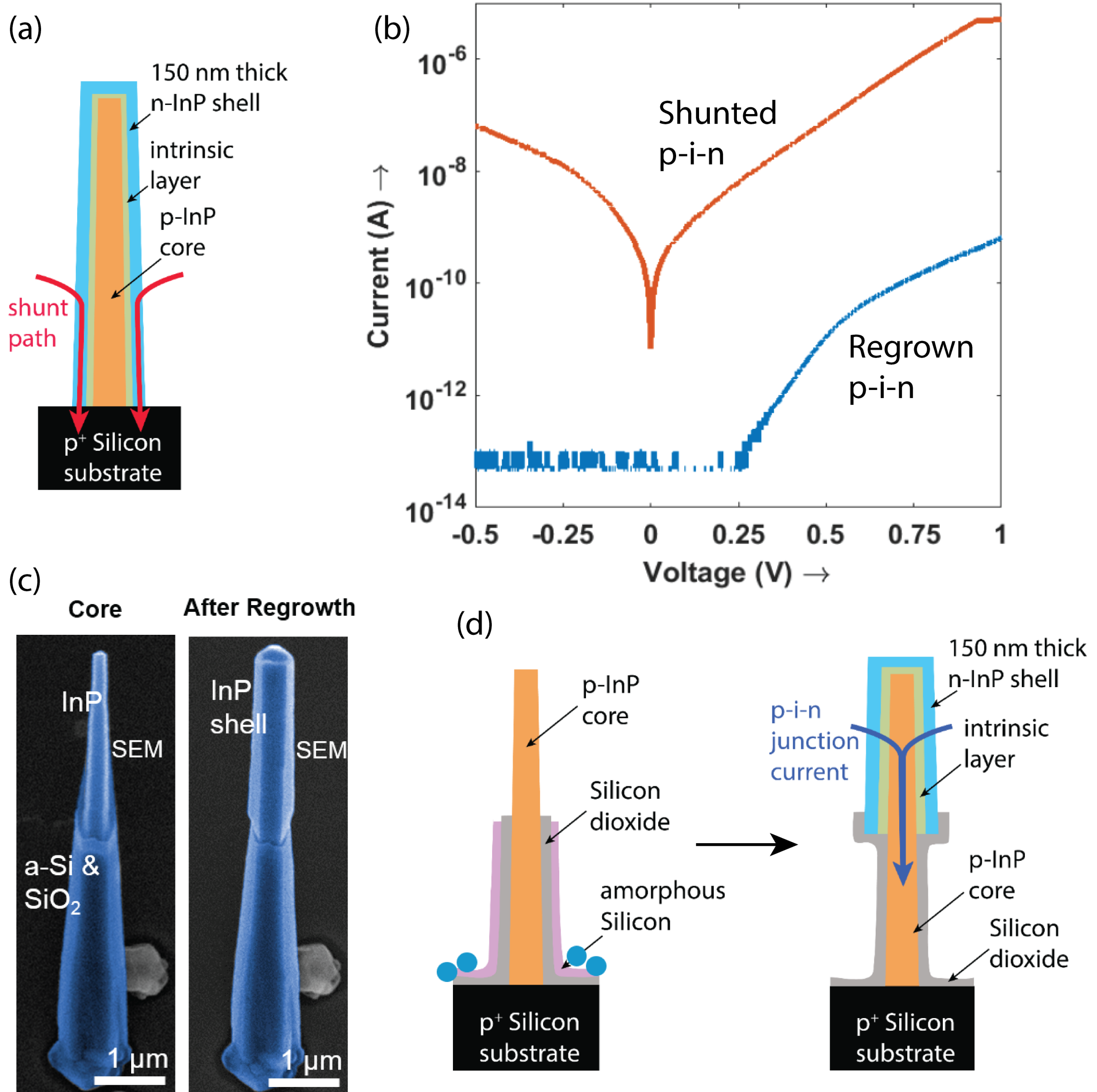

Figure 2.10: Nanopillar regrowth: (a) Direct core-shell device showing the presence of a shunt path, (b) I-V characteristic showing orders of magnitude improvement in dark current after regrowth, (c) SEM image of the same nanopillar before and after regrowth, (d) Schematic showing nanopillar and layer structure before and after regrowth

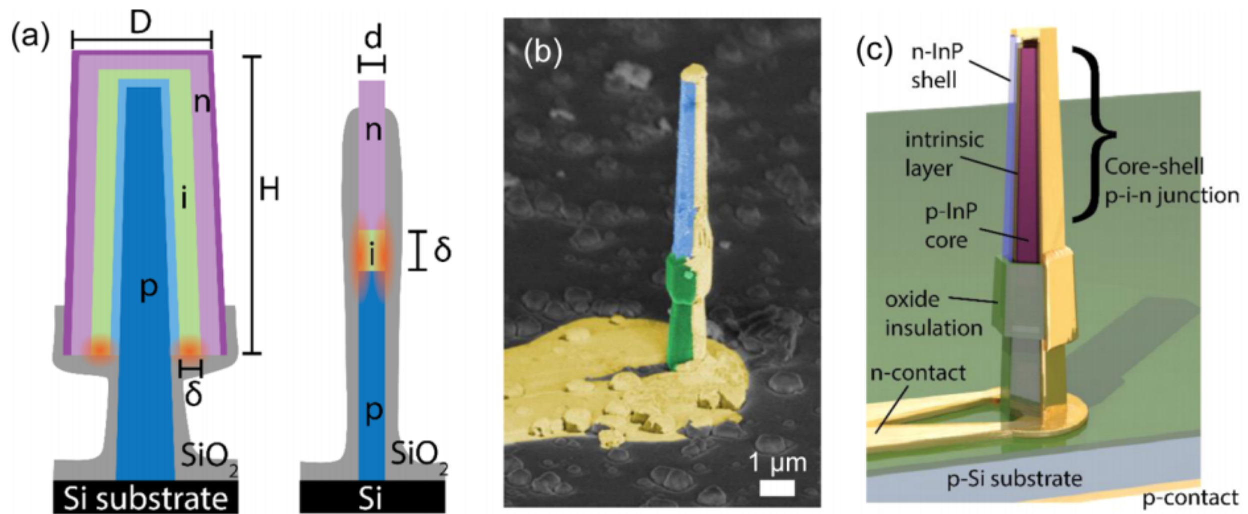

Figure 2.11: Nanopillar device schematic: (a) Comparison of active region exposure for core-shell vs. axial geometry, (b) Nanopillar device SEM, (c) Schematic illustrating corresponding structure

After regrowth, the outer n-doped layer of a single nanopillar was electrically contacted via electron beam lithography and angled Ti/Au (7 nm/150 nm) metal evaporation. The p-core contact was formed on the backside of the p-doped silicon substrate. The fabrication process was identical to that shown in figure 2.7. The schematic and SEM image of such a fabricated device are shown in Figure 2.11 In this case, because we use thick, nontransparent metal as the n-contact on the nanopillar, less than half of the nanopillar is exposed for surface normal light capturing. The efficiency calculation is therefore normalized to the actual exposed junction area of the nanopillar. In the future, the exposed area can be increased with the use of transparent electrodes, such as indium tin oxide (ITO), which has been successfully demonstrated to form good electrical contacts to InP nanowires.

The InP nanopillar solar cell is tested with a solar simulator with a calibrated AM 1.5 G solar radiation spectrum. A typical room-temperature current-voltage (IV) characteristic under dark testing conditions is shown in Figure 2.12. An extremely low dark current of less than 50 fA, limited by instrumentation noise floor, is achieved. This corresponds to a dark current density of less than $5.0fA\ \mu m^{-2}$. Further, the I-V characteristic can be fit to a dark current floor which is even lower, at $0.1fA\ \mu m^{-2}$, which is the lowest achieved for a nanowire or nanonanopillar based device to the best of our knowledge. This low dark current is a testament of the excellent quality of the regrowth material, device design and fabrication process. However, this is still rather high compared to what is required in order to achieve the Shockley-Queisser limit.

When illuminated by AM 1.5 G solar spectrum, the solar cell showed an open circuit voltage (V_{oc}) of 0.534 V, a short circuit current (I_{sc}) of 96.0 pA, and a fill factor of 48.2%. The relatively low V_{oc} and fill factor are thus far limited by a large $1M\Omega$ contact resistance, due

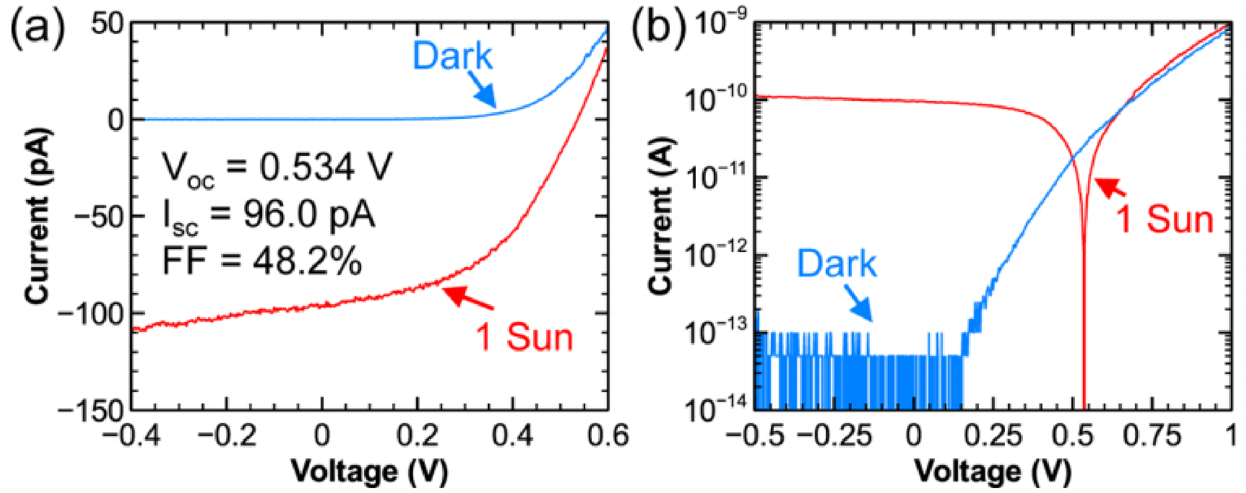

Figure 2.12: Nanopillar solar cell I-v: (a) linear scale I-V for an exemplary nanopillar device in dark and under AM1.5G illumination (b) Log scale for the same

to the lack of a heavily doped contact layer and contact annealing step. With better doping engineering and contact formation to reduce contact resistance, the solar cell performance is expected to improve. Normalizing ISC to the projected exposed area yields a short circuit current density (J_{sc}) of $76.3mAcm^{-2}$. This is more than a factor of two higher than the J_{sc} of $32.2mAcm^{-2}$ predicted by the Shockley-Queisser limit for a planar solar cell. This light concentrating effect allows the single nanopillar solar cell to collect light from an absorption cross section that is significantly larger than the physical cross section of the nanopillar. Further measurements and implications of this effect are discussed in the next chapter. Note that the power conversion efficiency of the single pillar device, from the above figures of merit, comes to a respectable 19.6%.

In order to further investigate the cause of the mediocre open circuit voltage, we performed temperature dependent measurements of the solar cell characteristics. In order to describe the significance of these measurements, we first derive the expected temperature dependence of a p-i-n junction solar cell, in the vicinity of room temperature. Note that the behavior is expected to deviate at very low temperatures due to dopant freeze out and other such effects, however the behavior is well described between 150-300 K. We first note that the open circuit voltage can be described as:

$$V_{oc}(T) = \frac{nk_BT}{q} ln\left(\frac{I_{sc}}{I_d}\right) \tag{2.27}$$

where $V_{oc}(T)$ is the temperature dependent open circuit voltage, n is the dark current ideality factor, k_B is the Boltzmann constant, T is the device temperature, q is the electron charge, I_{sc} is the short circuit current and I_d is the device dark current. Both short circuit current and dark current will have some temperature dependence. The temperature depen-

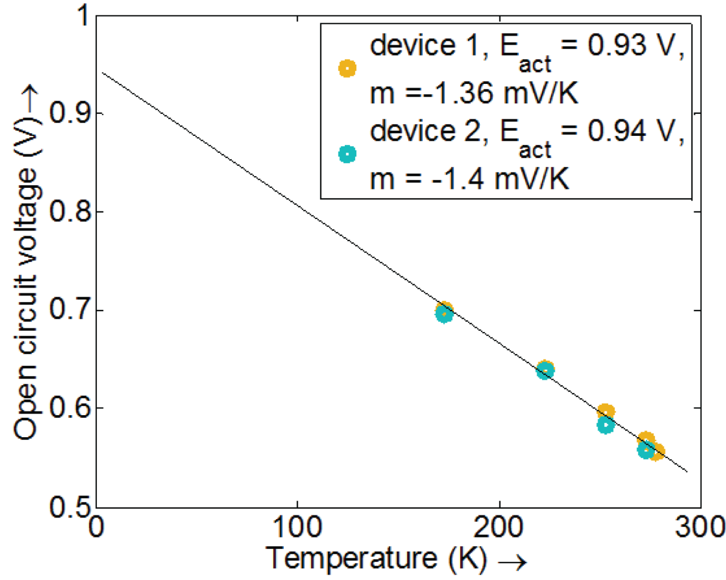

Figure 2.13: Nanopillar solar cell temperature dependence: open circuit voltage dependence for two exemplary devices

dence of the short circuit current arises from band gap narrowing as temperature is reduced, leading to a small reduction in short circuit current. However, note that the thermally activated dark current shows a very strong, exponential dependence on the temperature:

$$I_d(T) = I_d^o \left(\frac{T}{T_o}\right)^\gamma e^{\frac{E_a}{nk_B T_o} - \frac{E_a}{nk_B T}} \tag{2.28}$$

where the T^γ term denotes the temperature dependence of some of the pre-factors in the dark current density expression, T_o is the reference temperature at which the dark current is I_d^o and E_a is the activation energy of the dark current. Note that for a typical p-i-n junction diode where electrons and holes recombine across the material bandgap, the dark current activation energy is exactly equal to the bandgap $E_a = E_g$. Substituting the expression in 2.28 into the open circuit voltage expression in 2.27 gives us a more detailed expression for the temperature dependence:

$$V_{oc}(T) = \frac{E_a}{q} + \frac{nk_B T}{q} ln\left(\frac{I_{sc}}{I_d^o \frac{T}{T_o}^\gamma e^{\frac{E_a}{nk_B T_o}}}\right) \tag{2.29}$$

Note that the temperature dependence term within the logarithm only has a weak effect on the overall temperature dependence (especially in the vicinity of the reference temperature T_o). Thus, we may ignore the term, to obtain a linear fit for the open circuit voltage temperature of the form:

$$V_{oc}(T) = \frac{E_a}{q} + mT \tag{2.30}$$

where the slope coefficient m is a negative quantity and can be found by simplifying the expression in 2.29 to be simply related to the voltage penalty at the reference temperature:

$$m = -\frac{\frac{E_a}{q} - V_{oc}(T_o)}{T_o} \tag{2.31}$$

In case we are making temperature dependent measurements in a temperature range around the ambient temperature, then it is natural to take $T_o = 300K$. In this case, the voltage penalty for a good solar cell is typically 300-360 mV, leading to a temperature slope coefficient of -1 to -1.2 mV/K. Note that in figure 2.13, we indeed observe that the slope coefficient is quite reasonable for two exemplary devices and has a value of around -1.36 mV/K (indicating a fairly reasonable voltage penalty of 400-420 mV). However, the activation energy is quite surprising at a value of 0.94 eV: which is at a 500 mV deficit from the expected bandgap of InP.

This is substantially different from the case of poor quality solar cells where the activation energy (intercept of $V_{oc}(T)$ curve) is identical to the bandgap, but the slope is much steeper due to a larger voltage penalty. Another way to rephrase this observation is as follows: *the p-core devices behave as though they are good solar cells with a substantially lower bandgap than that of InP*. A potential cause for this could be the heterojunction barrier at the InP-silicon interface that starts to determine the forward characteristics of the solar cell. Other causes could also lead to a low activation energy, such as poor doping due to which the built in voltage might be low, or Schottky-like contacts. However, it is the author's opinion that the low V_{oc} of the regrown solar cells is due to poor electrical design or poor doping, rather than defective material quality. One approach for a different electrical design has been described in detail in the following section.

2.4 Position Controlled Nanopillar Solar Cells

In order for the benefits of the III/V nanopillar growth on silicon to translate into tangible applications, we require position controlled growth over large areas of the silicon substrate. Some indication of an approach for selective and controlled growth can be found from observations of growth patterns in the spontaneously nucleated random growth. Note that all the results in the preceding sections of this chapter are based on random growth without position control. In that case, the substrate preparation process involves deposition and patterning of a 100-200 nm thick silicon dioxide layer on the silicon substrate. Between the patterned silicon dioxide, there were exposed silicon trenches that were chemically roughened using a tetra methyl ammonium hydroxide etch. It was found that the nanopillars only nucleate on the silicon trench, and not on the silicon dioxide. Further, it was found that the nanopillar density is high at the edge between the silicon dioxide layer and the silicon

trench. From this observation, and other observations related to regrowth [38], it has been hypothesized that the diffusion of precursor adatoms across the substrate plays a key role in the nucleation. The precursor atoms may prefer to quickly diffuse across the silicon dioxide, and then slowly across the silicon substrate, thus allowing nucleation to be preferable on the silicon substrate. This is encouraging for achieving position controlled growth on the silicon substrate. As a first attempt, 300 nm holes were etched into the silicon dioxide layer using deep-UV lithography. The substrate was then chemically roughened using a similar procedure as the random growth. The growth temperature and precursor flow was initially kept similar to that of the random growth.

However, this initial attempt was not successful. The silicon exposed holes were found to contain poor quality polycrystalline material after the growth. The primary reason for the lack of nanopillar growth is that the fraction of the substrate now covered by oxide is substantially greater than in the case of the spontaneously nucleated growth. Hence, the group III precursor adatom concentration in the exposed silicon holes is higher than in the case of the spontaneous nucleation: leading to a very different V/III ratio. Therefore, it took several iterations of the growth recipe in order to narrow down on just the correct recipe window for high density nucleation of nanopillars.

Growth of InP nanostructures studied here was carried out between $450 - 460°C$ for 15 min. Under optimized growth conditions, nanopillar growth is performed under nominal TBP partial pressure of 56.3 mTorr and TMIn partial pressure of 0.55 mTorr. This results in highly regular arrays of InP nanopillars for various growth pitch sizes ($1\mu m$, $4\mu m$, and $40\mu m$), as shown in the large-scale tilt-view scanning electron microscopy (SEM) image in Fig. 2.14 (a). Site-controlled growth leads to increased uniformity of nanopillar dimensions, with a standard deviation in diameter of ¡10%. Due to the relatively large size of the oxide apertures, in addition to upright pillars, some growth apertures have slanted micropillars nucleating along the equivalent 111 directions of silicon. High growth yield exceeding 90% is obtained for all array periods. The pillars show some variation of taper angle in different arrays due to differences in local group V/III ratio. As seen in Fig 2.14 (b), the morphology and structure of nanopillars can be engineered considerably by controlling growth conditions. Under the same TMIn and TBP flow rates, nanoneedles are observed at a growth temperature of $450°C$. The taper angle decreases as temperature is increased to $455°C$. Nearly vertical pillar-shaped structures are obtained at $460°C$. Further increase in temperature, under a constant TMIn flow rate, adversely affects the nanopillar nucleation density. With an increase in substrate temperature, the cracking efficiency of tert-butyl phosphine (TBP) increases, which results in higher TBP partial pressure. Similar to the findings of Mohan *et al.* in InP nanowires grown on native InP [001] substrates, we observe an increase in lateral growth with higher TBP partial pressure **Mohan2005** Under high TBP partial pressure, this may be attributed to the adsorption and bonding of P atoms to In atoms along the [110] direction, providing additional dangling bonds for the attachment of the In species, thereby enhancing the lateral growth rate.

To investigate nanopillar nucleation and growth on silicon, we studied its cross-section using transmission electron microscopy. Using a micromanipulator and focused ion beam

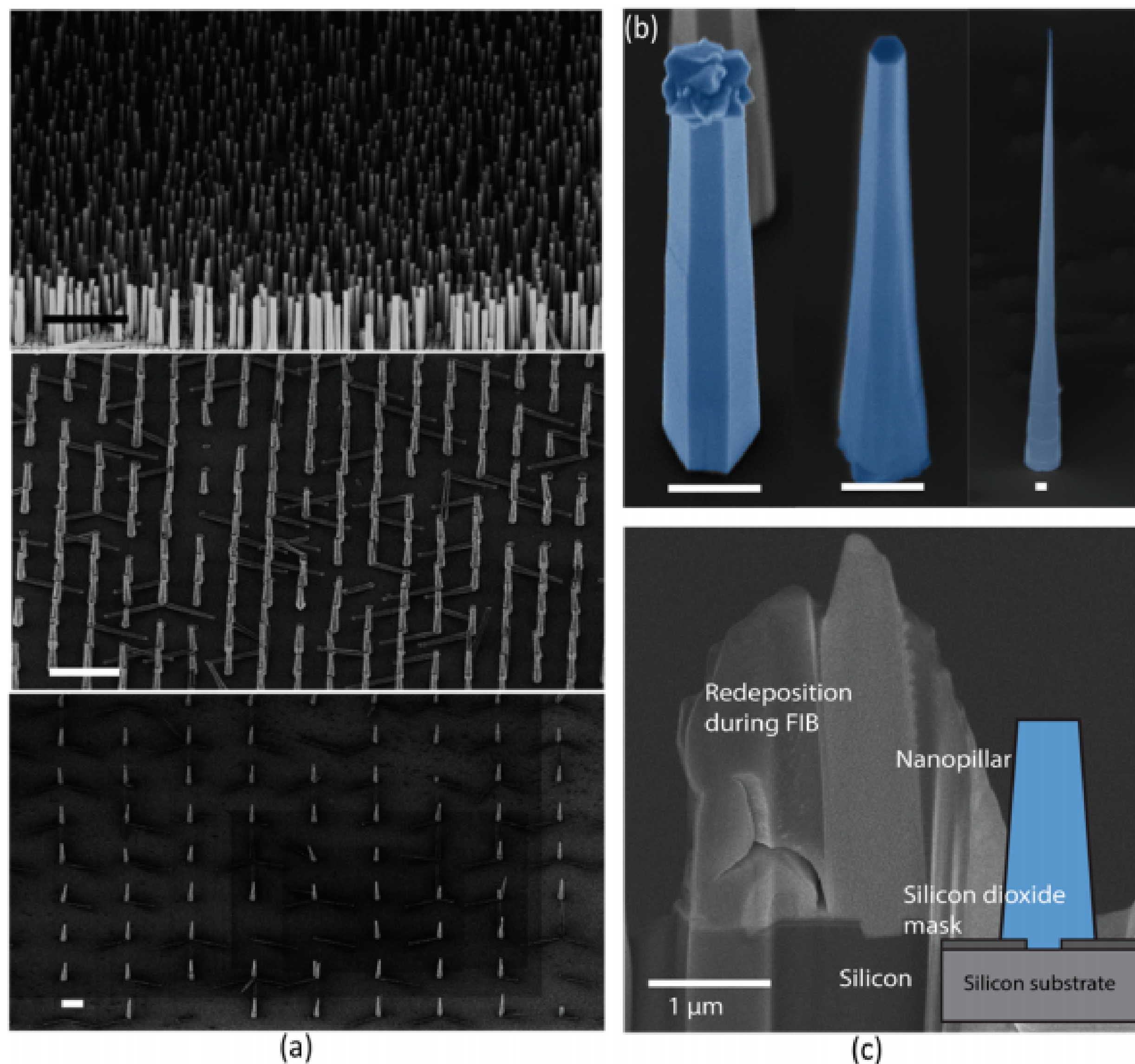

Figure 2.14: (a) Tilt-view low magnification SEM images of arrays of site-controlled InP nanopillars grown at 460°C. The scale bar in all images corresponds to 10 m and the growth periods (pitch) are 1 m, 4 and 40 m, respectively. (b) Nanopillars grown under the same nominal V/III ratio, for 15 min at 460, 455, and 450C, exhibit different taper angles. The scale bar in all figures is 1 m. (c) HAADF-STEM image of a cross-section of an InP nanopillar nucleating on Si, with a schematic representation in the inset

(FIB), a thin slice or lamella, of the heterointerface was prepared. The top part of the InP pillar was removed using the focused ion beam and Pt was then deposited onto the gap to passivate the heterointerface during the subsequent ion beam milling process. Figure 2.14(c) shows a cross-sectional high-angle annular dark field scanning transmission electron microscope (HAADF-STEM) image of the nanopillar nucleating directly on the silicon opening in the oxide. Due to its core-shell growth mode, the nanopillar grows out of the oxide opening and assumes a final diameter $\sim 1\mu m$. We previously found that periodic misfit dislocations effectively relax the misfit stress between Si/InP, leading to the high-quality defect-free growth in the bulk material of the InP pillar away from the heterointerface [37].

The core-shell growth of these nanopillars allows for in-situ doping in order to define a radial p-i-n junction. In designing the p-i-n junction we face a choice of whether to use a p-core structure or n-core for the nanopillar. We first consider the case of a simple p-type nanopillar resistor grown on a p-silicon substrate, as described in one of the previous sections on doping level characterization. The I-V characteristics of one such exemplary device are shown in figure 2.15, (a). Firstly, we note that the current is much lower than the n-doped nanopillar resistor. The sign convention for the current is positive from the p-silicon substrate to the p-InP nanopillar. We note that the current also shows strongly Schottky-like characteristics, with rectification in the forward direction (silicon substrate is biased positive with respect to nanopillar contact). This is likely due to the low doping and poor Schottky-like contact to the p-doped InP nanopillar. Further, we note that while the photocurrent continues to increase with higher optical excitation (light green), the photovoltage does not increase and instead shows an S-shape behavior under high optical power. This also has the effect of reducing the fill factor of the photovoltaic part of the characteristic. This behavior was also observed in multiple separate p-doped nanopillars, as well as in multiple p-core regrown p-i-n junction devices.

We suspect that the reason for this S-shaped characteristic is the presence of a heterojunction barrier to carrier transport. This effect has also been observed in organic photovoltaic devices due to the presence of excessive interface charge, which leads to an electrostatic potential that impedes carrier collection. In figure 2.15 (b), we depict the type II band alignment expected for wurtzite-InP and the silicon substrate. This suggests that the injection of holes from the silicon substrate into the InP will be impeded, whereas electron injection is going be much easier. This could lead to low forward current and a saturation in photovoltage in the forward direction. In order to address this issue, it was decided to use an n-core for fabricating position controlled solar cells.

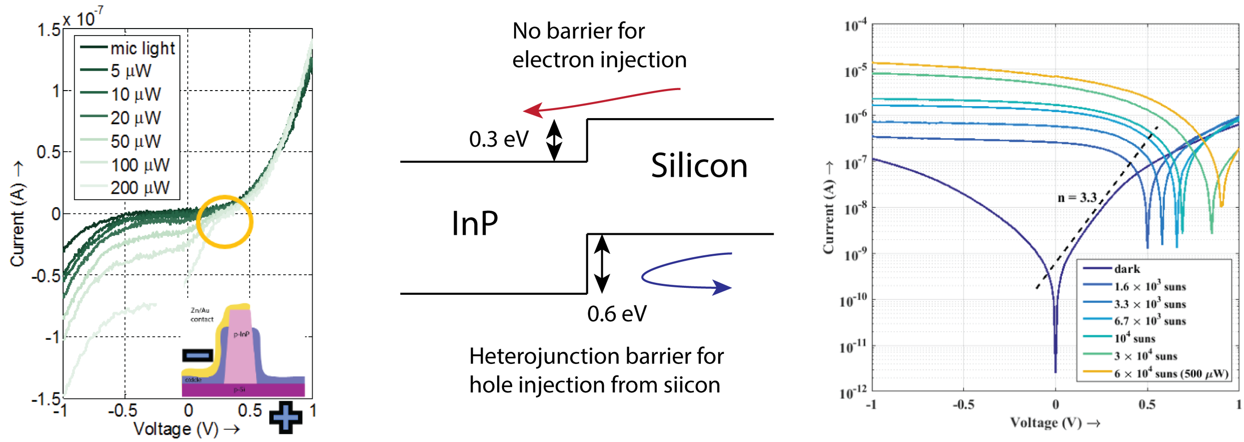

Figure 2.15: Comparison of S-shape I-V characteristic in p-core and n-core devices: (a) p-core isotype nanopillar device showing light response and s-shaped characteristic on increasing light intensity, (b) Type-II heterojunction alignment showing the impediment to hole transport, (c) S-shaped characteristics were eliminated in n-core nanopillars, and the open circuit voltage increases with excitation intensity

The process for the fabrication of position controlled nanopillar devices is described in more detail in the appendices and the chapter on the position controlled light emitting diode. However, we emphasize that the fabrication method was scalable and involved optical lithography with a photomask aligned to the growth substrate (as opposed to registration and e-beam lithography). The n-core, i, p-shell devices were grown sequentially via in-situ doping. Finally, a highly p-doped p-InGaAs layer was used to provide a good contact.

We note that no single pillar devices were obtained with the position controlled method, because the lift-off process tends to uproot isolated pillars, simply due to the mechanical agitation required. However, ensemble pillar devices survive and some of the ensemble pillar devices have less than five pillars. For one such device, we were able to measure a high photovoltage of 0.9 V. However, this high photovoltage was measured under high laser excitation power, since the leakage current in the device was too high for photoresponse under solar illumination conditions. While the S-shape characteristic and photovoltage saturation as observed in all the p-core devices has been eliminated, it still remains a challenge to obtain a sufficiently lowwer dark current to produce a high photovoltage under solar illumination. We speculate on a few possible causes of the high leakage. Firstly, we note that this batch of position controled devices has significant polycrystalline deposits at the tip of the pillar. These could potentially shunt out the p-i-n junction by allowing current to flow directly to the core of the nanopillar. Further, there could be fabrication issues associated with the lift-off and major agitation of the fabricated chip.

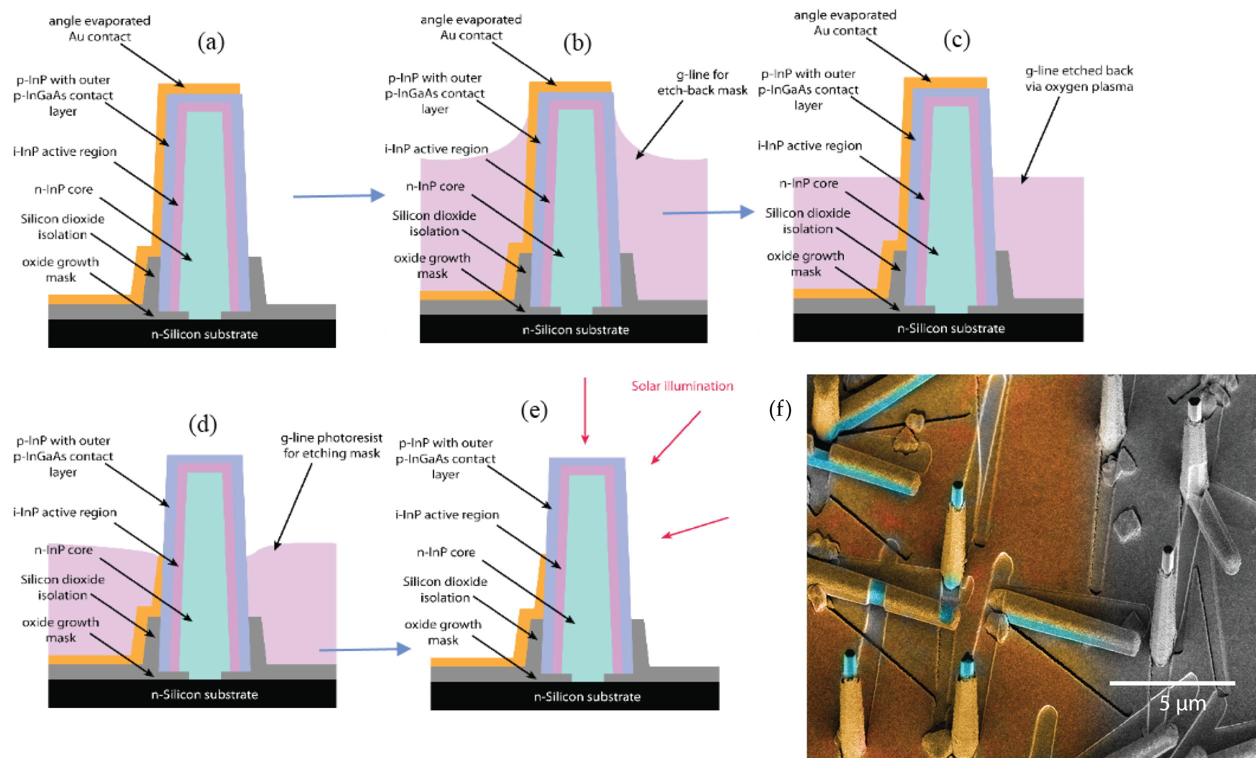

Figure 2.16: Gold etching for better optical access: (a) to (e) - see main text for details, (f) scanning electron microscope image of nanopillars with gold etched from tip for optical access

The lift-off process for contact definition has several disadvantages, most prominent of which is the tendency to uproot nanopillars in the agitation required to achieve liftoff. It would be extremely attractive to replace this process with an etching based process for contact definition, provided the etching was selective against the InP nanopillar. Further, such an etching process could potentially expose the tip of the nanopillar, which would significantly increase the photocurrent and light harvesting ability of the nanopillars. One such process is indicated in figure 2.16. The process is similar to the definition of the oxide shoulder on the nanopillar devices. However, instead of using buffered hydrofluoric acid to etch away oxide, we use a potassium iodide based etchant named TFA, that chemically etches gold but leaves the InP nanopillar untouched as seen in figure 2.16, (f). The gold was deposited using line of sight angled evaporation of gold, leading to prominent shadows determined by the nanopillars. Evaporation was performed from two directions in order to ensure a somewhat uniform coverage of the nanopillars. Following this, the photoresist etchback process was used to expose the tips of the nanopillars. We note that optical access was confirmed with photoluminescence on these nanopillars (which would not have been possible without the tip being exposed). A combination of this process, together with high quality nanopillars and a more gentle fabrication process could lead to excellent nanopillar

optoelectronic devices in the future.

Chapter 3

Omnidirectional Light Harvesting with Nanopillars

The Internet of Things (IoT) refers to a network of highly interconnected devices such as monitors, alarms, wireless sensor nodes or motes, mobile gadgets, various kinds of wearables and previously unforeseen smart systems with embedded microprocessors and network connectivity. These kinds of devices are expected to become omnipresent in our daily lives as well as in industrial, manufacturing and indoor agriculture environments [56], [57], [58]. However, it still remains a challenge to power such systems in a reliable and independent manner. Disposable batteries typically require frequent replacement and produce significant toxic waste [59], [60], [61]. On the other hand, photovoltaic (PV) powering based on energy harvested from indoor or ambient illumination would be sustainable, less wasteful and potentially produce sufficient power to render small devices completely autonomous [56], [62].

However, the available energy source from ambient illumination is roughly 100-1000 times lower in intensity compared to solar illumination [63], leading to a significantly lower carrier concentration compared to PV operation under the solar AM1.5G spectrum. In order to achieve high PV conversion efficiencies at such low and angularly diffuse light intensities, it is essential to have both excellent angle-insensitive light absorption as well as high photoluminescence external quantum efficiency (EQEPL) at these low illumination intensities [43]. Recombination losses in poorly passivated and defective material will be detrimental to operation under such low intensity. Careful attention to surface recombination and material quality is essential, while maintaining excellent optical absorption. In this chapter, we propose to use bottom-up grown InP-based nanopillars monolithically integrated with a suitable substrate (silicon here) for omnidirectional light absorption and photovoltaic power conversion. Using pristine Wurtzite crystalline phase nanopillars grown directly on silicon, we have already demonstrated high photoluminescence efficiency and Fermi level splitting under low light illumination [40]. Further, InP nanopillars have low surface recombination velocity and long lived minority carriers [37], [64]. We have also demonstrated the device potential for these high quality InP nanopillars in the course of this thesis, with single nanopillar solar

cells, phototransistors (chapter 4) with high gain at low light intensity as well as bright electroluminescence (chapter 6) [39], [38], [42].

In this chapter, we firstly calculate the power conversion efficiency limit for indoor lighting and demonstrate the excellent angle-insensitive absorption properties of the tapered nanopillar arrays, which will be essential to achieving these limits. The results are demonstrated for 50 μm size nanopillar arrays grown directly on silicon with lithographically defined position controlled growth (as described in chapter 6). Unlike previous demonstrations of anti-reflection coatings based on graded index nanostructures on silicon [65], the tapered direct bandgap InP nanopillars directly absorb the light within a few microns and can be used in thin film PV cells. In order to extend this method to thin film III/V solar cells, we also describe a novel anti-reflection coating based on a low-index nanopillar texture. This textured anti-reflection coating is expected to greatly reduce the reflection of light under diffuse illumination, thus greatly improving light scavenging from indoor illumination sources.

3.1 Detailed Balance Efficiency Limit for LED Energy Harvesting

The power conversion efficiency limit for photovoltaic (PV) energy harvesting from indoor lighting can be calculated by applying the Shockley-Queisser analysis [66] to the spectrum of a light emitting diode (blue LED) + yellow phosphor. The key difference from blackbody solar radiation is the narrower spectral distribution of photons. Particularly in the case of monochromatic LED illumination, the spectrum can be very narrow, leading to a significantly higher peak theoretical efficiency compared to the $\sim$ 31% solar PV efficiency limit. In the following, we describe the detailed balance PV efficiency calculation. The power conversion efficiency (subscript *opt* to denote optimized bandgap of PV) is given by:

$$\eta_{opt} = \frac{P_{out}}{P_{in}} = \frac{I_{sc} V_{oc} FF}{P_i nc} \tag{3.1}$$

where P_{out} is the output electrical power from the PV cell and P_{inc} is the incident power, all per unit PV cell area (W/m^2). The output power can be expressed in terms of the PV cell short circuit current density I_{sc} (in A/m^2), the open circuit voltage V_{oc} and the fill factor FF. P_{inc}, the power incident on the PV cell, can be calculated from the total flux of the LED light that is incident on the PV cell, using a view factor integral (used commonly in radiative heat transfer). If the number flux of photons from the LED (with units photons/m^2/eV/sr) is given by $I_{LED}(E, \theta, \phi)$, then:

$$P_{inc} = \frac{1}{A_{PV}} \int \int \int E \times I_{LED}(E, \theta, \phi) \frac{cos^2\theta dA_{PV} dA_{LED}}{\pi s^2} dE \tag{3.2}$$

where the integrals are performed over E the energy distribution of the LED emission spectrum, the surface of the LED emitter with total area A_{LED} and the surface of the PV cell with total area A_{PV}. Note that the term $cos\theta dA_{LED}/s^2$ is the differential solid angle

$d\Omega_s$ subtended by the LED area element at the PV cell. The geometry is illustrated in Fig. 3.1.

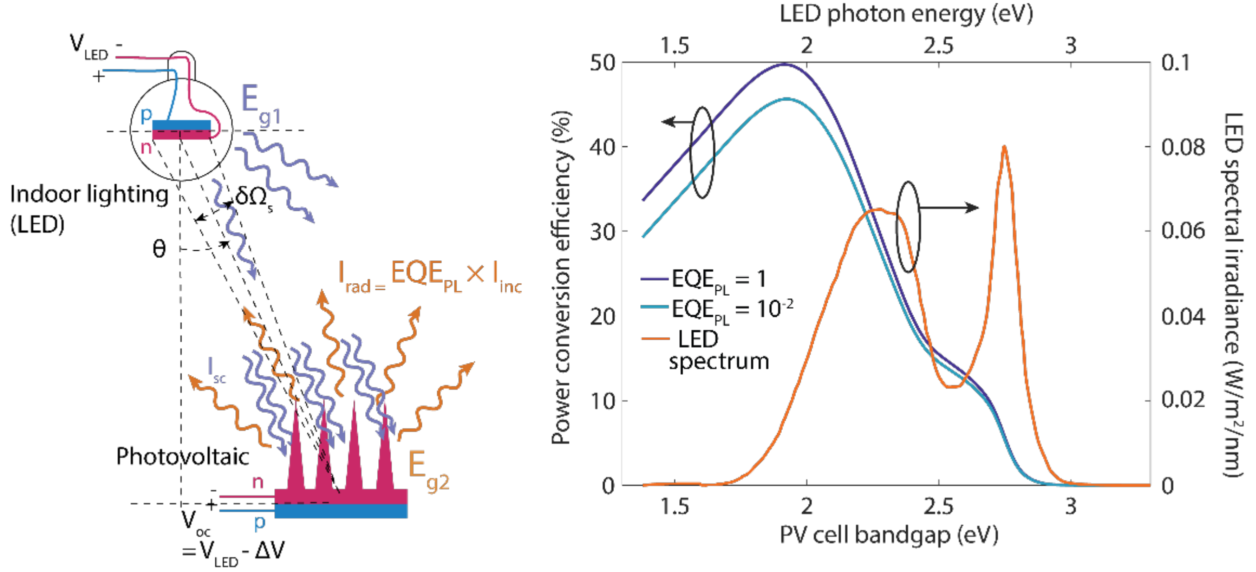

Figure 3.1: Detailed balance limit: (left) geometry showing light harvesting from LED at some distance to a PV cell PV-cell bandgap dependent. The annotated quantities are described in the main text. The efficiency limit will depend on the solid angle subtended by the LED at the PV cell. (right) Detailed balance efficiency limit for LED to PV energy conversion for a fixed LED spectral irradiance (warm white) shown in orange and PV cell bandgap dependent power conversion efficiency (blue curves). The two efficiency curves are for different external luminescence efficiencies.

The photon number flux from the LED is determined by the spontaneous emission rate of the LED and depends on the emissivity $a_{LED}(E,\theta,\phi)$, temperature T and LED bias (or more specifically, the Fermi level split/q) V_{LED}:

$$I_{LED}(E,\theta,\phi) = a_{LED}(E,\theta,\phi) \times \frac{2E^2}{h^3c^2}\frac{1}{e^{\left(\frac{E-qV_{LED}}{k_BT}\right)}-1} \tag{3.3}$$

Here, h is Plancks constant, q is the fundamental charge, k_B is the Boltzmann constant and T is the LED temperature, assumed to be same as the ambient and PV cell temperatures. It can be noted that this is a modified version of Planck's black body formula, with a non-zero chemical potential qV_{LED} associated with the photons. Equation 3.2 can then be simplified for an isotropic LED emitter, with power incident from a small LED onto a small PV cell (small with respect to the separation between the two devices) subtending a total solid angle $\delta\Omega_s$ and at angle θ (see Fig. 3.1 for configuration):

$$P_{inc} = \left(\int a_{LED}(E) \times E \times \frac{2E^2}{h^3c^2} \frac{1}{e^{\left(\frac{E-qV_{LED}}{k_BT}\right)} - 1} dE \right) \times \frac{\delta\Omega_s}{\pi} \times cos\theta \tag{3.4}$$

More generally, the power incident on the PV cell depends on the view factor of the PV cell at the LED, which can be satisfactorily approximated with the above for small areas for both the LED and PV. View factors for more complex geometries are presented in [67], [68]. One additional limiting case of interest is when the LED is infinitesimally close to or flush with the PV cell. Here, all the radiation emitted from the LED is collected by the PV cell, leading to a view factor of 100%. However, in application, it is expected that the IoT device will typically be some distance from the indoor lighting source. Continuing with the small area case, the incident photon current on the PV cell is given by:

$$I_{inc} = \left(\int q \times a_{LED}(E) \times \frac{2E^2}{h^3c^2} \frac{1}{e^{\left(\frac{E-qV_{LED}}{k_BT}\right)} - 1} dE \right) \times \frac{\delta\Omega_s}{\pi} \times cos\theta \tag{3.5}$$

In order to calculate the theoretical PV peak efficiency, we assume isotropic absorption of photons and perfect carrier collection. The latter is easily achieved in high quality III/V semiconductor materials. We will discuss how it is possible to achieve the former. Hence, the short circuit current I_{sc} is very close to I_{inc} for an optimally chosen PV cell bandgap. The calculation of the open circuit voltage V_{oc} is slightly more involved, and relies on a detailed balance argument [66], which states that at open circuit and ideal external luminescence efficiency, a photon is re-emitted at the band edge of the semiconductor PV absorber for every absorbed photon. Assuming a photovoltaic open circuit voltage Voc (Fermi level split qVoc) we can integrate the spontaneous emission rate over the hemisphere and obtain the total radiative output of the PV cell:

$$I_{rad} = \left(q \times a_{PV}(E) \times \frac{2E^2}{h^3c^2} \frac{1}{e^{\left(\frac{E-qV_{oc}}{k_BT}\right)} - 1} dE \right) \tag{3.6}$$

where $a_{PV}(E)$ is the absorptivity of the PV cell, assumed to be isotropic and energy dependent (through the bandgap and Urbach energy of the PV absorber material). Thus, the expression for the external quantum efficiency of photoluminescence at open circuit for the solar cell is given by:

$$EQE_{PL} = \frac{I_{rad}}{I_{inc}} = \frac{\int a_{PV}(E) \frac{E^2}{e^{\left(\frac{E-qV_{oc}}{k_BT}\right)} - 1} dE}{\int a_{LED}(E) \frac{E^2}{e^{\left(\frac{E-qV_{LED}}{k_BT}\right)} - 1} dE} \times \frac{\pi}{\delta\Omega_s cos\theta} \tag{3.7}$$

Here we point out that there are two potential routes to achieving meaningful energy conversion. It helps to recall that the LED is essentially a black body emitter with some emissivity. The photons are in steady state with a non-equilibrium electron hole population. A high LED intensity could then be achieved in two ways: either when the emitter is heated

very strongly, or when the electron-hole population above equilibrium is increased through an external excitation mechanism. The former approach is used for thermal emitters such as a lightbulb and is naturally present in stars such as our sun due to thermonuclear fusion. We will simplify the above formula to obtain the Shockley-Queisser limit for single junction solar photovoltaics. The latter approach is used for bright light emitting diodes for indoor illumination for instance. In what follows, we will also simplify eqn 3.7 to express the open circuit voltage for LED to PV conversion in a simple manner.

Since the open circuit voltage Voc is typically sufficiently below the bandgap for both the PV cell, we may use the Boltzmann approximation for the Bose-Einstein distribution and simplify the above expression to obtain an intermediate expression for the open circuit voltage (here we assume separate LED and PV temperatures):

$$EQE_{PL} = e^{\frac{qV_{oc}}{k_BT_{PV}}} \frac{\int_{E_g^{PV}}^{\infty} x^2 e^{-x} dx}{\int a_{LED}(yk_BT_{LED}) \frac{y^2}{e^{\left(y-\frac{qV_{LED}}{k_BT_{LED}}\right)}-1} dy} \times \left(\frac{T_{PV}}{T_{LED}}\right)^3 \times \frac{\pi}{\delta\Omega_s cos\theta} \tag{3.8}$$

where the dimensionless variables in the argument of the integral x and y are equal to $\frac{E}{k_BT_{PV}}$ and $\frac{E}{k_BT_{LED}}$ respectively. Note that we assume a step absorptivity function for the purpose of a simplified formula. Then, the integral in the numerator has a lower limit corresponding to the PV bandgap. This integral can be simplified using integration by parts, and the logarithm can be taken to yield the following:

$$\begin{aligned} V_{oc} - \frac{E_g^{PV}}{q} = {} & \frac{k_BT_{PV}}{q} \ln\left(\frac{\delta\Omega_s cos\theta}{\pi}\right) + \frac{k_BT_{PV}}{q} \ln\left(EQE_{PL}\right) \\ & + \frac{k_BT_{PV}}{q} \ln\left(\frac{\int a_{LED}(yk_BT_{LED}) y^2 \frac{1}{e^{y-\frac{qV_{LED}}{k_BT_{LED}}}-1} dy}{x_g^2 + 2x_g + 2}\right) + 3\frac{k_BT_{PV}}{q} \ln\left(\frac{T_{LED}}{T_{PV}}\right) \end{aligned} \tag{3.9}$$

Our first simplification is the case of solar photovoltaics. Here the LED bias is simply zero, and the LED spectrum resembles that of a blackbody. We make the approximation that the emissivity of the sun is unity over the spectral range of interest and simplify to obtain the following expression:

$$\begin{aligned} V_{oc} - \frac{E_g^{PV}}{q} = {} & \frac{k_BT_{PV}}{q} \ln\left(\frac{\delta\Omega_s}{\pi}\right) + \frac{k_BT_{PV}}{q} \ln\left(EQE_{PL}\right) \\ & + \frac{k_BT_{PV}}{q} \ln\left(\frac{\int_{\frac{E_g^{PV}}{(k_BT_{LED})}}^{\infty} y^2 \frac{1}{e^y-1} dy}{x_g^2 + 2x_g + 2}\right) + 3\frac{k_BT_{PV}}{q} \ln\left(\frac{T_{LED}}{T_{PV}}\right) \end{aligned} \tag{3.10}$$

This expression can be verified to be identical with the one derived by Miller [43]. Miller has made the additional assumption that $E_g^{PV}/(k_BT_{PV})$ is sufficiently larger than unity that

only the quadratic term in the denominator below the integral needs to be considered. This leads to some further simplifications.

We note that the low temperature limit of the open circuit voltage is simply the bandgap, and that there are three main loss terms. Experimentally, a temperature dependent measurement of the open circuit voltage at various light intensities is expected to provide important information regarding these loss terms, also known as *voltage penalties*. The first term is due to the limited view factor of the source at the PV cell, compared to the view factor of the entire enironment at the PV cell. This is also termed the solid angle loss. Note that the cosine term has been dropped in eqn. 3.10 since the sun is assumed to be a sphere and not a flat plate as shown in figure 3.1. The second voltage loss term is due to the less than unity external quantum efficiency of photoluminescence. For a perfect solar cell under open circuit, we have that every absorbed photon leads to an emitted external photon at the bandgap. The other terms are related to the different temperature and spectra of the emitters and are typically not significant.

Another simplification that can be made is when the LED is biased to emit light (as opposed to being heated to emit light). Typically, the Fermi level split of the electrons and holes in the LED active region is well below what is required for the transparency condition. More quantitatively, $E_g^{LED} - qV_{LED} < 5k_BT_{LED}$. In this case, the Boltzmann approximation can be applied to the Bose-Einstein integral in the numerator of eqn. 3.9. Further, we make the simplifying assumption that the LED emissivity is a step function to unity above the LED bandgap. This only introduces small errors into the calculation since the realistic emissivity profile typically has a sharp exponential drop at the band edge (Urbach tail). This allows the expression to be significantly simplified and expressed in terms of the LED and PV bandgaps as:

$$
\begin{aligned}
V_{oc} - \frac{E_g^{PV}}{q} = V_{LED} - \frac{E_g^{LED}}{q} + \frac{k_BT_{PV}}{q}\ln\left(\frac{\delta\Omega_s cos\theta}{\pi}\right) + \frac{k_BT_{PV}}{q}\ln\left(EQE_{PL}\right) \\
+ 3\frac{k_BT_{PV}}{q}\ln\left(\frac{T_{LED}}{T_{PV}}\right) + \frac{k_BT_{PV}}{q}\ln\left(\frac{y_g^2+2y_g+2}{x_g^2+2x_g+2}\right)
\end{aligned}
\tag{3.11}
$$

where x_g is the temperature normalized PV cell bandgap of $\frac{E_g^{PV}}{k_BT_{PV}}$ and y_g is the temperature normalized LED bandgap of $\frac{E_g^{LED}}{k_BT_{LED}}$. We have made the assumption that the LED bandgap is higher than that of the PV, which is generally true so that the PV can absorb most of the photons. Else, the short circuit current would be deficient and lead to suboptimal efficiency. We would like to further simplify this expression given that under close to room temperature operating conditions, the LED and PV bandgaps are significantly higher than the thermal voltage k_BT/q. Similar to Miller, this allows us to neglect all but the quadratic terms in the last voltage term on the right hand side of eqn. 3.11. This leads to the following simplified expression:

$$V_{oc} - \frac{E_g^{PV}}{q} = V_{LED} - \frac{E_g^{LED}}{q} + \frac{k_B T_{PV}}{q} \ln\left(\frac{\delta\Omega_s cos\theta}{\pi}\right) + \frac{k_B T_{PV}}{q} \ln\left(EQE_{PL}\right) + \frac{k_B T_{PV}}{q} \ln\left(\frac{T_{LED}}{T_{PV}}\right) + 2\frac{k_B T_{PV}}{q} \ln\left(\frac{E_g^{LED}}{E_g^{PV}}\right) \tag{3.12}$$

The key result is that the open circuit voltage V_{oc} is closely related to the LED bias V_{LED}. The differences from the respective bandgaps are the most relevant quantities. Note that the LED bias considered here is the actual quasi Fermi level split in the active region of the LED, with the bias voltage drop due to LED series resistance being irrelevant. Hence, the operating efficiency of the LED is irrelevant to the PV voltage: only the LED emissivity and brightness matters. The two terms following that are voltage penalties associated with non-idealities in the configuration and in the PV cell. The first loss term is due to the limited view factor of the PV cell at the LED and depends on the distance of the PV cell from the source. For a PV cell of size 5 cm at a distance of 5 m, we incur a voltage penalty of approximately 261.5 mV at room temperature. However, we would like to emphasize that under indoor illumination conditions, the ray-space of photons is often rather undirected. This is due to the multiple reflections from various surfaces within a given scene. In the computer graphics community, the use of physically based rendering techniques to simulate such indirect illumination is termed as *global illumination*. Depending on the position of the PV cell within a given illumination scene, a significant fraction of its illumination could be diffuse and indirect. Therefore, we ascribe importance to the ability of an indoor light harvesting PV cell to be able to absorb light incident at various incidence angles. In fact, for a more uniform illumination ray space, the angle voltage penalty can be significantly reduced, thus increasing the open circuit voltage of the PV cell.

The second voltage penalty term is due to the external photoluminescence quantum efficiency of the PV cell under illumination. It includes the internal quantum efficiency as well as the extraction efficiency of the photoluminescence. The last term is related to the different bandgaps of the PV cell and LED. Given the high absorption coefficient of III/V materials, the bandgaps of the two devices can be within a few $k_B T$ and still lead to near complete absorption. Therefore, this penalty is expected to be small in a PV cell chosen with an optimal bandgap. The largest penalty is typically the solid angle penalty due to the limited view factor of the LED source when viewed from the PV cell, which is expected to be reduced when the PV cell can accept illumination from a large range of angles.

Expanding this calculation further, we have used a realistic material model of the LED emitter and PV absorber to calculate short circuit current and power conversion efficiencies. The absorption coefficient has been modeled with the parameters for high quality GaAs, with an Urbach energy of 6.7 meV. Both the LED emitter and absorber thickness have both been assumed to be 5 μm for consistency, and the absorptivity was calculated from the material absorption coefficient, assuming perfect anti-reflection. The assumption of isotropic absorption holds fairly well since the high refractive index of the absorber leads to a critical

angle of about 15°, which implies that the distance travelled by light inside the absorber is insensitive to the angle of incidence in air. In the case of the nanopillar arrays, we have performed detailed fully 3-dimensional finite difference time domain simulations to show the simultaneous absorption and anti-reflection properties of the nanopillars (section 4 below). However, the theoretical efficiency results for the assumption based on absorption length serve as a good indicator of potential for high performance. They are summarized in the table below:

LED bandgap	$E_{g1} = 1.42$ eV ($\lambda = 873$ nm)	$E_{g1} = 1.88$ eV ($\lambda = 660$ nm)	$E_{g1} = 2.75$ eV ($\lambda = 451$ nm)
LED bias	$V_{LED} = 1.37$ V	$V_{LED} = 1.83$ V	$V_{LED} = 2.70$ V
E_{g2}^{opt}	1.40 eV	1.85 eV	2.72 eV
V_{oc}	1.08 V	1.54 V	2.41 V
PCE	67.0%	74.4%	81.9%
E_{g2}^{opt}	1.40 eV	1.85 eV	2.72 eV
V_{oc}	1.34 V	1.80 V	2.67 V
PCE	84.8%	87.9%	91.2%

Table 3.1: Calculated peak efficiencies for monochromatic LED sources and PV cells with corresponding optimized bandgaps. Note that the LED bias was chosen to be 50 mV below the bandgap, and the two different cases are chosen to contrast the effect of the solid angle penalty.

Table 3.1 shows the relationship between theoretical power conversion efficiency (PCE) and LED bandgap Eg_1 calculated using the detailed balance method. Material absorptivity parameters are used to calculate I_{sc}, with a finite absorber thickness. This was done to accurately model the absorption of below bandgap photons in the Urbach energy tail of the absorption spectrum. The absorption for above bandgap photons is nearly unity for a 5 μm thick semiconductor. The columns represent the data for different LED bandgaps. Additionally, as described in Eqn. **??**, the open circuit voltage closely depends on the LED bias V_{LED}. Note that the bias considered here is related to the chemical potential of the photons, rather than the electrical bias to the LED device. For each LED bandgap, we choose a high bias which is 50 mV below Eg_1. This high bias is more typical of high brightness solid state lighting. Lastly, the rows are split into a case with a solid angle penalty of 261.5 mV, and without this penalty. The penalty is minimal when the LED and PV are flush with each other, such that the view factor is 100%. The individual entries of the table provide the peak efficiency as well as the optimal PV bandgap Eg_2, which is typically less than 50 meV below the LED bandgap.

In order to describe some of the observed trends in the table, we provide an approximation for the theoretical efficiency based on the exact detailed balance formulation. The denominator, P_{inc} can be simplified for a narrow LED spectrum as: $P_{inc} = (Eg_1/q) \times I_{inc}$

where Eg_1 is the incident photon energy. For the output power of the PV cell, the open circuit voltage is related to the LED bias through a fixed voltage penalty dependent on EQE_{PL} (assumed to be perfect in Table) and solid angle penalty: $V_{oc} = V_{LED}\delta V$. The short circuit current, for near unity absorption, is nearly equal to the incident photon current. This leads to the following simple approximation for efficiency (from Eqn. 3.1):

$$\eta_{opt} \sim \frac{(V_{LED} - \delta V) \times FF}{E_{g1}/q} \tag{3.13}$$

From this approximation, we note that the theoretical efficiency will be high if the LED bias is close to the bandgap and the voltage penalties due to luminescence yield and view factor are low. The fill factor for ideality factor = 1 diode characteristic is typically around 85-95% depending on the exact Voc and Isc. It can be verified that the formula provides a reasonable approximation for the exact results in Table 3.1.

We emphasize that the detailed balance approach can also be applied to an arbitrary input spectrum of known irradiance. We have used the warm white LED spectrum (blue LED + yellow phosphor) shown in Fig. 3.1 to estimate the detailed balance efficiency limit and optimized PV bandgap for this spectrum. The irradiance was normalized to a spectrally integrated intensity of 10 W/m^2. There are currently no standards for characterizing ambient lighting PV, however this is within an order of magnitude of measured indoor light intensity, which is inherently quite variable [63]. This intensity of 10 W/m^2, or 1000 $\mu W/cm^2$ is roughly 100 times lower than AM1.5G solar radiation. As seen in Fig. 3.1, the optimal PV bandgap for this blue LED + phosphor combination is 1.91 eV (649 nm wavelength): achievable with InGaP closely lattice matched to a GaAs substrate. This efficiency limit is an order of magnitude higher than the $\sim 5\%$ efficiency achieved by currently ubiquitous amorphous silicon indoor PV, also chosen for its higher bandgap (eg: Texas Instruments Anylite calculators). At typical indoor office illumination conditions of $500 - 600\mu W/cm^2$, the 49.7% efficiency PV would lead to scavenged power on the order of $250 - 300\mu W/cm^2$, which is sufficient to autonomously power processors and data storage elements, with typical power consumption around 100 μW [62]. The detailed balance efficiency limit for compact fluorescence lighting, white LEDs and some other exemplary indoor illumination sources has previously been considered, however the explicit dependence on LED bias and analysis of voltage penalties has not been provided [69].

A similar analysis can be extended to the case of dual junction solar cells. Here, we have the choice to either current match the solar cells (series connection), or use a four terminal solar cell with the cells physically stacked on each other. The higher bandgap solar cell is placed on top of the lower bandgap, in order to absorb the high energy photons and lead to less thermalization loss compared to the absorption of the same spectrum within a single bandgap solar cell. For the electrical analysis in the case of the tandem (two terminal) dual junction solar cell, we have the same series current i_s flowing through the two junctions:

$$i_s = i_{sc}^{(1)} - i_d^{(1)}(e^{\frac{qV_1}{k_B T}} - 1) = i_{sc}^{(2)} - i_d^{(2)}(e^{\frac{qV_1}{k_B T}} - 1) \tag{3.14}$$

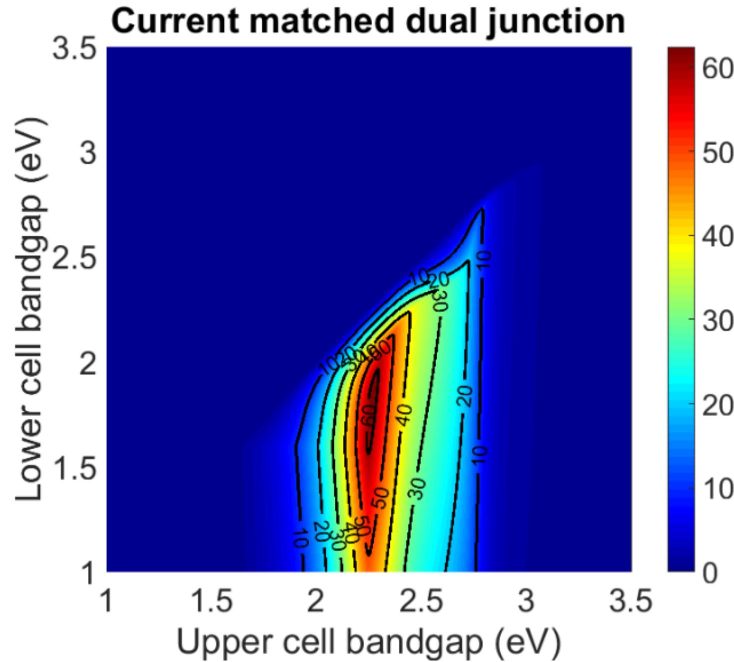

Figure 3.2: Two terminal dual junction: Efficiency contours for a two terminal dual junction solar cell. The overall efficiency suffers if the currents are not matched, leading to a narrow optimal range for the bandgaps.

where $i_{sc}^{(1)}$ and $i_{sc}^{(2)}$ are the respective short circuit currents for the higher and lower bandgap junctions (bandgaps E_{g1} and E_{g2}). Similarly for the saturation currents for each junction. Note that in this case, if one of the cells has a poor short circuit current i_{sc}, the series combination under zero bias will also have the poorer of the two currents and will detrimentally affect the performance of the combination. Essentially, when the series combination is under zero bias, the junction with higher short circuit current will have a positive bias, with limited carrier collection. Therefore, from purely an electrical point of view, it is important to ensure that the solar cell bandgaps are chosen so as to equalize photon absorption.

This brings us to the optical design of the dual junction. We consider a simplified case where both the sides of each of the solar cells have perfect antireflection so that the incident light makes a single pass. The absorber thickness assumed here is 5 μm, and absorptivity spectra equivalent to GaAs are considered (Urbach parameter). We consider the limiting efficiency as a function of the bandgaps, and under the ideal condition that each individual junction has unity external quantum efficiency of photoluminescence under open circuit, such that there is no reduction in voltage due to deficient external luminescence. Then, the limiting efficiency is determined purely from the light absorbed and current matching in the series connection. The case for the tandem cell is illustrated in fig. 3.2. We notice that the lower cell bandgap needs to be lower than the upper cell bandgap for power generation, and

the range of bandgaps for optimal performance is fairly narrow. A peak efficiency of 62% is observed for an upper cell bandgap of 2.25 eV and lower cell bandgap of 1.7 eV.

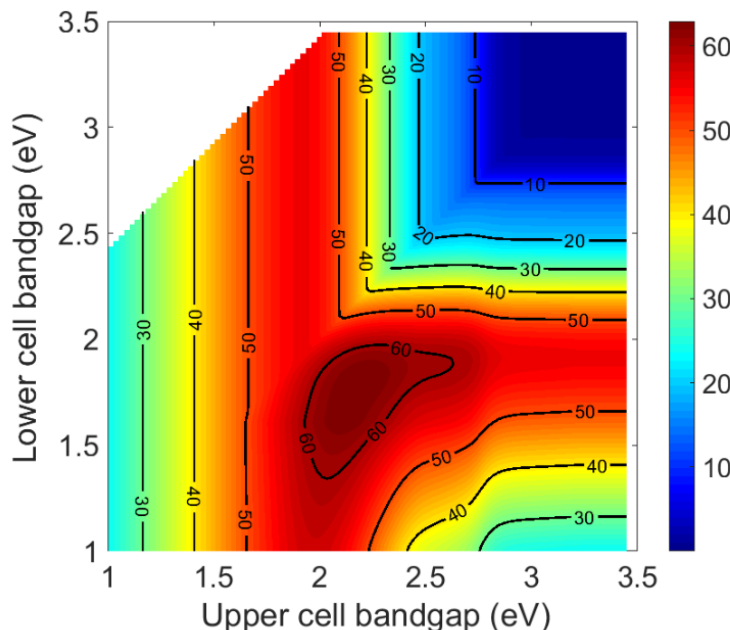

Figure 3.3: Four terminal dual junction: Efficiency contours for a dual junction solar cell with separate contacts. The are optically stacked and are assumed to have perfect anti reflection for this calculation. Note that the cells do not need to be current matched: one of the cells can absorb all the light, leading to an efficiency close to the single junction efficiency limit. The configuration is described in detail in the main text.

The case of the four terminal solar cell is shown in fig. 3.3. Here, the two junctions are connected separately and current matching is not a necessary requirement for efficient operation. Thus, one cell could be absorbing all the light, and have an efficiency close to that of the single junction. It is still desirable to match the bandgaps to the separate parts of the spectrum so that thermalization loss can be minimized. Note that these calculations have been performed for the warm-LED spectrum shown in fig. 3.1(b). The bimodal spectrum clearly has different amounts of energy associated with each of the lobes, since it is designed to be a warm lighting solution. The tandem or 4-terminal approach is expected to be significantly better for the cold LED case and other situations in which each part of the spectrum has roughly the same number of photons. We expect that if the need arises, ultra-high efficiency multijunction solar cells can be designed to match to the spectra of multicolored LED lighting. Each of the junctions can have a similar efficiency to that reported in the table above, leading to 70-80% efficiency for energy scavenging from indoor lighting.

3.2 Angle Insensitive Single Nanopillar Solar Cell

In chapter 2, we have described the fabrication and measurement of the single nanopillar solar cell. The single nanopillar device was fabricated using regrowth and was less than a micron in diameter. It was surprising to note that such a small device was capable of gathering light and producing photocurrent on the order of 100 pA. Here, we describe some measurements to quantitatively describe the nature of the absorption enhancement effect. Having studied the single nanopillar solar cell in detail, we will be in a position to examine large nanopillar arrays as well.

Fig. 3.4 shows the external quantum efficiency (EQE) as a function of wavelength for the solar cell under direct, top-down illumination. Absorption enhancement effect can be clearly seen, as evidenced by the EQE value of 200-400% for the wavelength range of 400-800 nm. This suggests a dielectric antenna effect enhancing photon absorption over a broad wavelength range. The antenna enhancement effect allows efficient coupling of light into the resonator modes of the nanopillar, allowing broadband, full solar spectrum absorption enhancement observed in the EQE data. The enhancement of normal incidence absorption is also related to a previously reported enhancement in emission in the normal direction [70]. The EQE data also shows insignificant absorption for wavelengths between 870 nm and 1100 nm, the band gap wavelengths of wurtzite phase InP and silicon, respectively, indicating that absorption in the silicon substrate does not contribute to the solar cell efficiency.

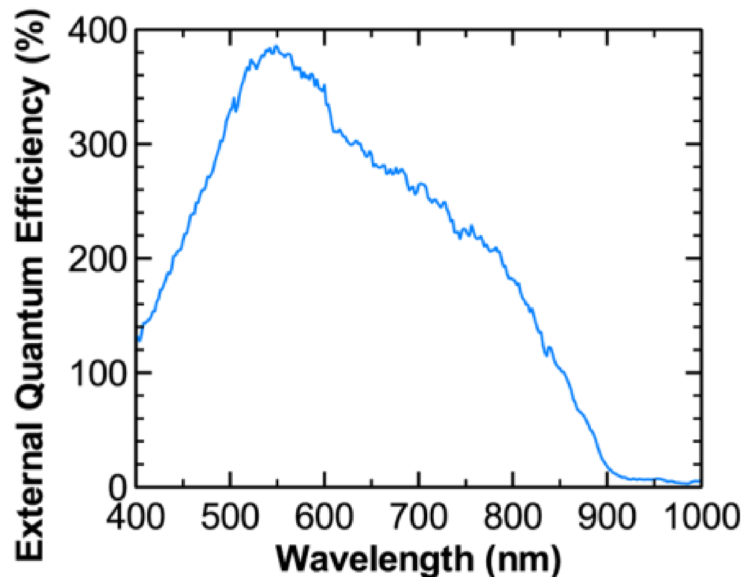

Figure 3.4: Spectrally resolved IPCE: The ratio of incident photons to collected electrons (IPCE), resolved along photon energy is higher than unity for a significant portion of the spectrum. IPCE and EQE are used interchangeably to describe the quantum efficiency at short circuit.

The photocurrent map displayed in Fig. 3.5 was generated by scanning a 2.4 μm wide 660 nm laser beam across the nanopillar solar cell. This map reveals negligible photocurrent contribution from the silicon substrate. The laser spot size of 2.4 μm was measured separately using a knife-edge method.28,29 As highlighted by the blue outline in Figure 3.5, the resulting photocurrent spot has a full-width at half-maximum of $\sim 2.3\mu m$, which is simply the width of the excitation laser beam. This result proves that the photocurrent measured indeed comes solely from carriers generated within the InP nanopillar, as photocurrent was collected only when the laser spot was shone directly onto the nanopillar solar cell.

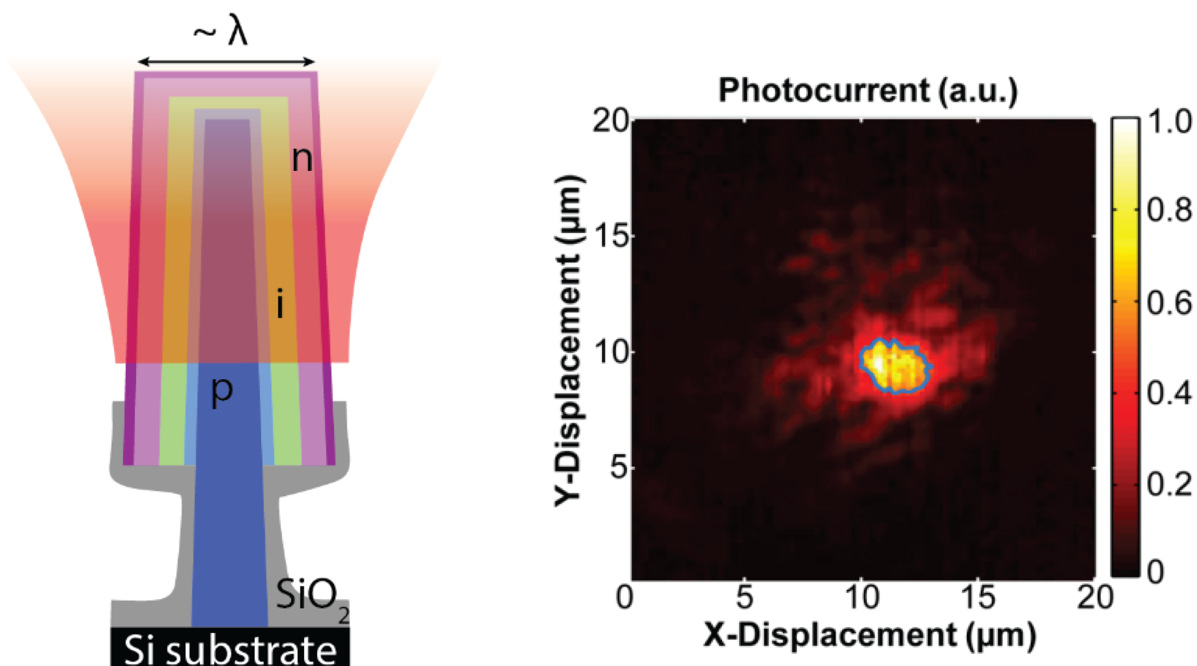

Figure 3.5: Enhanced absorption cross section: (left) Schematic showing light absorption enhancement due to the nanopillar geometry. (right) Photocurrent scanning reveals that the light absorption spot is a couple of microns in size, and the silicon substrate does not contribute to photocurrent generation. The scan was carried out using a diffraction limited spot of 660 nm light.

The dielectric antenna effect is evident in the IV measurements of the solar cell at different polar illumination angles made onto the uncovered side of the nanopillar. As shown in Figure 3.6a,b, both measured V_{oc} and I_{sc} increase as the incidence angle increases (angle defined in the inset of Figure 3.6(a). Instead of simply scaling proportionally to the capture area of the solar cell, the I_{sc} was found to increase by only a factor of 2.9 despite a calculated 33 times increase in solar cell exposed capture area. This rather angle insensitive photovoltaic

output is the result of the dielectric antenna effect enhancing optical absorption for near on-axis illumination, which can be clearly seen in the J_{sc} plot in Fig. 3.6c. Essentially, the absorption cross section for normal incidence illumination is more than an order of magnitude higher than what is expected simply from the physical cross section of the nanopillar.

The tapered sidewalls of the nanopillar also create a tighter focusing effect for on-axis illumination compared to non-tapered nanopillars. This allows for much greater absorption enhancement for near on-axis illumination that the pillars would not have otherwise experienced with non-tapered geometries. The pronounced enhancement effect for near on-axis illumination and the subsequent leveling off of this enhancement effect at higher incidence angles compensates for the change in the physical capture cross-section of the nanopillar solar cell, giving rise to its angle insensitive photocurrent. With further optimization of the taper angle and dimensions of the nanopillar, it will be possible to create a nanopillar solar cell that is almost completely angle insensitive, as described in the following sections. Hence, it is clear that the antenna effect not only improves the solar cell performance but also enables illumination angle insensitive response. This allows solar cells made with tapered nanopillars to have reliable and steady power output without the need of expensive solar tracking system to adjust for angle of illumination changes on a diurnal and seasonal basis.

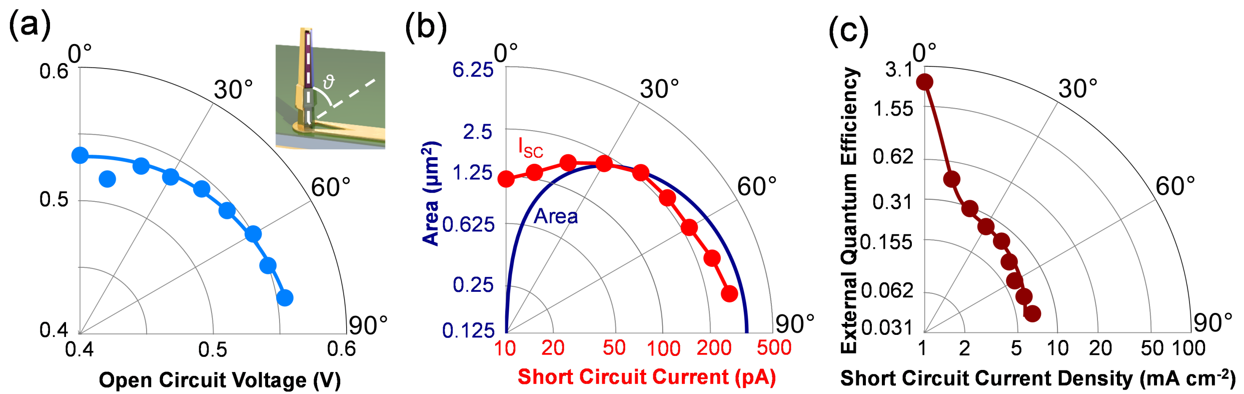

Figure 3.6: Angle-independent performance: Polar plots showing experimentally determined (a) open circuit voltage, (b) short circuit current and (c) external quantum efficiency (or equivalently, short circuit current density normalized to projected physical cross section). In particular, in (b) we note that for top down incidence ($\theta = 0$) the short circuit current is anomalously high compared to what we would expect from the small projected physical cross section. This is decribed in greater detail in the main text.

Simulation of the solar cell structure with finite-difference time-domain methods confirms our experimental results of enhancement expected due to the dielectric antenna effect. Fig. 3.7(a) shows the simulated short circuit current I_{sc} as a function of polar incidence angle θ,

co-plotted against the change in capture area (projected physical cross section). Again, the simulated I_{sc} changes much slowly with polar angle compared to the physical capture cross section of the solar cell. The simulated J_{sc} plot displayed in Fig. 3.7(b) also confirms the antenna enhancement effect favoring near on-axis illumination as the source of the insensitive angular response. Although the enhancement effect for the micron-sized nanopillars is somewhat smaller compared to that of nanowires with deep sub-wavelength diameters, the lower surface-to-volume ratio of the larger nanopillars significantly reduces the impact of surface recombination, which has been found to be especially detrimental to the efficiency of III-V nano*wire* solar cells [71], [72], [73]. The antenna enhancement effect also results in the absorption cross-section appearing larger than the physical capture cross-section, allowing a sparsely populated nanopillar array to most of the incident sunlight on an area of the substrate. The simulation data plotted in Figure 3.7(c) clearly supports this claim with two InP nanopillar arrays absorbing 90% of the solar spectrum with merely 17% of the solar cell volume filled with nanopillar material. Compared to nanopillar arrays with vertical sidewalls (red trace in Fig. 3.7(c)), tapered nanopillar arrays (blue trace in Figure 6c) display higher light absorption at 95% (versus 90% by the non-tapered nanopillar arrays), even when both arrays have the same 17% volume fill ratio. Therefore, solar cell efficiency can be further improved with tapered nanopillars. In the next section, we dig deeper into the tapered nanopillars and examine the mechanism behind their effectiveness.

3.3 Absorption in Sparse Nanopillar Arrays

Having studied the single nanopillar solar cell in detail, we are interested in extending the benefits of the optical enhancement effect to the case of larger nanopillar arrays. The nanopillar are taken to be of the same diameter as the single nanopillar solar cell studied in the previous section, but spaced sparsely so that only 10-15% of the volume is filled with InP material. This coresponds to an equivalent thin film thickness of around 500 nm or less.

Low-Q dielectric antenna behavior of the InP nanopillars ensures that light is absorbed from a larger cross section than the physical cross section of the pillar, allowing a sparse arrangement of these pillars to absorb a large fraction of the incident light. We have described the high absorption cross section and illumination angle insensitivity in the case of a single nanopillar solar cell device **Ko2015a** Here, we study the absorption properties of a sparse ensemble of tapered nanopillars. We model the absorption properties of tapered nanopillar arrays using the 3D finite difference time domain Maxwell solver Lumerical, with material parameters for Zinc Blende phase InP, since these parameters are well known. For an array of nanopillars of base diameter 650 nm and height 5 μm arranged in a square array with period 1.5 μm (volume fill factor of 5%), high angle insensitive absorption is achieved up to 40° incidence angle. The simulations were performed using the broad fixed angle source technique (split step method), in order to preserve incidence angle for broadband time domain simulations. The absorptivity was calculated by weighting with the LED+phosphor spectrum to be 90%, 92%, 89%, 94% and 95% for 0°,10°,20,30° and 40° respectively. Thus,

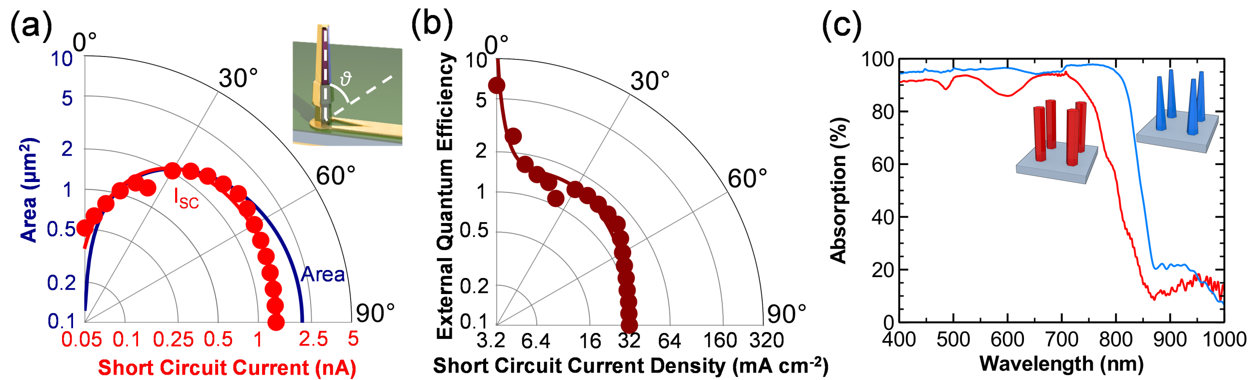

Figure 3.7: Nanopillar optical simulation: Simulated angular response of a single nanopillar solar cell and simulated absorption from a nanopillar array. (a) Simulated short circuit current I_{sc} (red) also shows angle insensitive response that scales slowly compared to the change in the capture area of the solar cell (blue). (b) Simulated short circuit current density J_{sc} confirms the directional antenna enhancement effect compensating for the change in capture cross-section as the illumination angle is changed, along with ultra-high external quantum efficienc for on-axis illumination. (c) Simulated absorption spectra of two nanopillar arrays showing greater than 90% absorption despite having only 17% volume fill ratio. The red curve shows the absorption spectrum of an array of 510 nm wide non-tapered nanopillars that are spaced 1 μm apart. The blue curve shows the absorption spectrum of a nanopillar array with tapered sidewalls. The array with tapered nanopillars is able to absorb 95% of the light, compared to 90% for the non-tapered nanopillars. To keep the volume fill ratio the same at 17%, the tapered nanopillars have upper and lower diameters of 325 nm and 650 nm, respectively, and are 6 μm tall. Micro/nanopillars of this dimension can be easily achieved by scaling growth time. The tapered nanopillars in this array are also spaced 1 μm apart.

we expect to achieve near-unity omnidirectional absorption with these InP nanopillars, using much less absorber material compared to tapered silicon microwire arrays as demonstrated in [74].

Fig. 3.8(a) shows the carrier generation profile at two different wavelengths of 660 nm and 850 nm. This is repeated for two different incidence angles of 0° and 40°. It is also important to resolve the polarization dependence of the absorption properties. The s-polarization (E-field perpendicular to plane of incidence) shows slightly less absorption compared to p-polarization, for the particular cross section chosen. Strong polarization anisotropy has been described in the absorption and emission properties of thin nanowires with 10s of nm diameter [75]. However, for the tapered nanopillars with diameter up to 650 nm, the polarization anisotropy is markedly lower, with high absorption maintained for the s-polarization. The polarization averaged results are plotted in Fig. 3.8(b), and show that the absorption effi-

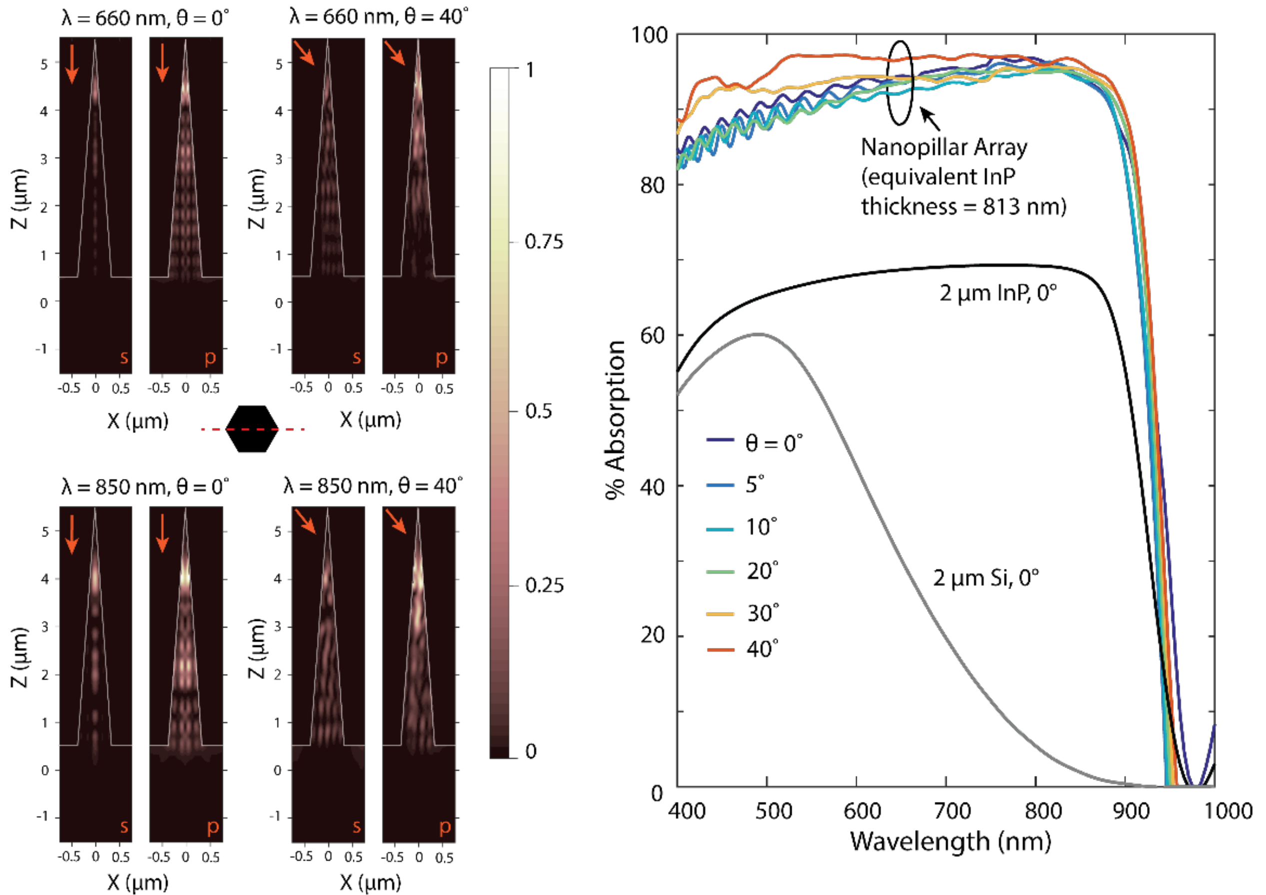

Figure 3.8: Nanopillar absorber: One particular special case of the gradient index texture is when the nanopillar itself absorbs light. The left panel shows the normalized carrier generation rate at two different wavelengths (660 nm, 800 nm), two different anges of incidence ($\theta = 0°, 40°$) and both s, p polarizations. It can be noted that most of the light is absorbed in the InP nanopillar, with little penetrating down to the substrate. The right figure compares the simulated absorption spectra of the nanopillar array at different angles of incidence, along with comparable equivalent thin films of InP and siicon.

ciency can be higher than 85% for a broad wavelength range, independent of incidence angle up to 40°, and substantially higher than the bare silicon and bare InP thin films. These results are highly encouraging for engineering towards perfect absorption of indoor light, insensitive to polarization and incidence angle.

3.4 Nanopillar Array Absorption Measurement

The position controlled growth of InP nanopillar arrays has been achieved at a low growth temperature of $450 - 455°$ using metal organic chemical vapor deposition. In this work, the pillar arrays were directly grown on a silicon substrate. However, growth is also possible on a native III/V substrate or other inexpensive substrates such as poly-silicon and sapphire [76], [77], [78]. Growth selectivity was obtained using a silicon dioxide growth template with holes patterned using scalable UV lithography. The pitch and arrangement of holes can be designed, and the hole size is chosen to be approximately 320 nm in diameter. Nanopillars nucleate only within the holes and not on the silicon dioxide mask. Within the same growth substrate, different growth pitches were defined, from 1 μm to 40 μm. Further details of the growth and precursor flows are described in [42], [46] and chapter 6 of this thesis. Scanning electron microscope images of pillar arrays for the densest pitch are shown in Fig. 3.4. In the right image, the pillar diameter is approximately 600 nm, and pitch is 1 μm. The array size used for the measurement was 50 μm, with an optical microscope image of the array in Fig. 3.10(b).

In order to confirm the angle insensitive absorption, the spectrally resolved absorption spectrum of the 50 μm nanopillar array was measured, and compared with that of a bare silicon substrate. The measurement was performed using an integrating sphere and a reference Lambertian sample with near-perfect reflectivity. Spatially localized measurements were performed by imaging a 50 μm diameter pinhole on the nanopillar array. The numerical aperture was kept small so as to minimize the angular spread ($\sim 2.5°$) at each angle of incidence.

The measurement setup is shown in Fig. 3.10(b). To obtain each absorption spectrum, three measurements were performed. Firstly, the monochromated light spot was incident on the Lambertian reference, and the reflected power was measured: $P_L(\lambda)$. Next, the spot was incident on a beam dump, and the background was measured: $P_D(\lambda)$. Finally, the spot was carefully positioned to the InP nanopillar array, and the final measurement was performed: $P_F(\lambda)$. The absorptivity of the nanopillar array is then given by (where $r(\lambda)$ is reflectivity):

$$a(\lambda) = 1 - r(\lambda) = 1 - \frac{P_F(\lambda) - P_D(\lambda)}{P_L(\lambda) - P_D(\lambda)} \tag{3.15}$$

Wavelength selectivity was obtained using a scanning monochromator to filter out the wavelength of interest from a broadband Xenon arc lamp source. The internal environment of the integrating sphere was identical for all three measurements. Only the polar incidence angle θ was varied and not the azimuthal angle ϕ since the highly symmetric hexagonal

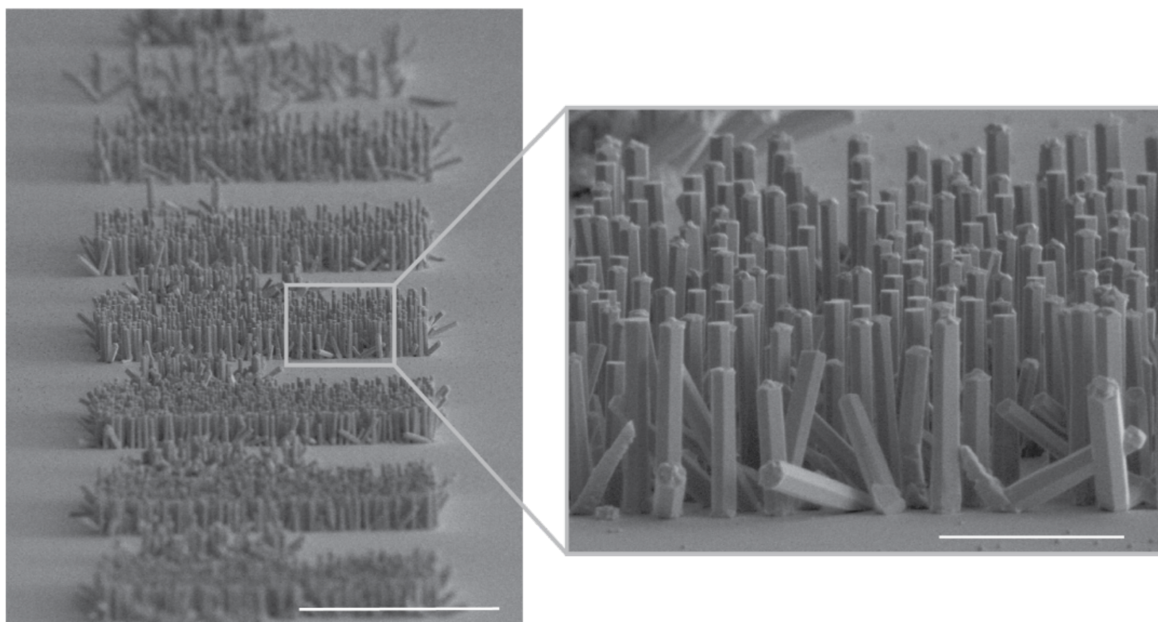

Figure 3.9: Nanopillar array SEM: (left) 85 degree tilt view SEM image of the nanopillar array and close up (right) showing high pillar density. Scale bars: left - 30 μm, right - 3 μm

cross section of the pillars makes the absorption azimuthally insensitive. The measured absorptivity (Fig. 3.10(a)) is slightly different from the simulated absorption spectrum of the tapered nanopillars due to the flat top geometry of the pillars. The results are expected to improve with a tapered tip. However, even with this geometry, it is highly encouraging that the absorption can be as high as 85-90% for substantial fractions of the spectrum, up to a high incidence angle. Further, it is possible to qualitatively confirm the high absorption of the pillar array compared to the substrate from the optical microscope image of Fig. 3.10(c), in which the pillars are dark, whereas the surrounding substrate is saturated with brightness due to the higher reflectivity. Note that most of the light absorption takes place in the nanopillars rather than the substrate. This was confirmed by removing the pillars from the substrate by embedding in PDMS and measuring the absorption coefficient. Here, the absorption was also found to be as high as 85% for a broad spectrum in the visible.

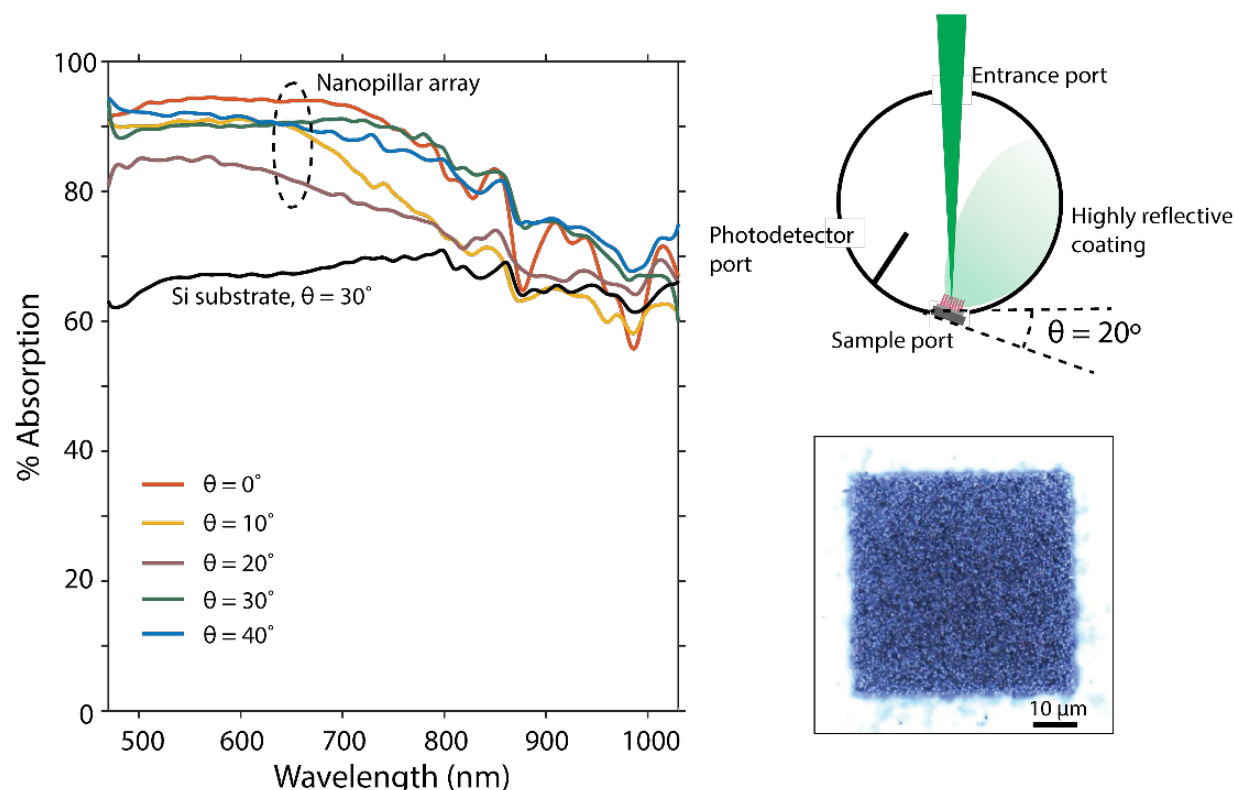

Figure 3.10: Absorption measurement: (right, top) Schematic showing the integrating sphere measurement setup, (right, bottom) optical microscope image of the dense nanopillar array, (left) Measured reflectivity spectra of the nanopillar array, compared with the thick silicon substrate.

3.5 Nanopillar Antireflection

In the previous sections, we have described how we can directly absorb light in the nanopillars, leading to near unity absorption even with minimal volume fill ratio. One of the ways to understand the minimal reflection is that the tapered nanopillars act as an impedance matching layer between air and the III/V semiconductor. The gradual change in impedance can more generally be used to construct a textured anti-reflection coating, allowing a greater degree of freedom wen it comes to the PV absorber. The case of the nanopillars directly absorbing light is a special case of this more general situation.

The key benefit of this kind of a passive nanopillar metasurface is the ability to provide an effective antireflection texture for a variety of different underlying substrates in a manner that is angle insensitive. This differentiates the nanopillar antireflection texture from a traditional quarter-wave antireflection (AR) coating. Note that a traditional AR coating is designed to operate via destructive interference of a coherent incident plane wave with itself.

Both the thickness and refractive index of the thin film coating need to be chosen carefully such that cancellation occurs. For normal incidence, this is achieved by using a film with refractive index that is the geometric mean of the two indices of refraction between which antireflection is desired. Further, the thickness of the AR coating is required to be a quarter of the wavelength (in the medium of the AR coating). Such thin film AR coatings can only operate well within a narrow range of wavelengths around the designed wavelength, and similarly for angles of incidence.

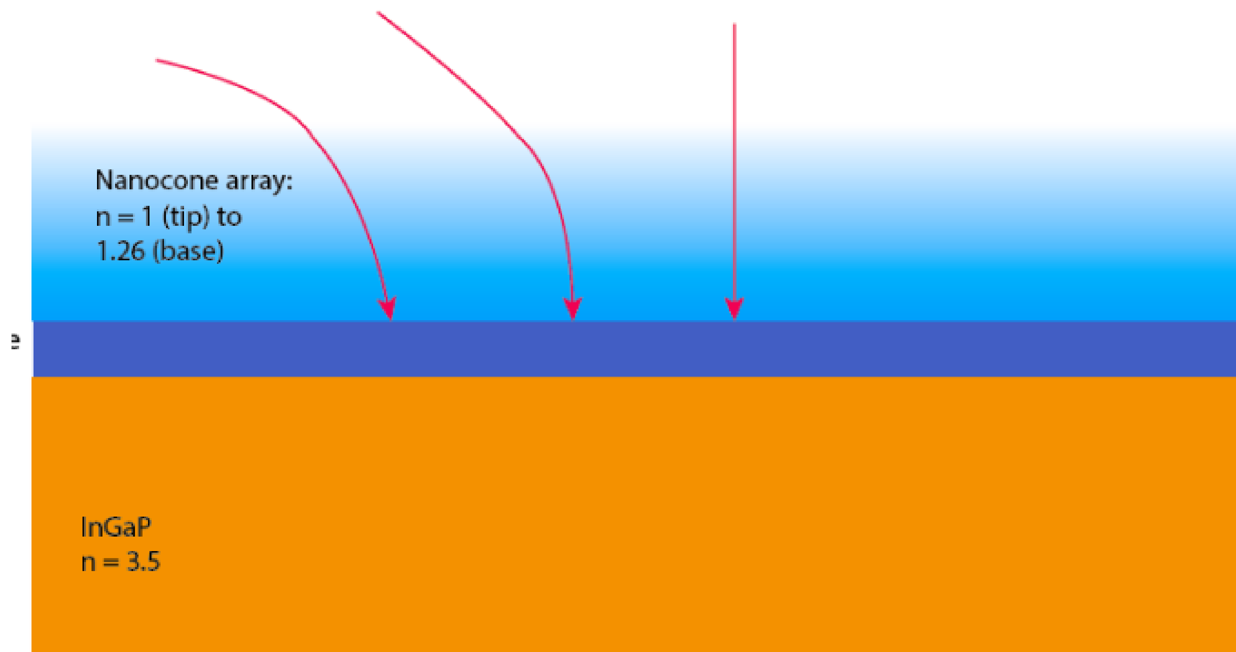

Figure 3.11: Gradient index anti reflection: Schematic illustrating the nanopillar AR coating principle. AR coatings are based on wave effects and typically only work well for a particular incidence angle. In this case, the gradient index structure has the effect of bending even the glancing incidence rays such that the angle of incidence at the AR coating is close to the normal. With incidence angle closer to the normal, the AR coating functions better and leads to improved anti-reflectivity.

However, the advantage of a graded refractive index layer is that it can be used bend the angle of incidence of rays closer to the normal. This is predicted simply from Snell's law: the angle of refraction becomes smaller when rays enter a high index medium. This situation is illustrated in fig. 3.11. This can be used to markedly improve the effectieness of a quarter wave coating. For instance, if the quarter wave coating refractive index is 2.1 (silicon nitride), and the underlying III/V solar cell substrate has a refractive index of 3.5, then the bottom of the gradient index structure needs to have an effective medium refractive index of 1.26 in order for the anti reflection condition to be met. The gradient index layer

can then be graded from the refractive index of the surrounding medium (air = 1) to 1.26, and prevent abrupt discontinuities that cause reflection.

A nanopillar based implementation of this gradient index structure is illustrated in Fig. 3.12. The requirement for having a refractive index of 1.26 at the base is maintained by using an appropriate pitch and diameter for the nanopillars. For ease of fabrication, the nanopillars can be fabricated using the same material as the underlying quarter wave layer. Then, the area fill factor at the base of the nanopillars has to be 60%. The diameter and pitch of the nanopillars should be chosen to be small enough so that an effective medium approach is valid. A pitch of around 100 nm, with a base diameter of 87.5 nm will satisfy these requirements.

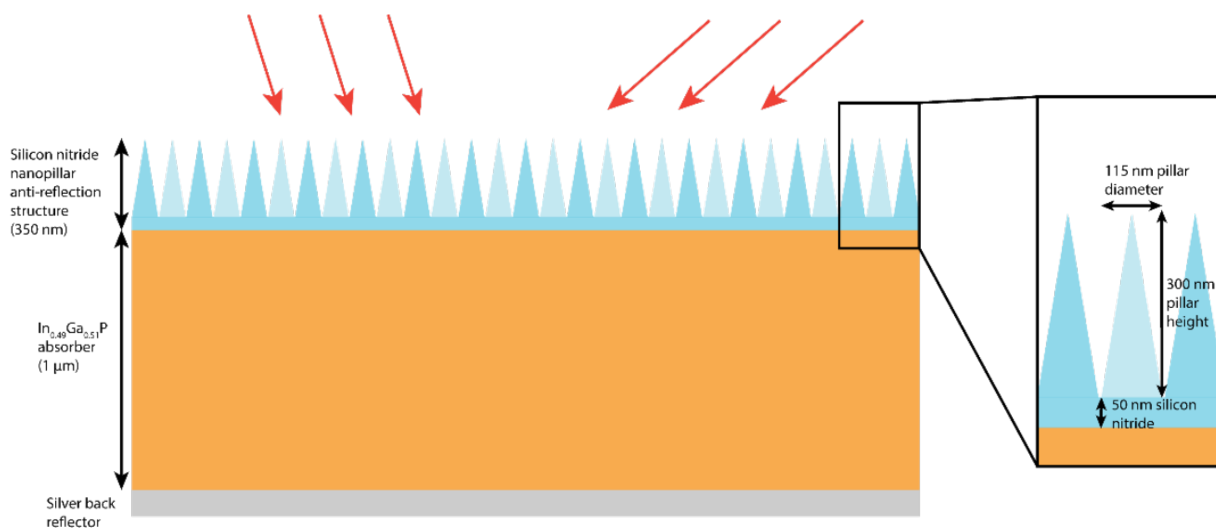

Figure 3.12: Nanopillar anti-reflection (AR) coating: Schematic describing the use of a transparent textured AR coating in order to allow omnidirectional anti-reflection for a III/V based solar cell. The pillar dimensions and spacing have been chosen to index match the underlying quarter-wave AR coating, which is the same material as the nanopillars (silicon nitride). The case when the nanopillar and AR coating are the same material as the underlying substrate is also possible.

Note that the gradient index principle is only effective when the index changes sufficiently slowly. In other words, the nanopillars need to be sufficiently tall for the impedance matching effect to be observed. A rough prescription for the height of the pillars is that it should be half the vacuum wavelength of light being considered. In this case, we are considering anti-reflection for indoor illumination around 400-600 nm, so the nanopillar texture should have a height of 200-300 nm. Along with the roughly 50 nm quarter wave layer, this amounts to a total of 250-350 nm thick anti-reflection layer. The deposition process may have to be optimized in order to deposit sufficiently thick films.

Fig. 3.13 shows simulation results for a gradient index structure with an effective medium approach. Note that these simulations were not performed for the nanopillar/nanocone structure shown in fig. 3.12, but rather for the effective index equivalent in fig. 3.11. Thus, they serve as an indication of the principle of anti-reflection, rather than an accurate simulation of the actual structure. The left graph shows a ray-optics based analytical calculation where the angle dependence is calculated from Snell's law and the reflectivity is calculated using interference between the multiple bounces within the quarter wave film. Note that the quarter wave coating works well at incidence angles below 40°. However, this rapidly degrades at higher incidence angles. Adding the gradient index nanopillar texture significantly reduces the reflectivity at higher incidence angles, simply due to the impedance matching effect and reduced angle of incidence at the quarter wave film. The quasi ray optics simulations have been repeated at both incidence polarizations.

However, to model the gradient index more accurately, a full vectorial wave-optics framework is necessary. This will also account for the 'abruptness' of the gradient index layer, in case the height is too small compared to the incidence wavelength. We note that Lord Rayleigh first approached the gradient index problem in order to analyze the manner in which sunlight gets scattered by the atmosphere. Maxwell's equations can be solved with the gradient index incorporated into the model. A rigorous coupled wave analysis (RCWA) technique was used to simulate both the case of no gradient index layer (quarter wave AR only), as well as the situation with the gradient index layer fabricated on top of the quarter-wave coating ('optimized nanocone'), as shown on the right graph in fig. 3.13. It can be seen that the nanopillar gradient index layer indeed leads to a significant reduction in reflection for angles of incidence above 40°, and that this effect is maintained up to 80° incidence angle. Finite difference time domain (FDTD) simulations also provide an indication of the behavior of the actual nanocone/nanopillar structure. It can be noted that FDTD suggests that a 300 nm tall nanopillar structure already reduces the amount of reflected light at 85° by nearly a factor of two compared to the thin-film only case. This is further improved by the 900 nm tall nanocones. Further investigation and optimization of the geometry based on an initial ray optics based intuition will likely lead to significant improvements.

To summarize this chapter, have calculated the theoretical PV efficiency limit for a warm LED spectrum to be as high as 49.7% and monochromatic LED to be higher than 80% for a properly chosen PV absorber. We have emphasized the importance of high and angle insensitive absorption, as well as excellent material quality for reaching this efficiency limit. Further, we have simulated the absorption characteristics of sparse (5% volume fill factor) nanopillar arrays up to a high incidence angle, and found that the absorption characteristics are maintained at oblique incidence. Lastly, we have measured 85-90% absorption of light for a nanopillar array grown on a silicon substrate. The high absorption was confirmed right up to 40° angle of incidence (Fig. 3.10(a)) which is very promising for diffuse light absorption. Material growth and the device active region can be defined on III/V substrates, in order to maintain the record performance possible with these materials. With such highly efficient III/V based solar cells harvesting 300 $\mu W/cm^2$ of energy, we expect to significantly lengthen battery lifetime and possibly even eliminate battery usage for IoT devices altogether.

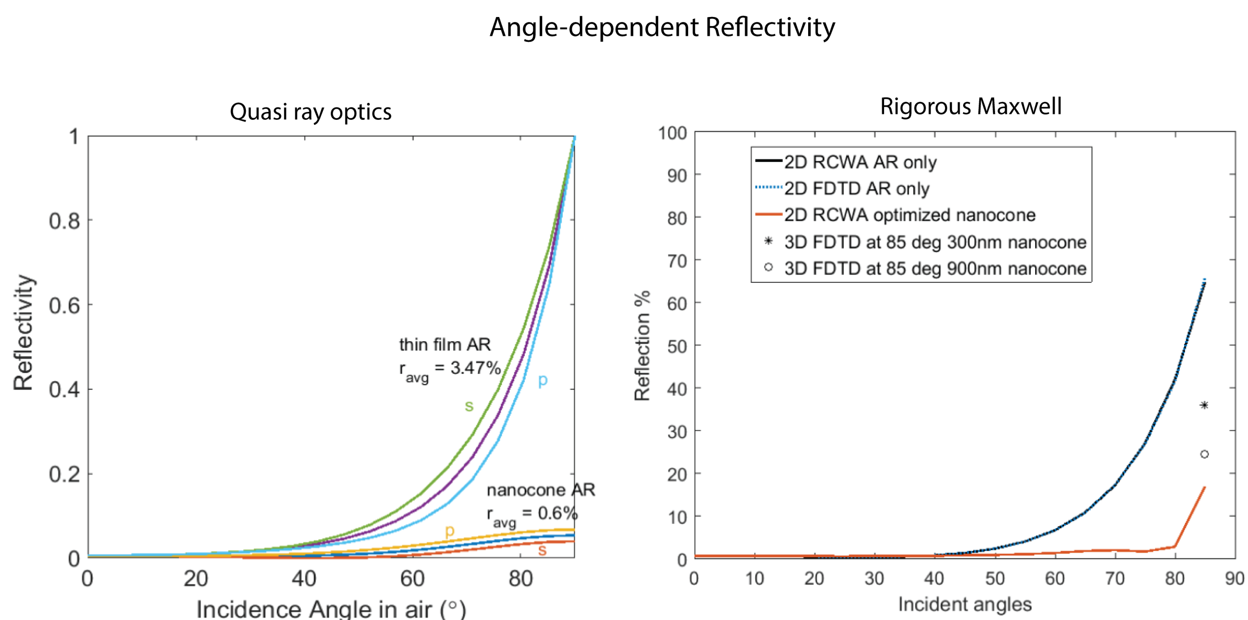

Figure 3.13: Angle dependent reflectivity: (a) Calculated angle-dependent reflectivity using an effective medium model for the nanopillar anti-reflective coating. In the case where only the quarter-wave coating is used, we have good anti-reflection for normal incidence. However this degrades beyond 60 degrees incidence angle. When a gradient index is used, the reflectivity improves significantly at higher angles. However, the effective medium approach becomes incorrect when the gradient index layer thickness is finite. In order to account for this, we use a rigorous Maxwell solver to obtain better estimates for the reflectivity spectrum, as shown in (b). Each of the curves is explained in detail in the main text.

Chapter 4

Nanopillar Phototransistors

With ever-increasing data rates and integration density in electronic integrated circuits, optical interconnects are becoming a compelling energy-saving choice for high speed, broadband communication links on and between chips. The power consumed at a certain data rate, equivalently expressed as the energy per bit, is heavily dependent on the capacitance of the receiver [2], [79]. A receiver with low total capacitance C_{tot} is able to produce a sufficiently high voltage signal V_{sig} for a reduced number of photons per bit: $V_{sig} = q \times n_{bit}/C_{tot}$. This lowers the minimum link power consumption by reducing both transmitter power through a reduction in n_{bit}: the number of photons per bit required in the link, as well as receiver power necessary to amplify the small voltage signal V_{sig} to eventually drive CMOS logic. With this goal, there has been significant work on reducing the capacitance of photodetectors with an indirect bandgap Germanium absorber grown on a technologically relevant silicon substrate [80], [81], [82], [83]. Thin 2-dimensional (2D) materials such as graphene and transition metal dichalcogenides are also being explored for fast photodetection due to the possibility of small transit times [84], [85]. An unresolved hurdle here is that light absorption is extremely weak due to the thin topology and integration with very long waveguides is required to provide any reasonable responsivity, leading to a large device area and high capacitance [86]. Direct bandgap III-V based compound semiconductors, particularly the InP/InGaAs system, have at least an order of magnitude higher absorption coefficient than silicon and germanium, and also permit heterostructures and bandgap engineering for highly functional devices [87], [88]. Such III-V devices can approach almost complete absorption with a near-wavelength scale volume and enable ultra-low capacitance photodetectors while maintaining excellent quantum efficiency and low dark current. From a link sensitivity analysis 12, a 100 nm diameter III-V compound semiconductor device would have a self-capacitance as low as 50 aF, potentially allowing low energy on-chip optical links to approach fundamental shot noise limited communication at a bit error ratio of 10^{-9} with merely 20 photons/bit in the link [89].

Despite the excellent potential to scale down the capacitance of III-V compound semiconductor detectors, an optical link with off-chip III-V devices suffers from the parasitic capacitance of the electrical wire connecting the detector to the next stage. Attempts to

overcome this have been made by bringing the photonic chips close to the electronic circuits using, for instance, through-oxide vias [90], [91]. Nonetheless, even a $10\mu m$ separation adds 2 fF of capacitance (see ITRS 2012 interconnect tables), which translates into a requirement for additional link power to maintain the same signal to noise ratio. This is particularly severe if the capacitance of the photodetector is much lower than the parasitic wire capacitance. The wires capacitance effectively reduces the sensitivity of the receiver: at the low link powers we would ideally like to use, the signal becomes swamped by the electronic noise of the first amplifier stage [2], [89].

To address this issue, it is important to integrate gain directly into the photodetector and improve sensitivity. This could also be viewed as an intimate integration of the first amplifier stage with the photodetector, thus eliminating the wire capacitance altogether. Several approaches have been attempted, including Si/Ge and In(Al,Ga)As avalanche photodiodes [92], [93], [94], [95], field effect phototransistors [96], [97] and bipolar junction phototransistors [87], [98], [99], [100], [101], [102], [103], [104], [105], [106]. Avalanche photodiodes with high gain-bandwidth product have been demonstrated [92], [93], [94]. However, the high gain does not necessarily translate into better sensitivity due to the fundamental excess noise associated with the avalanche process [107]. Additionally, APDs require a thermal compensation mechanism due to the sensitive dependence of impact ionization on temperature [108], [109], [110] and a high reverse bias voltage (10 V or higher), both of which are undesirable for densely integrated chip-scale applications. Approaches based on nanowire photoconductive devices also show very large gain due to long carrier lifetimes [111], [112], [113]. However, the long lifetime limits the speed of these devices with response times on the order of milliseconds to 100 seconds, leading to insufficient gain bandwidth product [112]. Phototransistors (both BJT and FET based) are expected to be highly sensitive due to the absence of multiplication noise and the fact that the gain bandwidth product can be increased by simply scaling the device size down, in analogy with transistor cutoff frequency scaling [114]. A phototransistor is in fact expected to be even more sensitive than a p-i-n photodiode and transistor combination due to the absence of the wire capacitance [115], [116]. The bipolar junction transistor is preferred due to a significantly higher transconductance compared to a field effect device. The transconductance for the BJT is linear and is determined by the thermal voltage of 25.9 mV rather than the $\sim$ 100 mV field effect transistor overdrive voltage. This allows a higher gain-bandwidth product to be reached at the same DC collector current [117]. While promising gain-bandwidth products have been achieved using III-V based phototransistors with highly scaled geometries, the small size leads to deficient photon absorption [98], [101], [105], [103], [102]. Additionally, the high lattice mismatch of InP and GaAs with silicon leads to defective material unsuitable for devices. In this work, a bipolar transistor gain mechanism is implemented in a direct bandgap III-V semiconductor material to achieve high intrinsic photoresponse, as well as high gain-bandwidth product in an integrated optoelectronic receiver grown on silicon.

4.1 Photoreceiver Scaling Reduces Link Energy

The total link energy is calculated based on the somewhat stringent requirement that the photons absorbed at the photodetector end of the optical link should be sufficient in number to result in the total receiver capacitance being charged up to a CMOS level voltage swing:

$$V_{CMOS} = Q/C_{tot} = q\frac{P_{abs}}{\hbar\omega} \times \frac{1}{C_{tot}} \tag{4.1}$$

where P_{abs} is the optical power absorbed, $\hbar\omega$ is the photon energy, f_{data} is the data rate in the optical link and C_{tot} is the total receiver capacitance. This is for the case of an amplifier-less photodetector with no additional gain such as a p-i-n photodiode (also termed receiverless detector). However, in the case of a photoreceiver with integrated gain, such as the phototransistor, the optical power requirement to reach the same voltage swing is lowered significantly due to the in-built amplification. There is some energy cost in the amplification, but this is offset by the reduction in transmitter power, which usually dominates the total link energy consumption. In what follows, we will justify that the total link energy is significantly less for a link with a phototransistor compared to a conventional p-i-n detector.

For consistency with Manipatruni *et al.* (Ref. [79]), we use 0.6 V as the required voltage swing for logic operation. From the same reference, the source energy/bit is then derived by accounting for the link losses (coupling, insertion and other optical losses), as well as the detector and laser efficiencies:

$$E_{src} = \frac{P_{abs}}{f_{data}} \times \frac{1}{\eta_D\eta_L\eta_M\eta_C} \times 10^{\alpha L \times 1/\beta} \tag{4.2}$$

$$= \frac{P_{abs}}{f_{data}} \times \frac{1}{\eta_D\eta_L\eta_M\eta_C} \times 10^{\alpha L \times 1/\beta} \tag{4.3}$$

$$= E_{src}(Rxless) \times C_{tot}/C_o \times 1/\beta \tag{4.4}$$

where the notation in the first line is based on the calculation in Manipatruni *et al.*, but modified to include the reduction in transmitter power due to photo-BJT current gain β. In addition, the total capacitance of the phototransistor C_{tot} may be different from that of the roadmap device $C_o(= 1fF)$. Finally, this leads to the third line, where the transmitter energy is directly related to the receiverless case, while accounting for the current gain and capacitance of the receiver. This provides for a useful comparison of the transmitter energy consumption in the receiverless case vs. the case with receiver gain.

The estimated receiverless source energy (not including wavelength tuning) in Manipatruni *et al.* is 50 fJ/bit under favourable assumptions for the link losses and quantum efficiencies (total 3 dB link loss, including detector quantum efficiency). In conventional optical links however, a link margin as large as 5-10 dB is included, beyond what is dictated by the link losses. Therefore, we make the assumption that an additional 3 dB of margin or unaccounted loss has to be included, and proceed with 100 fJ/bit purely for the source energy consumption (total link margin of 6 dB).

The receiver part of the energy consumption is estimated as follows. In the amplifier-less link, the p-i-n photodiode consumes a relatively negligible amount of energy:

$$E_{Rx}(Rxless) = \frac{1}{2} C_o V_{CMOS} V_d \tag{4.5}$$

where V_d, the p-i-n junction bias, is assumed to be set to 1 V. For the roadmap target of 1 fF for C_o the photodiode capacitance, this leads to an energy consumption of 0.3 fJ/bit. Since the receiver energy is minuscule compared to the transmitter energy consumption as described in equation 4.2, it makes sense to integrate gain, even with some energy penalty. We estimate the phototransistor gain assuming the high speed response is limited by the capacitive charging time rather than the carrier transit time. This has been the case for heterojunction bipolar transistors in most highly scaled phototransistor devices due to extensive 'vertical scaling' and attendant transit time reduction in such InP-based devices[118]. In that case, to reach a gain-bandwidth product of f_T, the collector DC bias current must be:

$$I_c = 2\pi f_T C_{tot} \times \frac{k_B T}{q} \tag{4.6}$$

where $k_B T/q$ is the thermal voltage of 25 mV and C_{tot} is the total device capacitance. The energy per bit for the receiver part can then be estimated as follows:

$$E_{Rx} = \frac{I_c V_d}{C_{data}} \tag{4.7}$$

$$= E_{Rx}(Rxless) \times \beta \times C_{tot}/C_o \times 4\pi \frac{k_B T}{q} \times \frac{1}{V_{CMOS}} \tag{4.8}$$

$$\tag{4.9}$$

$E_{Rx}(Rxless)$ is the previously calculated energy consumption of only the p-i-n photodiode, which is 0.3 fJ/bit. We have substituted the required I_c for a given f_T from equation 4.6, and used that f_T/f_{data} is the available BJT current gain of β. This leads to the second line in equation 4.7, where the receiver energy consumption for the phototransistor is related to the receiverless energy consumption in equation 4.5 by a multiplication factor corresponding to the gain and device capacitance. Note there is a factor that comes about from advantages inherent to the BJT operation mechanism: $\frac{k_B T/q}{v_{CMOS}}$. This is also related to the high transconductance associated with the bipolar gain.

We continue the analysis in order to determine the optimal bias conditions on the receiver phototransistor so that the entire system energy is minimized. We substitute the values of the receiverless energies calculated above based on the roadmap optical link in Manipatruni et al. ($E_{src}(Rxless)$=100 fJ/bit and $E_{Rx}(Rxless)$=0.3 fJ/bit). The current gain β needs to be chosen to minimize the total energy per bit E_{tot}:

$$E_{tot} = E_{Tx} + E_{Rx} = \frac{C_tot}{C_o} \times \left(100 \text{ fJ/bit} \times \frac{1}{\beta} + 0.3 \text{ fJ/bit} \times \beta \frac{4\pi k_B T/q}{V_{CMOS}}\right) \tag{4.10}$$

This formula expresses the idea that the phototransistor gain can be used as an additional degree of freedom to optimize the link performance, by trading off the source power requirement with the amplification energy. This is explicitly graphed in fig. 4.1. The optimal gain β is calculated from equation 4.10 to equal:

$$\beta_{opt} = \sqrt{\frac{E_{Tx}(Rxless)}{E_{Rx}(Rxless)}} \times V_{CMOS}/(4\pi k_B T/q) \sim 25 \tag{4.11}$$

which is consistent given the significant asymmetry in the receiver and transmitter power consumption in the amplifier-less link. With this optimized gain, the transmitter energy is reduced to about 4 fJ/bit and the receiver energy is increased to 4 fJ/bit leading to a much reduced total link energy of 8 fJ/bit compared to the amplifier-less value of 100 fJ/bit in the roadmap.

This impressive order of magnitude reduction in link energy has been calculated in the case that the total photoreceiver capacitance at the same scaling node is equal to the p-i-n diode capacitance. However, due to narrower junctions, the total capacitance of the NPT reported here is $\sim$ 14 fF, which is currently somewhat high compared to $\sim$ 2 fF for optimized germanium p-i-n photodiodes reported in the literature (eg: Chen *et al.*, Ref. [80]). Despite the higher capacitance of this device, the link energy would be 56 fJ/bit, half that of the receiverless case.

The tables (Table 1 and 2) below summarize the calculated energy per bit and other link parameters based on the above analysis. The two top rows correspond to the current scaling node, where the p-i-n diode capacitance is 2 fF. We estimate that the receiverless link will consume 200 fJ/bit. On the other hand, the estimated energy consumption of our current device, with sufficient bias to lead to a 375 GHz capacitive charging-limited gain-bandwidth product, is 146 fJ/bit. This can be further reduced to 112 fJ/bit by optimizing the gain. As discussed in the above analysis (equation 4.10), the receiver and transmitter consume equal power at the optimal gain.

k scaling node	Description	Data Rate	β	f_T	C_{tot}	E_{src}	E_{Rx}	E_{tot}
1	NPT in [39]	7 Gb/s	54	375 GHz	14 fF	26 fJ/bit	120 fJ/bit	146 fJ/bit
1	NPT in [39] with optimized bias	10 Gb/s ($\leq$ 15 Gb/s)	25	375 GHz	14 fF	56 fJ/bit	56 fJ/bit	112 fJ/bit

2	Optimized bias	20 Gb/s (≤ 30 Gb/s)	25	750 GHz	7 fF	28 fJ/bit	28 fJ/bit	56 fJ/bit
4	Optimized bias reduced capacitance	40 Gb/s (≤ 60 Gb/s)	25	1.5 THz	0.5 fF	2 fJ/bit	2 fJ/bit	4 fJ/bit

Table 4.1: Table showing the effect of photoreceiver scaling on reducing the link energy consumption. The first line is the device presented in paper [39]. The rest have been optimized to minimize link energy. The last two rows show the effect of shrinking the photoreceiver size, and hence improving f_T and reducing capacitance. This would have to be done in a manner so as to avoid reducing light absorption. The calculations are based on equation 4.12

Additionally, we can also make some dimensional scaling arguments for the photoreceiver performance. The per channel data rate at each scaling node is expected to be determined by system considerations and is considered to be an external target. Given the available device speeds and modulator performance, we specify the current node data rate as 10 Gb/s, and scale to 20 Gb/s for the next node (k=2) and 40 Gb/s (k=3) with 40 Gb/s being the final node of the roadmap in Manipatruni *et al.* At every node, the device dimensions shrink by a factor of 2 in our analysis, leading to the capacitance correspondingly reducing by that factor. As a conservative estimate, we assume that at every node, the phototransistor capacitance is 7x that of the p-i-n diode, due to the narrower junctions. Even with this estimate, the photo-BJT consumes only about half of the energy of the receiverless system at the corresponding node. Further, with improved device design and scaling of the emitter-base junction while maintaining the collector-base junction size at every node, we expect to have the capacitance of the phototransistor approach the capacitance of the p-i-n photodiode at that node. Under this condition, the energy/bit is reduced more than an order of magnitude compared to the receiverless system, as depicted in fig. 4.1.

We would also like to emphasize that the scaling is performed both vertically (epitaxial layer thickness reduction) and laterally (area reduction), to be consistent with terminology used in the reported body of work for heterojunction bipolar transistors. Thus, as we scale down, the gain-bandwidth product also increases linearly. In further detail:

$$f_T = \frac{1}{2\pi} \times \frac{1}{(C_{eb} + C_{bc})\frac{1}{k} \times \frac{k_B T}{q} \times \frac{1}{I_c} + \frac{(W/k)^2}{\eta D_B} + \frac{x_{dep}^c/k}{2v_{sst}}} \tag{4.12}$$

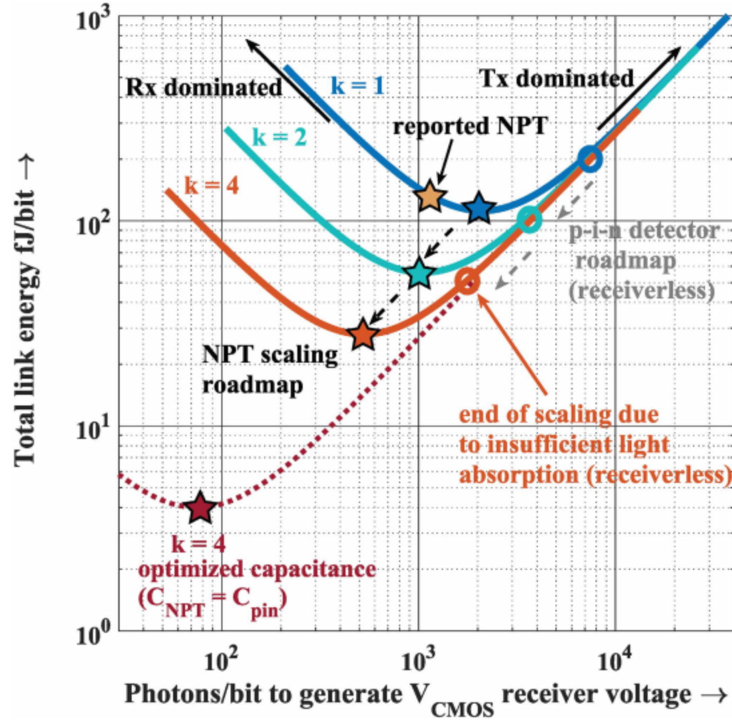

Figure 4.1: Total link energy consumption as a function of link power (in photons/bit). As the number of photons is reduced, the receiver needs to work harder to amplify the photocurrent to the swing voltage. On the other hand, higher photons/bit leads to increasing transmitter power consumption. The optimum is when the receiver and transmitter consume the same power. The minimal link energy consumption can be reduced by shrinking the photoreceiver capacitance, as shown for the family of curves.

where the notation for the capacitive charging times and transit times is the same as in equation 4.17 below, with the understanding that the dimensional quantities are referred to a base dimensional node (current device size). The factor k is the dimensional scaling factor with the same meaning as in Table 4.1. A factor of k scaling is taken to imply simultaneous 'vertical scaling' as well as 'lateral scaling' by the same factor, so the device aspect ratio is maintained in this scaling analysis. Vertical scaling of the epitaxial layer thicknesses is achieved through growth time reduction, as demonstrated in the core-shell growth mode (Ren *et al.*, ref. [36]). Lateral scaling in the nanopillar phototransistor case is achieved by reducing the active region height by controlling the height of the regrowth oxide sleeve.

In the case of the waveguide integrated germanium photodetector (Chen *et al.*, Ref. [80] and DeRose *et al.*, Ref. [119]) dimensional scaling is expected to continue down to the k = 4 node. This could lead to a photodetector capacitance as low as 500 aF. However, this is expected to be the end of the roadmap for scaling the photodiode size in terms of maintaining a reasonable quantum efficiency. From this perspective, the low capacitance phototransistor

is expected to play a key role in overcoming the end of roadmap barrier in terms of reducing the link energy, by as much as an order of magnitude or three scaling nodes below the expected energy achievable with the receiverless approach. This has been shown in figure 4.1.

4.2 Regrown Nanopillar Bipolar Phototransistor

Despite the high absorption and low dark current of III-V detectors, applications have been challenged by the difficulty of integrating with large scale CMOS technology and silicon based read out circuitry. In this work, a major technological hurdle has been overcome by monolithically growing optoelectronic quality III-V material on silicon at a substantially lower growth temperature than the $\sim 800°$C growth temperature that is usual for conventional III-V thin film epitaxy. The InP photoBJT was synthesized on silicon using a novel metastable nanopillar growth mode. Single crystalline InP nanopillars were grown under conditions demonstrated to be CMOS post-process compatible [25]. The bulk of the pillar was defect free in spite of a large crystal lattice mismatch of 8%. The strain due to lattice mismatch is locally relaxed through arrays of misfit dislocations at the base of the InP nanopillar, right at the Silicon interface [37]. TEM images confirm pristine Wurtzite phase in the body of the pillar.

The growth is in a radial manner, with tunable material composition and doping possible in the core-shell direction, using which p-i-n junction diode devices have been demonstrated [36], [32]. As opposed to an axial distribution of dopants, the core-shell junction geometry is highly beneficial in terms of minimizing surface exposure of the minority carriers and leads to a far reduced dark current for the base-emitter junction [38]. Another benefit of the core-shell or wrap-around geometry, in analogy with waveguide integrated photodetectors, is that it decouples the light propagation direction from the carrier transport direction, thus allowing the photogenerated carriers to diffuse to the p-n-p junction within a short distance [81], [120]. This facilitates a rapid photoresponse and high responsivity-bandwidth product.

In-situ dopant incorporation with nanometer scale precision eliminates the requirement for implantation and diffusion based doping. The resulting sharp electrical junctions are important for obtaining rapid device operation. The base transit time is kept low by having a thin base with electrical width of ten nanometers or less. In addition, the collector-base junction depletion width is kept thin by using a high base and collector doping, reducing the collector transit time. The base doping was measured in an isotype n-doped pillar with the same dopant precursor flow rate. The doping level for the isotype pillars was measured using the Burstein-Moss shift in photoluminescence peak (band-filling effect) and estimated to be approximately $10^{18}\ cm^{-3}$.

On directly growing a p-n-p junction device on silicon, the outer p-shell, which is heavily doped as the emitter, comes into contact with the p-type silicon substrate, thus shunting the actual device junction (see fig. 4.3). Therefore, it is critical to electrically isolate the outer layers from the substrate. This challenge was also encountered for p-i-n junction fabrication

and alleviated using a carefully engineered regrown junction. The process is illustrated in fig. 4.3 and summarized here. Once the primary growth is completed, an amorphous Silicon sleeve is defined on the lower section of the nanopillars. After this, the regrowth occurs selectively on the upper section in a core-shell manner and at a slightly elevated growth temperature compared to the original growth. The active region is completely in the regrown portion. In this manner, it can be seen that the current is directed through the p-n-p junction as desired (Fig. 4.2 c). The device has a floating base, with the intention of providing optical bias. An optically biased device eliminates the parasitic base capacitance that an electrical base contact would necessarily include.

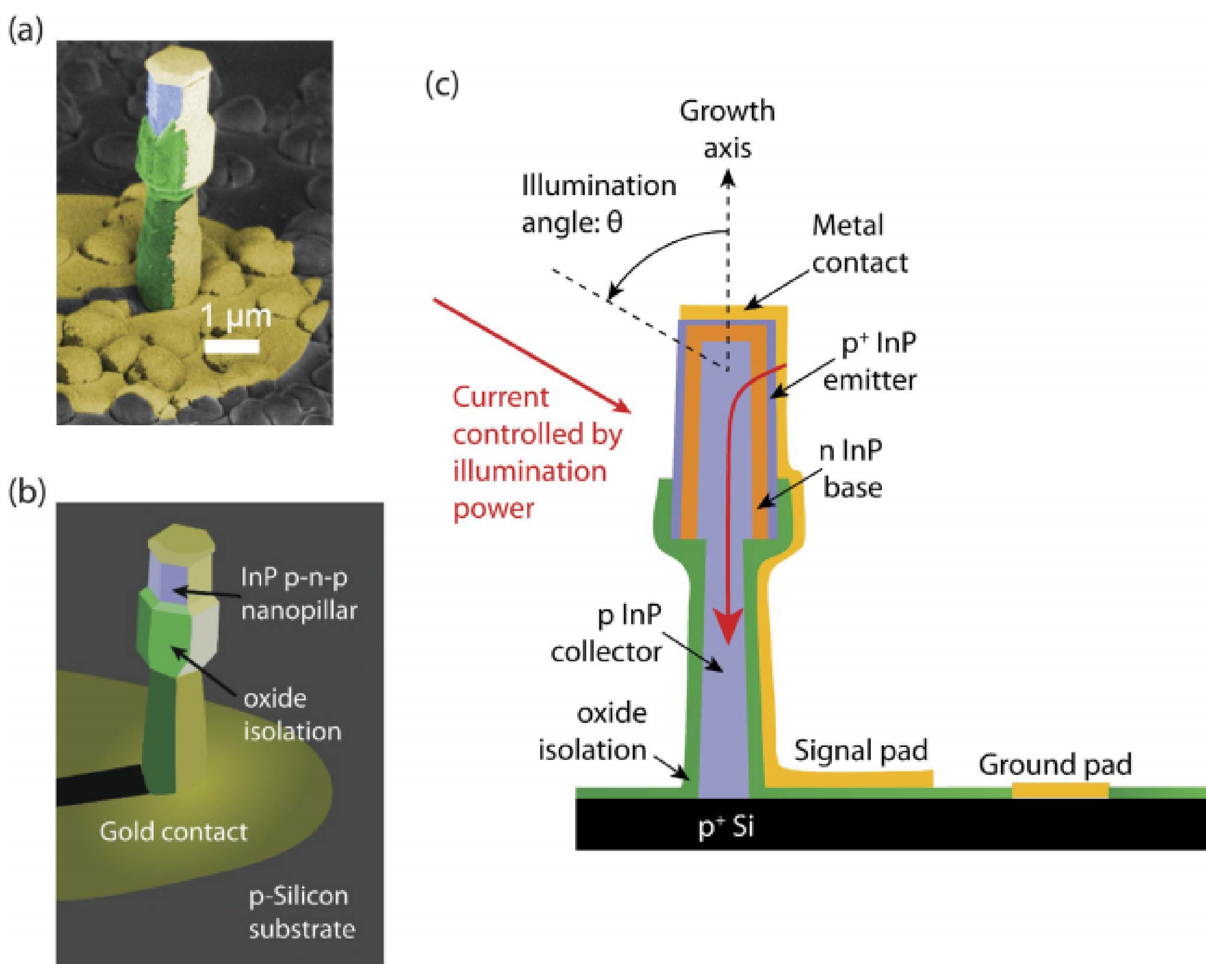

Figure 4.2: Bipolar phototransistor: (a) Scanning electron microscope image of an exemplary device, (b) Schematic labeling the corresponding parts, (c) Cross section showing p-n-p regrown layers.

Here we describe the two-step regrowth method used to synthesize the nanopillars. The

p-core collector region was grown first, followed by regrowth selectively on the upper region of the nanopillar. The core of the phototransistor was grown directly on silicon and p-doped in-situ using DEZn precursor (Fig. 4.3a). Using a calibration of the core-shell growth rate from a timed growth study (Ref. [36]) we determine that 25 nm zinc doped (p-emitter), 75 nm tellurium doped (n-base) and 100 nm zinc doped (p-collector) layers were respectively regrown onto the upper portion of the nanopillars at 450°C. The emitter was doped slightly higher than the collector. The base doping was approximately 10^{18} cm^{-3}, as determined by a Burstein-Moss shift in photoluminescence. The doping levels were kept high for the high speed devices in order to keep junction depletion lengths small and minimize transit times.

The device was fabricated to make sure contact was achieved with an individual pillar, and that the top contact is insulated from the silicon substrate. A silicon dioxide sleeve (green in Fig. 4.3 d) was defined with plasma-enhanced chemical vapor deposition at 250°C. The height of the oxide sleeve was controlled with a timed oxygen plasma etch of a photoresist mask, followed by a buffered hydrofluoric acid etch to remove the exposed oxide. The oxide sleeve serves to electrically isolate the top contact from the ground. In addition, this timed plasma is also used to control the emitter contact length to be 1 μm. The small size of the junction helps in reducing device capacitance.

Finally, the contacts were defined using metal evaporation and lift-off. First, the ground contact was defined by selectively etching through the oxide using a photoresist etch mask and a timed buffered hydrofluoric acid etch. Then, using a separate mask, the ground and top contacts were simultaneously patterned for metal evaporation, using e-beam lithography. The contact layers were deposited using angled electron-beam evaporation under high vacuum: first a 10 nm titanium adhesion layer, and then 150 nm of gold. The angled e-beam process creates a shadow on the substrate, as can be seen in the scanning electron microscope image of Fig. 4.2 b. The exposed (non-metallized) half of the device permits angled light illumination, which was performed at 30 degrees angle to the substrate.

A control device was also fabricated using direct growth of all layers, with similar thicknesses and doping levels. Although the doping and thickness will not be exactly the same as the regrowth when we perform direct growth, this control structure still serves as a useful comparison for dark current order of magnitude. As can be seen in Fig. 4.3 e, the direct growth leads to the device being shunted to the substrate. Measurement of the dark i-v characteristic (Fig 4.3 f) of the devices shows that the regrown device has 3-4 orders of magnitude lower leakage. This is the key factor in allowing the regrown devices to show response to extremely low levels of light.

4.3 Phototransistor Operation

Gain in the homojunction bipolar junction transistor (BJT) is obtained when a small base current can reduce the barrier to current flow for a large current from the emitter to the collector [121], [122]. Considering a p-n-p transistor with heavily doped emitter, a large hole current is injected into the n-doped base when the energy barrier is lowered. A small fraction

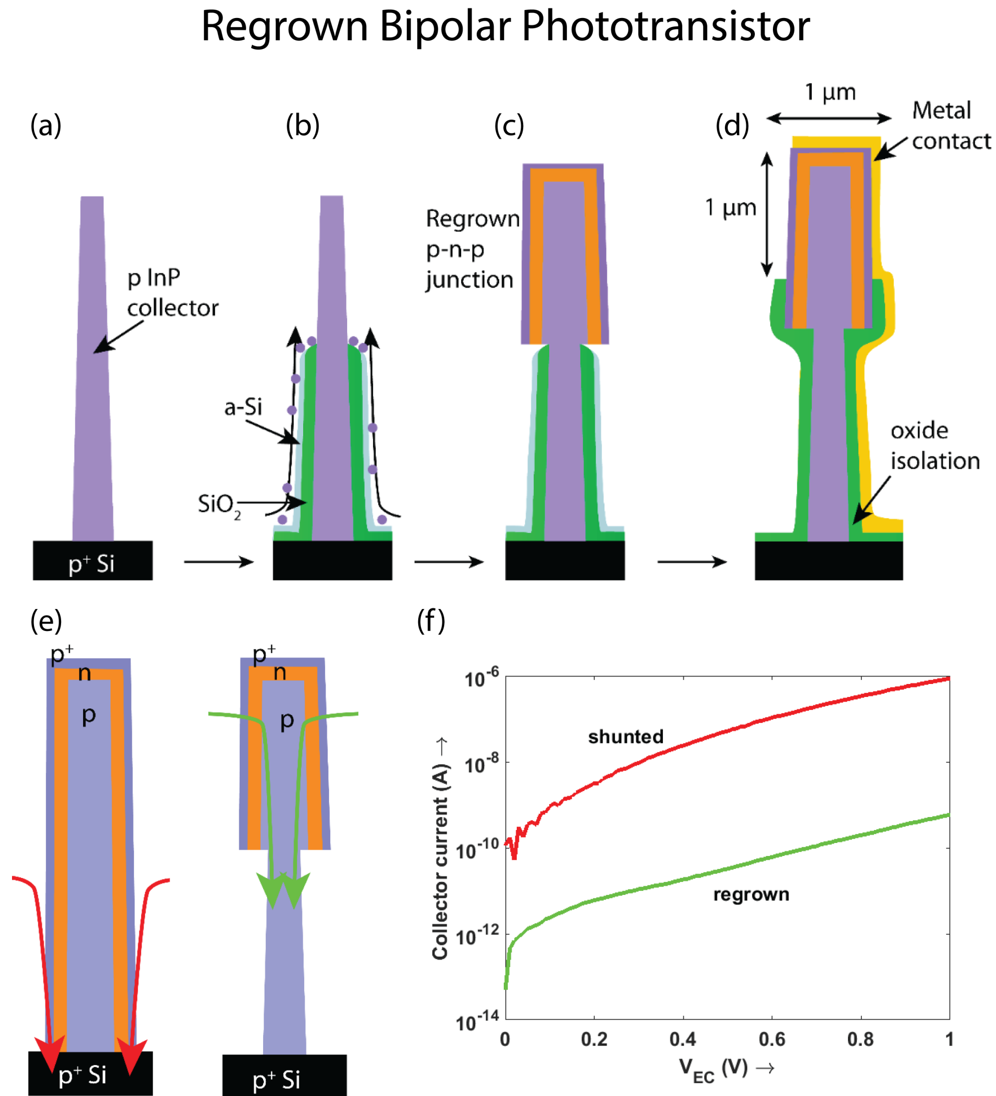

Figure 4.3: Regrowth process: (a) P-core nanopillar, (b) amorphous silicon coating, followed by MOCVD precursor flow, (c) Regrown p-n-p junction, (d) Fabricated device with one side exposed for light access, (e) comparison of structure with regrowth and shunted core-shell structure, (f) I-V characteristics of regrowth vs. shunt

of these holes recombine with the electron current supplied at the base terminal, but the base length is designed to be short so that a majority of these holes diffuse to the base-collector junction where they are swept by the high reverse bias electric field into the collector (see Fig. 4.4 a,c). The current gain is then the ratio of the collector hole current divided by the significantly smaller portion of the hole current that recombines with the electron current at the base, and can be described using a charge control model as the ratio of two Gummel numbers. From this recombination picture, it is clear that for a high gain, it is imperative to have low minority carrier recombination rate in the base or equivalently a low base dark current.

Exactly the same gain mechanism is also valid for photogenerated carriers in the device. As described pictorially in Fig. 4.4 a,c, photons generate electron-hole pairs in the absorber and the electrons lower the energy barrier for the diffusion of holes into the base, a situation similar to the generation of excess carriers in the forward biased base-emitter junction. The quasi Fermi level split(ΔF), or equivalently base emitter forward bias voltage(V_{be}) due to excess injected carriers is determined by the optical carrier injection and the electron dark current component at the base-emitter junction:

$$\Delta F \sim qV_{be} = qnV_{th}ln\left(\frac{P_{inc}/(\eta\hbar\omega)}{I_d}\right) \tag{4.13}$$

where n is the ideality factor of the base-emitter dark current, V_{th} is the thermal voltage which is 25 mV at room temperature, P_{inc} is the incident optical power, $\hbar\omega$ is the photon energy $\sim$ 1.58 eV in our case, η the external quantum efficiency of photon absorption (a number less than 1) and I_d the electron component of the diode dark current. Based on eqn. 4.13, it is clear that it is critical to obtain a low dark current to attain a large V_{be} and thus turn on the current flow in the BJT. Hence, having a high quality, defect free p-n-p junction, electically isolated from the substrate is essential. As can be seen in Fig. 4.3 f, the regrown nanopillar photoBJT has a 4 orders of magnitude lower dark current than the shunted junction. Since the shot noise current is proportional to $\sqrt{I_d}$, the low dark current also leads to improved sensitivity for the device.

Device operation can further be examined from the wavelength dependent light response as shown in Fig 4.4. Illumination has been performed at an angle of 30 degrees to the substrate. Light was incident with a single mode fiber and forms a broad Gaussian intensity distribution at the device substrate. The input number of photons is determined purely from this distribution without accounting for the absorption efficiency of the pillar. At 660 nm pump, the light response is poor since the absorption occurs superficially and the electrons recombine at the surface rather than being injected into the base. With 785 nm illumination, the photons penetrate further into the device and lead to carrier generation in the base and collector regions. The electrons lower the barrier to hole current flow, resulting in transistor action and observable gain. The difference in spatial absorption can also be appreciated from the fact that the bandgap for Wurtzite-phase InP at 870 nm, is about 55 nm lower in wavelength compared to Zinc Blende-phase InP, which makes 785 nm close enough to the band edge for the photons to penetrate significantly deeper into the device than the 660 nm

case. The 785 nm wavelength was also chosen for characterizing the dynamic response of the device.

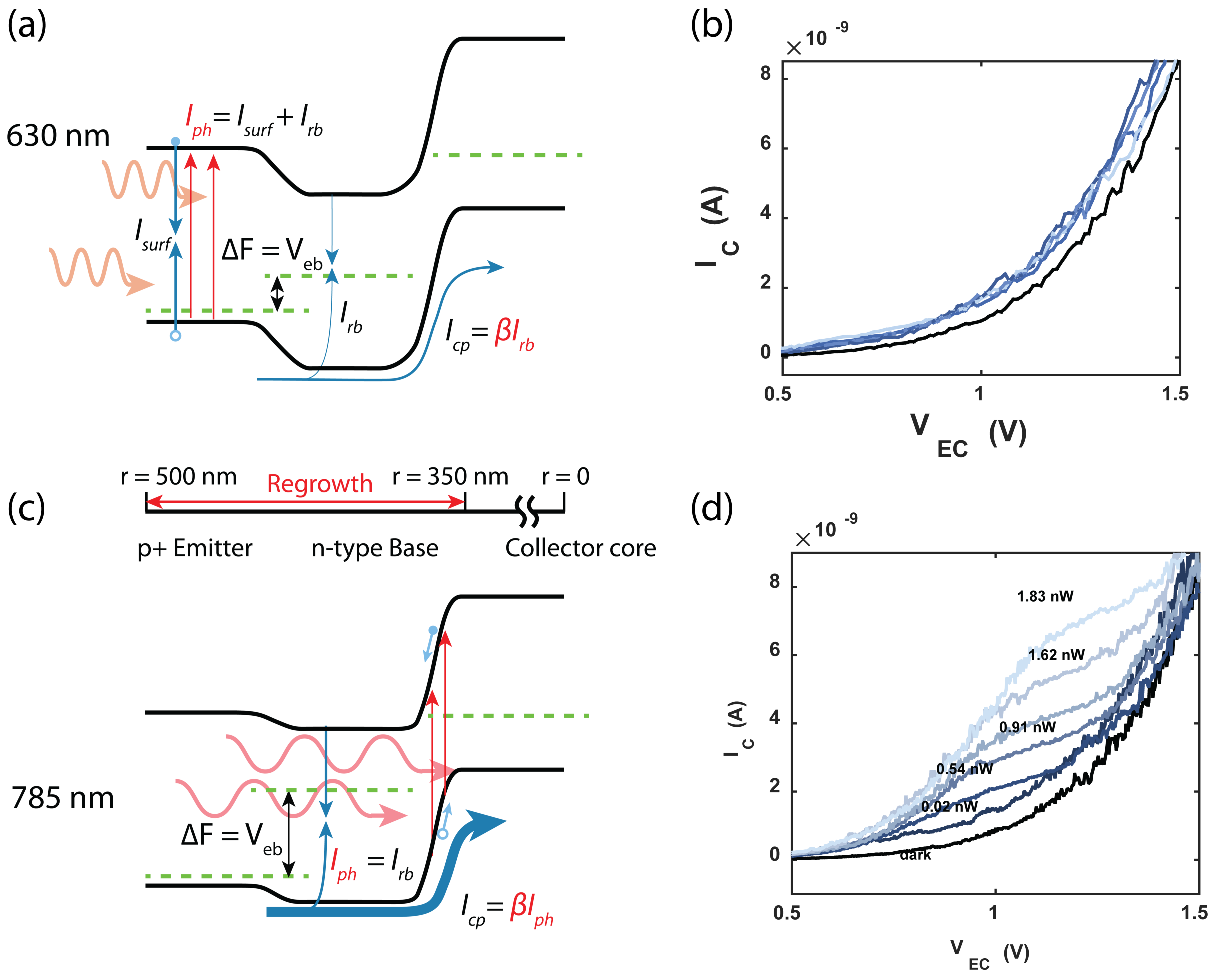

Figure 4.4: Bipolar gain and illumination conditions: this experiment shows how the bipolar gain mechanism can be discerned from the excitation wavelength. (a) 660 nm optical bias and (b) corresponding device characteristics, (c) 780 nm optical bias and (d) 780 nm I-V characteristics showing photoBJT gain. See main text for further details.

We also emphasize that the core-shell geometry of the nanopillar has significant benefits for device performance. In the solar cell chapter, we have emphasized how the exposed surface to active region volume is significantly reduced for the core-shell structure due to surface passivation. Here, we also note that in the top-down illumination case for the axial geometry, there exists a significant tradeoff between responsivity and capacitance. This is illustrated in

figure 4.5 (left). In order to provide sufficient absorption, the active region thickness δ must be large enough (typically a few microns or longer for Germanium). However, the carrier transit time, which limits the gain-bandwidth frequency f_T will suffer due to the long distance required for the carriers to travel. Hence there is a clear absorption(η)-bandwidth($f_T \sim 1/\tau_T$) tradeoff in the case of an axial junction with normal incidence illumination:

$$\eta \times f_T \sim (1 - e^{-\alpha\delta}) \times \frac{v_h}{\delta} \sim \alpha v_h \leq 30 \text{ Gb/s} \tag{4.14}$$

where we have made a simple approximation for the absorption for the case of the absorption for a thin active region, in order to more clearly elucidate the tradeoff. This has also been remarked on by Michel *et al.* in ref. [81], where the suggested approach to overcome this responsivity bandwidth tradeoff is to use waveguide integrated photodetectors, which decouples the absorption direction from the epitaxy direction. While the waveguide integration approach is attractive for silicon photonics, we note that there may still be some use cases for a vertical illumination geometry (fast image sensors, VCSEL-dominated short distance optical interconnects). In this case, the nanopillar geometry is ideal for avoiding the responsivity-bandwidth tradeoff since the responsivity can be improved by increasing the height of the nanopillar, while the transit time can be reduced by lowering the shell thickness. We note that the mode overlap with the active region does play a role in the nanopillar geometry:

$$\eta \sim 1 - e^{-\alpha\Gamma H} \tag{4.15}$$

where H is the nanopillar height, Γ is the mode overlap and α is the absorption coefficient. More detailed calculations of the mode overlap will be required to determine the tradeoff more quantitatively. However, we note that no matter how thin the shell is, this can always be compensated by increasing the active region height (upto tens of micrometers) - with the nanopillar naturally acting as a waveguiding photodetector for normal illumination.

4.4 Device Characteristics

The optoelectronic response of the device was measured using calibrated illumination from a 785 nm laser source shone on the device at an angle of 30 degrees to the growth substrate. The fiber-coupled source has a low numerical aperture of 0.1 and the illumination spot size is several orders of magnitude larger than the pillar. Hence, the illumination can be assumed to be spatially invariant across the pillar. The position of the pillar was optimized to the peak of the Gaussian illumination spot. The responsivity was determined by calculating the ratio of the photocurrent in amperes to the absolute optical power incident on the projected cross section of the pillar. This responsivity was measured to be 9.5 A/W for an exemplary high speed device, which corresponds to an optical to electronic gain of 15 for 785 nm photons. In order to determine the true electronic gain or β, the absorption efficiency was experimentally determined in the same geometry for various angles and resolved against wavelengths, as

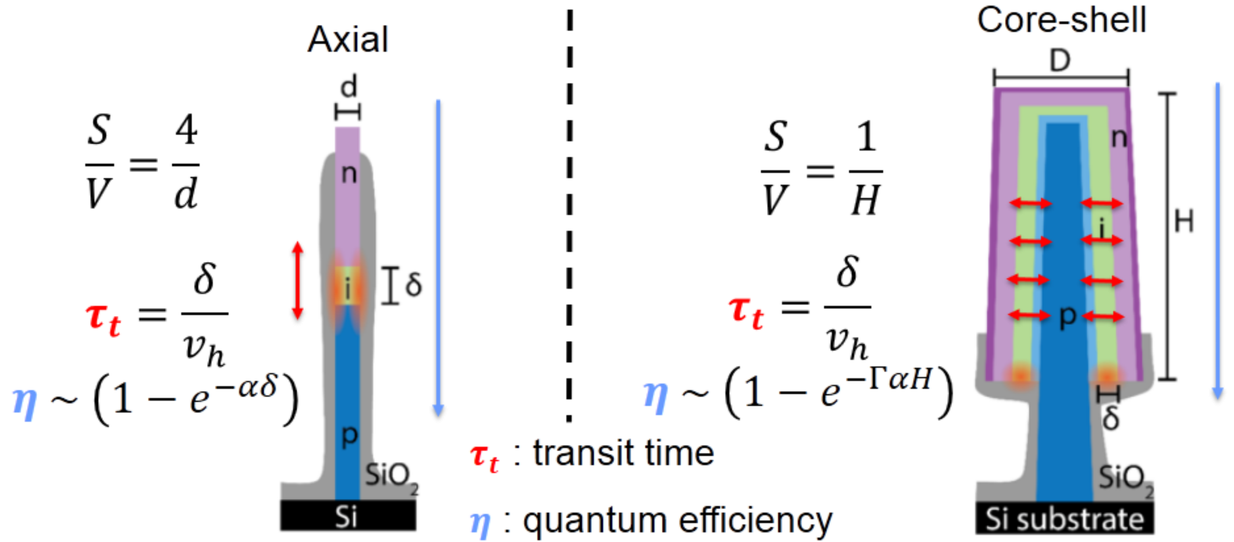

Figure 4.5: Comparison of device characteristics for axial (left) and core-shell (right) nanopillars. Note that the axial device has a tradeoff between transit time and absorption that the core-shell device can overcome.

illustrated in fig. 4.9. A Xenon arc lamp source, filtered through a monochromator was used for the measurement. The absorption efficiency of photons, which we term the external quantum efficiency to be consistent with published literature, is as high as 28% for despite the ultracompact device geometry. The enhanced absorption can be elucidated in terms of the high-index dielectric antenna characteristics of the nanopillar absorber [38], [123] combined with the double pass due to the back reflection from the contact metal.

The current gain β is then as high as 53.6 (obtained by dividing the optical gain by the absorption efficiency). This was the same device for which high speed characteristics were measured. Note that in a homojunction bipolar junction transistor, the current gain is determined by a ratio of the two Gummel numbers for the emitter and base currents:

$$\beta = \frac{G_E}{G_B} = \frac{W_E N_E D_B}{W_B N_B D_E} \tag{4.16}$$

where $W_E(W_B)$ is the undepleted electrical width of the emitter(base), $N_E(N_B)$ is the emitter(base) doping concentration and $D_B(D_E)$ is the base(emitter) minority carrier diffusion coefficient. Therefore, we have kept the electrical base width low and emitter doping high in order to achieve a high current gain. Current gain on the order of 100 is routinely achievable with BJTs and even higher with heterojunction bipolar transistors.

Figure 4.6 b shows a linear photo response from another nanopillar photoBJT when it is biased with 0.5 V collector bias and observed down to the picoWatt light level. This device did not have a ground pad fabricated and was instead grounded from the back side of the silicon substrate. This prevented the measurement of high speed RF characteristics (due

to excessively large pad capacitance). However, the DC characteristics were exemplary and could be used to verify transistor operation. Similar to the high speed deviuce, no electric bias was provided to the base junction a low quiescent optical bias was sufficient to turn the device on. This attests to the quality of the base-emitter junction in the regrowth. A gain of 39.5, including light absorption efficiency, for this exemplary device corresponds to a sensitivity improvement of 16.0 dB. Given the small noise figure of phototransistors[115], this has significant implications for building a sensitive photoreceiver. Figure 4.6c shows the responsivity vs. collector bias characteristic in order to highlight key regimes of operation of the device. The responsivity of the device increases with collector bias under the saturation regime (between 0 to 0.4 V collector bias), and eventually peaks at 25 A/W for 0.5 V collector bias in forward active mode. As the collector bias continues to increase, the responsivity eventually decreases. The reduction in responsivity is likely caused by the Early effect observed in the device an effect of base width reduction[124]. This effect also led to base punch-through above 1.0 V collector bias.

Pulsed response measurements were used to obtain device high speed characteristics at 785 nm illumination. This exemplary device had a measured responsivity of 9.5 A/W, and had ground-signal RF contacts fabricated so that the high speed electrical characteristics could be measured. A tunable mode locked solid state laser with small pulse width of $\sim$ 100 fs was used to excite the device. The device full duration at half maximum from a time resolved measurement, was roughly 300 picoseconds, which corresponds to a device bandwidth of 1.5 GHz (Fig. 4.8(a)). This is limited by the large pad capacitance of the 100 μm size contacts which can be as high as 2-3 pF. For 50 Ω RF connectors, this leads to an RC-limited bandwidth of 1.1 GHz (Fig. 4.7 b). This pad capacitance can be reduced by an order of magnitude by simply scaling down the size of the contacts and increasing the insulator thickness. Therefore, in order to obtain the true dynamic response of the device, we have de-embedded the capacitive response of the pads from the frequency response of the device, following the circuit model in Fig 4.8 b. This was additionally verified with an open test device which was fabricated without a nanopillar but on the same wafer, using the same oxide thickness. With this de-embedding procedure, the actual 3-dB bandwidth was found to be 7 GHz (Fig. 4.8 c). The 3-dB bandwidth decreases from 7 GHz to 6 GHz on increasing the bias from 1 to 1.5 V. The collector-base depletion region is expected to widen on increasing voltage bias, thus leading to increased transit time. This indicates that the device speed is limited by carrier drift through the collector-base depletion region. The peak power of the pulsed laser is sufficiently high to ensure that the device response is dominated by transit time rather than capacitive charging delays.

Here we discuss the de-embedding procedure using the S11 reflection measurement. This was used to determine the S-parameters of the open device. An Agilent E8361 PNA network analyser was used to perform the measurement. The S parameters were then converted to corresponding impedances, or Z parameters. The plot in Fig. 4.7 (a) shows the absolute value of the imaginary part of the impedance of the open device as a function of frequency. The first order roll off clearly indicates a capacitive transfer function: $Z = 1/(2\pi jfC)$Z, which is well fitted to a capacitance of 2.93 pF. There is also a small real part to the pad

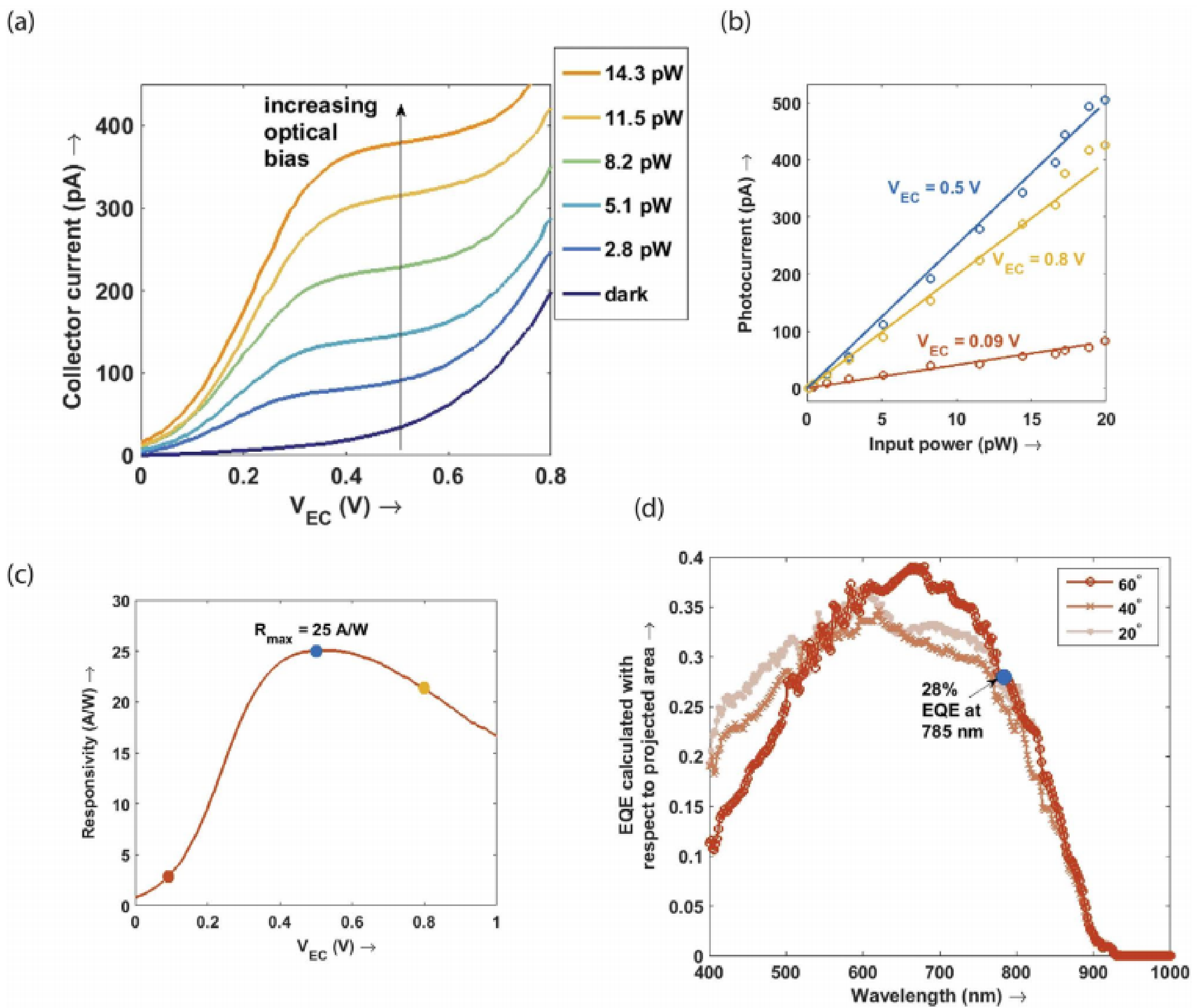

Figure 4.6: DC responsivity characteristics of the nanopillar: (a) Transfer characteristics of an exemplary photo-BJT showing dark current below 25 pA at 0.5 V bias, and a high responsivity of 25 A/W. (b) Responsivity as a function of input power at a few different collector biases. (c) Responsivity as a function of collector bias and (d) measured external quantum efficiency for a p-i-n device of the same dimensions, showing approximately 30-40 % quantum efficiency without BJT gain

impedance from the series resistance of the gold contact ($2-5\Omega$). Combined with the 50Ω standardized RF cable used to perform the measurement, this leads to a low-pass transfer function corresponding to a 3-dB cut-off frequency of ~ 1 GHz, which completely overwhelms the true high speed response (as seen in Fig. 4.7 c). On dividing the fourier transform of the pulsed temporal response by the parasitic transfer function we obtain the true 3 dB frequency of the device. We note that the capacitance can easily be reduced by using smaller pads and a thicker oxide insulator. The pad size used for these devices was $\sim 100\mu m$. The pad size can be reduced by a factor of 4 in each dimension and the oxide thickness can be doubled, thus leading to a 32x reduction in pad parasitic capacitance.

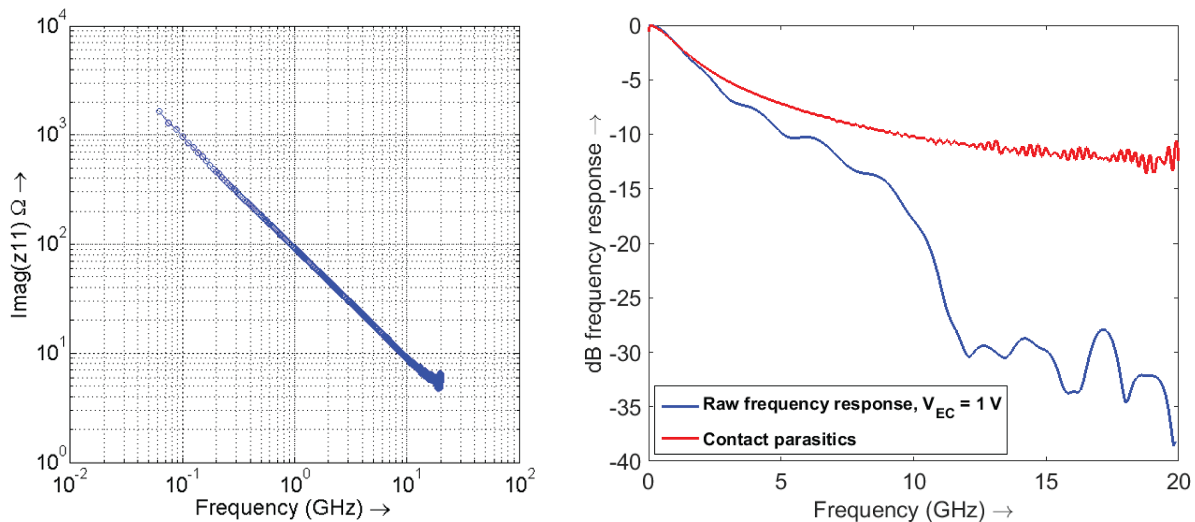

Figure 4.7: Removal of pad parasitics: (a) Reactive component of measured impedance, showing a clear fit to a capacitive load, (b) Comparison of S12 characteristic of an open pad (red) and the p-n-p photo-BJT, showing the effect of the pad parasitic on the device.

The electrical transition frequency (f_T) is therefore estimated to be 375 GHz given the measured current gain *beta* of 53.6 and 3 dB frequency of 7 GHz. Note that the current gain was measured by obtaining the total gain(39.5) and factoring in the absorption efficiency. The estimated transition frequency approaches the Terahertz scale frequencies of highly scaled heterojunction bipolar transistors fabricated from high quality InP-based systems [118]. This device has the highest gain-bandwidth product accounting for intrinsic photoresponse (or equivalently, $EQE \times f_T$) in the published literature for InP-based phototransistors, even though higher electronic f_T has been obtained with a drastic penalty on the light absorption (see Fig. 4.9). A high gain bandwidth product also necessitates a sufficiently high DC bias. Here, the bias is provided optically which has the advantage of eliminating any base capacitance that an electrical bias would necessarily have.

Here we discuss the de-embedding procedure for determining the true high speed response of the device. As shown in Fig. 4b of the manuscript, the parasitic pad capacitance has the effect of low pass filtering the high speed current signal from the phototransistor. In order to determine the true response, open devices with the same pad dimensions of 100 m100 m and same oxide thickness were fabricated adjacent to the nanopillar devices.

4.5 Responsivity-Bandwidth Tradeoff

Having determined the low frequency current gain of 53.6 and the true 3-dB bandwidth of 7 GHz for the same phototransistor device, operating at 1 V of voltage bias we calculate the electronic gain-bandwidth product or transition frequency f_T to be 375 GHz. We briefly discuss the factors that determine f_T for the reported device.

The temporal delays that determine f_T consist of the RC limit due to the charging of the device internal capacitances, the base transit time and the collector depletion layer transit time:

$$Gain \times BW = f_T = \frac{1}{2\pi \times ((V_t C_{tot})/I_c + W^2/(\eta D_B) + x^c_{dep}/(2v_{sat}))} \tag{4.17}$$

where I_c is the collector bias current, V_t is the thermal voltage of 25 mV, C_{tot} consists of the parallel combination of base-emitter and base-collector capacitances, W is the undepleted base width, D_B is the hole diffusion coefficient in the base for our hole injection device, η is a dimensionless number describing the base transit time, that can be increased by engineering a built in field, x^c_{dep} is the collector depletion region width and v_{sat} is the hole saturation velocity (see Ref. [117], section 3.3.1 Cutoff frequency). We would like to note that carriers do not need to be generated in the base: if the electrons can diffuse to the base-collector junction faster than the 3-dB frequency, or equivalently the data rate, then they can be amplified by fast transistor action. This is a much less stringent requirement than the f_T for the amplified carriers since it is not subject to the Miller effect.

The capacitance limited charging time is dependent on the collector current through the RC-time: CV_t/I_c where C is the total device capacitance, I_c is the collector current and V_t is the thermal voltage. The capacitance is estimated using a co-axial capacitor model:

$$C = \frac{2\pi\epsilon_{InP} L}{ln(r_{out}/r_{in})} \tag{4.18}$$

where the depletion region extends from a radius of r_{in} to r_{out} and the junction length is L. In our case, the regrown junction length L is controlled by the regrowth oxide mask height to be $\sim 1\mu m$. The depletion regions are rather thin at 40-50 nm, due to the high doping. The average radius of the junction is estimated to be 450 nm for the C-B junction and 500 nm for the E-B junction (based on growth time as in Ren et al., Ref. [36]). We estimate the emitter base junction capacitance to be 7.6 fF and the collector base junction capacitance to be 6.6 fF. Such low capacitance values can be attained in spite of the thin

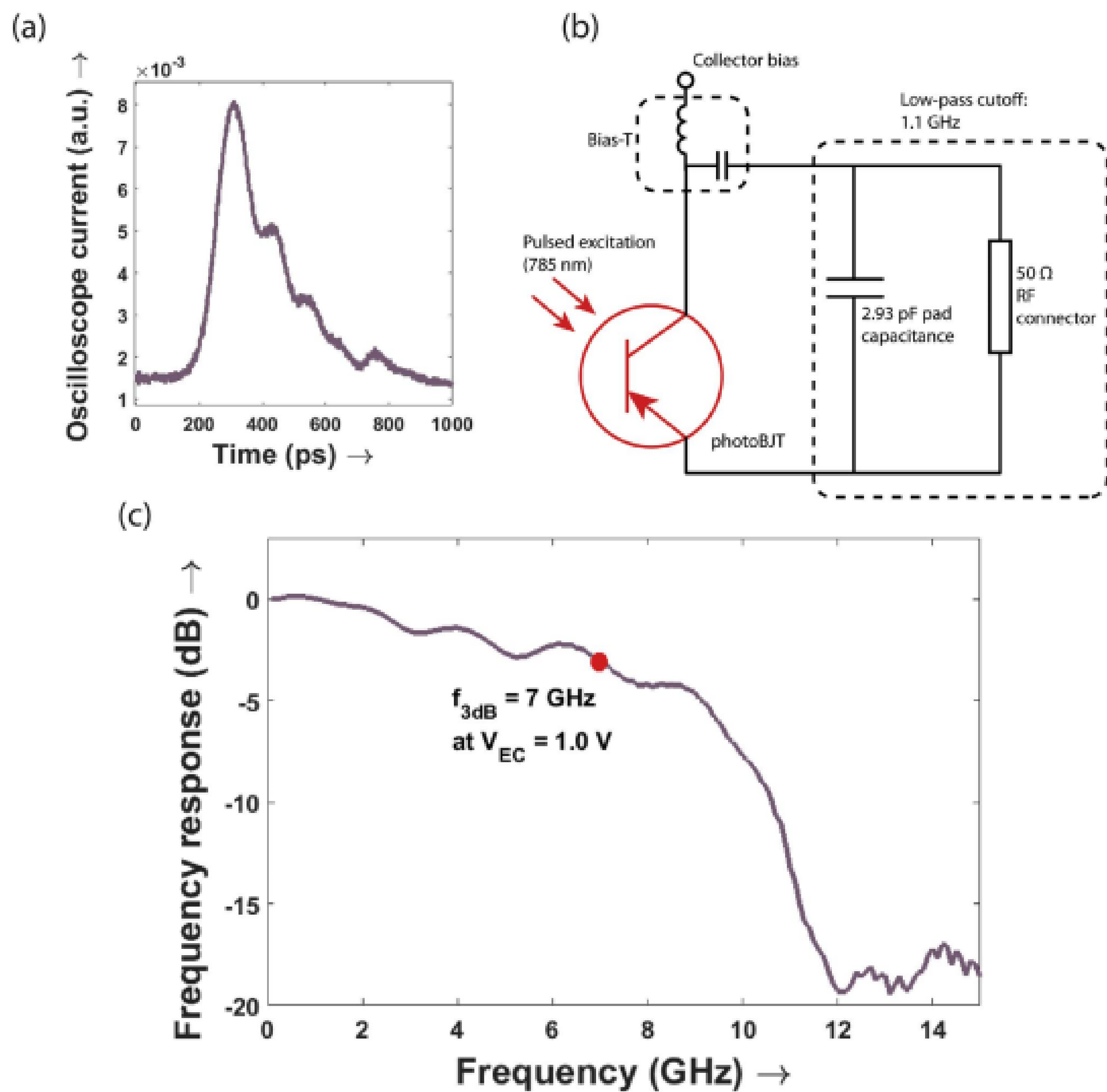

Figure 4.8: De-embedded high speed characteristics of nanopillar phototransistor: (a) Impulse response measured under pulsed optical excitation shows a somewhat large 120 picosecond full width at half maximum due to the pad parasitics, (b) Circuit showing device and pad capacitance, (c) High speed characteristic showing a 3dB frequency of 7 GHz after de-embedding pad parasitics.

depletion regions due to the compact size of the device. The forward-biased emitter-base junction also has capacitance due to minority carrier charge storage in the base, which has been accounted for in the transit time calculation.

The f_T increases by increasing the collector current until the transit time limit becomes the main limitation. The transit time therefore provides an upper limit on the device gain-bandwidth product. We have approached the transit limited bandwidth by using a pulsed measurement in which the peak current can be sufficiently high. The average optical power used for the pulsed measurement was P_{abs} = 150 nW absorbed by the pillar at 785 nm wavelength. Given the laser pulse period T of 12.5 μs, the typical minority carrier lifetime in the doped semiconductor τ of 1 ns (Ref. [37]), the fundamental charge q, and the base for the natural logarithm e, we estimate the average quiescent base bias current in each pulse:

$$I_b = \frac{1}{e} \times q \times \frac{P_{abs}T}{hc/\lambda} \times \frac{1}{\tau} \sim 430\ \mu A \tag{4.19}$$

The reported transition frequency of 375 GHz is well within the upper limit imposed by the capacitive charging limit (=$1/(2\pi) \times \beta I_{dc}/CV_t$ for the above base current (I_b) and junction capacitances. Thus, using the pulsed measurement, we have effectively measured the transit time limit to the gain bandwidth product for our device geometry.

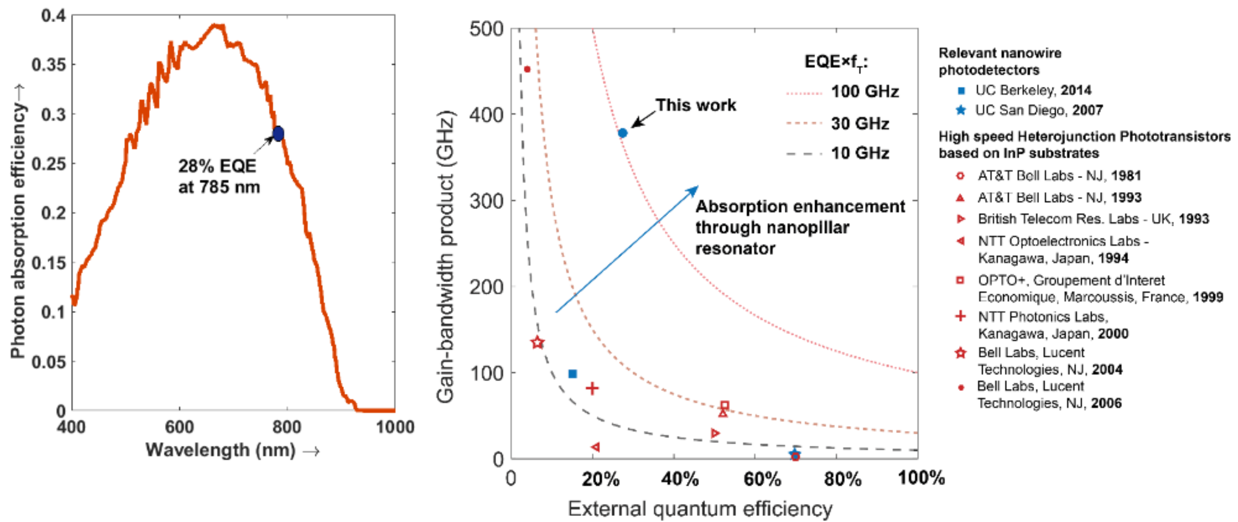

Figure 4.9: Tradeoff between responsivity and bandwidth: (a) high external quantum efficiency of the nanopillar diode without gain shows that the intrinsic light absorption efficiency of the structure is quite good, (b) Tradeoff empirically observed in reported phototransistor devices due to the competing requirements of low transit time against high light absorption efficiency

4.6 Prospects for Silicon Photonics Integration

A major advantage of the low temperature growth of nanopillars is the possibility of back-end integration with CMOS silicon electronics. We have demonstrated growth on silicon transistors, with optically pumped lasing of the nanopillars, along with un-degraded operation of the transistors after going through the MOCVD growth process (Lu *et al.*, Ref. [25]).

In addition, growth of InP nanopillars with InGaAs active region has been recently accomplished on a silicon-on-insulator platform. Waveguides have been patterned using e-beam lithography combined with a dry etch process based on an $SF_6 + O_2$ plasma that selectively etches the silicon, and does not affect the InP-based nanopillars. Further, InP/InGaAs/InP multiple quantum well light emitting diodes have been demonstrated on chip at silicon transparent wavelengths of 1.3-1.55 μm (Lu *et al.*, [27]). A first demonstration of waveguide coupling shows that the silicon-transparent emission of the nanopillars is coupled to the waveguide patterned at the base of the nanopillar (Malheiros-Silveiras *et al.*, Ref. [41]). This will be the subject of future study, in order to improve sensitivity in highly scaled nanopillar structures with optimized coupling to waveguides. Relevant prior work on waveguide-nanophotodetector critical coupling to enhance photodetection in ¡100 aF capacitance devices includes that of Going *et al.*, Ref. [125] and Ref. [83]. The advantage of using III-V here (which has higher absorption than Germanium) would be to enable a resonant cavity photodetector with smaller size and lower capacitance, while maintaining light absorption efficiency.

Chapter 5

InP-based Nanopillar Lasers on Silicon

Optical interconnections at short length scales, on and between microprocessor chips, have tremendous prospects to scale communication bandwidth density and reduce energy consumption for next-generation silicon integrated circuits [126], [2]. An intimate integration of active optoelectronic devices, including lasers, modulators and photodetectors, with silicon photonic waveguides is important to best leverage the scalable manufacturing capabilities of silicon and reduce energy consumption. Indium-phosphide (InP) based compound semiconductors are an ideal material choice for active photonic devices because they facilitate direct-bandgap quantum-wells for the efficient emission and absorption of light in the silicon transparent 1150-1550 nm wavelength range which has minimal absorptive propagation loss in silicon waveguides.

However, direct epitaxial growth of InP-based compound semiconductors on silicon has proven to be extremely challenging due to mismatches in lattice constant and thermal expansion coefficients with silicon, leading to defects that are detrimental to device performance. Further, the temperature for InP epitaxial growth is very high (typically higher than 650°C), making it incompatible with CMOS post-process requirements [12], [127], [17]. One of the proposed solutions is to wafer bond group III-V lasers onto a silicon substrate, a technique known as heterogeneous integration. The most popular approach thus far is evanescent coupling of light between the III-V gain medium and silicon-based cavity [11], [128], [129]. However, typical integration approaches implement edge emitting laser structures which have a very large footprint (hundreds of square micrometers to form a Fabry-Perot cavity). These sizes are orders of magnitude too large to be viable for integration with dense electronic integrated circuits or silicon photonics. In addition, proportional to the active volume of the lasers, the power consumption of such devices is also extremely high, many orders of magnitude higher than that required for short on-chip optical interconnects.

Recently, III-V compound semiconductor nano*wires* with footprints on the order of tens of nanometers have been shown to grow directly on silicon at low temperatures with excellent crystalline quality [29]. Work has also been reported on broad-area edge emitting lasers using

an ensemble nanowire based active region [130], [131]. However, a single as-grown nanowire laser would be highly desirable for high density, low power consumption applications [132]. One key issue with the nano*wires* is that the lateral dimension is too small to result in a reasonable optical confinement. To date, most single nanowire lasers are demonstrated by removing from the growth substrate [133], [134], [135], [136], [137], [138], [139], [140], [141], [142] and the only as-grown nanowire laser emits at 825 nm wavelength [143]. These are not suitable for monolithic integration with silicon photonics.

We have recently reported a novel core-shell growth mode that results in single crystalline Wurzite phase III-V nanopillars directly on a silicon substrate. Growth is achieved in a catalyst-free manner, using metal-organic chemical vapor deposition [30], **Ren2013a** Due to the 3-dimensional core-shell growth, nanopillars can scale up to several microns in height while maintaining sub-micron diameter footprint with pristine crystalline quality in the bulk [31]. One major advantage of this core-shell structure is the minimal exposed surface of the active region, leading to brighter luminescence and lower dark current in devices. The importance of mitigated surface recombination and resulting low dark current has been emphasized in chapter 2 (solar cell) and chapter 4 (phototransistor) of this thesis.

Using the nanopillar growth mode, we reported the first demonstration of an InGaAs/GaAs nanolaser monolithically grown on silicon [24] and nanopillar lasers grown on transistors without compromising MOSFET electronic performance. This provides a direct proof of the CMOS-compatibility of the low temperature growth mode [25]. In addition, we demonstrated as-grown InGaAs/GaAs nanopillar light emitting diodes (LED) directly modulated at 2.5 Gb/s and photodetectors at 1 Gb/s, all as-grown on a silicon substrate. With these devices, we demonstrated the first photonic link using as-grown nanopillar devices on a silicon substrate [33]. However, all these results are based on InGaAs nanopillars with a lasing wavelength around 900nm. Most recently, we investigated InP-based nanopillar growth using the same growth mode to eventually achieve longer wavelengths. We demonstrated a compact InP bipolar junction phototransistor with a simultaneously high current gain (53.6), bandwidth (7 GHz) and responsivity (9.5 A/W) using a single crystalline InP nanopillar directly grown on a silicon substrate as described in chapter 4 of this thesis and in ref. [39].

In this chapter, we report the first quantum-well (QW)-in-nanopillar laser as-grown on a silicon substrate with silicon-transparent emission with sub-micron footprint, by directly synthesizing high quality InP/InGaAs/InP QWs on nanopillars on silicon. We demonstrate a novel resonator with a silicon undercut-post structure to improve the optical quality factor. Further, we demonstrate the capability to tailor lasing wavelengths by changing the indium composition and thickness in InGaAs/InP QWs during growth, with emission ranging from 1.15 μm up to 1.3 μm, in spite of lattice mismatch between QW and InP barrier.

5.1 Transparency Condition in Nanopillar with Quantum Well

The $In_xGa_{1-x}As$ (x $\sim$ 0.53) material system is ubiquitous as the active region for lasers at telecommunication wavelengths. Such an active region typically consists of InGaAs/InAlGaAs quantum wells grown lattice-matched or with a small strain on a (100)-InP substrate with Zinc-Blende crystalline phase. We previously reported very efficient elastic stress relaxation at the $GaAs/In_{0.2}Ga_{0.8}As$ interface due to the core-shell geometry and small diameter, resulting in a drastic increase of critical thickness as compared to the thin film case [144]. However, it was unclear that multiple lattice mismatched layers can be grown on such pillars subsequently. In particular, it was not clear if a single or multiple $In_xGa_{1-x}As/InP$ quantum well region can be grown on these Wurtzite-phase nanopillars with the side walls having an undetermined crystalline facet. Here, we demonstrate such growth with excellent optical quality for the first time.

First, the InP nanopillars are grown on a Si [111] substrate. Subsequently, a series of samples with varied numbers of InGaAs/InP quantum wells were grown onto the InP core in a core-shell manner by controlling organometallic precursor flows. A final 100 nm InP layer is grown as the surface passivation layer, thus cladding the interfaces of the active region. Fig. 5.1(a) shows the 85° tilt view scanning electron microscopy (SEM) image of spontaneously nucleated nanopillars grown on a silicon substrate. The nanopillars align to the four degenerate [111] directions of the silicon substrate, further evidence of monolithic crystalline growth. Note that the silicon substrate surface is clean and free of polycrystalline deposition, in sharp contrast to those with InGaAs/GaAs nanopillars [31], [24], [25], [33]. This clean silicon substrate facilitates simple silicon etch processing to be performed after growth of the nanopillars, as described in the section on the undercut cavity laser below. The quantum wells (QWs) inside the nanopillar are visualized using cross-sectional transmission electron microscopy (TEM). Figure 5.1 (b), (d) and (e) show the cross-sectional TEM images of a nanopillar with one, five and two QWs inside respectively. Due to an atomic mass difference, the InGaAs QW can be distinguished from InP as a brighter hexagonal ring. The thickness of the QW is measured to be $\sim$ 5nm. The interface between InP and InGaAs is sharp and free of any defects or dislocations, attesting to the superior quality of the active region. Fig. 5.1(c) shows an exemplary nanopillar, with a typical diameter of $\sim$ 800nm and a height of 6-7 μm. Multiple QWs are desirable to provide sufficient gain for lasing. It is interesting to note in Fig. 5.1(d) that the multiple quantum wells show up as hexagonal rings conformal to the core-shell growth. Fig. 5.1(f) is a high resolution TEM image inset of the two quantum well cross section. Seamless continuity of the Wurzite crystal lattice through the heterostructure can be observed, with image contrast from the different atomic masses.

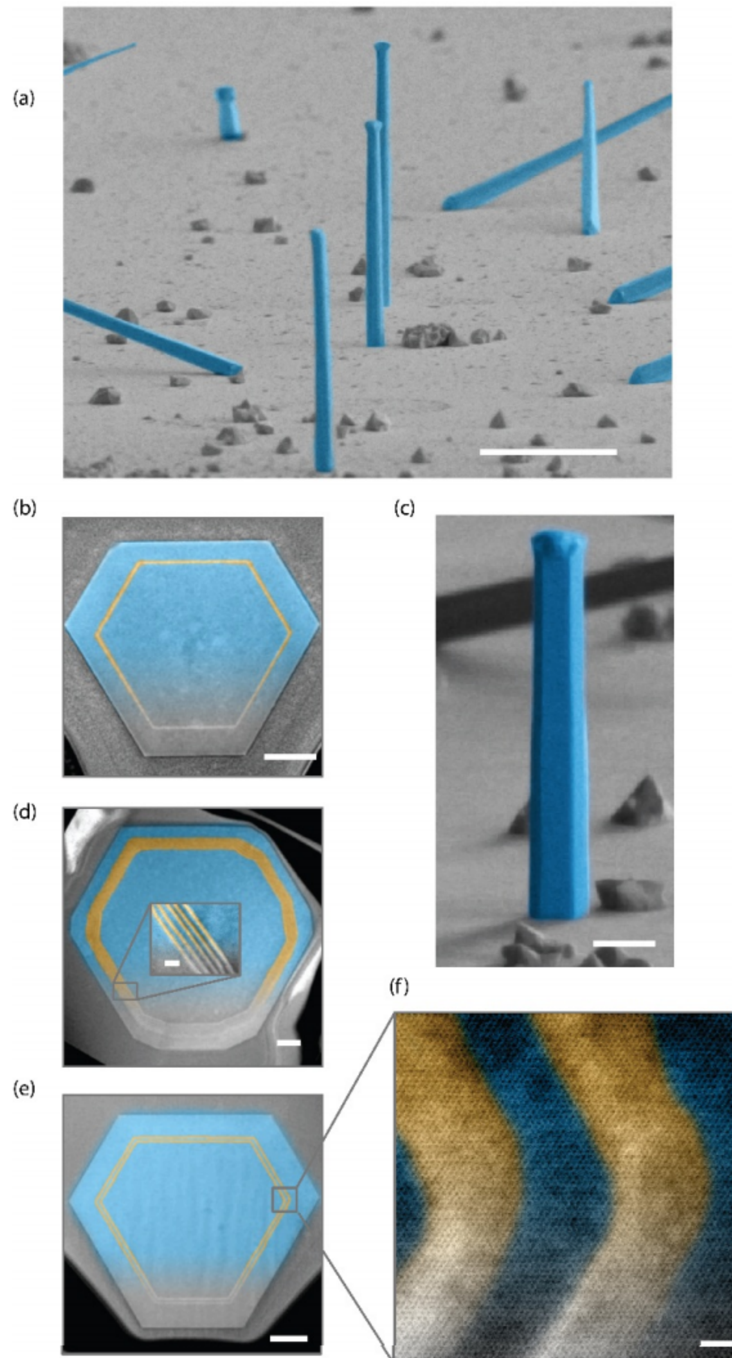

Figure 5.1: Electron microscope images of nanopillars with QWs: (a) 85° tilt view scanning electron microscope (SEM) image of nanopillars containing 5 QWs (pillars are aligned to four degenerate [111] directions), (b) Cross sectional transmission electron microscope (TEM) image of a nanopillar containing a single QW (highlighted in yellow), (c) Close-up SEM image of an exemplary single nanopillar, (d) Cross sectional TEM of a nanopillar with 5 core-shell conformally grown QWs, with an inset showing the individual QWs, (e) cross sectional TEM of a nanopillar with 2 conformal QWs, with inset (f) showing a high resolution TEM image where individual atoms can be seen. The continuity of the crystal lattice across InP and InGaAs is clearly visible. Scale bars: (a) 5 μm, (b) 100 nm, (c) 1 μm, (d) 100 nm (inset: 20 nm), (e) 100 nm, and (f) 2 nm

Excellent optical quality of the quantum wells is attested by photoluminescence measurements on as-grown InP/InGaAs/InP nanopillars. A calibrated absolute luminescence measurement can be used to measure the Fermi level split of the electrons and hole ΔF, since the spontaneous emission counts r_{sp} (photons /s /cm^2 /eV) depend exponentially on the difference of ΔF and the photon energy $\hbar\omega$. This technique has been described in detail in chapter 2, and here we focus on its utility for qualifying laser active region material properties. Note that this is a new extension of the widely adapted 'contactless I-V' technique used in the characterization of solar cells [55], [40], [145], [146]. Absolute counts can be determined using a calibration with known reflective properties. In this case, the calibration was performed using a 1550 nm laser reflected off a Lambertian reflecting surface (Spectralon). Using an absolute measurement of the laser power, the counts measured on the spectrometer can be converted into photons, and the Fermi level split is determined as:

$$\Delta F - h\nu = k_B T ln\left(\frac{r_{sp}}{r_0}\right) \tag{5.1}$$

where r_0 depends on fundamental constants and the emissivity of the luminescing layer. This technique is valuable in gauging the excitation intensity at which the quantum well active material starts to show optical gain. More precisely, this helps us determine the current density at which the Fermi level split equals the bandgap or the *transparency current density*. Typically, good quality quantum well heterostructures have a transparency current density of 50-100 A/cm^2 per quantum well layer [147]. In order to determine this metric using photoluminescence, the nanopillar is excited with a continuous wave 660 nm (1.88 eV) laser that is absorbed efficiently by the InP cladding layer. The same individual InP nanopillar is measured at 5K and 293K. Similarly for the InP/InGaAs/InP nanopillar case. Since the InP nanopillars have a very low surface recombination velocity, as reported in Ref. **Li2015a** the carriers generated in the InP cladding are captured efficiently by the quantum wells. This enables us to achieve a very high carrier concentration in the quantum wells, resulting in a low continuous wave room temperature transparency pump power density for the quantum wells. Fig. 5.2(a) shows a schematic of the process, with low excitation PL spectra of a single quantum well nanopillar in Fig. 5.2(b). As seen in Fig. 5.2b, the emission from the quantum well is orders of magnitude higher than that from the InP barrier layer, a clear indication of efficient carrier collection. This effect is even more significant at room temperature due to the surface passivation effect from the high bandgap cladding layer, which preserves the heterostructure emission even at higher temperatures.

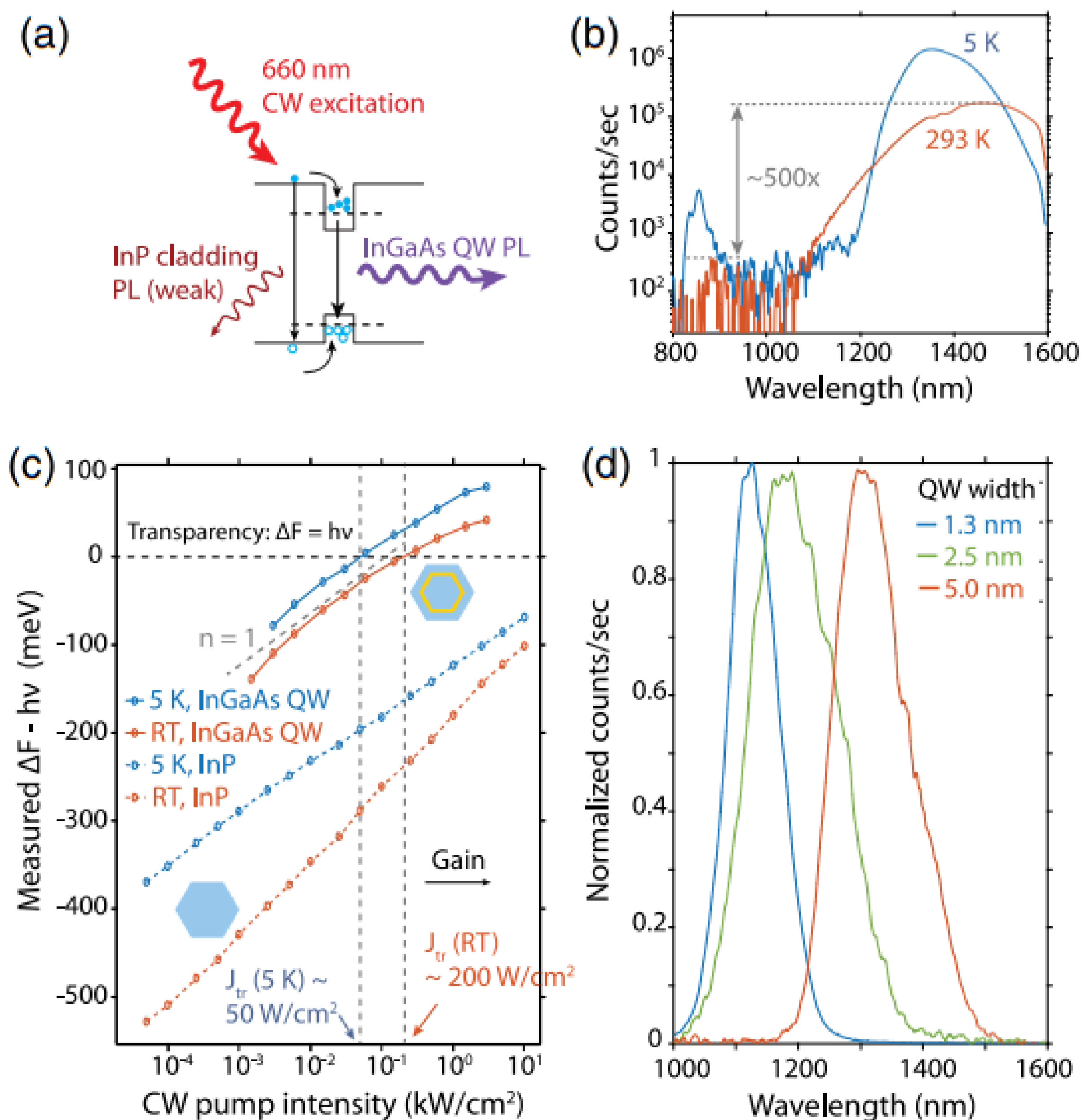

Figure 5.2: QW luminescence and transparency condition: (a) Schematic showing indirect excitation of QWs using rapid capture of electrons and holes from the InP cladding layer, (b) Photoluminescence (PL) spectra for indirect excitation of a QW, showing minimal cladding luminescence, (c) Quantitative Fermi level split, inferred from luminescence intensity. It is found that the difference $\Delta F - h\nu$ is significantly higher (and exceeds 0 i.e. transparency) for the QW as compared to the 'bulk' InP nanopillar. (d) Quantum size effect showing wavelength tuning over 200 nm in the silicon transparent window by simply changing the quantum well thickness.

The excitation dependence is plotted in Fig. 5.2(c) at 5K as well as room temperature. The Y-axis shows the difference from transparency $\Delta F - h\nu$ in meV using equation 5.1. In order to interpret this graph, we firstly calculate the internal luminescence yield from the ratio of room temperature to low temperature counts. This corresponds to the difference between each set of orange and blue curves in fig. 5.2(c). We find that the internal yield is as high as 25% and stays fairly constant even at low pump powers. This can be fit to a carrier recombination model, with the dominant non-radiative recombination path being Shockley-Read-Hall recombination at the InP/InGaAs interface with an extremely low interfacial recombination velocity of $\sim$ 10 cm/s. This has also been discussed in detail in chapter 2. This internal luminescence yield is two orders of magnitude higher than that for undoped InP nanopillars, which is measured to be 0.3% and increases with pump intensity due to the saturation of non-radiative centers at the naked InP surface (dashed curves). In addition, the luminescence yield is on par with that of a commercial planar InGaAs quantum well epitaxially grown on a lattice matched InP substrate, measured to be 30-33% using the same technique. A plot of the excitation dependent internal luminescence yield is shown in figure 5.3.

We point out that the transparency condition is easily achieved for quantum wells at a pump excitation power of 200 W/cm^2 at room temperature. Even if one assumes that 100% of the incident pump power on the nanopillar cross section is absorbed, this corresponds to an equivalent electrical pump current density of $\sim 110A/cm^2$ for the 660 nm (1.88 eV) photons. To the best of our knowledge, this is the first time this metric has been measured for nanowire or nanopillar based gain media and is on par with reported values for traditional III-V thin film quantum wells [147]. The low transparency power is very promising for energy efficient nanopillar based light sources on chip.

A verification of the physical dimension of the quantum wells is obtained from the quantum size effect. The quantization energy will increase as the thickness of quantum wells reduces, leading to a shorter wavelength emission. The PL measurement results in fig. 5.2(d) show that as quantum well thickness reduces from 5 nm to 1.3 nm, the wavelength blue-shifts by approximately 200nm. This is consistent with a finite barrier quantum well analysis for $In_{0.45}Ga_{0.55}As$, which has a 0.55% lattice constant mismatch with the InP nanopillar core. In spite of this, we have been able to grow multiple quantum wells at this alloy concentration, with total thickness 2-3x the critical thickness for this lattice mismatch.

5.2 Hakki-Paoli Gain Measurement

Having demonstrated the high luminescence yield and ability to produce a high Fermi level split in the quantum well based nanopillars, the next step is to use the high gain to produce a laser. A laser requires an optical resonator in order to produce feedback and allow a lasing mode to dominate. In order to enhance optical feedback, as-grown InP nanopillars with five InGaAs quantum wells were transferred to sapphire substrate by mechanical wiping. In the lying-down nanopillar, semiconductor-air interfaces at both top and bottom of nanopillar

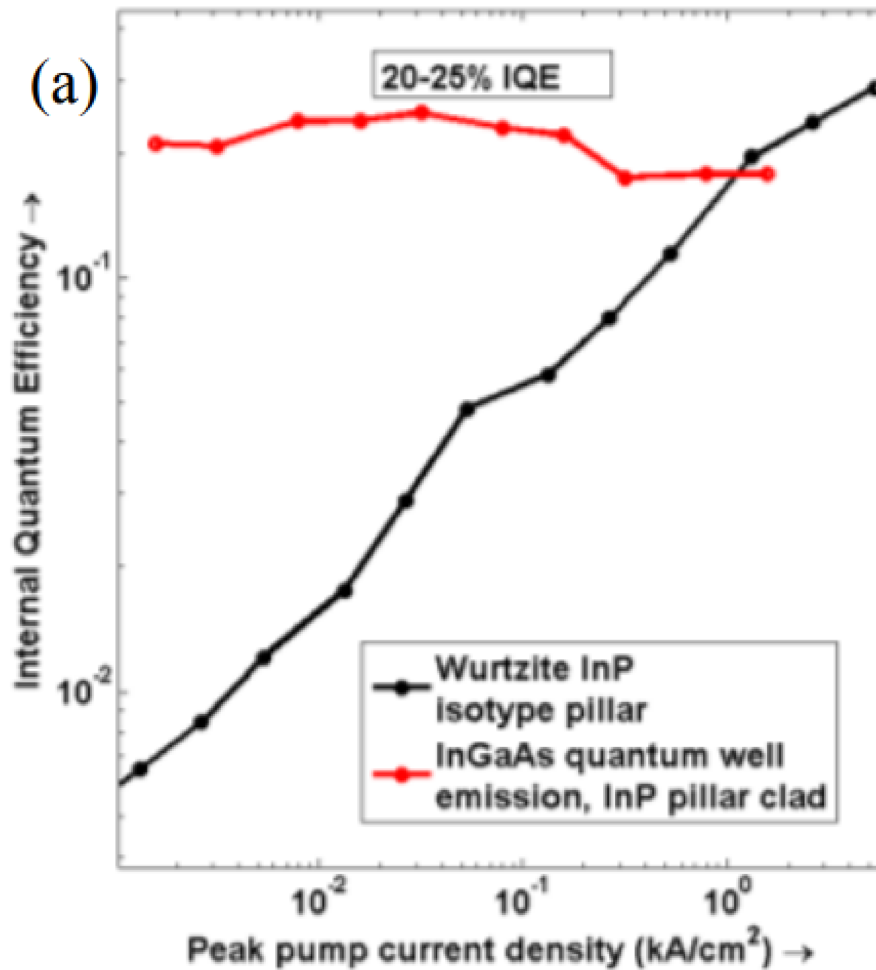

Figure 5.3: Internal Quantum Efficiency (IQE) of nanopillars: The IQE was measured by dividing room temperature total PL counts by low temperature total PL counts, and was found to be significantly higher for the QW active region at low pump excitation (note log scale in y-axis). The bulk InP nanopillar IQE is significantly poorer at low excitation intensity and improves as the radiative process becomes more competitive at higher injection level. However, due to the super-injection effect in the QWs, we have high carrier densities in the QW even at low pump excitation levels.

provide strong reflections, forming a horizontal high quality factor Fabry-Prot cavity. This is the typical configuration for studying nanowire lasing behavior, and we have characterized this for completion and consistency with the body of work on short-wavelength lasers. The structure has been illustrated in the inset of Fig. 5.4(a).

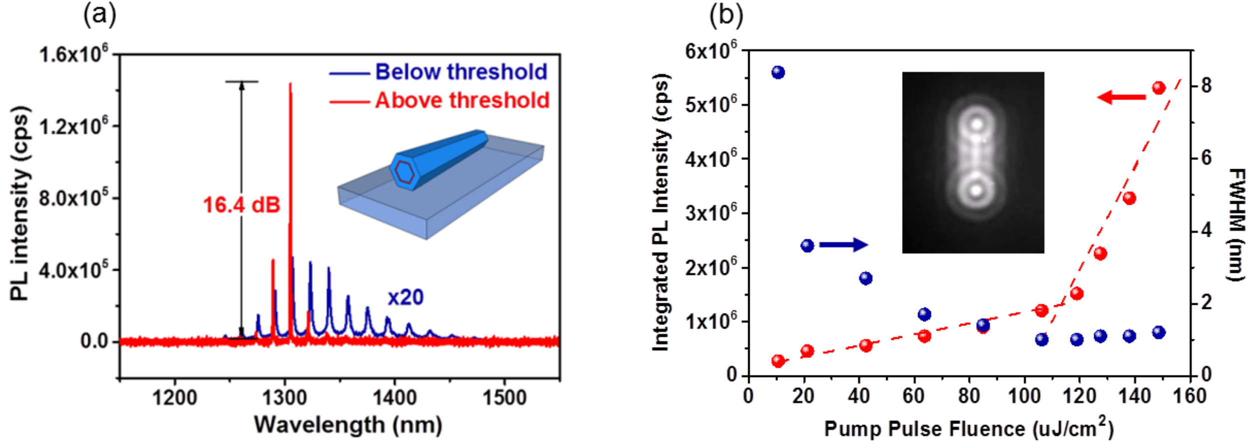

Figure 5.4: Transferred Nanopillar Laser: (a) PL spectra of a transferred nanopillar laser below and above threshold (inset shows laser structure schematic - QWs condensed together for clarity), (b) PL intensity and full width-at-half-maximum (FWHM) of the lasing mode at $\sim 1.3\mu m$ as a function of pump pulse fluence. The inset is the near field image of nanopillar emission above lasing threshold.

Lasing at the wavelength of 1300nm is achieved using an optical pump (femtosecond titanium:Sapphire pulses at a wavelength of 900 nm) at 5 K. Fig. 5.4(a) shows the PL spectra below and above lasing threshold. Under low pump power (blue curve in Fig. 5.4(a)), Fabry-Prot modes are clearly observed, with a distinctive feature that optical mode wavelengths are equally spaced. The mode spacing is measured to be 17nm, matching the theoretical value determined by:

$$\delta\lambda = \frac{\lambda^2}{2n_g L} \tag{5.2}$$

where n_g is the group index (~ 4.2) and L is the cavity length (12 μm). When the pump power exceeds lasing threshold, one of the Fabry-Prot modes at the wavelength of $\sim$ 1300nm starts to laser with a side mode suppression ratio of 16.4 dB.

Several other characteristics confirm the lasing behavior. First, as shown in the red trace in Fig. 5.4(b), photoluminescence peak emission intensity plot as a function of pump pulse fluence exhibits a non-linear threshold, highlighting the lasing transition for this transferred nanopillar. Additionally, the blue trace of Fig. 5.4(b) shows that full-width-at-half-maximum (FWHM) of the lasing mode at $\sim$ 1.3m narrows to around 1 nm around the lasing threshold. Finally, a near-field image above lasing threshold (the inset of Fig. 5.4(b)) shows the

interference pattern between the top and bottom end facet emission from the nanopillar, confirming the spatial coherence of light.

As the continuous wave pump power exciting the quantum well active region is increased, the carrier concentration increases and the material starts to produce optical gain. In the previous section, we have described a technique to quantitatively measure the excitation power at which the material first starts to show gain (related to transparency current density). However, we are also interested in determining the optical gain quantitatively. In order to do this, we excite a nanopillar optical cavity until it starts to show pronounced optical modes. The Hakki-Paoli method describes how to infer the gain from the shape of the amplified spontaneous emission spectrum [148]. In order to apply this technique, a simple Fabry-Perot cavity is ideal. The nanopillars do not naturally form a suitable cavity on the silicon substrate, due to the higher refractive index of silicon. However, mechanically transferring nanopillars to a low index substrate, as described above, will lead to a Fabry-Perot cavity due to reflection from the end facets of the nanopillar.

Nanopillars containing three quantum wells were mechanically transferred to a silicon dioxide substrate for the Hakki-Paoli study. These wiped-down nanopillars were then excited using a 980 nm laser. The laser spot was made elliptical using a cylindrical lens in order to provide uniform excitation and hence spatially uniform gain across the length of the nanopillar. Fig. 5.5 shows results from an exemplary wiped down nanopillar under high continuous wave excitation. As seen in fig. 5.5(b), the measured PL shows pronounced regularly spaced modes. We note that the 13 nm spacing of the modes can be confirmed to arise from the 15 μm cavity length (eqn. 5.2). The counts at the mode peak (P_i) and two neighboring troughs (V_i, V_{i+1}) are noted for each peak. This allows us to determine the peak to valley modulation in the luminescence spectrum induced by the cavity:

$$r_i = \frac{2P_i}{V_i + V_{i+1}} \tag{5.3}$$

From this, the gain at the position of the cavity mode can then be determined as follows:

$$-g_m = \frac{1}{L} ln\left(\frac{r_i^{0.5}+1}{r_i^{0.5}-1}\right) + \frac{1}{L} ln\left(R_1 R_2\right) \tag{5.4}$$

where g_m is the modal gain for the ith mode, L is the cavity length, r_i is the peak to trough modulation as described in eqn 5.3, and R_1 and R_2 are the facet reflectivities. Note that when the cavity starts to lase ($r_i \rightarrow \infty$), the gain clamps to the mirror loss in the cavity. Using the expression in eqn. 5.4, the modal gain at every peak position has been plotted in fig. 5.5(c) for two different pump excitation intensities (0.1 and 1 kW/cm^2).

We note that the spacing of data along the photon energy axis is limited to the mode spacing, which is somewhat large for the shorter cavity length of the nanopillar laser (compared to conventional edge-emitting Fabry-Perot laser caviites). The peak gain achieved at a pump excitation of 1 kW/cm^2 was approximately 340 $/cm$ for the three quantum well active region. The high modal gain achieved is due to a combination of the high quality III/V active region, and high mode overlap in the core-shell geometry nanopillar Fabry-Perot cavity.

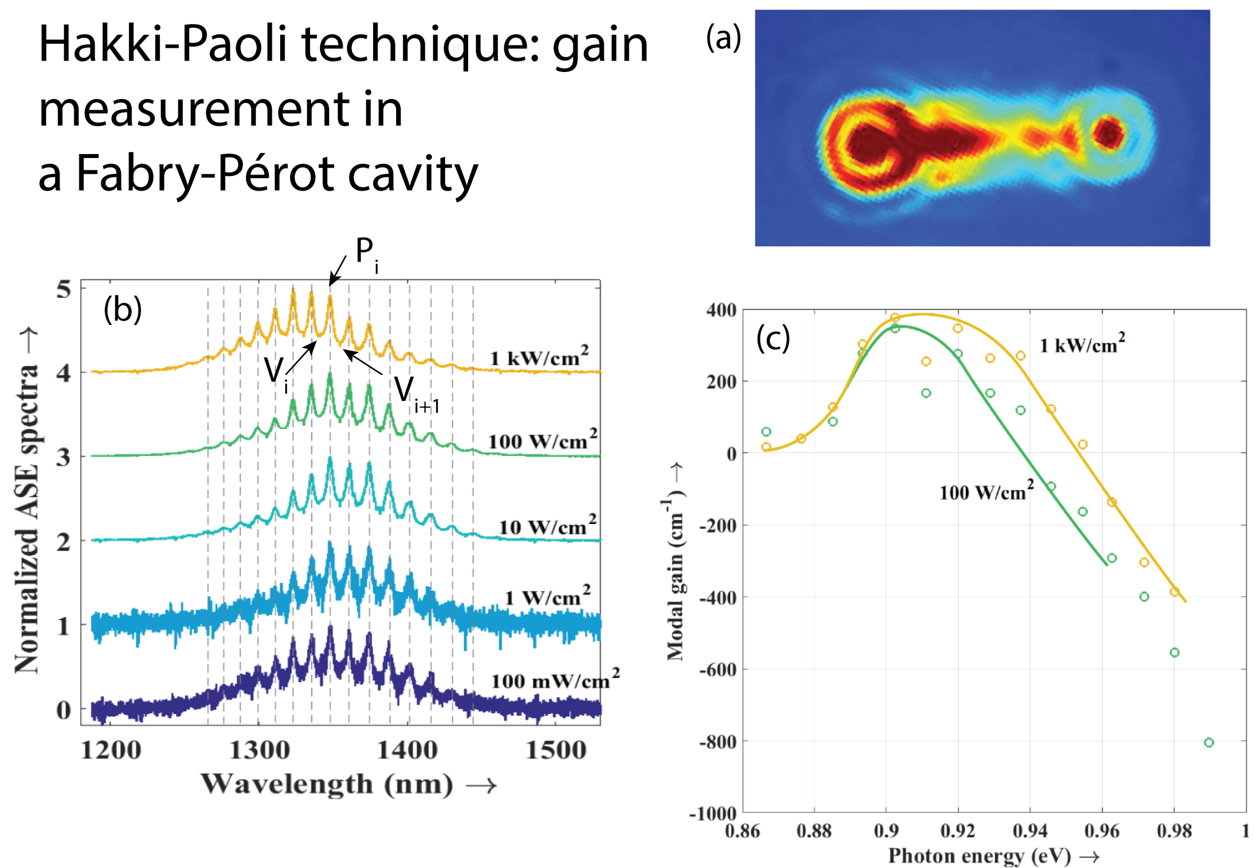

Figure 5.5: Hakki-Paoli method: (a) Microscope image of a transferred nanopillar showing amplified spontaneous emission (ASE), (b) ASE spectra of the nanopillars at different CW pump excitation intensities. The peak to valley modulation in the spectrum can be used to infer the gain at each wavelength, as shown in (c)

5.3 Undercut Cavity Laser

InGaAs nanopillars grown directly on silicon are able to sustain significant optical feedback via helically propagating modes in spite of the small refractive index difference with the silicon substrate [24]. In that case, the pillar has a slightly higher refractive index compared to the substrate. Hence, a mode propagating at a grazing angle to the substrate interface can still experience total internal reflection. However, in the InP case, the refractive index of the silicon substrate is higher, thus making it challenging to achieve optical feedback at the substrate interface. One approach is to grow the nanopillars onto a silicon-on-insulator (SOI) substrate, where the $Si - SiO_2$ layers enhances the bottom reflection of the nanopillar cavity mode due to the low index of the oxide. In the SOI substrate, the buried silicon dioxide layer is $\sim 2\mu m$ thick, whereas the silicon layer is as thin as 500nm, so that reflected light at the $Si - SiO_2$ interface can be efficiently collected back to the nanopillar cavity and contribute to cavity feedback. An advantage of this approach is that the strongly confined fundamental transverse order mode can experience sufficient optical feedback for lasing. The detailed lasing characteristics and wavelength tunability with this laser structure have been described in ref. [27].

An alternative and novel approach to increase the nanopillar/Si interface reflection is to create an abrupt structural discontinuity at the interface, shown in Fig. 5.6(a). The nanopillar is supported by a silicon post having a smaller diameter than the nanopillar, created by a selective undercut etching process of the silicon substrate. Figure 5.6(a) shows an 85° tilt-view SEM image of a nanopillar supported by an undercut silicon post, where the nanopillar is highlighted in blue. As seen in the zoomed-in scanning electron microscope image, the InP nanopillar remains intact after the silicon etching, with hexagonal crystal facets visible. The exposed silicon substrate can be etched using this method because of the absence of any polycrystalline III-V thin film, unlike the case of the InGaAs nanopillars. The small air gap at the nanopillar base provides an enhanced reflection for the helically propagating nanopillar modes. Figure 5.6(b) shows the optical cavity quality factor Q calculated using 3D finite difference time domain simulations for different undercut dimensions δ in the silicon structure. As the undercut δ increases above 200nm, Q is simulated to exceed 1000, and is no longer limited by proximity to the silicon. The inset of Fig. 5.6(b) shows that the simulated cross sectional field distribution is a symmetric high order mode with intensity peaks close to the edge of the nanopillar.

By incorporating five InGaAs quantum wells into this novel high-Q undercut cavity, long wavelength nanopillar lasers are achieved under pulsed optical pumping from 5K up to room temperature. Fig. 5.7(a) shows the photoluminescence spectra below and above threshold, with the lasing wavelength at 1220-1230 nm, with redshift the lasing peak at higher temperature. The lasing peak power is plotted as a function of the pump pulse fluence in Fig. 5.7(b) for various temperatures. A typical S-shape near the threshold is observed. These L-L curves can be fit with a rate equation model and spontaneous emission coupling factor β of 1-5%, which is typical for such compact laser cavities. An important outcome of the low dimensional heterostructure is the reduced temperature sensitivity of

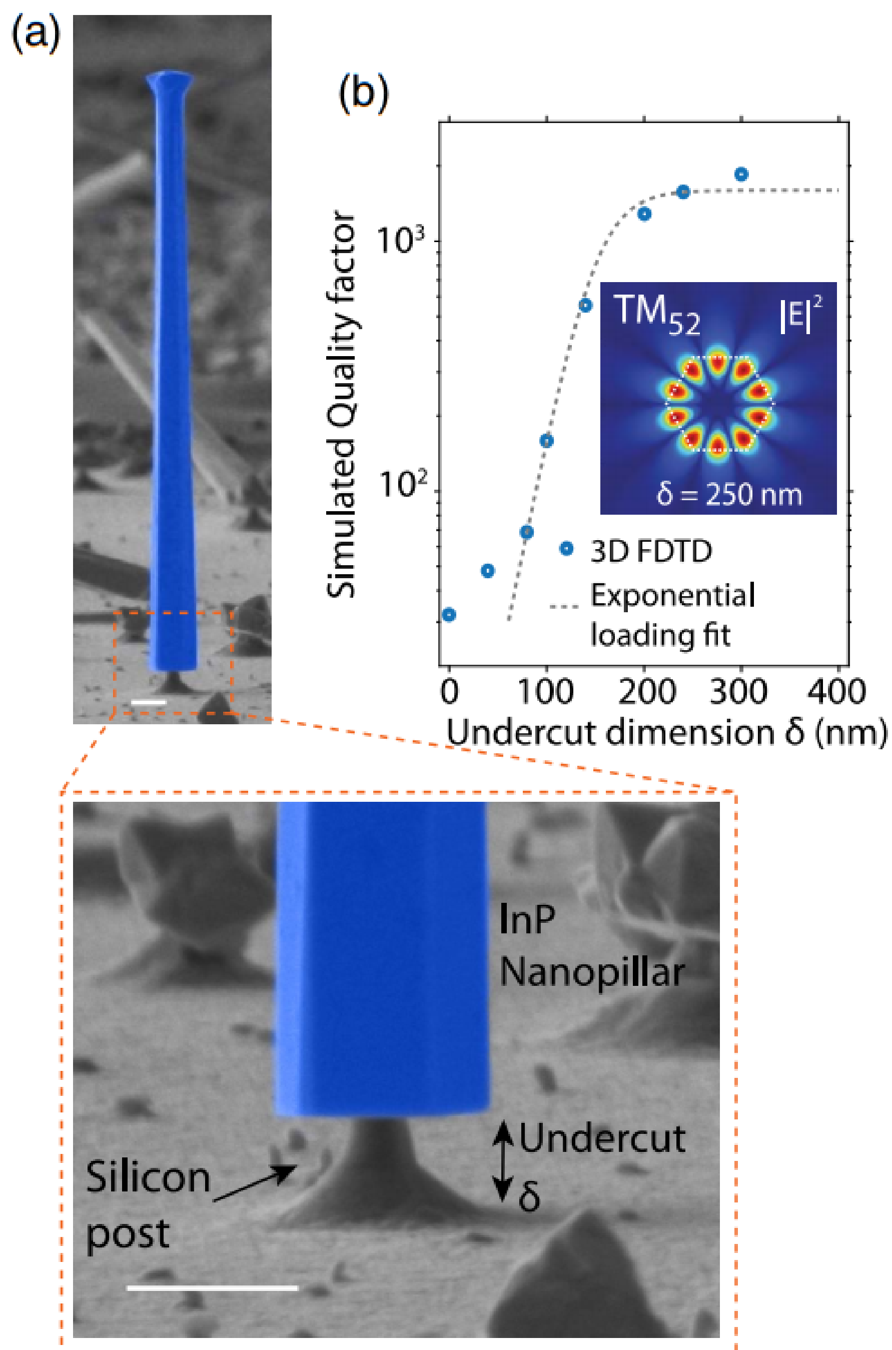

Figure 5.6: Undercut cavity structure: (a) SEM image of a nanopillar with selectie silicon etch using the $SF_6 + O_2$ plasma. The inset below shows how the pillar is left unaffected, while etching away the silicon in an isotropic manner. The process is self aligned, with the nanopillar providing an etch mask. (b) Simulated (FDTD) quality factor of an exemplary TM_{52} mode in a nanopillar shows significant improvement in quality factor as the undercut dimension δ is increased above 150 nm. Scale bars: 1 μm

the lasing threshold as predicted by Arakawa and Sakaki [149]. From 5K to 300K, the threshold pump fluence increases from $\sim 20\ \mu J/cm^2$ to $200\ \mu J/cm^2$. This corresponds to a laser characteristic temperature T_0 of 128 K. This T_0 value is surprisingly high compared to typical InGaAs QW edge-emitting lasers on a lattice matched InP substrate, despite the small footprint on the Si substrate acting as a heat sink. In the next section, we describe measurements to ascertain the thermal resistance of a single nanopillar device. The robust temperature performance attests to the superior quality of the nanopillar quantum well gain material.

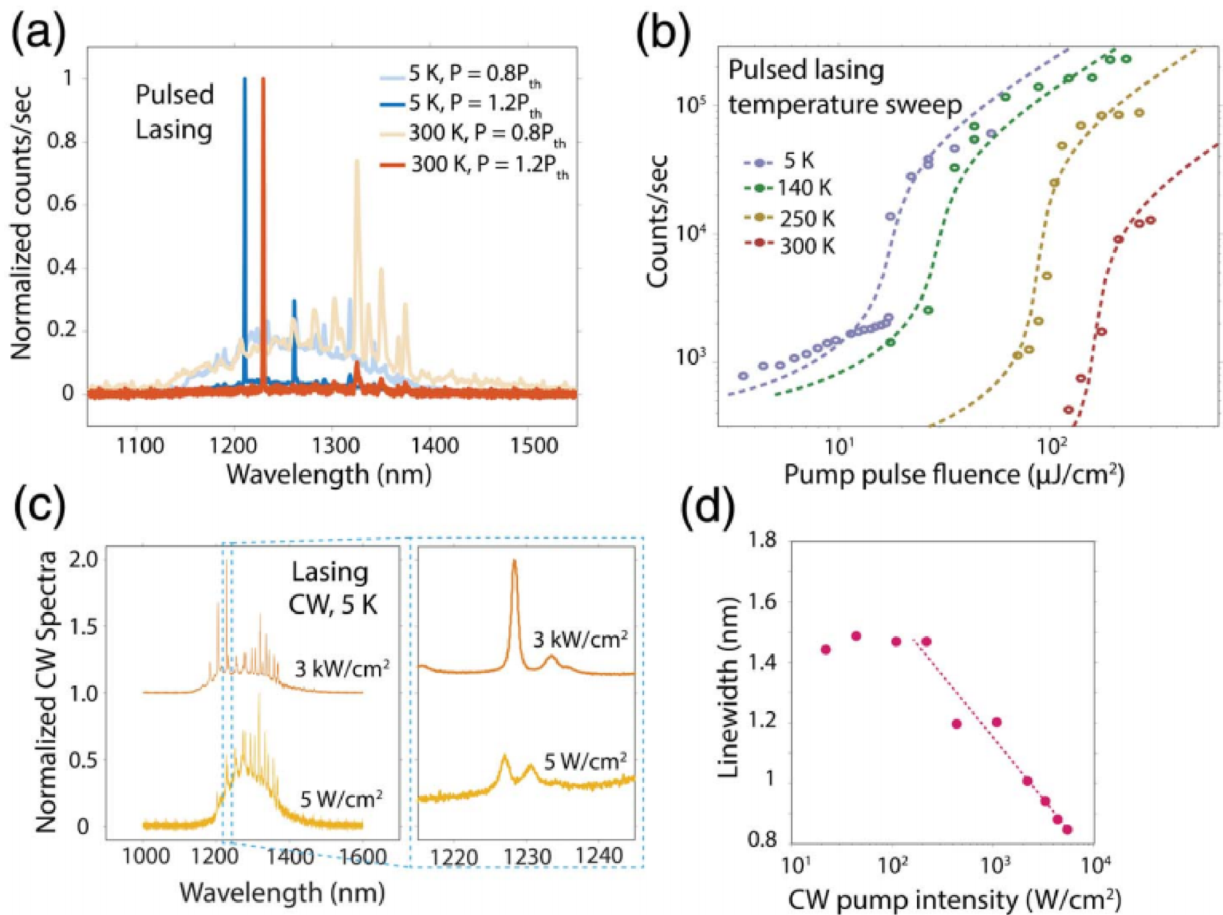

Figure 5.7: Undercut cavity lasing upto room temperature: (a) Pulsed optical excitation leads to lasing from 5K up to room temperature, (b) The lasing light-light curves show a characteristic S-shape all the way up to room temperature and can be fit with a rate equation model, (c) Continuous wave low temperature (5K) luminescence spectra showing linewidth narrowing with increasing pump power, (d) to ~ 0.8 nm linewidth at the onset of lasing

The same nanopillar was also measured under continuous wave (CW) pump. Figure

5.7(c) shows the PL spectrum at low temperature with direct excitation of the quantum well with a 980 nm CW pump. At low pump power of 5 W/cm^2, the PL spectrum shows narrow modes with 1.6 nm linewidth. The onset of continuous wave lasing is indicated by linewidth collapse to 0.8 nm when the pump power is increased to 3 kW/cm^2. To the best of our knowledge, this is the first report of continuous wave lasing from nanopillar or nanowire based structures at a silicon-transparent wavelength.

5.4 Thermal Resistance

Most conventional quantum well based semiconductor lasers typically support high current densities on the order 1-10 kA/cm^2. At such a high current density, it is important to engineer contact resistances and other dissipative losses so that the cavity does not heat up significantly. Nevertheless, it is important to ensure that any heat that is generated in the nanopillar structure is rapidly dissipated to the substrate. This ensures that the cavity does not significantly heat up beyond the substrate temperature. In general, it is desirable to keep the temperature reasonable in the laser active region, as higher temperatures typically degrade performance, leading to higher threshold current and temperature induced shifts in spectra.

One metric to measure the thermal dissipation of the nanopillar structure is the thermal resistance R_{th}, the temperature increase in the nanopillar active region per unit power dissipation in the device (measured in K/mW). Typically, a compact vertical cavity surface emitting laser (VCSEL) has a thermal resistance of 1-2 K/mW. This implies that for 10 mW of power dissipation in the VCSEL device, the active region temperature increases by 10-20 Kelvin. We are interested in determining this metric for the nanopillar structure as well.

Note that the thermal resistance is a lumped metric that can be calculated from more elementary material characteristics and device geometry. The material parameter of interest is known as the thermal conductivity, in analogy to electrical conductivity. For a slab of material of length L, cross sectional area A and thermal conductivity σ_{th}, the lumped thermal resistance R_{th} for a heat gradient existing across the length of the block is given by:

$$R_{th} = \frac{L}{\sigma_{th} A} \tag{5.5}$$

This is in analogy to electrical resistance, except voltage gradients are replaced by temperature gradients and current flow is replaced by heat flux. Thermal resistances can also be combined in series and parallel in exact analogy to electrical resistances. We desire a low thermal resistance, in which case a large heat flux can flow due to a small thermal gradient, leading to very effective thermal dissipation in the device active region. Materials that have good thermal conductivity are also typically electrically conductive. Hence, gold and silver have the best specific thermal conductivities at 318 and 428 $Wm^{-1}K^{-1}$ respectively. Semiconductors are mediocre with InP, GaAs and silicon at 80, 56 and 149 $Wm^{-1}K^{-1}$. Electrical insulators such as silicon dioxide and silicon nitride are notably poor at 1.1 and

0.7 $Wm^{-1}K^{-1}$ respectively. One notably exception is the case of $\alpha - Al_2O_3$ and aluminum nitride which are both electrically insulating but can have thermal conductivities of the order of 20-50 $Wm^{-1}K^{-1}$ and 170-190 $Wm^{-1}K^{-1}$ respectively. Gu *et al.* have described the use of amorphous aluminum oxide for thermal management in nanolasers [150].

Here, we focus on the nanopillar geometry as depicted in fig. 5.8. Without going into a detailed finite element simulation of the thermal dissipation in the structure depicted in 5.8(a), we attempt to provide some trends using lumped resistances. Note that much of the heat would also be generated in a distributed manner in the core-shell quantum well region and the electrical contact. One path for the heat to flow is vertically down the length of the InP nanopillar. Using the formula:

$$R_{InP} = \frac{1}{\sigma_{th}^{InP}} \frac{H}{A} \tag{5.6}$$

we find that for every micron of pillar height, a series thermal resistance of approximately 17 K/mW is added. Here, we consider a typical pillar cross section of 1 μm diameter. Therefore, a few microns of pillar length can easily add up in excess 50 K/mW of thermal resistance. This is highly detrimental for device operation at high current densities.

An alternative parallel thermal dissipation path is through the contact metal, assumed to be surrounding the pillar for this calculation. If we assume that much of the heat is generated at or close to the contacts, this could be a useful thermal dissipation path to exploit. Considering a 200 nm thick gold contact layer, this leads to a thermal resistance of only 4 K/mW for every micron of contact length. This is further reduced to only 1.3 K/mW per micron, for the case of a 500 nm gold contact. These estimates were made using the simple formula in equation 5.7, where r_{out} and r_{in} are respectively the outer and inner radii of the contact layer.

$$R_{Au} = \frac{1}{\sigma_{th}^{Au}} \frac{H}{\pi(r_{out}^2 - r_{in}^2)} \tag{5.7}$$

We note that the radial heat flow path across the InP cross section presents negligible thermal resistance, as shown in fig. 5.8(b). However, the silicon dioxide insulator sleeve does present a signficant series resistance in the heat conduction path. Considering a thin silicon dioxide layer of width 100 nm, the added series thermal resistance for lateral heat conduction is given by (making a cylindrical cross section assumption):

$$R_{SiO_2} \sim \frac{1}{\sigma_{th}^{SiO_2}} \frac{r_{out} - r_{in}}{2\pi r_{avg} H} \tag{5.8}$$

where r_{in} is the radius of the InP nanopillar, r_{out} is the radius at which the oxide coating ends and H is the height of the oxide coating. For a micron of height and 50 nm oxide thickness, this leads to a thermal resistance of around 14.5 K/mW, and reduces to about 4.8 K/mW for a three micron tall oxide (fig. 5.8 (c)). Note that we are referring to the lateral heat conduction path here, which has a lower thermal resistance when the height increases.

It is clear that the oxide adds a significant thermal resistance and it may be beneficial to completely eliminate the oxide, so that the heat can rapidly dissipate to the metal contacts. This will negatively impact the optical quality factor and is a careful design tradeoff that will depend on the required device metrics. Note that a micron height pillar with 500 nm radius carrying 10 kA/cm^2 of current density with a voltage bias of 2 V dissipates a total of only 0.6 mW of power. Hence, we may be able to manage with a higher thermal resistance than conventional VCSELs and edge emitting lasers.

In order to experimentally measure the thermal performance of a nanopillar/nanowire based laser structure, we fabricated a simple n-doped InP nanopillar resistor. The goal is to characterize the thermal dissipation of the nanopillar structure that we already have, before attempting to improve the thermal resistance. The single nanopillar resistor is electrically biased at a certain current and voltage, while simultaneously being illuminated at low excitation intensity with a 660 nm pump laser. The low excitation intensity ensures that the nanopillar is not being heated by the excitation laser itself. The photoluminescence (PL) counts are recorded. This is repeated as a function of current bias, in order to determine the PL peak red-shift as the bias is increased. The temperature of the nanopillar can then be determined from the Varshni coefficient for InP.

This allows us to determine the temperature at different dissipation powers in the nanopillar resistor structure allowing the thermal resistance in K/mW to be measured. This is an important metric, since it allows us to determine the rise in the active region temperature as the device is pumped harder. Ideally, a low thermal resistance is good for device performance. However, due to the high surface to volume ratio and geometry of the pillar, the measured thermal resistance is rather high at $\sim$ 33 K/mW (see fig. 5.9). As discussed above, the high thermal resistance can be significanty mitigated by using a thicker metal contact layer that carries heat down to the substrate or by reducing the oxide thickness to allow lateral heat dissipation to the contact.

Due to the poor thermal dissipation, under typical laser bias conditions, we will expect to have the nanopillar active region be $\sim$ 50 K above the substrate temperature. In this case, it becomes all the more important to develop a thermally robust active region. In the undercut laser, we have performed temperature dependent characterization and determined that the characteristic temperature of the lasing threshold is 128 K (with reference to the substrate heat sink temperature). This attests to the robust thermal performance of the active region, in spite of the high thermal resistance.

5.5 Silicon Photonics Integration

The manipulation and guiding of light using highly integrated silicon waveguides and monolithic devices is going to be key to truly bring the advantages of optical interconnections into practice. In particular, wavelength division multiplexing (WDM) has had a great impact on increasing the information bandwidth carried by singe mode waveguides across great distances (telecom). To truly implement WDM on chip, we will require wavelength controlled

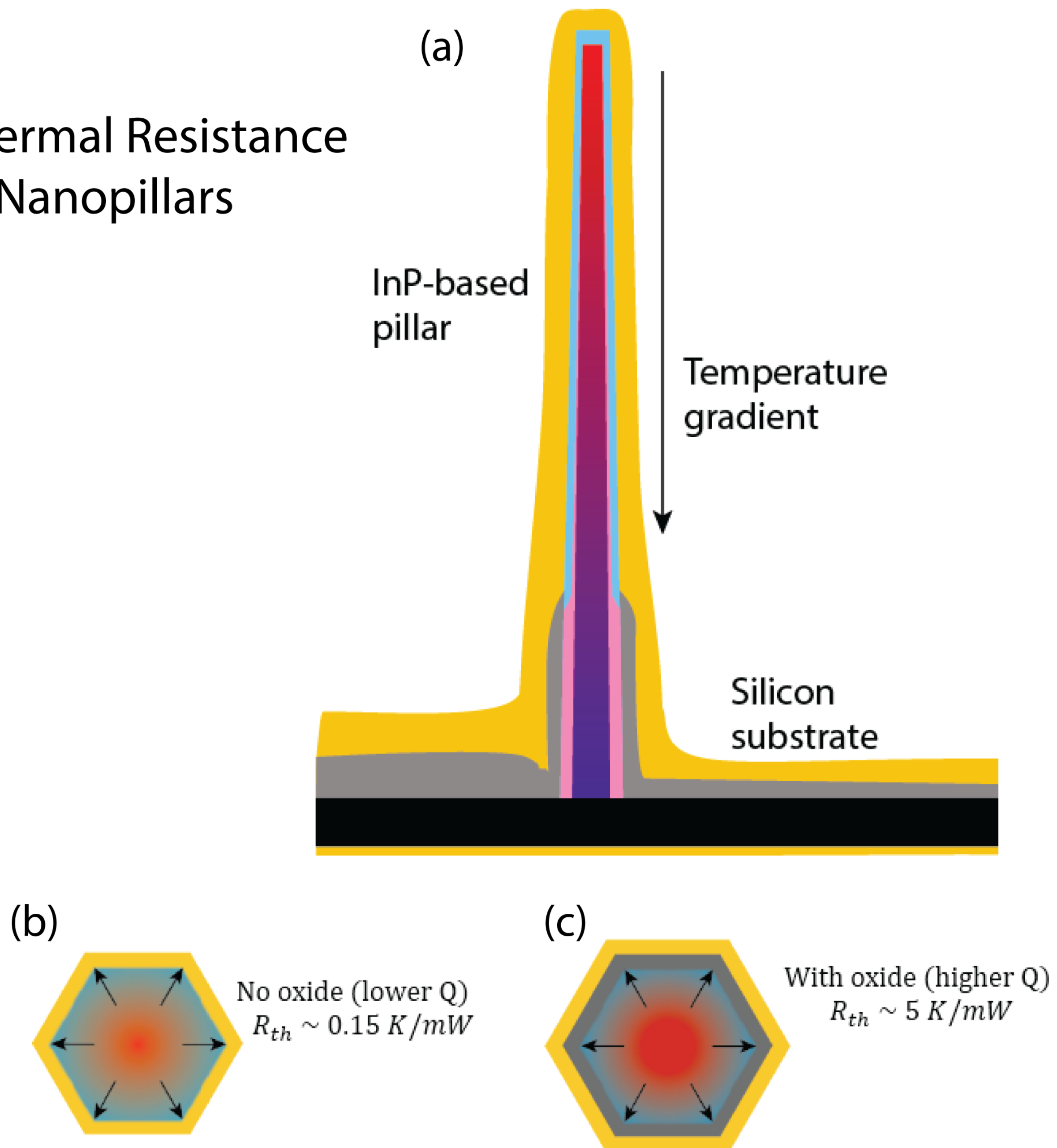

Figure 5.8: Thermal dissipation in nanopillars: (a) Schematic showing temperature gradients in a nanopillar under high current injection. The two main paths for heat conduction are the metal (gold) layer and long InP nanopillar body. The metal contact is a significantly more effective heat conductor, as discussed in the text. (b) A situation in which there is no insulating oxide is better for heat dissipation, but would lead to higher optical loss. (c) An oxide coating would add a significant series resistance in the thermal conduction path, but allows for a higher cavity quality factor.

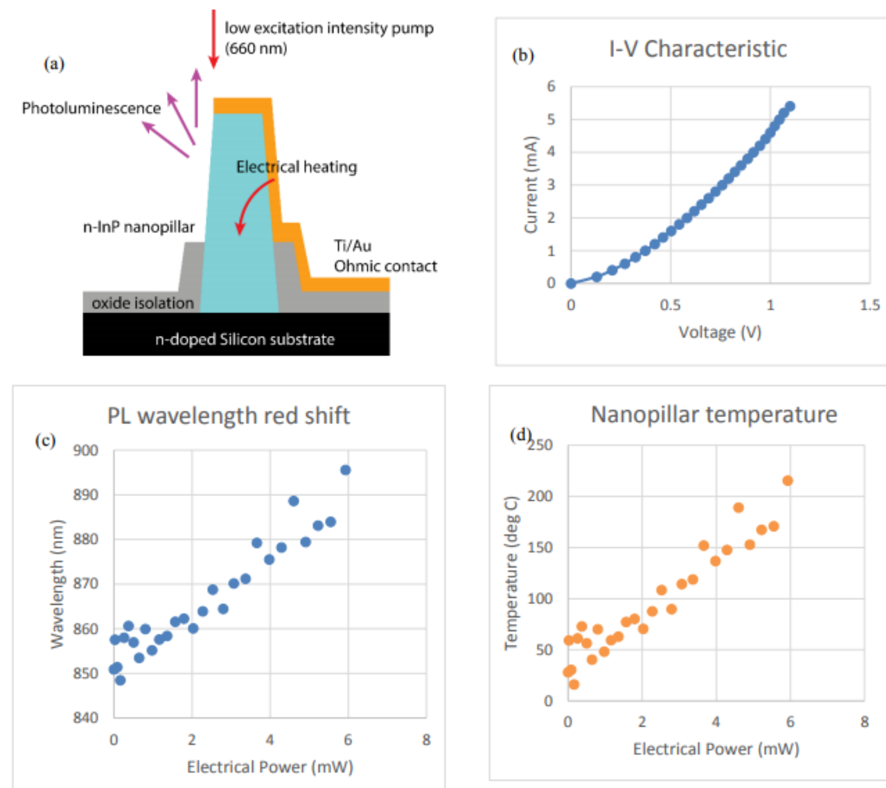

Figure 5.9: Thermal resistance measurement in fabricated nanopillars: (a) Schematic of the fabricated device and current conduction path, with details of the fabrication process in chapter 2. (b) I-V characteristics of the single nanopillar resistor, showing close to Ohmic characteristics. (c) Photoluminescence peak wavelength red shift with increasing power dissipation, note that the wavelength under no heat dissipation is blue shifted compared to the InP Wurtzite bandgap due to the Burstein-Moss blue shift that arises from heavy doping. (d) Inferred nanopillar temperature from the graph in (c) and using the Varshni coefficients for InP. A linear fit to this curve allows us to extract the thermal resistance of the device.

coherent light sources (lasers), passive devices such as multiplexers, and other active photonic devices such as modulators and photodetectors corresponding to each WDM channel. Essentially, a vast number of individual components will have to be integrated on chip in order to realize a high information density. The dense and intimate monolithic integration of nanopillars onto silicon photonics waveguides and patterned SOI substrates has been pursued by our group [41] towards this end. There has also been recent interest from other groups on approaches towards monolithic integration of nanowires and nanowire based silicon transparent lasers on a silicon substrate [151], [152].

In this section, we describe how we have experimentally demonstrated the monolithic integration of III-V compound semiconductors in nano and micro scale geometries to silicon waveguide geometries. This has been validated by characterizing the optical coupling of spontaneous and stimulated emission with silicon waveguides. A nanopillar-waveguide integration platform can be obtained by two different approaches: top down (when nanopillars are grown in specific positions on top of a silicon photonic circuit) or bottom up (when photonic circuit is defined after nanopillars growth). We present the latter approach where an optical source is monolithically integrated to silicon photonics platform. The former approach has become possible only recently, after the demonstration of position controlled growth of nanopillars. This will be discussed in detail in chapter 6 of this thesis.

The waveguide coupling results pave way for the realization of novel optical and optoelectronic devices which can fulfill the requirements of having ultracompact sources of light directly integrated to silicon photonics. The proposal and results show complete compatibility with the CMOS platform since the growth process is free of metal catalysts, it is performed at low temperatures, and is cost effective given the use of MOCVD to monolithically growth III-V onto silicon platform.

Two different samples were grown in order to assess the aforementioned proposal. In sample-1, InP nanopillars were grown onto a silicon substrate for short wavelength emission experiments. For sample-2, InGaAs/InP quantum wells (QWs) on nanopillars were grown on a silicon-on-insulator (SOI) substrate in order to demonstrate silicon-transparent wavelength emission. Details of the sample preparation of samples and growth can be found in ref. [41]. The fabrication process is summarized here. Alignment markers have been used to map the positions of spontaneously nucleated nanopillars that were desirable for fabrication. A silicon dioxide hard mask was defined around these nanopillars in order to etch waveguides. A selective $SF_6 + O_2$ etch was used to selectively etch silicon and define waveguides, while the conformal oxide coating continued to protect the nanopillars. We have also discussed in the section on undercut lasers that this silicon etch is selective against the nanopillars and has minimal effect on the nanopillar luminescence characteristics or minority carrier lifetime [41].

The micro-photoluminescence of an exemplary nanopillar on a silicon waveguide geometry is shown in Figure 5.10(a) (in blue), with emission centered at 825 nm at low temperature (4 K), indicating that it is single crystalline and has Wurtzite phase. The inset shows a top-view scanning electron microscope image from that structure. As the optical pumping power is increased, the nanopillar emission reaches lasing threshold. The red curve in Figure 5.10(a)

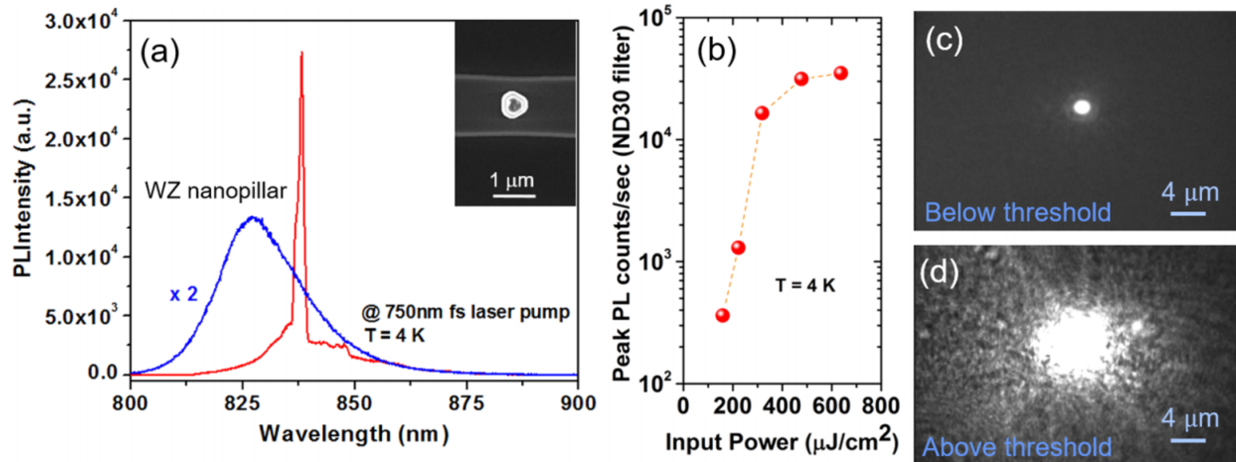

Figure 5.10: Nanopillar lasers on silicon photonics structures: (a) Lasing spectra under low temperature pulsed excitation for the structure shown in the inset. This proves that the fabrication process is robust and preserves material quality. (b) light-light curve of the nanopillar laser on silicon-photonics. Microscope images of the excited nanopillar both below (c) and above (d) threshold are also shown for comparison.

shows the narrowing of optical spectrum above lasing threshold. The laser peak dominates above the background spontaneous emission achieving about 7.88 dB of background suppression. In Figure 5.10(b), the light-light curve from the same nanopillar is plotted. The L-L curve has an abrupt 'S-shape', with lasing threshold at 57 kW/cm^2. Finally, microscope images of a single InP nanopillar emission below threshold show just a spot of light from spontaneous emission (Figure 5.10 (c)), and above threshold (upon lasing) strong speckle patterns can be noticed (d). Speckled pattern results from high degree of coherent emission, a classic signature of laser oscillation.

Figure 5.11 shows results for two nanopillars on waveguide structures fabricated using sample-2 (QW nanopillar on SOI), one each for upright and slanted nanopillars. The different orientations arise because the nanopillars grow along the degenerate [111] directions of the silicon substrate, and the angle between [111] and [11-1] is approximately 55 degrees. Figure 5.11(a) shows an SEM image (30° tilted view) of an InGaAs/InP 5-QWs upright nanopillar on top of the center of two crossing silicon waveguides. The structure with crossing waveguides has four ports (S1, S2, S3, and S4). The SiO2 cladding layer used as a mask for fabrication partially covers the nanopillar and was not etched away for the experiment. The nanopillars here have a hexagonal frustum shape with a diameter of about 900 nm, and height of $\sim 4.5\mu$m. The patterned silicon waveguides have a width of $\sim 1\mu$m, and height of 900 nm. The buried oxide (BOX) layer below the silicon waveguides has a thickness of 2.2 μm. A microscope image of the photoluminescence emitted from this nanopillar, after filtering out the excitation source ($\lambda = 750$ nm), is shown in top view in Figure 5b. Optical coupling into all four ports is clearly observed.

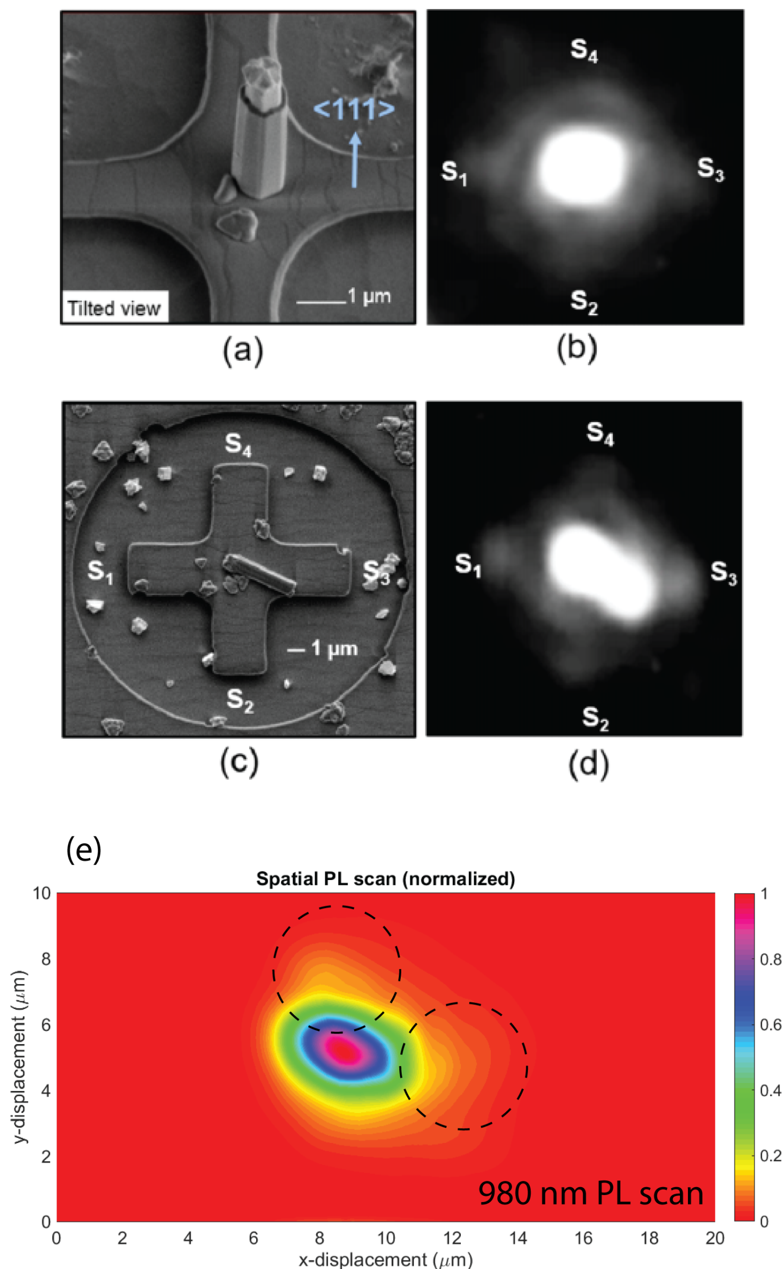

Figure 5.11: Waveguide coupling: These images show waveguide coupling of silicon transparent emission in the nanopillars. (a) Scanning electron microscope (SEM) image of an upright nanopillar with aligned waveguide crossing fabricated post-growth. (b) Photoluminescence (PL) microscope image captured with an InGaAs camera, showing PL emission around 1300 nm from the ends of the waveguides. (c) top view SEM image of a slanted nanopillar again showing PL coupling into waveguides in the camera image of (d). (e) PL intensity map captured by raster scanning a 980 nm excitation laser, showing how a small portion of the laser light is actually coupled into the waveguides and delivered to the nanopillars.

Crossing waveguides were also designed below a slanted pillars in order to create an asymmetry in the structure and highlight another advantaged of this approach. An SEM image from the top view of this structure is shown in Figure 5.11(c). The light emitted from that nanopillar is shown in Figure 5.11(d). Bright emission from the nanopillar can be seen as well as output from the two crossing waveguides all the way to the four output ports: S1, S2, S3, and S4. It is interesting to note that the nanopillar does not need to be upright in order to couple light through silicon waveguide. Furthermore, nanopillars in both configurations are working like a dielectric resonator nanoantenna, composed of active materials, integrated to a dielectric waveguide. The microscope images provide qualitative indication of the coupling of light from nanopillars into waveguides.

In order to obtain more quantitative information, we also performed a 2D spatial scan with a 980 nm laser excitation source. The laser spot (roughly 2μm in size) was raster scanned across a 20 μm field centered around the slanted nanopillar sample. At each location, the spectrum from the nanopillar is measured, and the total PL counts are integrated. The total PL counts are plotted as a function of laser position in figure 5.11(e). This provides an indication of coupling of 980 nm excitation light into the silicon waveguides, and direct excitation of quantum wells. From the highlighted lobes in the image, it can be observed that a small fraction of the light incident on the waveguide ends is actually able to couple in and excite the nanopillar. There are several sources of optical loss in this experiment: loss in the passive waveguide coupling from pump spot into silicon waveguide, absorption of 980 nm pump light in the waveguide, loss in coupling from silicon waveguide to nanopillar and excitation power dependent internal quantum efficiency of the nanopillar. However, it is interesting to note that the counts when the laser spot is placed on the waveguide ends are as much as 10% in intensity compared to when the laser spot is directly on the nanopillar. Further experiments with optimized coupling geometries such as grating couplers and single mode waveguides aligned to position controlled nanopillars have immense promise in demonstrating a high coupling efficiency.

5.6 Regrown Nanocavity Laser

In chapter 2 (nanopillar solar cell), we have described in detail how a regrowth process was used to eliminate shunt paths to the silicon substrate and allow the p-i-n junction to achieve a very low dark current. The total thickness of the secondary growth shell containing the active region was about 200 nm. In addition to eliminating the substrate leakage path, the regrowth shelf can also support optical modes. This becomes particularly useful in the case of InP nanopillars. As described previously, in the InGaAs nanopillars [24], the higher refractive index of InGaAs compared to silicon still allows high-Q modes to be sustained within the nanopillar structure. However, in the case of InP, light tends to leak into the higher index silicon substrate, especially at longer wavelengths. Although lasing has been measured with InP nanopillars grown directly on silicon, it is challenging to find room temperature optically pumped lasers. Additionally, the lasing threshold is typically an order of magnitude higher

than in the case of the InGaAs nanopillars. For instance, Chen *et al.* reported nanopillars with threshold pump fluence on the order of 20-50 $\mu J/cm^2$. However, as described in chapter 6, InP nanopillars grown directly on silicon (inspite of the oxide growth mask) typically have lasing thresholds of the order of a few mJ/cm^2, nearly two orders of magnitude higher than that of the InGaAs nanopillars.

The key benefit of the regrown nanocavity laser is the refractive index mismatch provided by the InP shelf with respect to the surrounding air. Similar to the undercut cavity laser described above, a 200 nm regrowth shelf is expected to be sufficient to allow a high-Q mode to exist. This has been confirmed with intrinsic InP nanopillars grown on a silicon substrate. The lower half of these pillars was then coated with silicon dioxide and amorphous silicon to facilitate regrowth, which was then performed via MOCVD (as described in chapter 2). An exemplary regrown nanopillar is shown in fig. 5.12(a). The rough texture on the lower half of the pillar is due to the amorphous silicon coating to facilitate regrowth. The upper regrown shelf is intrinsic InP and is noticed to be smoother. The lasing characteristics of the nanopillar were measured under room temperature pulsed excitation with a tunable Ti:sapphire femtosecond pulsed laser tuned to a wavelength of 730 nm. The single nanopillar regrown nanocavity laser shows the lasing transition at a low pump pulse fluence of around 10-12 $\mu J/cm^2$, which is an order of magnitude lower than for typical InP nanopillars grown on silicon and similar to the InGaAs nanopillar lasers reported by Chen *et al.* in ref. [24]. The lasing peak is at a wavelength of 870 nm, which corresponds to the room temperature photoluminescence peak of Wurtzite InP. The lasing light-light curve shows a clear non-linear threshold characteristic, as seen in fig. 5.12 (d).

An interesting next step to consider is the incorporation of quantum wells in the regrown nanopillar structure. The high quality factor of the regrowth structure, together with the low transparency current density for the quantum well active region may be a viable path towards room temperature continuous wave lasing. There are two potential options for the placement of the quantum wells: within the original core or within the secondary regrowth. The latter option may be more suitable due to better mode overlap of the high-Q lasing modes in the nanopillar structure. Further, the original growth experiences the high temperature secondary growth, due to which the quantum well morphology may change. It may be beneficial to develop a growth recipe for quantum wells in the regrown portion of the nanopillar.

5.7 Resonant Second Harmonic Generation in Nanopillar Lasers

A second order non-linear polarization density can arise in certain classes of crystalline materials when a suitably polarized electric field is incident. The second order non-linearity corresponds to the case when the complex refractive index is proportional to the electric field. Third order non-linearities in general correspond to the case when the complex refractive

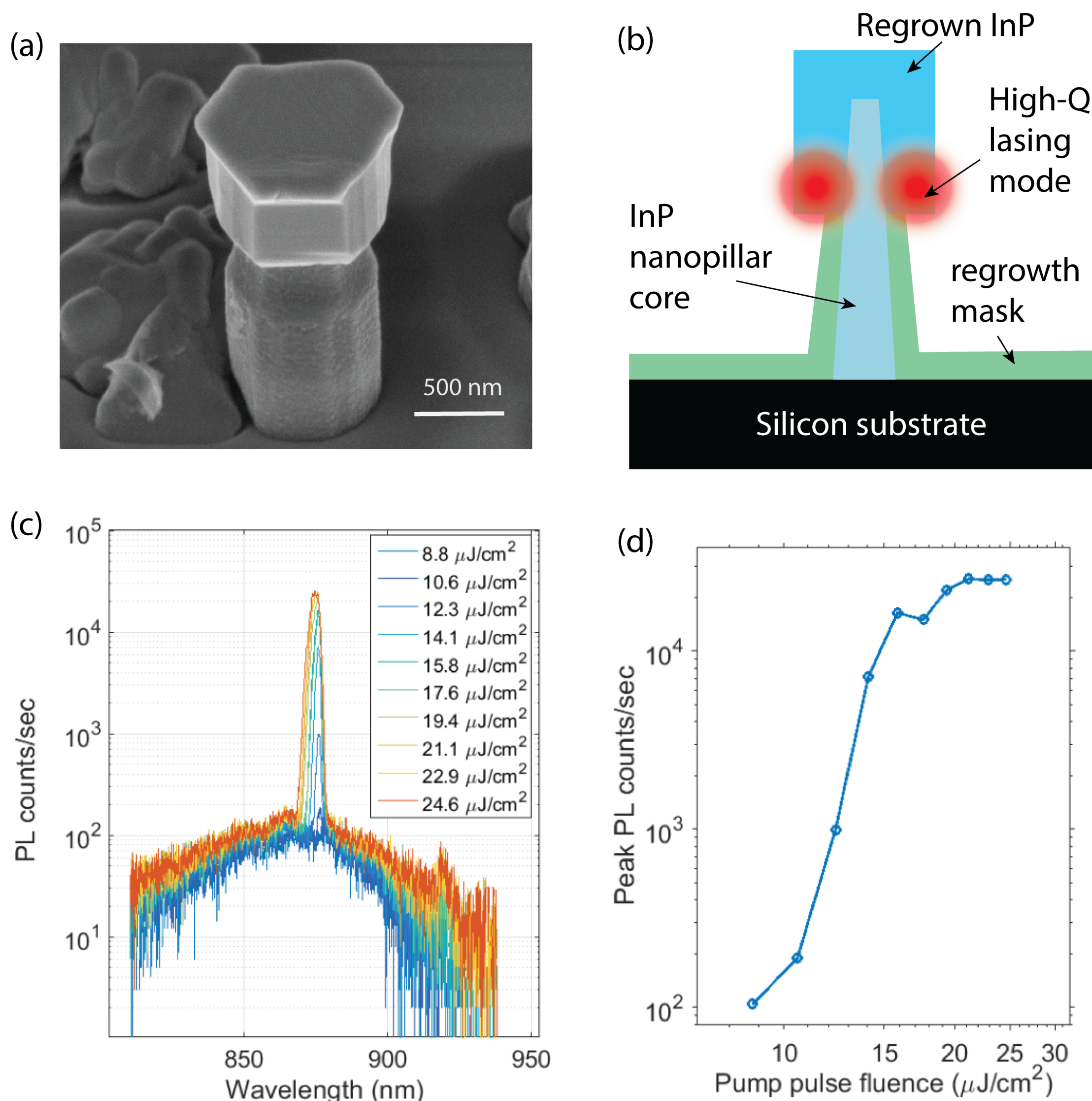

Figure 5.12: Regrown nanocavity laser: (a) Scanning electron microscope image of a regrown laser, without removing the oxide+amorphous silicon regrowth coating. The shelf due to secondary growth on the top portion of the nanopillar is clearly visible. (b) Schematic of the cross section of a regrown nanopillar, showing spatially where the high quality factor mode is expected to be supported. (c) Room temperature pulsed excitation lasing spectra from an exemplary single regrown nanopillar. We note that the lasing threshold pulse energy is an order of magnitude lower than that required for similar InP nanopillars grown directly on silicon. (d) Light-light curve from the data in (c) shows a clear S-shape behavior. The saturation in peak PL counts at high pump excitation power is due to pulse broadening, as observed in (c).

index is proportional to field intensity. There are several important applications for second and third order nonlinearities in optics, and we would like to exploit the unique crystal structure and geometry of the nanopillars to engineer non-linear optical frequency conversion.

We frame the discussion in terms of polarization density for consistency with the convention followed by Boyd [153]. Note that the induced polarization density refers to the volume density of electric dipoles, which can act as current sources to generate electromagnetic radiation. Hence, a nonlinear polarization at a certain frequency and along a certain polarization axis generates a corresponding electric field. A formulation for the non-linear second order polarization density can be expressed in terms of the second order susceptibility tensor χ^2:

$$P_k^{(2)}(-(\omega_1 + \omega_2)) = \epsilon_0 \chi_{i,j,k}^{(2)} E_i(\omega_2) E_j(\omega_1) \tag{5.9}$$

where $P_k^{(2)}$ is the second order polarization along a direction labelled k, and E_i, E_j are the electrical fields along directions labeled i and j respectively. In the Wurtzite crystal structure, we will be referring mainly to the c-axis (nanopillar growth axis: [0 0 0 1]) and the a-axis (degenerate in-plane directions along: [-1 -1 2 0]). Note that the non-linear tensor is an intensive material property and follows symmetry constraints imposed by the crystal. Additionally, it also follows causality constraints expressed in a manner analogous to the linear Kramers-Kronig relations [153].

The formulation in eqn. 5.9 captures several effects in a medium with two elecromagnetic waves with frequencies ω_1 and ω_2, including:

- Sum frequency generation (SFG): electric fields with two smaller frequencies ω_1 and ω_2 produce a polarization with a frequency that equals the sum of the two.
- Second harmonic generation (SHG): A special case of SFG occurs when the two smaller frequencies are equal, and the *second harmonic* of the original frequencies is produced. This is known as second harmonic generation. This can happen from either ω_1 or ω_2 producing double of each respectively. The green laser pointer incorporates a crystal that produces SHG at 532 nm from a 1064 nm laser.
- Difference frequency generation (DFG): fields with one larger frequency ω_1 and one smaller frequency ω_2, produce a polarization with a signal frequency given by the difference of the two frequencies $\omega_1 - \omega_2$. The wave with the smaller of the two original frequencies is also amplified, and may be referred to as the idler frequency. This process is also known as optical parametric amplification, or when it is enhanced by a resonant cavity at the signal frequency, as optical parametric oscillation. Optical parametric oscillators are used to produce tunable infrared coherent light.
- Spontaneous parametric down-conversion: Similar to spontaneous emission, a high frequency photon can decay into photons with lower energy spontaneously. DFG can be considered a stimulated version of this process. Note that spontaneous parametric generation is stimulated by random fluctuations of the vacuum potential, similar to

spontaneous emission. Phase matching requirements typically lead to the condition that the two photons have the same energy, which will be half that of the pump photon energy. Spontaneous parametric down-conversion is predominantly used for entangled photon pair generation, which has applications in quantum communication.

- Electro-optic rectification (EOR): This is a special case of DFG, when the generated polarization is quasi-DC (the two mixed frequencies are equal). This process is used for the generation 0.5-3 THz optical frequency (millimeter wave) using ultrafast laser pulses in a second harmonic crystal.

It is interesting to note that there is a plethora of effects that can arise even from the simple second order non-linearity, as described above. However, a *phase matching condition* is required in order to vector match the propagation directions of the waves involved in the process (conservation of momentum). This typically allows only one of the above processes to dominate. Phase matching can often be achieved in crystals that are birefringent or have been periodically poled so that the propagation vector can be matched in spite of dispersion for different propagating frequencies. We also note that second harmonic and other non-linear effects typically become observable under high power, using a femtosecond pulsed laser source for excitation. Anharmonic deviations from the harmonic oscillator potential (Lorentz oscillator dipole model) will become important when the displacement is of the order of the crystal lattice dimension, or the electric field is of the order of the characteristic atomic field. A more detailed description of this can be formulated in terms of the Miller approximation [153] and provides an order of magnitude estimate for the second harmonic tensor coefficients $\chi^2 \sim 5 - 10$ pm/V.

In addition, we note that crystalline symmetry plays a very important role in second harmonic generation. Centrosymmetric crystals such as silicon and diamond do not exhibit SHG. Amorphous or glassy substances, as well as liquids also do not exhibit second order non-linearities. Even in the case of the Zinc Blende lattice (conventional III/V semiconductors), symmetry considerations only allow the permuted x,y,z tensor components to be non-vanishing. In other words, for the -43m cubic symmetry crystal class (Zinc blende), we have that $\chi^{(2)}_{xyz} = \chi^{(2)}_{xzy} = \chi^{(2)}_{yxz} = \chi^{(2)}_{yzx} = \chi^{(2)}_{zxy} = \chi^{(2)}_{zyx}$ and all the other components vanish. The coordinate system used considers the [100] axis to be the X-axis, [010] to be y and [001] is z. In this case, we carefully note that a single electric field polarized along one of the x,y,z axes will not lead to any SHG. Any fabricated resonant structure to enhance second order effects must consider the crystal alignment to allow interactions.

An interesting feature of the Wurtzite (WZ) crystal structure is its lack of spatial inversion symmetry and anisotropy with respect to the c-axis. This allows for several interesting physical effects to arise in this material that could have important applications. As explained above, some of these effects are quite difficult to observe in Zinc Blende (ZB) phase III/V compound semiconductors. In particular, piezoelectricity and second order nonlinear optics such as second harmonic generation are challenging to observe in non-centrosymmetric materials. In the same notation as above where the Z-direction refers to the c-axis, the

non-vanishing components of the second harmonic tensor can be writtens as (Wurtzite 6mm crystal symmetry class):

1. $\chi^{(2)}_{xzx} = \chi^{(2)}_{yzy} = \chi^{(2)}_{xxz} = \chi^{(2)}_{yyz} = \chi^{(2)}_{zxx} = \chi^{(2)}_{zyy} = \chi^{(2)}_{aca} = \chi^{(2)}_{caa}$
2. $\chi^{(2)}_{zzz} = \chi^{(2)}_{ccc}$

Note that the first index refers to the polarization direction of the output field and the two other indices refer to the polarizations of the input. In writing the first equation above, we have made use of Kleinman symmetry, neglecting the dispersion of the susceptibility. In case the second harmonic also shows dispersion (two photon absorption and other material resonances), the $\chi^{(2)}_{zxx}$ and $\chi^{(2)}_{zyy}$ terms will be different.

In what follows, we describe how second harmonic generation can be easily observed in InP-based nanopillars. The polarization of the second harmonic is consistent with what is expected from the Wurtzite crystal symmetry, as described above. Further, we make the remarkable observation that in two different nanopillar laser cavities, *internal second harmonic generation* is observed. This refers to the case in which the second harmonic of the lasing wavelength is also generated from the cavity, and arises due to the high intra-cavity optical power in the nanopillar laser. This is the technique used to generate coherent green light in the ubiquitous green laser, and is also a completely novel observation for a nanolaser.

Before we investigate the internal, resonance-enhanced second harmonic generation effect, we would like to characterize the external second harmonic generation from the pump light. It is interesting to perform this measurement in a polarization resolved manner, so that the second harmonic tensor components can be verified with theoretical predictions based on symmetry considerations [154], [153]. The optical setup for performing this measurement is shown in fig. 5.13. The pump wavelength was chosen to be 830 nm due to the availability of optical elements to control polarization. The output from the femtosecond pulsed laser was polarized, with the polarization angle continuously controlled using a rotary half wave plate. In this manner, full control of the incident polarization was maintained.

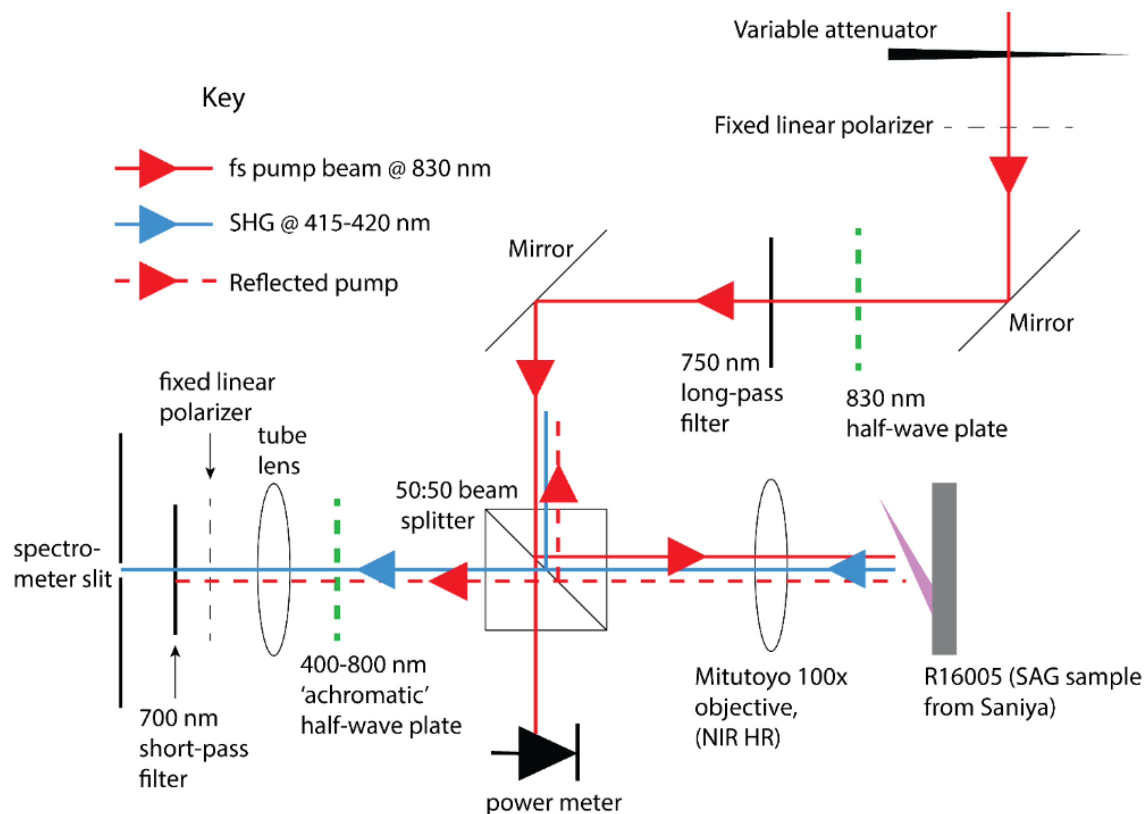

Figure 5.13: Second harmonic measurement setup: This setup was used to measure direct second harmonic generation of the excitation laser. Half wave plates were used to control both the illumination and output polarization, as explained in the text.

The output second harmonic light was transmitted into the spectrometer while rejecting the pump light using a short-pass filter. The second harmonic polarization was analyzed using a linear polarizer placed at the input to the spectrometer. In order to make quantitative measurements, it is important to keep the polarization at the input to the spectrometer fixed, since the grating efficiency is different for transverse electric and transverse magnetic polarized light. The linear polarizer at the spectrometer input slit serves to maintain a fixed input polarization at the entrance slit. However, an achromatic half wave plate before the tube lens in the optical path allows us to rotate the polarization axes of the second harmonic light and fully analyze the output polarization as well. Thus, we are able to control both the input polarization as well as the output in a continuous manner. The output polarization needs to be measured only for the two perpendicular polarization axes in order to completely analyze it. However, the input polarization needs to be carefully controlled since the second harmonic efficiency depends on the orientation of the input electric field with respect to the nanopillar crystal axes.

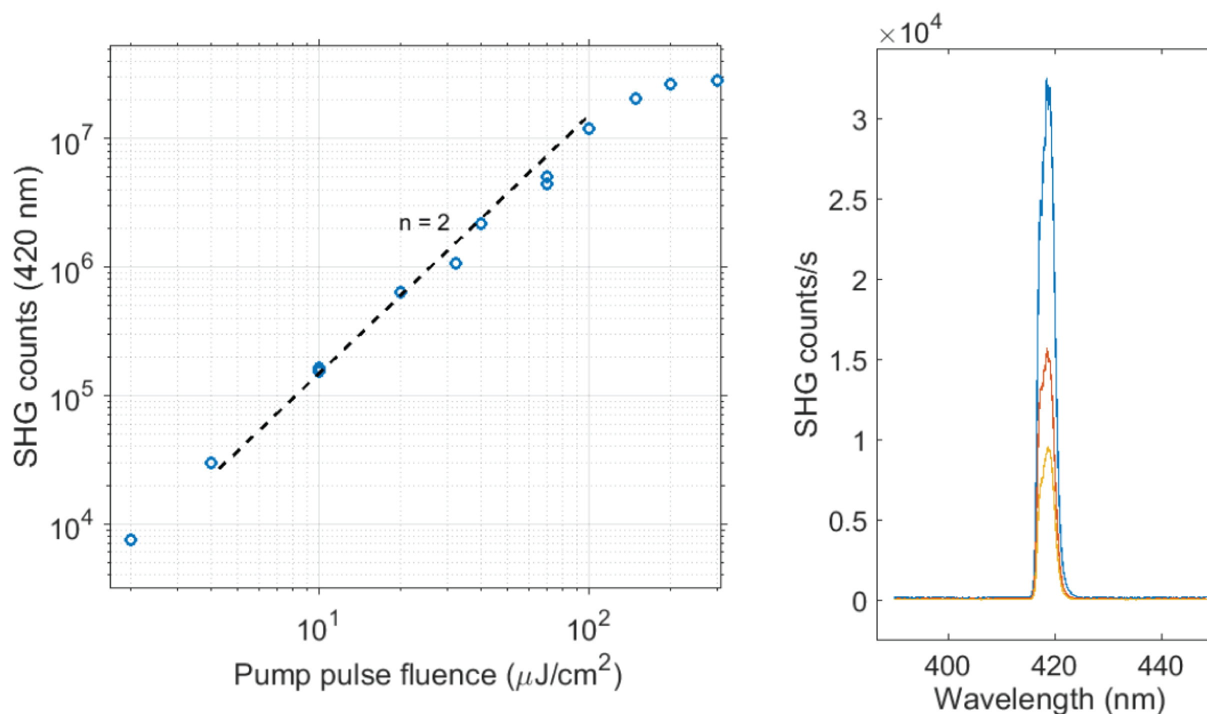

Figure 5.14: SHG from pump: (left) light-light curve of 420 nm output as a function of pump pulse fluence at 840 nm showing a quadratic dependence, (right) spectrum of second harmonic generation from the 840 nm femtosecond laser

Measuring the excitation power dependent second harmonic output counts reveals a quadratic intensity dependence, as shown in fig. 5.14(a). The second harmonic output wavelength is at 420 nm, which is roughly half the incident wavelength, as expected from photon energy doubling. While the efficiency for second harmonic generation is typically quite low, it is notable that significant counts can be measured in spite of the strong attenuation of 420 nm wavelength light in the InP nanopillar.

In order to further confirm that this is bulk second harmonic generation from the InP nanopillar, as opposed to surface effects or other phenomena, we completely measured the polarization dependence of second harmonic counts in the nanopillar. Two exemplary pillars were measured: one was slanted (nearly horizontal) and the other was upright. The 830 nm pump was linearly polarized and this polarization was continuously varied across 180 degrees using a half wave plate as depicted in fig. 5.13. For each configuration, the output second harmonic polarization was measured for two perpendicular orientations, thus completely determining the output polarization. The results for the polarization resolved measurements are described in 5.15.

When analyzing the case when the output polarization is maintained parallel to the c-

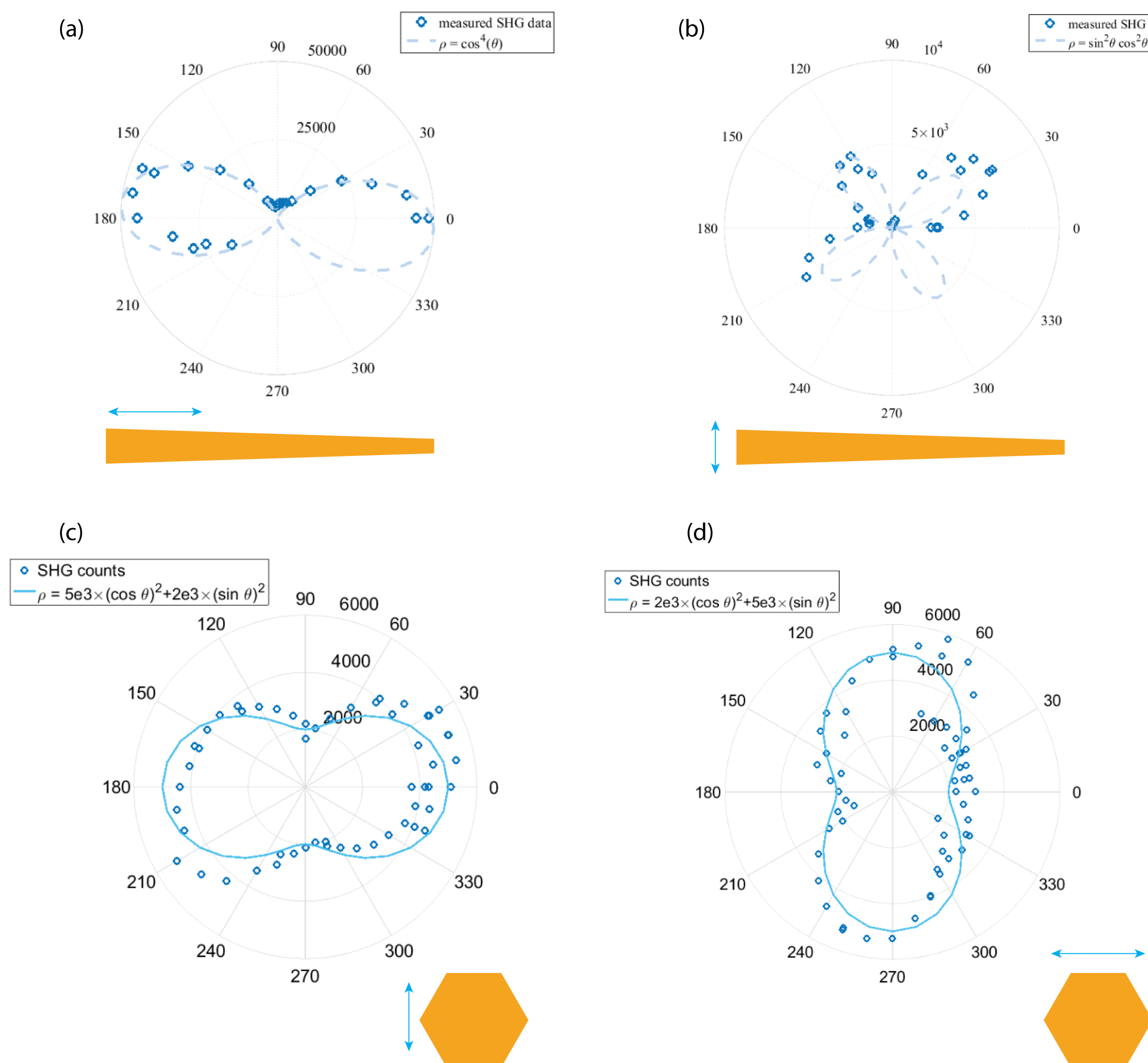

Figure 5.15: Second harmonic polarization: These polar plots were obtained by varying the excitation laser polarization for a fixed output polarization, using the setup depicted in figure 5.13. (a) SHG output is analyzed at a polarization parallel to the pillar, while the excitation polarization is rotated using a half wave plate. The polar plot angle is with respect to the growth axis of the pillar. The data very closely follows what is theoretically expected from the Wurtzite second harmonic tensor. Note that measuring over 180 degrees is sufficient, but a few more measurements were carried out for consistency. (b) Here, the SHG output is analyzed in an orientation perpendicular to the growth axis of the pillar. (c) and (d) Similar measurements on an upright pillar, for the orientation shown below each.

axis or equivalently growth axis in the slanted pillar case (fig. 5.15(a)), we note that the expected intensity variation (from the SHG tensor elements) is:

$$I_c = (\chi^{(2)}_{ccc} cos^2\theta + \chi(2)_{caa} sin^2\theta)^2 I_{in}^2 \tag{5.10}$$

where I_{in} is the incident field intensity, and θ is the angle of the input polarization with respect to the c-axis of the nanopillar. From fig. 5.15 (a) we note that the dependence is predominantly $\sim cos^4\theta$, indicating that the $\chi^{(2)}_{ccc}$ tensor element is significantly larger than the $\chi^{(2)}_{caa}$ term. This is also consistent with the polarization dependence reported by Chen *et al.* in ref. [155].

When the output polarization is analyzed perpendicular to the c-axis, the expected dependence is (fig. 5.15 (b)):

$$I_a = (\chi^{(2)}_{aca} sin\theta cos\theta)^2 I_{in}^2 \tag{5.11}$$

which is consistent with the variation noted in the figure. We also emphasize that the second harmonic tensor component $\chi^{(2)}_{ccc}$ seems to be the most important, with the greatest counts for both output and input along the c-axis of the nanopillar. In order to qualitatively confirm this, we also measured an upright nanopillar, such that the field component along the c-axis (longitudinal direction of beam propagation) is nearly zero. The SHG counts are rather low in this orientation, and the polarization dependence on the in-plane electric field polarization direction is quite weak. This is shown in the lower panel of fig. 5.15.

In a previous section, we have described how the nanopillar cavity with a silicon undercut has a high quality factor and shows lasing at 1200 nm under pulsed excitation. We also observed second harmonic generation from the undercut nanopillar cavity. Surprisingly, the second harmonic generation effect we are going to describe was observed from the cavity lasing wavelength rather than the pump wavelength. As observed in fig. 5.16(a), the spectrum shows a second harmonic tone of the cavity lasing wavelength. The integrated counts at 600 nm are graphed against the integrated counts at the lasing wavelength of 1200 nm, clearly showing a quadratic dependence in fig. 5.16(b). Additionally, the polarizations of the lasing mode and second harmonic light have been analyzed in the lower panel (fig. 5.16(b)). The in-plane component of the lasing mode is radially polarized, as can be seen from the polarized lobe patterns in the top panel. The arrows indicate the polarization directions being analyzed in each image. The images for the lasing wavelength were captured on an InGaAs camera. Corresponding to each polarization for the lasing mode, we also measured the polarization image of the second harmonic light on a silicon CCD array. The lobes for the second harmonic are complementary to that of the lasing mode, which is consistent with a radial polarization for the second harmonic light. Note that this orientation of the nanopillar does not reveal information about the axial field components (c-axis), which are expected to be more important for SHG. This experiment was carried out at a low temperature of 4.2 K and under pulsed excitation of the laser with a femtosecond pulsed laser tuned to 980 nm.

The regrown nanopillar laser also exhibits internal second harmonic generation from its lasing wavelength around the InP bandgap of 870 nm. The lasing characteristics of the

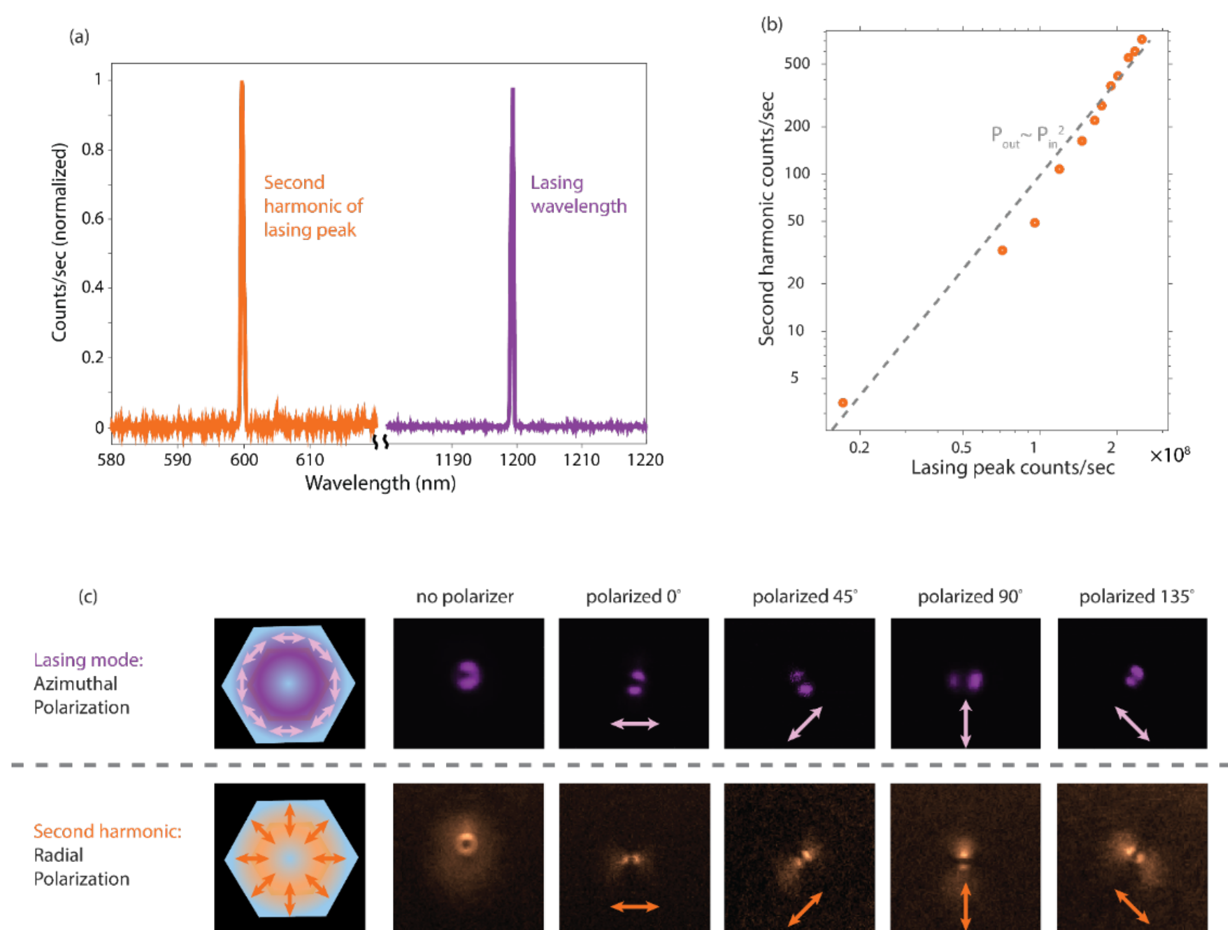

Figure 5.16: Resonant SHG from QW nanopillar: Experimental data for undercut laser showing resonance enhanced second harmonic from the lasing wavelength of the pillar (a) Lasing and SHG spectra from an exemplary undercut nanopillar. (b) light-light curve of the SHG output counts vs. the lasing counts shows a quadratic dependence. (c) Polarization analysis of the lasing mode (top panel) and second harmonic light (bottom panel) shows that the former is azimuthally polarized whereas the latter is radially polarized.

regrown nanopillars have been described above in fig. 5.12. The second harmonic generation effect in the regrown nanopillars could be observed from multiple individual nanopillars, at room temperature under pulsed excitation at 730 nm. In ever such regrown nanopillar laser, the second harmonic wavelength was half the lasing wavelength, as shown in fig. 5.17(a). In spite of the strong attenuation of the 430 nm light, substantial counts could still be observed. The lasing spectrum is broadened since it is a pulsed laser. Corresponding to the lasing wavelength, the second harmonic is also observed in the lower panel.

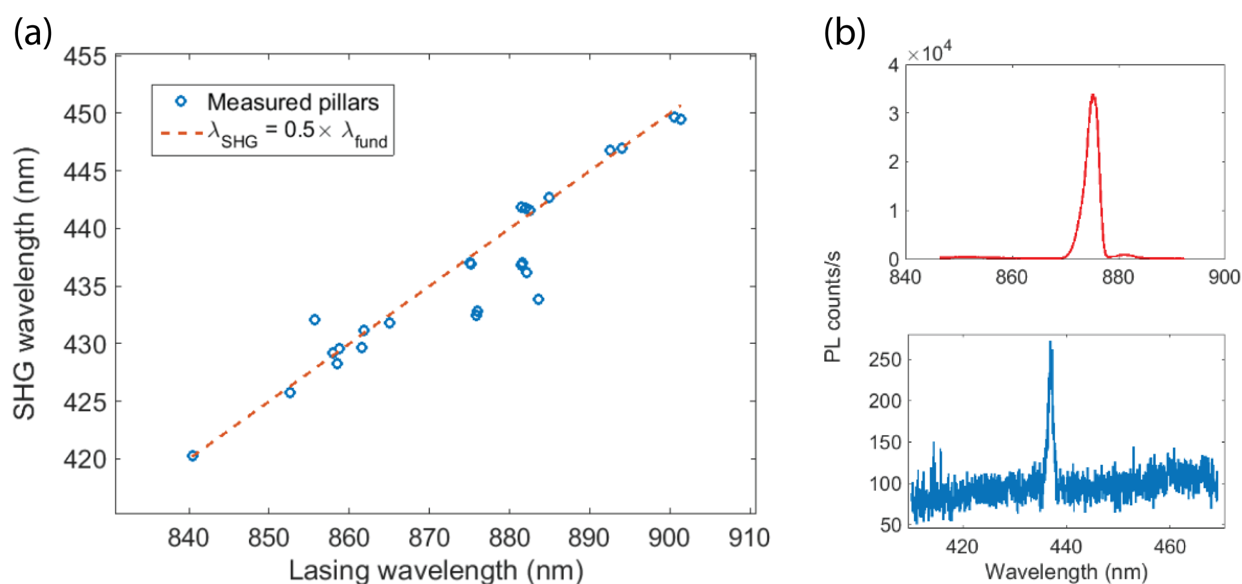

Figure 5.17: Resonant SHG from regrown nanopillars: (a) Plot of resonant second harmonic wavelength against fundamental lasing wavelength for multiple individual regrown nanopillars exhibiting internal SHG (all at room temperature and under pulsed excitation), (b) Lasing spectrum (top) and resulting SHG spectrum (bottom) from an exemplary regrown nanopillar showing resonant second harmonic generation.

In summary, we report two long-wavelength QW-in-nanopillar laser configurations, both monolithically grown on silicon and with subwavelength footprint. InGaAs quantum well (QW) active gain material is obtained for the first time on InP nanopillars with various Indium composition and thickness to tailor emission wavelength. The optical material quality was verified to be on par with III-V epitaxial QWs, using the transparency power density and luminescence yield as metrics. Due to the unique 3-dimensional core-shell growth mode, the nanopillar can scale in diameter up to a micrometer size, leading to sufficient optical confinement and modal gain at long wavelengths. We demonstrated two different methods to fabricate optical resonators monolithically on silicon-based platforms. A selective silicon etch has been used to define an undercut nanopillar cavity with quality factor higher than

103 while maintaining subwavelength footprint. This undercut cavity laser operates up to room temperature, and displays a high laser characteristic temperature T_0 of 128 K. Further, the undercut cavity nanolaser exhibits an internal non-linear generation effect, allowing the second harmonic of the cavity lasing wavelength to be generated. This has also been conirmed with high-Q regrown nanocavity lasers. These results could open up opportunities in designing novel high-Q nanoresonators, as well as in studying the physics of non-linear generation in these laser cavities. In particular, it may be interesting to exploit the strong second harmonic non linearity to generate spontaneously down converted photons from the high energy lasing wavelength. A strong source of spontaneous down conversion would be very useful for generating entangled photon pairs for quantum optics experiments and quantum communication.

Chapter 6

Position Controlled 1.5 μm Nanopillar LEDs

Highly compact III-V compound semiconductor active nanophotonic devices integrated with silicon are important for future low power optical interconnects. One approach towards realizing heterogeneous integration and miniaturization of photonic devices is through nanopillars grown directly on silicon substrates. However, to realize their full potential, the integration of nanopillars with silicon-based electronics must be made scalable via precise control of the nanopillar growth site and dimensions. In this chapter, we focus on electrically-pumped InGaAs/InP multi-quantum-well (MQW) light emitting diodes (LED) using both individual nanopillars and nanopillar arrays grown directly on a Si substrate with site control. The pillars are connected monolithically with the silicon substrate, and devices are processed without transferring to another substrate, such that current conduction is directly through the silicon. The growth occurs via catalyst-free, low-temperature metal organic chemical vapor deposition, which is CMOS post process compatible. We report excellent optical properties, including long minority carrier lifetimes and room-temperature lasing under optical excitation. InGaAs/InP quantum wells are incorporated in the nanopillars in a core-shell growth mode, to obtain silicon transparent emission at a wavelength range of 1450-1550 nm with high internal quantum efficiency ($\sim$30%). Despite the small LED footprint, a high output power (4 μW) was measured, and the device could be electrically biased beyond the transparency condition to produce optical gain. CMOS-compatible site-controlled growth and electrically driven long-wavelength emission make the InP nano-LED an ideal component in advanced photonic integrated circuits.

Our group has previously reported InGaAs and InP nanoneedle or nanopillar structures on silicon substrates, grown at low-temperature (400450°C) by metalorganic chemical vapor deposition (MOCVD) [36], [37] [24], [29], [76], [31]. The growth condition was verified to be back-end-of-line CMOS compatible [25]. The coreshell growth mode allows scaling up the diameters beyond lattice-mismatched critical dimensions, while still maintaining single crystallinity [36]. Due to their micron-scale dimensions, these structures do not suffer from the debilitating effects of surface recombination commonly seen in nanowires. InP nanopil-

lars, in particular, exhibit a very low surface recombination velocity of 1100 cm/s, which is comparable to InP bulk [37].

Due to these unique properties, InP nanopillars have shown remarkable material and device performance in the form of optically pumped lasers [36], [26], photodetectors [39] and solar cells [38]. However, for truly seamless and scalable integration of InP photonic devices on silicon, it is imperative to grow InP nanopillars at predetermined locations. Additionally, randomly nucleated nanopillars suffer from indeterminate variations in their morphology and structural properties, which ultimately affects uniformity of device characteristics. Note that some of these variations are due to the physical placement, packing of nanopillars and precursor competition effects - which will be identified when we are able to control these parameters. Stated more broadly, position controlled growth will allow for a systematic study of the properties of the nanopillars. Previous reports of selective area growth on silicon have relied on gold nanoparticle catalysts or high growth temperature (usually greater than 550°C) [156], [157], both of which are completely incompatible with CMOS back-end process requirements. There have also have been several reports of site-controlled epitaxy of InP nanostructures on expensive native InP substrates [158], [78].

Here, we describe the first site-controlled growth of high-yield, uniform arrays of InP nanopillars on silicon, grown under CMOS compatible conditions: low temperature and without gold catalysts. The structural properties such as taper angle and nanopillar diameter are functions of MOCVD growth conditions. Excellent optical properties were verified through micro-photoluminescence and time resolved photoluminescence measurements. Some of these details have already been described in chapter 2 (section: Position controlled solar cells).

Additionally, in order to achieve silicon transparent emission from the nanopillars, InGaAs/InP quantum wells were grown in the core-shell mode. It has been found that photoluminescence from the InGaAs multi-quantum wells is a systematic function of the nanopillar period/pitch, which adds another degree of freedom to control emission wavelength - beyond explicit growth parameter variation. The InGaAs/InP quantum wells in the nanopillars were investigated through temperature and pump dependent photoluminescence, which reveals bright, efficient and sharp emission. Finally, nanopillar based multi-quantum well LEDs were successfully grown and fabricated using an all optical-lithography process, with electrical conduction directly through the silicon substrate. Nanopillar LEDs exhibit radiative dominant electroluminescence around 1500 nm with high output power (4 μW), despite their small footprint. The details are described in the following sections.

6.1 Growth of Position Controlled Nanopillar Devices

Position controlled growth of InP nanopillars on [111] silicon is achieved using a silicon dioxide growth mask. Approximately, 140 nm of silicon dioxide is deposited on a clean silicon wafer by low temperature (350 °C) plasma enhanced chemical vapor deposition (PECVD). Nanoscale apertures (~320 nm diameter) are defined in the oxide using deep ultraviolet

lithography. The photoresist is then removed using oxygen plasma and PRS 3000 solvent. The 6-inch wafer is diced into 1 cm^2 pieces, which fit the MOCVD substrate platters. Reactive ion etching is used to etch the oxide and access the Si substrate. The growth mask contains apertures with the pitch varying from 1 μm to 40 μm. Prior to loading the substrate in the MOCVD, the silicon surface is chemically roughened using tetramethyl ammonium hydroxide (TMAH), and deoxidized using dilute-buffered hydrofluoric acid (BHF). Prior to growth, the chips are thoroughly cleaned and treated to heated TMAH at 80C. Finally the substrate is deoxidized using 1:10 dilute BOE and immediately loaded in the Emcore D75 MOCVD reactor. In the MOCVD chamber, the substrate is first heated in a tert-butylPhosphine ambient before initiation of growth.

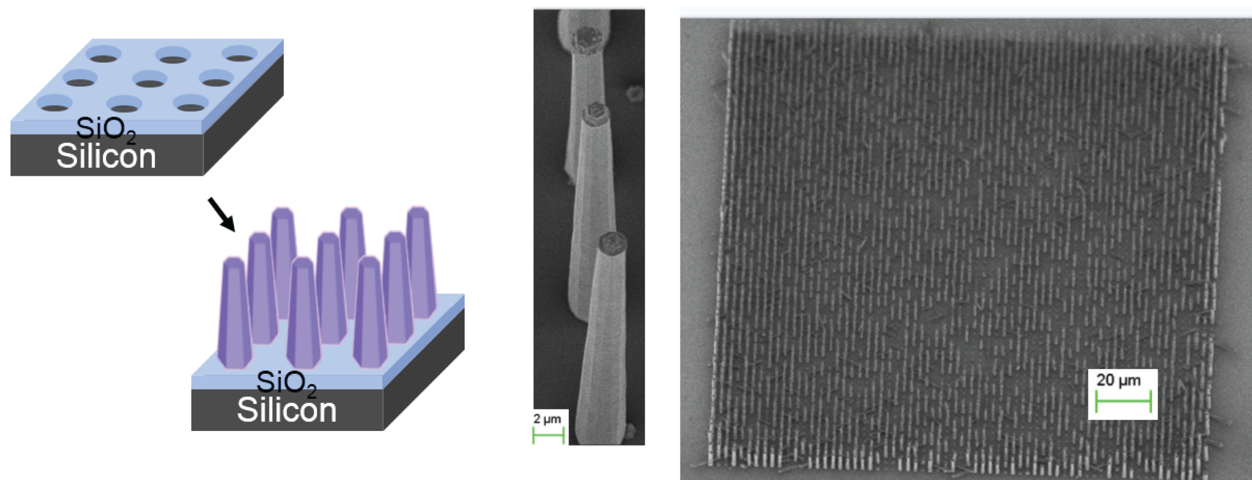

Figure 6.1: Selective area growth of nanopillars: (left) schematic showing growth process, starting with lithographically defined nucleation positions. (right) Scanning electron microscope image of position controlled array of nanopillars, showing the regular placement of the pillars. The inset shows a closeup of a few individual nanopillars from the array.

Nanopillars are grown under a typical hydrogen carrier gas flow of 12 liter/min, tert-Butylphosphine (TBP) mole fraction of 5.86E-4, and Trimethylindium (TMIn) mole fraction of 5.7E-7. Quantum wells are grown by switching off the TBP flow and switching on tertiary butyl arsine (TBA) (mole fraction 3.2E-4), and triethylgallium (TEGa). For impurity doping, diethylzinc (DeZn) and diethyltellurium (DeTe) were used with molar fractions of approximately 1E-8 for nominal doping levels of $\sim 10^{17}\ cm^{-3}$ in both cases. In the LED structure, a final layer of highly ($\sim 10^{18}\ cm^{-3}$) doped p-InGaAs is grown as a contact layer. The growth process and scanning electron microscope images of grown nanopillars with quantum wells inside have been shown in figure 6.1. An initial transmission electron microscope study of these nanopillars has also been performed in order to obtain a more detailed

look at the various interfaces. Firstly, we note that the aperture in the oxide is significantly smaller than the final diameter of the nanopillar. Thus, the nanopillar has a significant part of the base in contact with the oxide below. A high resolution TEM study on a nanopillar cross section has indeed revealed that the base continues to be somewhat defective (although crystalline), whereas the main body of the nanopillar is largely free of defects.

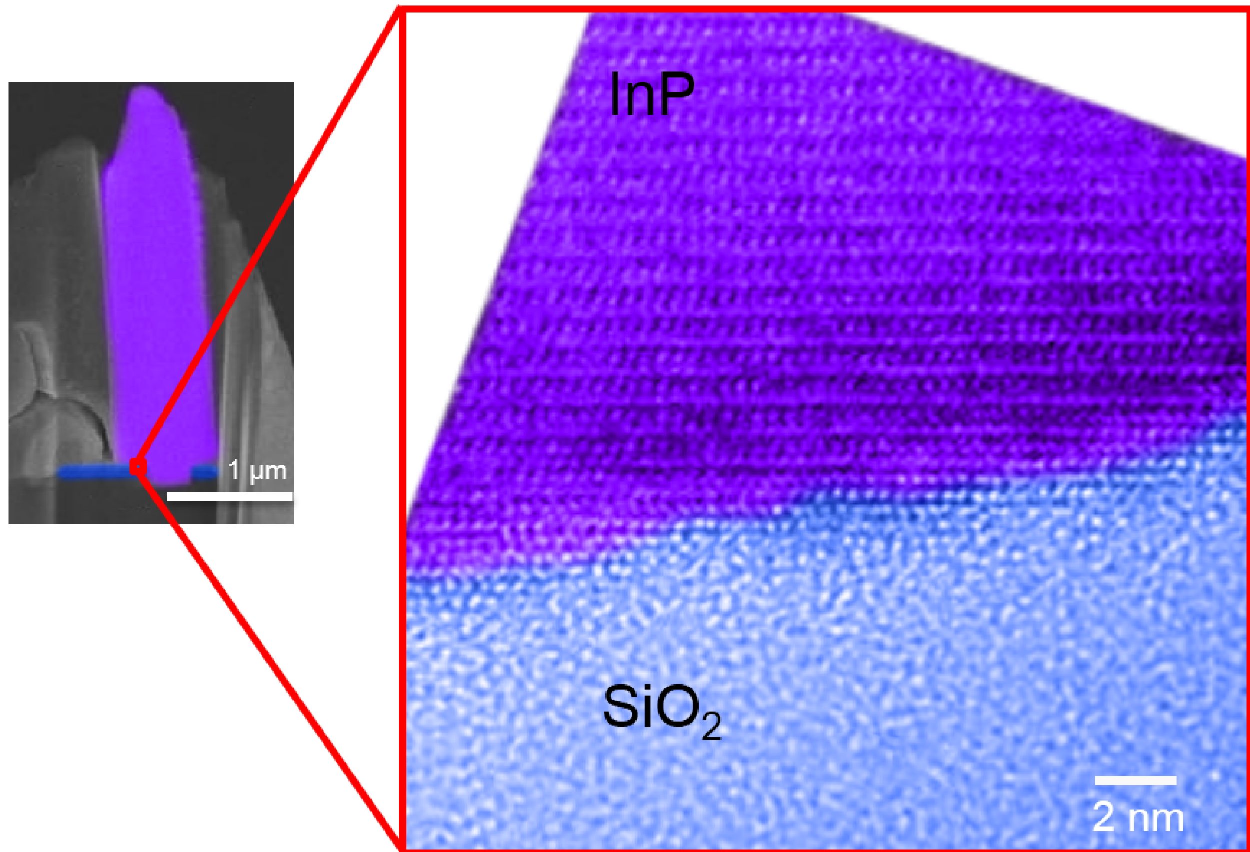

Figure 6.2: TEM image showing the interface of the silicon and oxide: the crystal lattice is shown in the high resolution TEM image in the inset, with the transition from the amorphous oxide to crystalline InP clearly visible.

6.2 Optical Characterization

Excellent optical material quality of the site-controlled InP nanopillars is confirmed by photoluminescence measurements on as-grown pillars on the silicon substrate. Figure 6.3 (a) shows room temperature PL spectra measured from a single nanopillar grown at 460°C, for increasing excitation intensities of a continuous wave (CW) 660 nm pump. The strong peak at 1.42 eV corresponds to Wurtzite InP and remains invariant with excitation intensity. No

secondary peaks related to defects or polytypism were observed in the excitation dependent spectra. The emission linewidths from site-controlled nanopillars were typically around 50 meV, which is comparable to emission observed from spontaneously grown pillars, as shown in Fig. 6.3(b). The exponential tails, as clearly observed from the PL spectra in Fig. 6.3(a) correspond to the Boltzmann tail (high energy tail) and Urbach tail (low energy) respectively. We conclude that the presence of the silicon dioxide growth mask does not lead to formation of defects or polytypism in the nanopillar, and the material quality is equivalent to previously demonstrated, state-of-the-art InP nanopillars.

Time resolved photoluminescence (TRPL) was measured using femtosecond pulsed laser excitation at 680 nm and the data is analyzed using a monoexponential model (Fig. 6.3(c)). The TRPL measurement was used to probe the carrier decay rate by incorporating a triggered avalanche photodiode (APD) into the micro-photoluminescence setup. The measurement was carried out on a single nanopillar at a time. The exponential PL decay reveals room temperature lifetime in the range of 1.5-3.7 ns. As shown in the inset of Fig. 6.3(c), the lifetime increases with incident excitation and reaches a maximum value of 3.7 ns, following that it decreases again due to enhanced non-radiative recombination rate associated with Auger recombinations. The lifetime values are comparable to those measured in spontaneously nucleated InP nanopillars, which have previously showed a record long lifetime in the range of 2-7 ns [37]. Such a long room temperature minority carrier lifetime points towards excellent optical properties, low defect density and a low, surface recombination velocity. The key metric is that the radiative recombination lifetime tends to be on the order of 5-10 ns under high injection. Thus, a minority carrier lifetime approaching this is highly promising for internal luminescence efficiency. We estimate the surface recombination velocity to be of the order 1000 cm/sec.

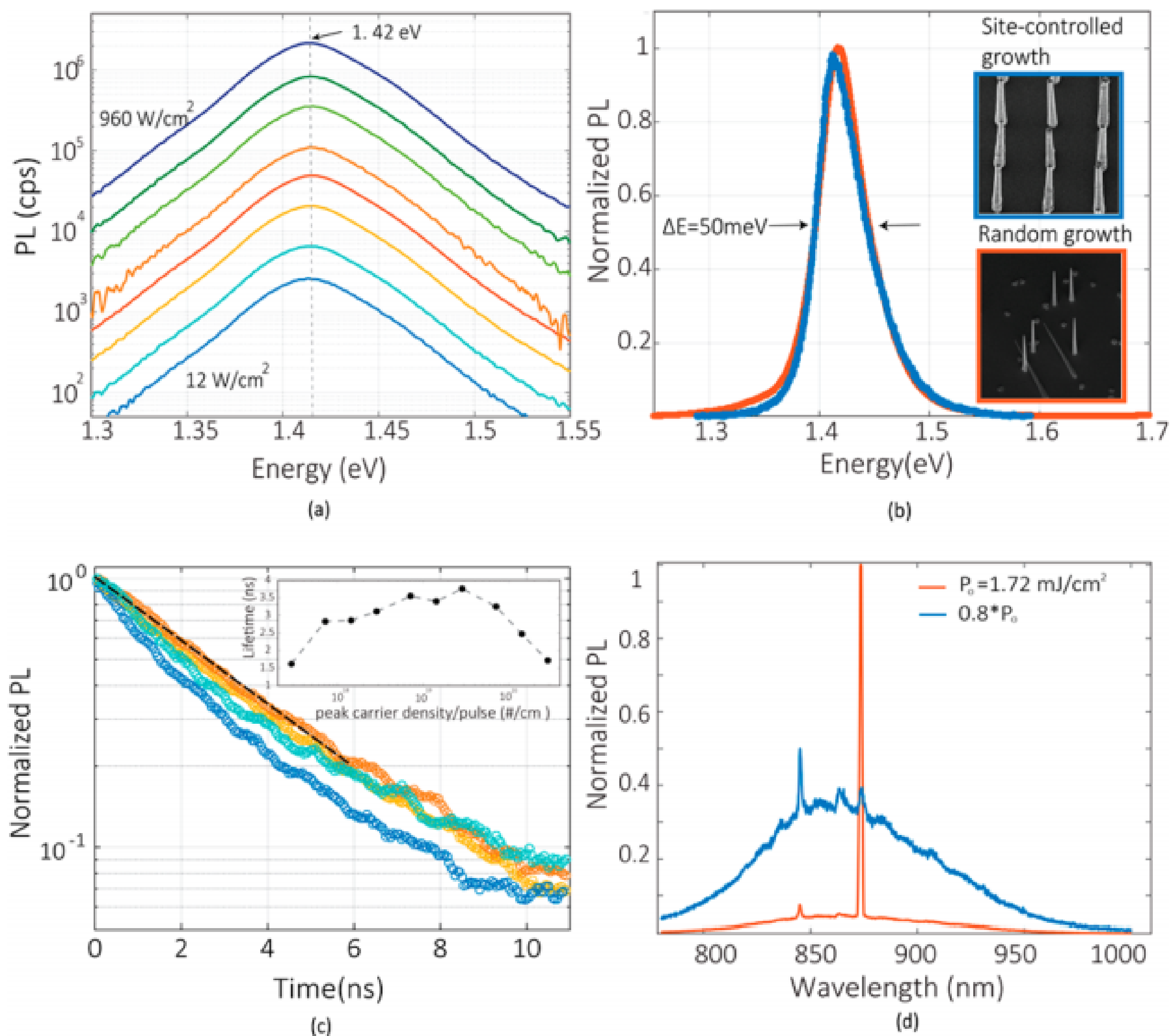

Figure 6.3: PL from InP position controlled nanopillars: (a) Excitation power dependent spectral series for an individual InP nanopillar, showing expected Wurtzite peak at 1.42 eV and exponential tails in the PL spectrum, (b) Comparison of PL spectral lineshape of randomly nucleated and selectively grown nanopillars, showing similarity. (c) Time resolved photoluminescence from an exemplary individual undoped InP nanopillar showing a good minority carrier lifetime on the order of 3-4 nanoseconds, (d) Room temperature pulsed lasing characteristic of an exemplary individual InP nanopillar, showing clear lasing transition below and above threshold.

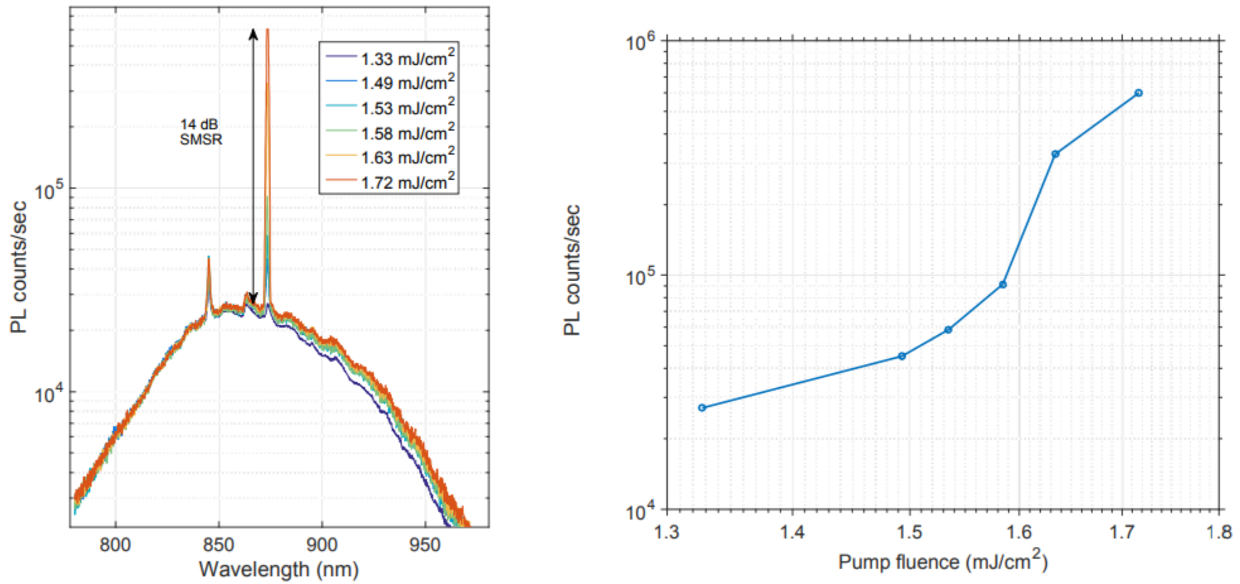

Figure 6.4: RT, pulsed lasing of SAG nanopillar: (left) Excitation pulse energy dependent lasing spectral series showing that the nanopillar laser exhibits a clear transition at about 1.5 mJ/cm^2. (right) Lasing S-curve (log-log scale L-L curve) showing a sudden increase in peak counts above lasing threshold.

Each as-grown nanopillar behaves as an optical cavity and supports helically propagating resonances[24], [159]. The modes are well-confined inside the cavity due to its micron-scale size, which allows large gain-mode overlap. As a result, we observe lasing in as-grown single nanopillars. Figure 6.3(d) demonstrates the spectra obtained when a single nanopillar is pumped optically by titanium-sapphire femtosecond laser at 750 nm. Below threshold, broad spontaneous emission is observed. A strong lasing peak at 873.5 nm dominates emission above threshold with a sideband suppression ratio of 14 dB. A transition from spontaneous emission to single mode lasing is observed at 1.6 mJ/cm^2 at room temperature, as shown in figure 6.4. The linewidth collapses to 1.5 nm and Q-factor of the nanopillar cavity can be estimated to be $Q \sim \delta\lambda/\lambda_{th} \sim 530$. While this value is not equal to the cold-cavity quality factor, it still provides a useful metric of the cavity's optical finesse.

We have also used the calibrated luminescence technique as described in ref. [40] to determine the absolute brightness and quasi Fermi level split in an exemplary undoped nanopillar. This was also compared with a reference undoped nanopillar grown through the random nucleation method on a [111] silicon substrate. The reference nanopillar and position controlled nanopillar both have similar 1 sun Fermi level splitting of 0.85-0.9 eV, which is comparable to that reported by Tran *et al.* The ideality factor (exponential dependence of light output) is also between 1 and 2 for the new position controlled growth as well as the original spontaneously nucleated growth. The calibrated L-L curve has been shown in figure 6.5.

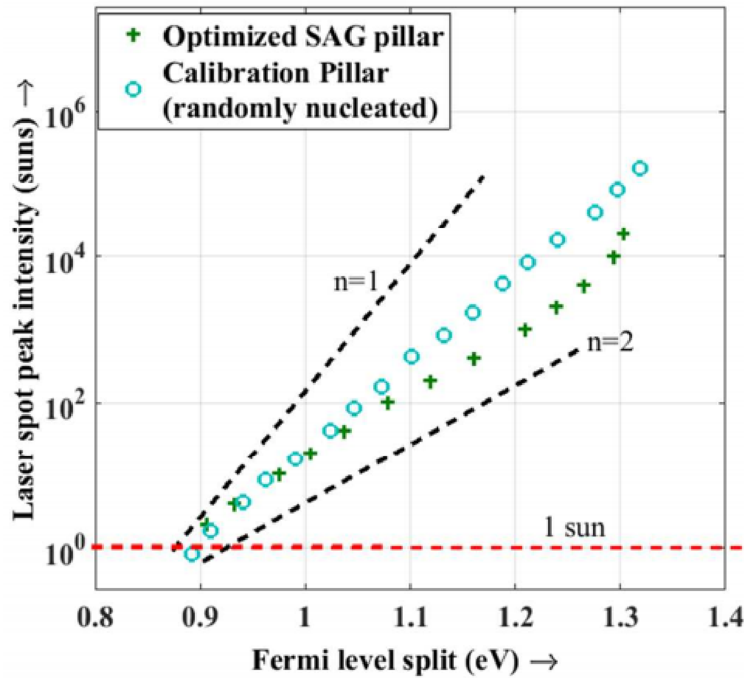

Figure 6.5: Absolute Luminescence counts: it is important to compare the absolute brightness of the selectively grown nanopillars with that of the randomly nucleated nanopillars. This shows that the Fermi level split for the selectively grown and randomly nucleated pillars is somewhat comparable, although the selectively grown pillars were typically slightly larger than the randomly nucleated nanopillars.

For a silicon photonics optical link, the light emitter should operate in the silicon transparent regime, ideally in the 1310-1550 nm range. This allows the generated photons to be guided and manipulated across a silicon chip using silicon based waveguides and modulators. We achieved silicon transparent emission by incorporating core-shell InGaAs/InP quantum wells in the site-controlled nanopillars. Quantum well growth is achieved by switching MOCVD precursors from TMIn and TBP to TMIn, TeGa and TBAs, while maintaining group V overpressure throughout. The growth of the multiquantum (MQW) well stack is carried out at 455°, in the same growth mode as the n-InP core. The high optical quality of MQW growth is confirmed through non-resonant micro-photoluminescence measurements on a single nanopillar. Pump light at 660 nm is used to excite electron-hole pairs in the InP cladding, which are then rapidly captured into the quantum well. Pump dependent PL measurement from a single nanopillar with five MQW shows emission in the silicon transparent wavelength range is shown in Fig. 6.6(a). No shift in emission wavelength or emergence of secondary peaks was observed with increase in pumping.

The superior optical quality of the InGaAs quantum wells is attested by internal quantum efficiency of 30% measured from temperature dependent photoluminescence measurements.

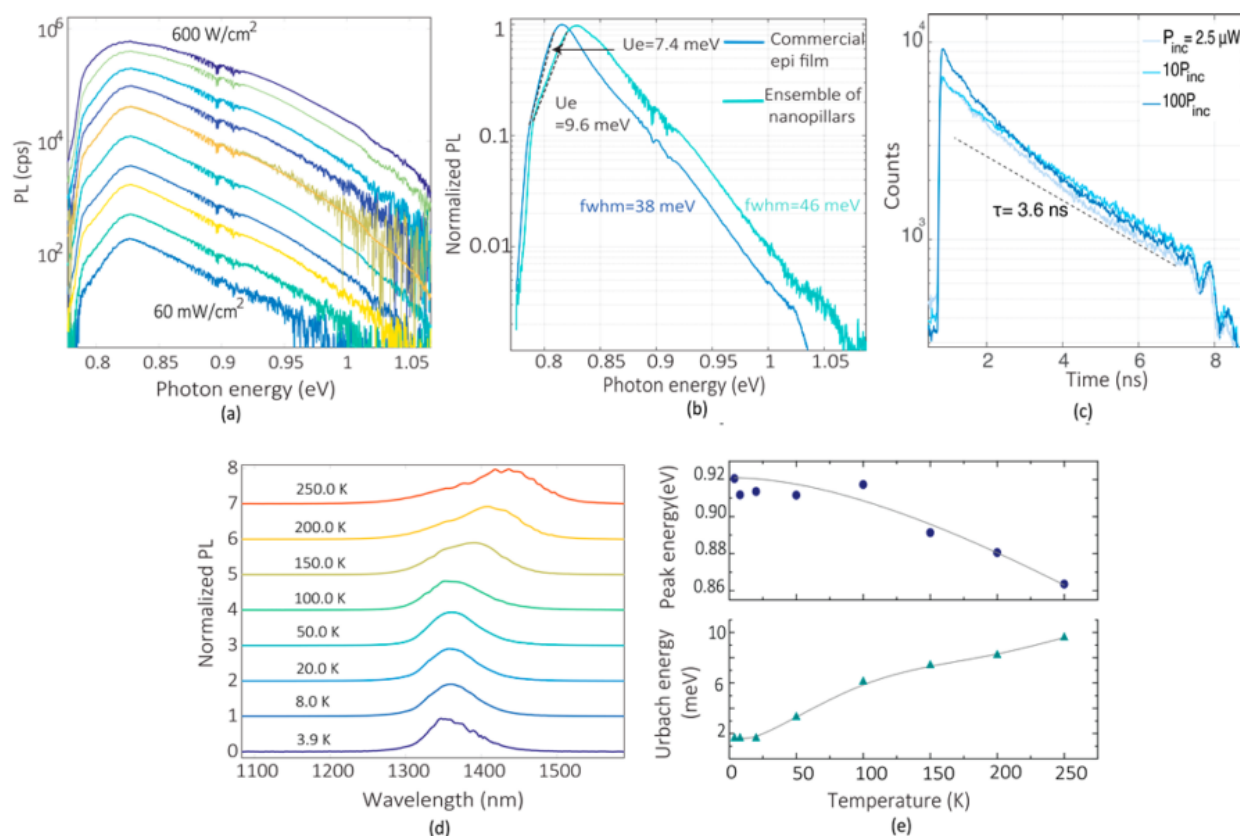

Figure 6.6: Optical characterization of nanopillars containing QWs: (a) excitation dependent PL spectra of InGaAs QWs in InP nanopillars, showing exponential tails and peak around 0.83 eV, approximately 1490 nm. (b) PL lineshape comparison of a commercial epi thin film (blue) with an ensemble of nanopillars, showing comparable exponential tails in the PL spectrum and attesting to the low inhomogeneous broadening. (c) Time resolved PL from the InGaAs QW showing a good minority carrier lifetime of 3-4 ns in the quantum wells. (d) Temperature dependent normalized PL spectra showing a typical Varshni dependence in the quantum well energ, which is displayed in top inset of (e). The temperature dependence of the Urbach energy can also be determined from these spectra (bottom inset, (e)).

We compared the MQW emission characteristics with a commercial epitaxy wafer consisting of 6 pairs of InGaAs quantum wells (Fig. 6.6(b)). The nanopillar MQW sample shows a narrow room-temperature linewidth of 46 meV, which is comparable to 38 meV measured in the epitaxial wafer, suggesting quantum well uniformity and minimal inhomogenous broadening. The spectrum over the 0.78-0.82 eV low energy exponential tail is determined by the Urbach energy. An exponential tailing of the sub-bandgap states in the PL spectra gives a measure of material disorder and is expected to be the main cause of the Urbach tail. Typically, the Urbach tail is broad in nanowires and nanostructures due to crystallographic defects and surface states. Surprisingly, the Urbach energy in the MQW nanopillars is 10 meV, when compared to 7.4 meV measured in the commercial epitaxial wafer. Previous reports of Urbach energy in InP based nanowires are significantly higher (wurtzite 33 meV and zinc blende 24 meV) [160]. Minority carrier lifetime of the InGaAs MQW emission was measured at room temperature under incident powers varying from 2.5-250 μW using a 1000 nm pulsed excitation. The temporal decay was detected using an InGaAs CCD and reveals a good minority carrier lifetime of 3.6 ns (Fig. 6.6(c)). The long lifetime and its invariance with pump power is attributed to the excellent material quality and carrier confinement in the MQW. Temperature dependent PL spectra from nanopillar MQWs are presented in Fig. 6.6(d). A dominant InGaAs quantum well peak is observed down to 4 K. The peak energy of the InGaAs MQW shows a red shift with increasing temperature due to bandgap shrinkage. The peak energy as a function of temperature follows the trend predicted by the Varshni relation, as shown in Fig. 6.6(e). The data measured from the nanopillar MQW agrees with the Varshni relation with fitting parameters $\alpha = 5.45 \times 10^{-4}$ eV/K and $\beta = 337.78$ K, which are typical for InGaAs [24]. The Urbach energy was also extracted from the temperature dependent spectra. As seen in Fig. 6.6(e), the Urbach energy reduces with decrease in temperature and reaches its minimum value of 1.6 meV around 20 K. This corresponds to the disorder originating from the inhomogeneous broadening inherent in InGaAs quantum wells.

6.3 Pitch-defined Wavelength in Nanopillar Arrays

Silicon transparent emission in the range from 1400-1500 nm is observed for different growth periods on the same chip. The MQW emission red-shifts from 1405 nm to 1512 nm, with increasing growth pitch. This effect may be due to two concurrent factors: (a) Increased In incorporation on [110] m-plane quantum wells in larger pitch arrays due to reduced competition for TMIn adatoms during MQW growth, and (b) increase in InGaAs quantum well thickness due higher growth rate resulting from larger local TMIn flux (as shown in fig. 6.7). Transmission electron microscopy studies on similarly grown InGaAs quantum wells in spontaneously nucleated InP pillars show a radial InGaAs thickness of 5 nm [161]. These spontaneous nanopillars are identical to pillars in 1 μm arrays in dimension, where we may assume a quantum well thickness of 5 nm. Both InP and InGaAs growth rates increase, as local group III (TMIn) flux increases with pitch. The InGaAs quantum well thickness in subsequent higher pitch arrays can be assumed to scale up with the diameter of nanopillar.

The measured PL energy is plotted in Fig. 6.8 along with modeled energies derived from a finite quantum well taking into account quantum well thickness variation. The experimentally measured MQW emission is in good agreement with the modeled data.

Pillar Pitch Controls QW Wavelength

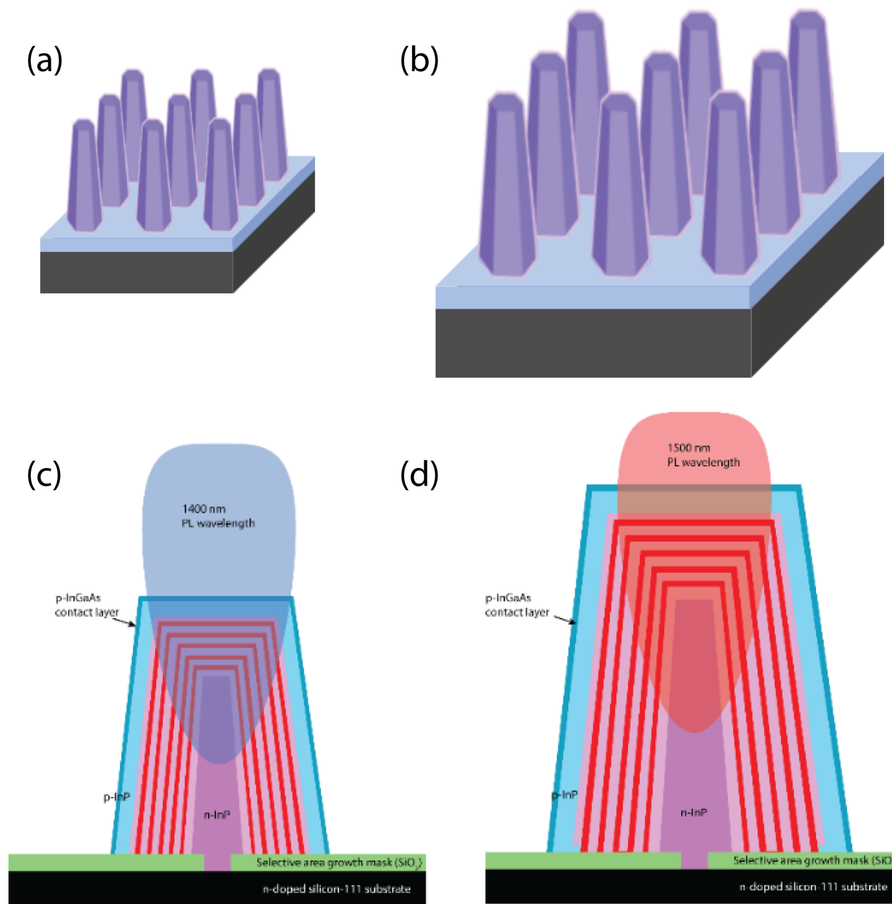

Figure 6.7: Pitch dependence of pillar dimensions: this schematic shows how the nanopillar dimensions vary systematically as a function of the pillar pitch. Due to precursor competition, pillars grown at a smaller pitch,(a) tend to be smaller and have thinner quantum wells than those at a larger pitch (b). This leads to a pitch-dependent systematic variation in the QW PL.

Here, we describe further experimental details of the photoluminescence measurements. For the pitch variation study, quantum wells in a single nanopillar were directly excited using a continuous wave pump at 980 nm, focused to a spot less than 5 microns in diameter using a 100x objective. By using a lower magnification objective, nanopillar ensembles could also be measured. Excitation dependent measurements were performed using a calibrated silicon

photodiode to monitor pick-off power. After filtering the pump wavelength, the quantum well photoluminescence was dispersed using a Princeton Instruments SP2750 spectrometer, and collected on an LN2 cooled OMA-V InGaAs array. For temperature controlled measurements, the nanopillar sample was placed in a continuous-flow liquid helium cooled cryostat, with closed loop temperature control between 5 K and 300 K. Lasing experiments on the n-doped InP nanopillars were performed using a Coherent ultra-II tunable femtosecond pulsed laser with 140 fs pulse width and 80 MHz repetition rate. The wavelength was tuned to 730 nm in order to uniformly excite the InP nanopillar, with PL emission peak around 850-860 nm. This experiment was performed under ambient conditions. The lasing spectra were dispersed and then measured on a silicon CCD array. Time resolved photoluminescence measurements on the quantum wells was performed using the same tunable laser, but with excitation wavelength tuned to 1000 nm.

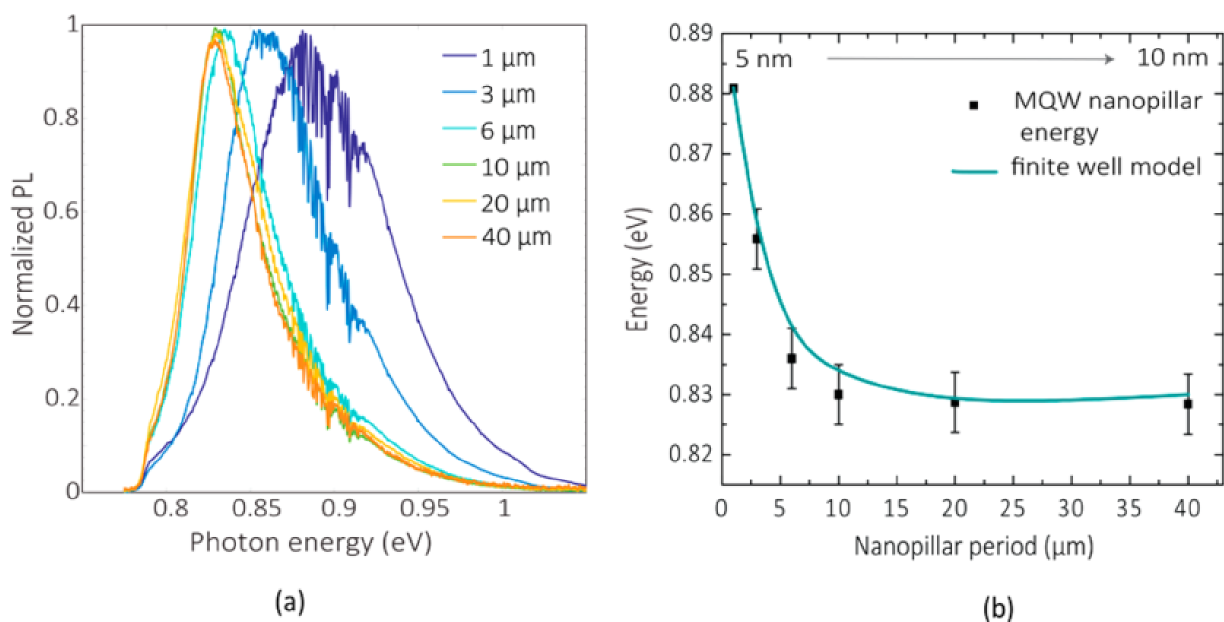

Figure 6.8: Pitch dependence of QW PL: (a) PL spectral dependence on pillar pitch, showing substantial blue shift as the pitch is reduced. The different amounts of inhomogeneous broadening reflect the number of pillars captured within the excitation laser spot. (b) The dependence can be captured using a simple finite quantum well model with a pitch dependent quantum well width.

6.4 Scalable Fabrication of Position Controlled Nanopillar Devices

The benefits of position controlled growth lie not only in being able to study nanopillar density and proximity dependent growth and PL characteristics, but also to allow scalable photomask lithography. Note that prior to this, an additional alignment marker step, followed by SEM mapping and e-beam lithography was required to allow electrical contacts to be defined to individual nanopillars. This procedure is not scalable and requires manual mask creation and metrology for every different chip. Hence, there was significant interest in demonstrating repeatable position controlled growth. The idea is that once the nanopillars are grown in a position controlled manner, a photomask for defining electrical contacts can be easily aligned to the growth substrate, thus allowing scalable device fabrication - with thousands of devices being defined on the same silicon chip using one lithography step.

The fabrication process flow is summarized in figure 6.9. The nanopillars grow in core-shell form. Thus, the n-doped core of the nanopillar is in contact with n-Si, which the p-doped shell grows over the oxide mask, eliminating the shunt path from the p-doped shell and n-Si substrate. For additional electrical isolation, a PECVD process is used to conformally deposit silicon dioxide on the nanopillars at 250°C, a temperature low enough to preserve pillar quality. Photoresist was then coated onto the chip and etched back using oxygen plasma to expose the tips of oxide-coated nanopillars. The oxide is then etched away from the top regions of nanopillars using buffered oxide etch, exposing their p-GaAs shells for electrical contacts. The photoresist was then removed by plasma etch and acetone, and the remaining oxide on the bottom of the nanopillars electrically isolate p- and n-layers of the nanopillar diode. The original DUV lithography mask contains alignment marks along with the nanopillar growth apertures. These alignment marks are used to align contact lines and contact pads to individual and ensemble nanopillar LEDs.

A standard photolithography process was used to pattern device contacts and pads. Moving from e-beam lithography to photolithography was feasible since the contact dimensions and alignment tolerance is micron scale. After photoresist development and a gentle descum, the nanopillar surface is deoxidized using dilute HCl. Metal evaporation is then performed by mounting the sample at an angle such that the directional metal deposition coats only one side of pillars. This leaves an uncovered region to collect light in our experiments. We deposited a thin layer of Ti (20 nm) for adhesion and Au (200 nm) for electrical contacts. Figure 6.10 shows a scanning electron microscope image and labeling for an exemplary nanopillar, after the fabrication process has been completed. Figure 6.11 shows a microscope image of the chip, containing hundreds of devices, with electrical contacts aligned exactly to the position of pillar nucleation.

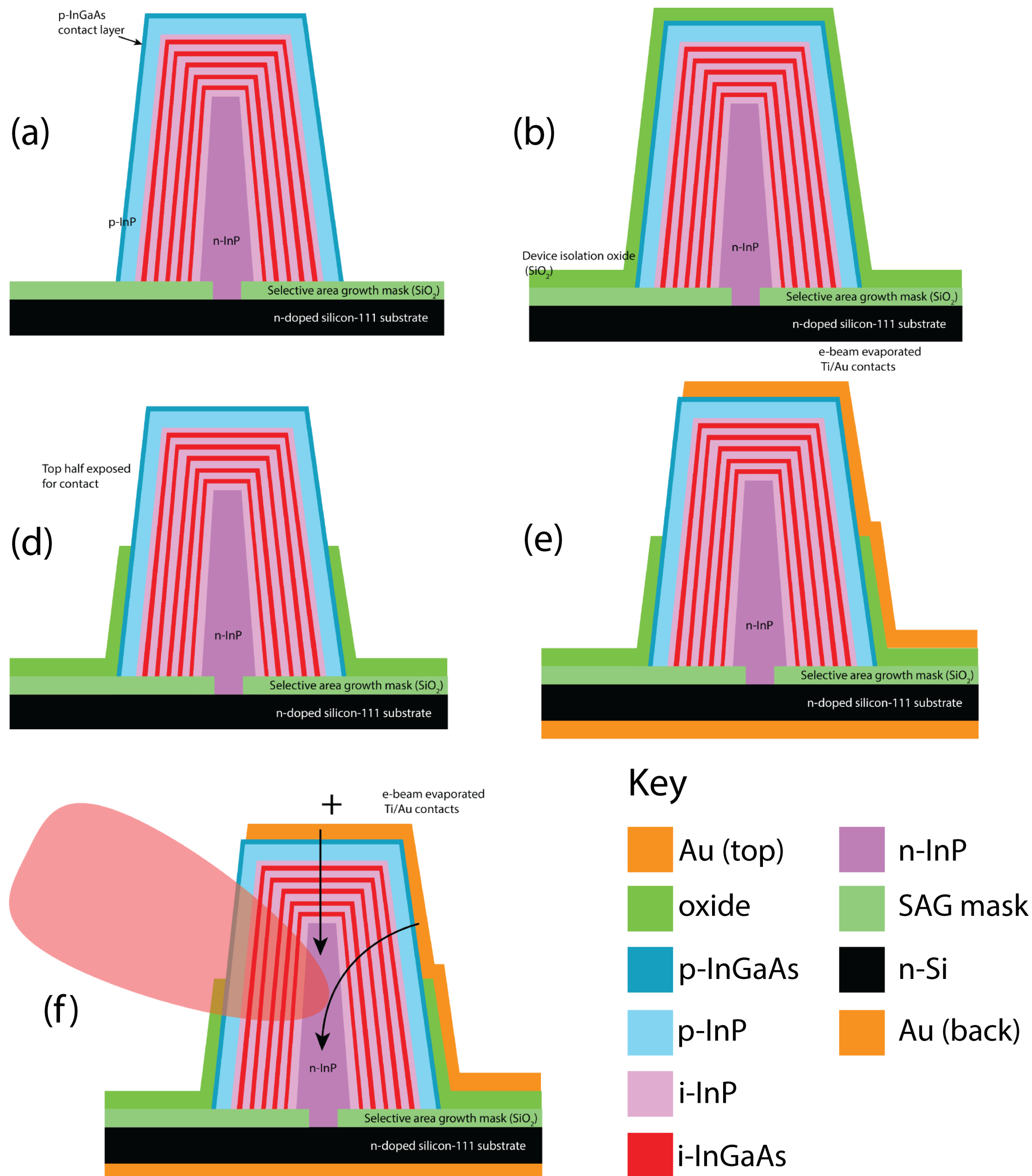

Figure 6.9: Scalable fabrication of SAG nanopillars: (a) The full nanopillar core-shell stack is grown in a position-controlled manner on the silicon substrate, (b) isolation oxide deposited, (c) photoresist etch back mask followed by an oxide etch allows only the top of the oxide to be removed, (d) the gold pads are defined using patterning (aligned to markers on the growth substrate), followed by liftoff. A back contact is also deposited on the n-silicon substrate. (e) The pillars are then ready for electrical characterization.

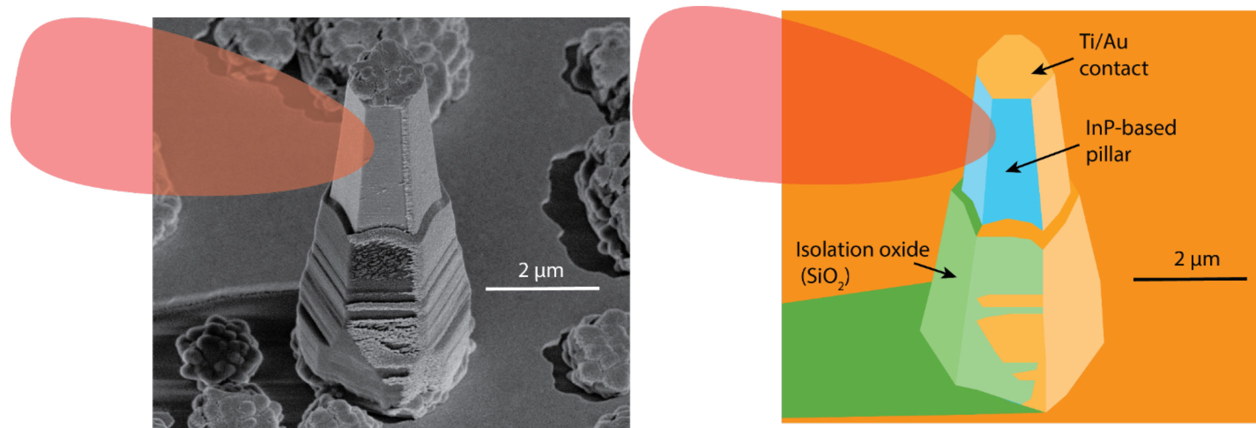

Figure 6.10: Single pillar after fabrication: (left) Scanning electron microscope image of an individual nanopillar after gold deposition and liftoff, (right) matching schematic showing the different materials, starting from the outermost gold to the InP nanopillar within.

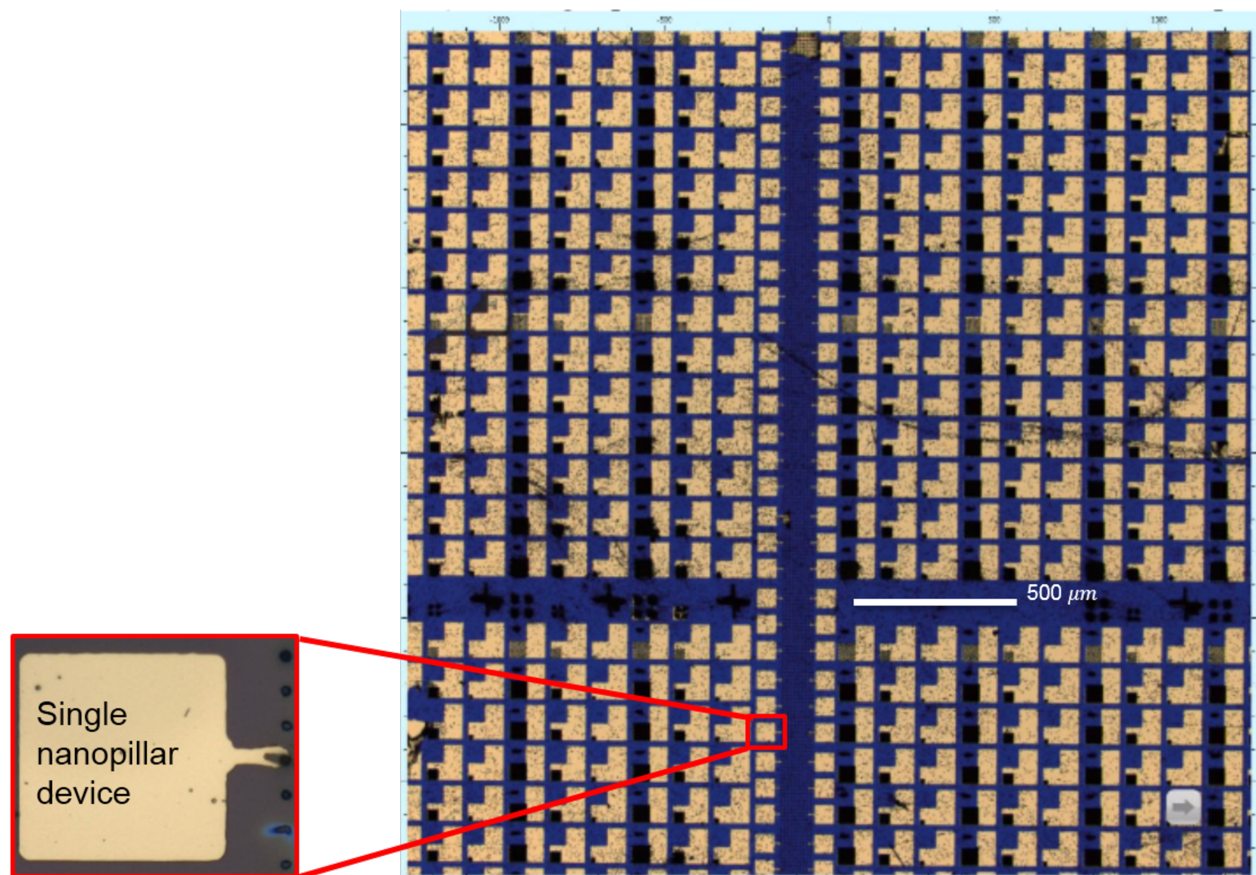

Figure 6.11: Microscope image of fabricated chip containing hundreds of devices. The chip has been organized to grow ensemble nanopillar devices (with some pitch variation) as well as single nanopillar devices. The dense black squares seen in the microscope image are the ensemble devices. They have L-shaped pads for providing electrical contact. Through the middle of the field of view, there is a line of single pillar devices with the inset showing one such device, with a small circular pad contacting the nanopillar. This pad has a nanopillar-shaped shadow on it from the line of sight gold evaporation.

6.5 Bright Silicon Transparent Electroluminescence

To realize an electrically driven nano-LED, five InGaAs quantum wells were incorporated in the active region of a p-n diode. The grown structure consists of n-InP/InGaAs MQW/p-InP/p-InGaAs, grown in core-shell mode on n+-Si. The inner core is doped n-type so that the type II band alignment of InP with silicon is favorable for the p-i-n junction forward current (as explained in chapter 2). The device active region structure is shown in the band diagram of fig. 6.12 and schematically in Fig. 6.14(a). Impurity doping is achieved using in-situ precursor flow of DeTe and DeZn as n- and p-dopants, respectively. Because each single pillar is grown at a predetermined position on the chip, it can be processed via optical lithography process and used as a single nano-LED device. Room temperature current-voltage characteristics from a single pillar show diode behavior with a series resistance of around 1-4 $k\Omega$, which is expected for the small dimensions of the device. This would allows us to inject milli-amperes of current into the small nanopillar device. At low pump currents (below 100 μA) the injected carriers recombine non-radiatively, leading to a quadratic dependence of light output on current as shown in Fig. 6.14(d). However, at higher current densities (on the order of kA/cm^2), the radiative process starts to dominate and we note that the ideality factor becomes close to unity.

Figure 6.14(b) shows the L-I-V characteristics of a nanopillar LED. The light output was measured using a Germanium detector and a 100x objective lens. Details on the measurement set-up are shown in figure 6.13. The LED exhibits bright emission with measured output power as high as 200 nW. The collection efficiency of the setup is estimated to be around 5%, which leads to an estimated light output 4 μW. This is the highest reported power output from a nanopillar or nanostructure-based LED [162], [163], [164]. The inset of Fig. 6.14(b) shows a high magnification SEM image of a single nanopillar after fabrication. Figure. 6.14(c) shows room temperature electroluminescence spectra from a single nanopillar at 1510 nm with increasing injection current. The inset of Fig. 6.14(c) shows the emission of a nanopillar LED imaged on an InGaAs CCD array, showing a single bright spot.

We note that the measured room temperature electroluminescence shows strong quantum well emission, with no signal from the InP cladding. A calibrated electroluminescence measurement was used to determine the quasi Fermi level splitting of the carriers injected into the quantum well, similar to the method proposed by Tran *et al.* [40]. The Fermi level split is directly related to the externally emitted EL counts from the nanopillars. Under sufficiently high pump, intense electroluminescence counts lead to a calculated Fermi level split ΔF exceeding the EL peak energy $\hbar\omega$ -indicating that the device has been electrically biased beyond the transparency condition and into optical gain (see Fig. 6.14(d)). Note that the inferred Fermi level split is less than the applied voltage due to significant resistive voltage drops in the current conduction path. At very high electrical injection current density, the EL spectrum blue shifts due to the filling of the QW states, further corroborating the conclusion that the device has been biased beyond transparency. Heating-induced red shift was observed in the spectra only at the highest injection currents ($\sim 10kA/cm^2$), attesting to the thermal robustness of the device.

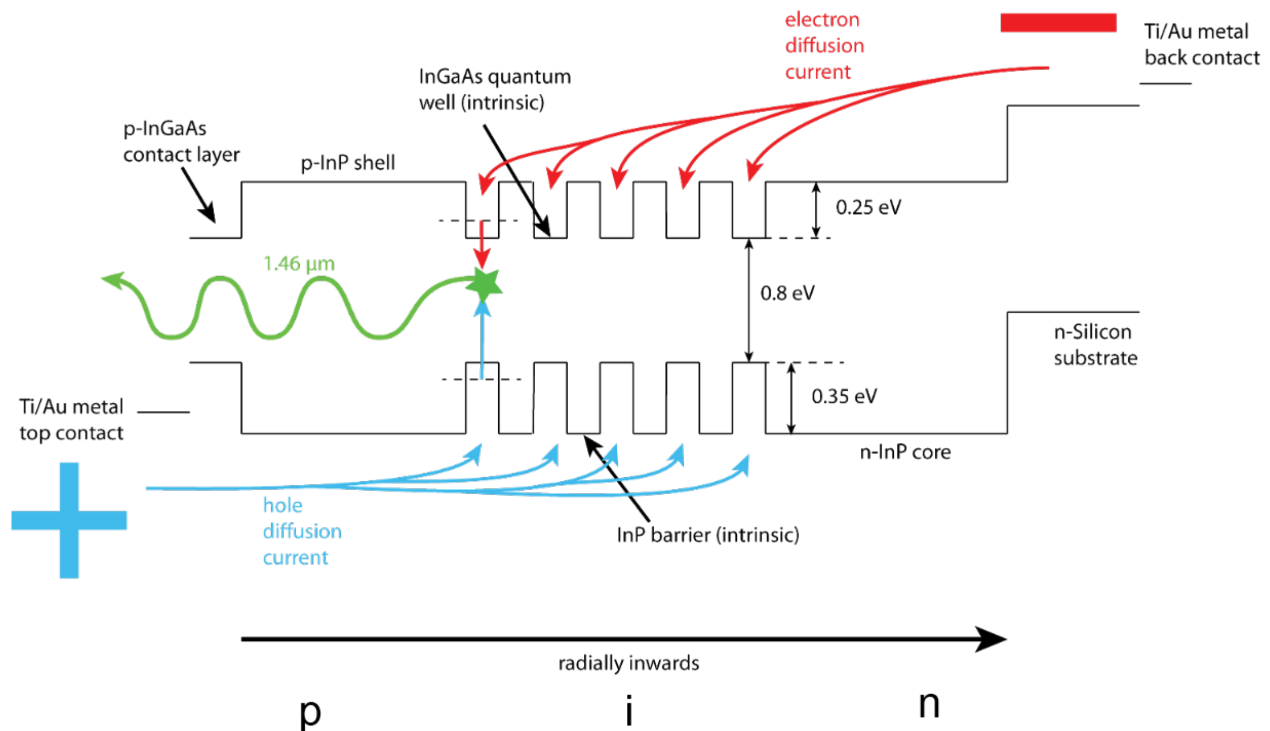

Figure 6.12: Active region band diagram: the band offsets from core to shell for the nanopillar device are shown. Electrical contact is directly through the silicon substrate, with the type II band alignment aiding rather than impeding the preferred direction of current flow in the n-core, p-shell device. Note that a p-InGaAs contact layer is used in order to reduce contact resistance.

Both single and ensemble nanopillar LED devices were probed electrically to measure light-current-voltage characteristics. As described in the fabrication section, the top contact is p-type, and is isolated from the substrate via a silicon dioxide layer, with the pillar body exposed. The p-contact is specific to each device. The common n-contact is directly through the substrate, via a Ti/Au contact on the back side of the silicon substrate. On DC electrical bias, the nanopillar LEDs emit light. This is collected using a 100x objective focused to the nanopillar position and measured on an S122C (Thorlabs) large area germanium detector, with a Thorlabs PM320E calibrated power meter (see Fig. 6.13). The power meter converts the measured light output to a voltage signal that can then be conveniently measured on an HP4145B semiconductor parameter analyzer. Electrical bias was performed with the HP4145B as a current source, with a compliance set to the measured voltage. The same bias conditions were used for measuring wavelength resolved EL spectra, except the current bias was applied for the duration of spectrum acquisition at each current level. The spectra did not change or degrade during the measurement sweep, up to very high estimated current densities of up to 10 kA/cm^2 through the nanopillar.

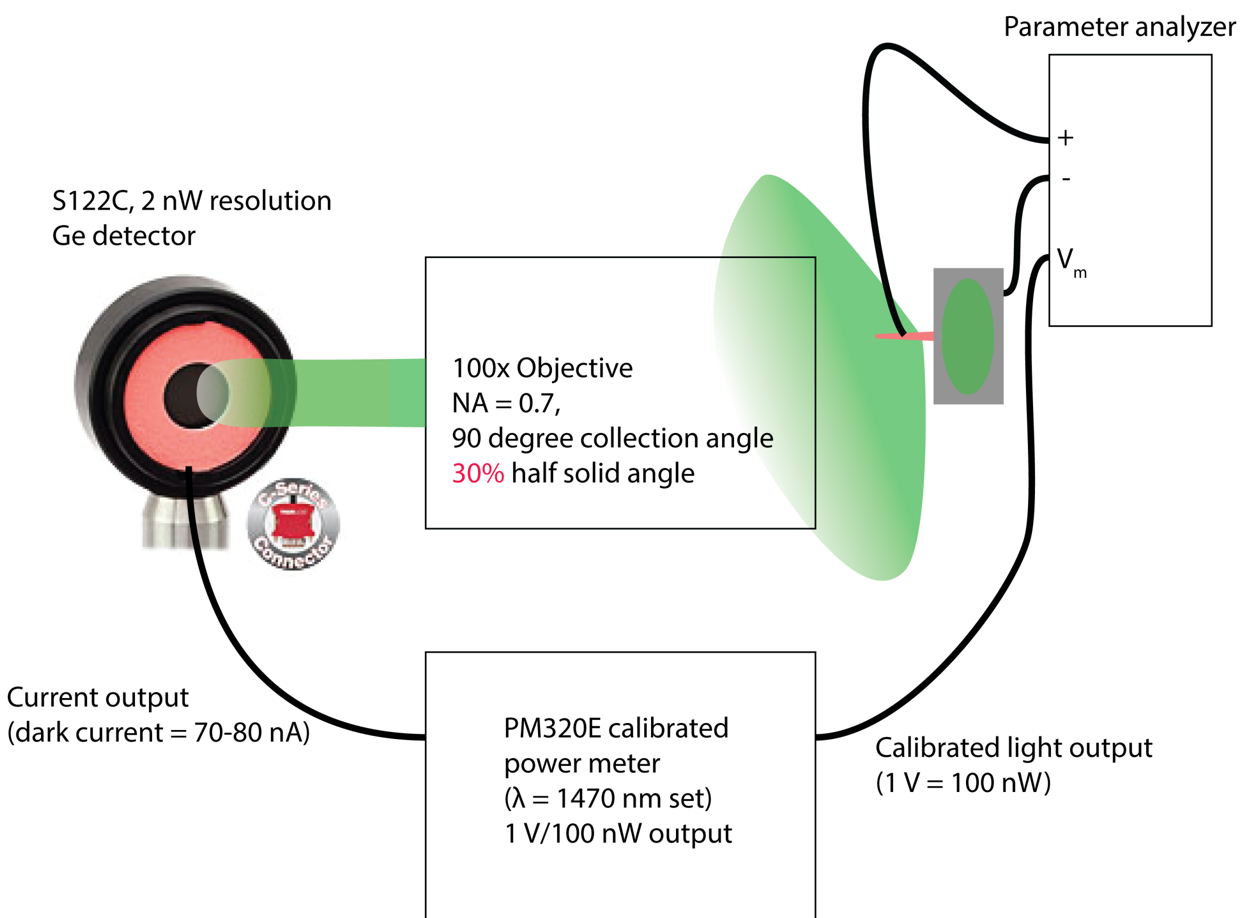

Figure 6.13: Measurement setup schematic: the single nanopillar device is electrically swept using a parameter analyzer, while simultaneously, the power is measured using a calibrated germanium photodiode. The photodiode is placed directly behind the objective, which has a high numerical aperture of 0.7.

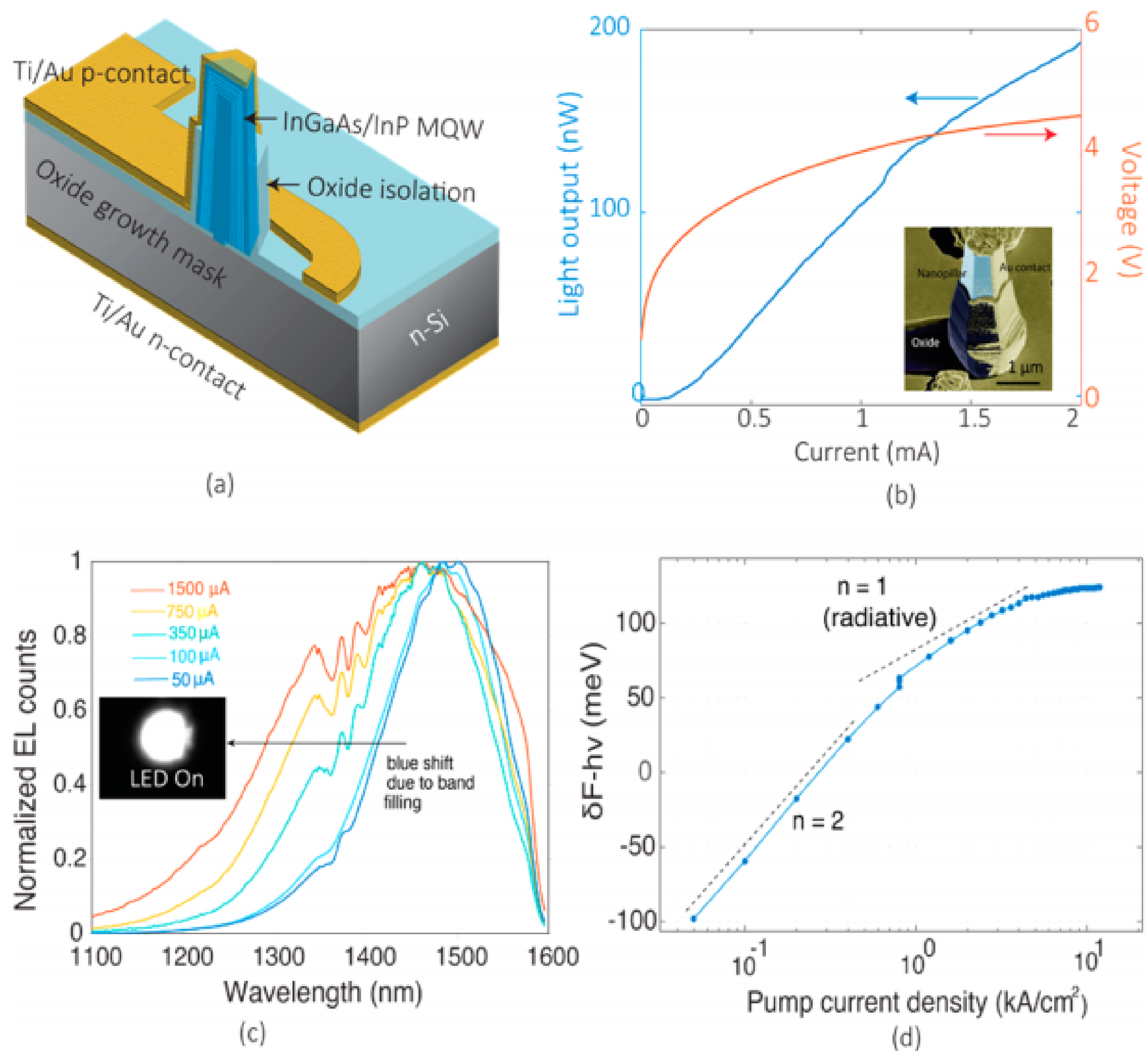

Figure 6.14: Nanopillar LEDs with silicon transparent emission: (a) 3D-schematic of a single nanopillar device showing the active region cross section and device geometry. (b) Absolute measured light output from the nanopillar LED, as a function of current. The light output in 100s of nanoWatts was measured using the setup described in figure 6.13. The light output is quite linear with current (except at very low current injection), indicating high internal quantum efficiency. (c) Normalized electroluminescence spectra measured as a function of current injected. The small device can sustain a current as high as 2 mA, with blue shift due to band filling at the high current levels (showing that the Fermi level split exceeds bandgap qualitatively). (d) Calibrated electroluminescence counts can be directly converted to Fermi level splits, demonstrating that indeed the brightness exceeds what would be expected at transparency.

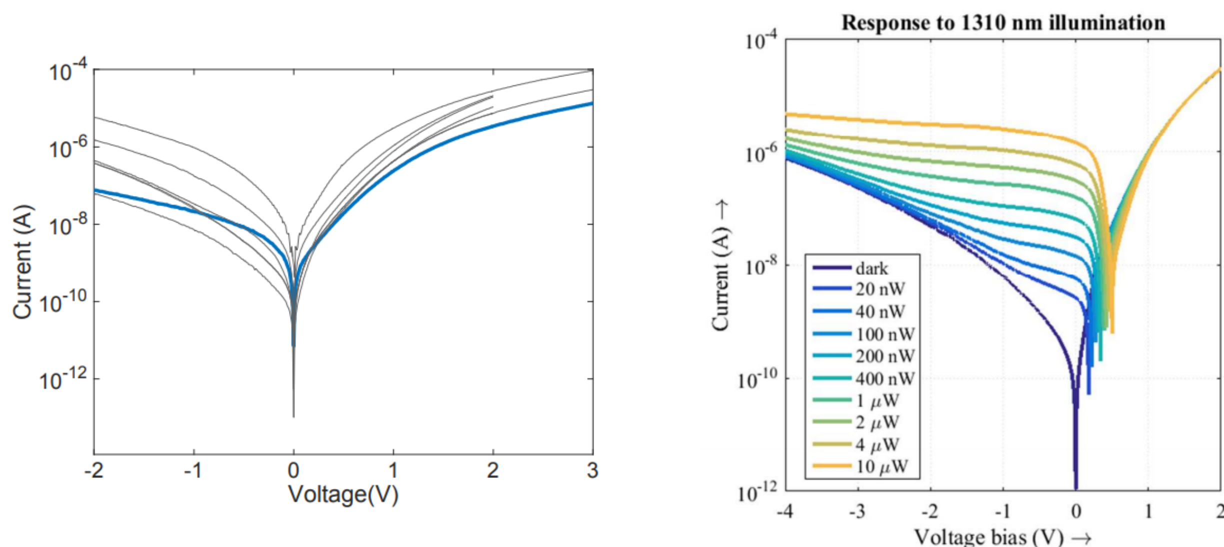

Figure 6.15: Photodetection of silicon transparent light: (left) I-V characteristics of multiple devices. (b) The QW p-i-n devices also show pronounced photodetection of 1310 nm illumination light, which is important for on-chip silicon photonics.

In conclusion, we have investigated the site-controlled MOCVD growth of InP nanopillar heterostructures, directly on silicon (111), under CMOS-compatible conditions. The catalyst-free, low temperature nanopillar growth results in high yield of nanopillars. Their excellent optical performance is demonstrated by long lifetime (3.7 ns), low surface recombination velocity and room temperature lasing. Silicon transparent emission in the range of 1400-1500 nm is observed by incorporating InGaAs/InP quantum wells. The nanopillar quantum wells show remarkable optical properties, comparable to commercial epitaxial wafers and are introduced in the active region of a p-i-n nanopillar heterostructure. The device shows excellent diode behavior and bright electroluminescence around 1500 nm, with an output power of 4 μW. Additionally, nanopillar diode devices also demonstrate strong photoresponse under 1310 nm illumination. This device is a first step towards the large-scale integration of highly efficient, ultra-compact, bright light sources and in general, nanophotonic devices for the silicon photonics toolbox.

Chapter 7

Conclusion and Outlook

Indium Phosphide (InP) is the material of choice for building the optoelectronic devices that form the physical basis of the Internet. InP monolithic integration on silicon in a CMOS post-process compatible manner would have tremendous implications for the intimate integration of electronic and photonic functionality on the same platform. The low temperature, self-catalyzed growth of high crystalline quality Wurtzite-phase InP nanopillars directly on silicon presents a viable approach to monolithically integrate high performance nano-optoelectronic devices. In this thesis, I have focused on how we have advanced from qualifying the material properties of these pillars to demonstrating some key monolithic devices fabricated with them: for both electrical to optical conversion and vice versa.

We have delved into photovoltaic(PV) energy harvesting based on the nanopillars in chapter 2. We have measured high Fermi level splitting and long minority carrier lifetimes from the nanopillars. Additionally, we have performed detailed characterization of impurity doping in the nanopillars and fabricated regrown nanopillar devices with low dark current. In chapter 3, we described how a sparsely packed InP nanopillar array can absorb 92-97% of the incident light (insensitive to angle) because of the large absorption cross section of these near-wavelength nanopillars. In particular, tapered nanoneedles with a base diameter of 650 nm exhibit better absorption characteristics than equivalent straight nanopillars, and significantly improved absorption over a bare III/V substrate. We experimentally demonstrated enhanced and angle insensitive absorption over a broad wavelength range for spontaneously nucleated InP nanopillars on a silicon substrate. Lastly, we used detailed balance arguments to calculate the PV power conversion efficiency for harvesting energy from indoor illumination sources. For the LED + yellow phosphor spectrum, we found that a single junction PV with bandgap of 1.9 eV has a detailed balance efficiency limit of nearly 50%, which rises to 63% for dual junction PV. We have also described a passive anti-reflection texture using the nanopillars that is nearly omnidirectional. With illumination angle insensitive PV using nanopillar arrays, we proposed to achieve sustainable and long lasting energy harvesting for powering ubiquitous devices connected to the Internet of Everything.

In chapter 4, we have also demonstrated an InP nanopillar phototransistor as a sensitive, low-capacitance photoreceiver for the energy-efficient operation of a complete optical

link. The high absorption coefficient and potential for heterostructure engineering with the InP/InGaAs material system opens new opportunities for engineering a high performance phototransistor. As a first step, we have demonstrated a compact single-nanopillar InP photo-BJT with a simultaneously high responsivity of 9.5 A/W and high 3dB-bandwidth of 7 GHz. The high responsivity was enabled by the low dark current and leakage free regrown active region of the phototransistor.

The excellent material quality of the nanopillars allowed for a measured transparency power density of 200 W/cm^2/ QW layer under optical pump, which translated to 105 A/cm^2/ QW layer. The low current density for the onset of optical gain is a characteristic of the reduced dimensionality active region, as described in chapter 5. Following this, we have investigated another requirement for achieving lasing oscillation: a good optical cavity. First, we transferred these QW-nanopillars to a low index substrate and demonstrated a high modal gain of 300 cm^{-1} for Fabry-Perot modes sustained within the nanopillar cavity under continuous wave pumping (using the Hakki-Paoli method). Further, a high quality factor (Q$\sim$1000) undercut cavity quantum well nanolaser is demonstrated, operating in the silicon-transparent wavelength range up to room temperature under optical excitation. The optically pumped QW laser emitted at 1.21μm and had a high characteristic temperature of 130 K. Another structure that was encouraging for sustaining high-Q modes was the regrown cavity. Regrown InP nanopillar lasers operating in the short wave infrared regime have been demonstrated, and show low pulsed lasing threshold on the order of $10 - 20\mu$J/cm^2, an order of magnitude lower than the non-regrown pillars. Further, the high-Q and high second order susceptibility $\chi^{(2)}$ of the regrown InP nanopillar allows for the generation of cavity enhanced second harmonic light at a wavelength of 425 nm, from the doubling of the lasing mode at 850 nm. This demonstrates, for the first time, internal second harmonic generation in the InP nanolasers, a technique used ubiquitously in the green laser pointer. We have also examined some preliminary qualitative efforts for the integration of nanopillars with silicon photonics by growing nanopillars on SOI and observing the transmission of light into waveguides.

For the optical transmitter side of the photonic link, Indium Gallium Arsenide quantum wells (QWs) have been incorporated as a core-shell heterostructure within InP nanopillars that were grown in a position controlled manner on silicon. Within the same growth run, it is possible to tailor the quantum well emission by simply controlling the pitch of the nanopillars. These results have been described in detail in chapter 6. Precursor molecule competition leads to a change in the width and composition of the quantum wells, leading to epitaxial control of the gain spectrum, which is highly encouraging for wavelength multiplexing. These nanopillars have been fabricated into electrically-injected quantum well in nanopillar light emitting diodes (LEDs) monolithically on silicon and operate within the 1310-1550 nm spectral window of interest for silicon photonics. The heterostructure passivation leads to a high luminescence yield of 25-30% and quantum well carrier lifetime on the order of nanoseconds, ultimately leading to efficient single nanopillar LEDs emitting micro-watts of power.

Here, we pause to speculate on some possible future opportunities in this area, and where

the work could potentially lead. The Internet of Everything is experiencing an explosion in terms of the number of connected devices that need to autonomously navigate and interact with the environment. Highly efficient PV for powering these may soon become a reality, and the passive nanopillar texture could play an important role in ensuring angle insensitive light harvesting with these PV cells. The approach described in chapter 3 could be a promising starting point. Another area of interest is the integration of a monolithic light source on a silicon chip, which continues to remain an unsolved challenge. There are a few requirements that need to be met in order for a solution to be meaningful: the device needs to be modulated at a high data rate, it must be energy efficient (to be compelling as a replacement for electrical links) and it must also be able to interface with silicon photonics. A monolithic electrically injected nanolaser could be a potential solution, but it is not clear that this is possible at the small size required and that such a device would be energy efficient. Two other potential approaches are LED based: one could either produce a single mode LED that is then interfaced with a well designed optical modulator, or an extremely small directly modulated LED as described by Eggleston *et al.* [165]. It may be more straightforward to achieve a high quantum efficiency for the light emitter with the former approach, where the cavity is required to be on the order of the size of the optical wavelength rather than the electron wavelength (the antenna approach). Investigating the monolithic single mode LED approach, alongside efforts to build on the initial silicon photonics coupling experiments with the nanopillars could be quite interesting and relevant for attojoule/bit optoelectronics. Lastly, it may also be interesting to explore the potential of the nanopillar cavity for enhanced spontaneous parametric fluorescence (downconversion) from the lasing wavelength. If the nanopillar cavity could be used as a bright source for 1550 nm correlated photon pairs from a 785 nm lasing oscillation, this would be very interesting for applications based on quantum cryptography and quantum information.

References

[1] M. Y. Lanzerotti, G. Fiorenza, and R. A. Rand, “Microminiature packaging and integrated circuitry: The work of E . F . Rent, with an application to on-chip interconnection requirements,” vol. 49, no. 4, pp. 777–803, 2005.

[2] D. A. B. Miller, “Device Requirement for Optical Interconnects to Silicon Chips,” *Proc. IEEE Spec. Issue Silicon Photonics*, vol. 97, no. 7, 2009.

[3] S. Goossens, G. Navickaite, C. Monasterio, S. Gupta, J. J. Piqueras, R. Pérez, G. Burwell, I. Nikitskiy, T. Lasanta, T. Galán, E. Puma, A. Centeno, A. Pesquera, A. Zurutuza, G. Konstantatos, and F. Koppens, “Image sensor array based on graphene-CMOS integration,” *arXiv.org*, vol. 11, no. 6, pp. 366–371, 2017.

[4] C. Posch, T. Serrano-Gotarredona, B. Linares-Barranco, and T. Delbruck, “Retinomorphic event-based vision sensors: Bioinspired cameras with spiking output,” *Proc. IEEE*, vol. 102, no. 10, pp. 1470–1484, 2014.

[5] D. Fattal, Z. Peng, T. Tran, S. Vo, M. Fiorentino, J. Brug, and R. G. Beausoleil, “A multi-directional backlight for a wide-angle, glasses-free three-dimensional display,” *Nature*, vol. 495, no. 7441, pp. 348–351, 2013.

[6] J. Sun, E. Timurdogan, A. Yaacobi, E. S. Hosseini, and M. R. Watts, “Large-scale nanophotonic phased array,” *Nature*, vol. 493, no. 7431, pp. 195–199, 2013.

[7] R. E. Camacho-Aguilera, Y. Cai, N. Patel, J. T. Bessette, M. Romagnoli, L. C. Kimerling, and J. Michel, “An electrically pumped germanium laser,” *Opt. Express*, vol. 20, no. 10, p. 11 316, 2012.

[8] J. Liu, X. Sun, L. C. Kimerling, and J. Michel, “Direct-gap optical gain of Ge on Si at room temperature,” *Opt. Lett.*, vol. 34, no. 11, p. 1738, 2009.

[9] S. Wirths, R. Geiger, N. von den Driesch, G. Mussler, T. Stoica, S. Mantl, Z. Ikonic, M. Luysberg, S. Chiussi, J. M. Hartmann, H. Sigg, J. Faist, D. Buca, and D. Grützmacher, “Lasing in direct-bandgap GeSn alloy grown on Si,” *Nat. Photonics*, vol. 9, no. 2, pp. 88–92, 2015.

[10] J. Matthews and A. Blakeslee, “Defects in epitaxial multilayers,” *J. Cryst. Growth*, vol. 27, pp. 118–125, 1974.

[11] A. W. Fang, H. Park, O. Cohen, R. Jones, M. J. Paniccia, and J. E. Bowers, "Electrically pumped hybrid AlGaInAs-silicon evanescent laser.," *Opt. Express*, vol. 14, no. 20 SRC - GoogleScholar FG - 0, pp. 9203–9210, 2006.

[12] H. Liu, T. Wang, Q. Jiang, R. Hogg, F. Tutu, F. Pozzi, and A. Seeds, "Long-wavelength InAs/GaAs quantum-dot laser diode monolithically grown on Ge substrate.," *Nat Photonics*, vol. 5 SRC - G, pp. 416–419, 2011.

[13] S. Chen, M. Tang, J. Wu, Q. Jiang, V. G. Dorogan, M. Benamara, Y. I. Mazur, G. J. Salamo, A. Seeds, and H. Liu, "1.3 um InAs/GaAs quantum-dot laser monolithically grown on Si substrates using InAlAs/GaAs dislocation filter layers," *Conf. Dig. - IEEE Int. Semicond. Laser Conf.*, vol. 22, no. 10, pp. 88–89, 2014.

[14] S. Chen, W. Li, J. Wu, Q. Jiang, M. Tang, S. Shutts, S. N. Elliott, A. Sobiesierski, A. J. Seeds, I. Ross, P. M. Smowton, and H. Liu, "Electrically pumped continuous-wave III-V quantum dot lasers on silicon," *Nat. Photonics*, vol. 10, no. 5, pp. 307–311, 2016.

[15] S. Chen, M. Liao, M. Tang, J. Wu, M. Martin, T. Baron, A. Seeds, and H. Liu, "Electrically pumped continuous-wave 1.3 um InAs / GaAs quantum dot lasers monolithically grown on on-axis Si (001) substrates," *Opt. Express*, vol. 25, no. 5, pp. 4632–4639, 2017.

[16] A. Y. Liu, C. Zhang, J. Norman, A. Snyder, D. Lubyshev, J. M. Fastenau, A. W. K. Liu, A. C. Gossard, and J. E. Bowers, "High performance continuous wave 1.3 um quantum dot lasers on silicon," *Appl. Phys. Lett.*, vol. 104, no. 4, pp. 3–7, 2014.

[17] Y. Wan, Q. Li, A. Y. Liu, A. C. Gossard, J. E. Bowers, E. L. Hu, and K. M. Lau, "Optically pumped 1.3 um room-temperature InAs quantum-dot micro-disk lasers directly grown on (001) silicon," *Opt. Lett.*, vol. 41, no. 7, p. 1664, 2016.

[18] Y. Wan, Q. Li, A. Y. Liu, W. W. Chow, A. C. Gossard, J. E. Bowers, E. L. Hu, and K. M. Lau, "Sub-wavelength InAs quantum dot micro-disk lasers epitaxially grown on exact Si (001) substrates," *Appl. Phys. Lett.*, vol. 108, no. 22, 2016.

[19] Y. Wan, J. Norman, Q. Li, M. J. Kennedy, D. Liang, C. Zhang, D. Huang, A. Y. Liu, A. Torres, D. Jung, A. C. Gossard, E. L. Hu, K. M. Lau, and J. E. Bowers, "Sub-mA threshold 1.3 um CW lasing from electrically pumped micro-rings grown on (001) Si," vol. 2, no. 001, pp. 6–7, 2017.

[20] B. Shi, S. Zhu, Q. Li, C. W. Tang, Y. Wan, E. L. Hu, and K. M. Lau, "1.55 um room-temperature lasing from subwavelength quantum-dot microdisks directly grown on (001) Si," *Appl. Phys. Lett.*, vol. 110, no. 12, p. 121 109, 2017.

[21] Justin Norman, M. J. Kennedy, Jennifer Selvidge, Qiang Li, Yating Wan, Alan Y. Liu, Patrick G. Callahan, McLean P. Echlin, Tresa M. Pollock, Kei May Lau, Arthur C. Gossard, and John E. Bowers, "Electrically pumped continuous wave quantum dot lasers epitaxially grown on patterned, on-axis (001) Si," *Opt. Express*, vol. 25, no. 4, p. 3927, 2017.

[22] Z. Wang, B. Tian, M. Pantouvaki, W. Guo, P. Absil, J. Van Campenhout, C. Merckling, and D. Van Thourhout, "Room-temperature InP distributed feedback laser array directly grown on silicon," *Nat. Photonics*, vol. 9, no. 12, pp. 837–842, 2015.

[23] B. Tian, Z. Wang, M. Pantouvaki, P. Absil, J. Van Campenhout, C. Merckling, and D. Van Thourhout, "Room Temperature O-band DFB Laser Array Directly Grown on (001) Silicon," *Nano Lett.*, vol. 17, no. 1, pp. 559–564, 2017.

[24] R. Chen, T.-T. D. Tran, K. W. Ng, W. S. Ko, L. C. Chuang, F. G. Sedgwick, and C. J. Chang-Hasnain, "Nanolasers grown on silicon.," *Nat Photonics*, vol. 5, pp. 170–175, 2011.

[25] F. Lu, T.-T. D. Tran, W. S. Ko, K. W. Ng, R. Chen, and C. J. Chang-Hasnain, "Nanolasers grown on silicon-based MOSFETs.," *Opt Express*, vol. 20, no. 11, pp. 12 171–12 176, 2012.

[26] K. Li, H. Sun, F. Ren, K. W. Ng, T. T. D. Tran, R. Chen, and C. J. Chang-Hasnain, "Tailoring the optical characteristics of microsized InP nanoneedles directly grown on silicon," *Nano Lett.*, vol. 14, no. 1, pp. 183–190, 2014.

[27] F. Lu, I. Bhattacharya, H. Sun, T.-T. D. Tran, K. W. Ng, G. N. Malheiros-Silveira, and C. J. Chang-Hasnain, "Nanopillar quantum well lasers directly grown on silicon and emitting at silicon-transparent wavelengths," *Optica*, vol. 4, no. 7, 2017.

[28] H. Takeuchi, A. Wung, X. Sun, R. T. Howe, and T. J. King, "Thermal budget limits of quarter-micrometer foundry CMOS for post-processing MEMS devices," *IEEE Trans. Electron Devices*, vol. 52, no. 9, pp. 2081–2086, 2005.

[29] L. C. Chuang, M. Moewe, C. Chase, N. P. Kobayashi, and C. Chang-Hasnain, "Critical diameter for III-V nanowires grown on lattice-mismatched substrates.," *Appl Phys Lett*, vol. 90, no. 043115, 2007.

[30] M. Moewe, L. C. Chuang, S. Crankshaw, C. Chase, and C. Chang-Hasnain, "Atomically sharp catalyst-free wurtzite GaAs/AlGaAs nanoneedles grown on silicon.," *Appl Phys Lett*, vol. 90, no. 023116, 2008.

[31] K. W. Ng, "Unconventional growth mechanism for monolithic integration of III-V on silicon.," vol. 7, no. 1 SRC - GoogleScholar FG - 0, pp. 100–107, 2013.

[32] L. C. Chuang, F. G. Sedgwick, R. Chen, W. S. Ko, M. Moewe, K. W. Ng, T. T. Tran, and C. Chang-Hasnain, "GaAs-based nanoneedle light emitting diode and avalanche photodiode monolithically integrated on a silicon substrate," *Nano Lett*, vol. 11, no. 2, pp. 385–390, 2011.

[33] R. Chen, K. W. Ng, W. S. Ko, D. Parekh, F. Lu, T.-T. D. Tran, K. Li, and C. Chang-Hasnain, "Nanophotonic integrated circuits from nanoresonators grown on silicon.," *Nat. Commun.*, vol. 5, p. 4325, 2014.

[34] K. W. Ng, W. S. Ko, R. Chen, F. Lu, T. T. D. Tran, K. Li, and C. J. Chang-Hasnain, "Composition homogeneity in InGaAs/GaAs core-shell nanopillars monolithically grown on silicon," *ACS Appl. Mater. Interfaces*, vol. 6, no. 19, pp. 16 706–16 711, 2014.

[35] H. Sun, F. Ren, K. W. Ng, T. T. D. Tran, K. Li, and C. J. Chang-Hasnain, "Nanopillar lasers directly grown on silicon with heterostructure surface passivation," *ACS Nano*, vol. 8, no. 7, pp. 6833–6839, 2014.

[36] F. Ren, K. W. Ng, K. Li, C. J. Chang-Hasnain, K. Wei Ng, K. Li, H. Sun, and C. J. Chang-Hasnain, "High-quality InP nanoneedles grown on silicon.," *Appl Phys Lett*, vol. 102, no. 012115 SRC - GoogleScholar FG - 0, 2013.

[37] K. Li, K. W. Ng, T.-T. D. Tran, H. Sun, F. Lu, and C. J. Chang-Hasnain, "Wurtzite-phased InP Micropillars Grown on Silicon with Low Surface Recombination Velocity," *Nano Lett.*, vol. 11, no. 11, pp. 7189–7198, 2015.

[38] W. S. Ko, T. T. D. Tran, I. Bhattacharya, K. W. Ng, H. Sun, and C. Chang-hasnain, "Illumination Angle Insensitive Single Indium Phosphide Tapered Nanopillar Solar Cell," *Nano Lett.*, vol. 15, no. 8, pp. 4961–4967, 2015.

[39] W. S. Ko, I. Bhattacharya, T.-D. Tran, K. W. Ng, S. Gerke, and C. Chang-Hasnain, "Ultrahigh responsivity-bandwidth product in a compact InP nanopillar phototransistor directly grown on silicon.," *Sci. Rep.*, vol. 6, no. 33368, p. 1, 2016.

[40] T. T. D. Tran, H. Sun, K. W. Ng, F. Ren, K. Li, F. Lu, E. Yablonovitch, and C. J. Chang-Hasnain, "High brightness InP micropillars grown on silicon with Fermi level splitting larger than 1 eV," *Nano Lett*, vol. 14, no. 6, pp. 3235–3240, 2014.

[41] G. N. Malheiros-Silveira, F. Lu, I. Bhattacharya, T.-T. D. Tran, H. Sun, and C. J. Chang-Hasnain, "III-V compound semiconductor nanopillars monolithically integrated to silicon photonics," *ACS Photonics*, vol. 4, no. 5, pp. 1021–1025, 2017.

[42] S. Deshpande, I. Bhattacharya, G. Malheiros-Silveira, K. W. Ng, F. Schuster, W. Mantei, K. Cook, and C. Chang-Hasnain, "Ultracompact Position-Controlled InP Nanopillar LEDs on Silicon with Bright Electroluminescence at Telecommunication Wavelengths," *ACS Photonics*, vol. 4, no. 3, pp. 695–702, 2017.

[43] O. D. Miller, E. Yablonovitch, and S. R. Kurtz, "Intense internal and external fluorescence as solar cell approach the SQ efficiency limit," *Photovoltaics, IEEE J.*, vol. 2, no. 3, pp. 1–27, 2012.

[44] E. Yablonovitch, C. Caneau, and T. J. Gmitter, "Ultrahigh spontaneous emission quantum efficiency, 99.7% internally and 72% externally, from AlGaAs/GaAs/AlGaAs double heterostructures," *Appl. Phys. Lett.*, vol. 62, no. 2, pp. 131–133, 1993.

[45] M. Konagai, M. Sugimoto, and K. Takahashi, "High efficiency GaAs thin film solar cells by peeled film technology," *J. Cryst. Growth*, vol. 45, no. C, pp. 277–280, 1978.

[46] F. Schuster, J. Kapraun, G. N. Malheiros-Silveira, S. Deshpande, and C. J. Chang-Hasnain, “Site-Controlled Growth of Monolithic InGaAs/InP Quantum Well Nanopillar Lasers on Silicon,” *Nano Lett.*, vol. 17, no. 4, pp. 2697–2702, 2017.

[47] R. Sinton and A. Cuevas, “A quasi-steady-state open-circuit voltage method for solar cell characterization,” *16th Eur. Photovolt. Sol. ...*, no. May, pp. 1–4, 2000.

[48] O. Breitenstein, H. Höffler, and J. Haunschild, “Photoluminescence image evaluation of solar cells based on implied voltage distribution,” *Sol. Energy Mater. Sol. Cells*, vol. 128, pp. 296–299, 2014.

[49] J. Liu, A. Melnikov, and A. Mandelis, “Contactless measurement of electrical parameters and estimation of current-voltage characteristics of Si solar cells using the illumination intensity dependence of lock-in carrierography (photoluminescence) images,” *J. Appl. Phys.*, vol. 114, no. 10, pp. 1–6, 2013.

[50] Y. Suzaki and A. Tachibana, “Measurement of the um sized radius of Gaussian laser beam using the scanning knife-edge,” *Appl. Opt.*, vol. 14, no. 12, pp. 2809–2810, 1975.

[51] M. Beaudoin, a. J. G. Devries, S. R. Johnson, H. Laman, and T. Tiedje, “Optical absorption edge of semi-insulating GaAs and InP at high temperatures,” *Semiconductors*, vol. 70, no. June, pp. 3540–3542, 1997.

[52] W. Shockley and W. T. Read, “Statistics of the Recombination of Holes and Electrons,” *Phys. Rev.*, vol. 87, no. 46, pp. 835–842, 1952.

[53] E. Yablonovitch, D. L. Allara, C. C. Chang, T. Gmitter, and T. B. Bright, “Unusually low surface-recombination velocity on silicon and germanium surfaces,” *Phys. Rev. Lett.*, vol. 57, no. 2, pp. 249–252, 1986.

[54] W. D. Eades and R. M. Swanson, “Calculation of surface generation and recombination velocities at the Si-SiO2 interface,” *J. Appl. Phys.*, vol. 58, no. 11, pp. 4267–4276, 1985.

[55] P. Wurfel, “The chemical potential of radiation,” *J. Phys. C Solid State Phys.*, vol. 15, no. 18, pp. 3967–3985, 1982.

[56] D. Estrin, D. Culler, K. Pister, and G. Sukhatme, “Connecting the Physical World with Pervasive Networks,” *IEEE Pervasive Comput.*, vol. 1, pp. 59–69, 2002.

[57] S. Li, L. D. Xu, S. Zhao, L. Da Xu, and S. Zhao, “The internet of things: a survey,” *Inf. Syst. Front.*, vol. 17, no. 2, pp. 243–259, 2015.

[58] J. Gubbi, R. Buyya, S. Marusic, and M. Palaniswami, “Internet of Things (IoT): A vision, architectural elements, and future directions,” *Futur. Gener. Comput. Syst.*, vol. 29, no. 7, pp. 1645–1660, 2013.

[59] L. Doherty, B. A. Warneke, B. E. Boser, and K. S. J. Pister, *Energy and performance considerations for smart dust*, 2001.

[60] T. Sanchez Lopez, D. C. Ranasinghe, M. Harrison, and D. McFarlane, "Adding sense to the internet of things: an architecture framework for smart object systems," *Pers. Ubiquitous Comput.*, vol. 16, no. 3, pp. 291–308, 2012.

[61] E. Borgia, "The internet of things vision: Key features, applications and open issues," *Comput. Commun.*, vol. 54, pp. 1–31, 2014.

[62] R. Haight, W. Haensch, and D. Friedman, "Solar-powering the Internet of Things," *Science (80-.).*, vol. 353, no. 6295, pp. 124–125, 2016.

[63] G. Apostolou, A. Reinders, and M. Verwaal, "Comparison of the indoor performance of 12 commercial PV products by a simple model," *Energy Sci. Eng.*, vol. 4, no. 1, pp. 69–85, 2016.

[64] H. J. Joyce, J. Wong-Leung, C. K. Yong, C. J. Docherty, S. Paiman, Q. Gao, H. H. Tan, C. Jagadish, J. Lloyd-Hughes, L. M. Herz, and M. B. Johnston, "Ultralow surface recombination velocity in InP nanowires probed by terahertz spectroscopy," *Nano Lett.*, vol. 12, no. 10, pp. 5325–5330, 2012.

[65] Y.-F. Huang, S. Chattopadhyay, Y.-J. Jen, C.-Y. Peng, T.-A. Liu, Y.-K. Hsu, C.-L. Pan, H.-C. Lo, C.-H. Hsu, Y.-H. Chang, C.-S. Lee, K.-H. Chen, and L.-C. Chen, "Improved broadband and quasi-omnidirectional anti-reflection properties with biomimetic silicon nanostructures," *Nat. Nanotechnol.*, vol. 2, no. 12, pp. 770–774, 2007.

[66] W. Shockley and H. J. Queisser, "Detailed balance limit of efficiency of p-n junction solar cells," *J. Appl. Phys.*, vol. 32, no. 3, pp. 510–519, 1961.

[67] J. R. Howell, M. P. Menguc, and R. Siegel, *Thermal Radiation Heat Transfer*, 6th ed. Taylor and Francis group, 2016.

[68] J. R. Howell, *A Catalog of Radiation Heat Transfer Configuration Factors*. [Online]. Available: `http://www.thermalradiation.net/tablecon.html%7B%5C#%7DC`.

[69] M. F. Müller, M. Freunek, and L. M. Reindl, "Maximum efficiencies of indoor photovoltaic devices," *IEEE J. Photovoltaics*, vol. 3, no. 1, pp. 59–64, 2013.

[70] G. Grzela, R. Paniagua-Dominguez, T. Barten, Y. Fontana, J. A. Sanchez-Gil, and J. G. Rivas, "Nanowire antenna emission," *Nano Lett.*, vol. 12, no. 11, pp. 5481–5486, 2012.

[71] P. Krogstrup, H. I. Jørgensen, M. Heiss, O. Demichel, J. V. Holm, M. Aagesen, J. Nygard, and A. Fontcuberta i Morral, "Single-nanowire solar cells beyond the ShockleyfffdfffdfffdQueisser limit," *Nat. Photonics*, vol. 7, no. March, pp. 1–5, 2013.

[72] Y. Cui, J. Wang, S. R. Plissard, A. Cavalli, T. T. T. Vu, R. P. J. van Veldhoven, L. Gao, M. Trainor, M. A. Verheijen, J. E. M. Haverkort, and E. P. A. M. Bakkers, "Efficiency enhancement of InP nanowire solar cells by surface cleaning," *Nano Lett.*, vol. 13, no. 9, pp. 4113–4117, 2013.

[73] G. Mariani, A. C. Scofield, C.-H. Hung, and D. L. Huffaker, "GaAs nanopillar-array solar cells employing in situ surface passivation- suppinfo," *Nat. Commun.*, vol. 4, p. 1497, 2013.

[74] S. Yalamanchili, H. S. Emmer, K. T. Fountaine, C. T. Chen, N. S. Lewis, and H. A. Atwater, "Enhanced Absorption and ¡1% Spectrum-and-Angle-Averaged Reflection in Tapered Microwire Arrays," *ACS Photonics*, vol. 3, no. 10, pp. 1854–1861, 2016.

[75] J. Wang, M. S. Gudiksen, X. Duan, Y. Cui, and C. M. Lieber, "Highly Polarized Photoluminescence and Photodetection from Single Indium Phosphide Nanowires," *Science (80-.).*, vol. 293, no. 5534, pp. 1455–1457, 2001.

[76] K. W. Ng, T. T. D. Tran, W. S. Ko, R. Chen, F. Lu, and C. J. Chang-Hasnain, "Single crystalline InGaAs nanopillar grown on polysilicon with dimensions beyond the substrate grain size limit," *Nano Lett.*, vol. 13, no. 12, pp. 5931–5937, 2013.

[77] L. C. Chuang, M. Moewe, K. W. Ng, T. T. D. Tran, S. Crankshaw, R. Chen, W. S. Ko, and C. Chang-Hasnain, "GaAs nanoneedles grown on sapphire," *Appl. Phys. Lett.*, vol. 98, no. 12, pp. 12–14, 2011.

[78] Q. Gao, D. Saxena, F. Wang, L. Fu, S. Mokkapati, Y. Guo, L. Li, J. Wong-Leung, P. Caroff, H. H. Tan, and C. Jagadish, "Selective-area Epitaxy of Pure Wurtzite InP Nanowires: High Quantum Efficiency and Room Temperature Lasing," *Nano Lett*, vol. 14, no. 9, pp. 5206–5211, 2014.

[79] S. Manipatruni, M. Lipson, and I. A. Young, "Device scaling considerations for nanophotonic CMOS global interconnects," *IEEE J Sel. Top. Quant.*, vol. 2, no. 19, 2013.

[80] L. Chen and M. Lipson, "Ultra-low capacitance and high speed germanium photodetectors on silicon," *Opt Express*, vol. 17, pp. 7901–7906, 2009.

[81] J. Michel, J. Liu, L. C. Kimmerling, and L. C. Kimerling, "High performance Ge-on-Si photodetectors," *Nat Photonics*, vol. 4, no. 8, pp. 527–534, 2010.

[82] L. Tang and D. A. B. Miller, "Nanometre-scale germanium photodetector enhanced by a near-infrared dipole antenna," *Nat Photonics*, no. 2, pp. 226–229, 2008.

[83] R. W. Going, M.-K. Kim, and M. C. Wu, "Metal-optic cavity for a high-efficiency sub-fF germanium photodiode on a silicon waveguide," *Opt Express*, vol. 21, no. 19, pp. 22 429–22 440, 2013.

[84] M. Massicotte, P. Schmidt, F. Vialla, L. Schaedler, A. Reserbat-Plantey, K. Watanabe, T. Taniguchi, J. Tielrooij, and F. H. L. Koppens, "Picosecond photoresponse in van der Waals heterostructures," *Nat. Nanotechnol.*, vol. 11, pp. 42–46, 2015.

[85] N. Youngblood, C. Chen, S. J. Koester, and M. Li, "Waveguide-integrated black phosphorus photodetector with high responsivity and low dark current," *Nat Photonics*, no. 9, pp. 247–252, 2015.

[86] F. H. L. Koppens, T. Mueller, P. Avouris, A. C. Ferrari, M. S. Vitiello, and M. Polini, "Photodetectors based on graphene, other two-dimensional materials and hybrid systems," *Nat. Nanotechnol.*, no. 9, pp. 780–793, 2014.

[87] J. C. Campbell, C. A. Burrus, A. G. Dentai, and K. Ogawa, "Small-area high-speed InP/InGaAs phototransistor," *Appl Phys Lett*, vol. 39, no. 820, 1981.

[88] J. C. Campbell, "Photodetectors and compatible low-noise amplifiers amplifiers for long-wavelength light wave systems," *Fiber Integr. Opt.*, vol. 5, no. 1, 1984.

[89] S. B. Alexander, *Optical communication receiver design*. SPIE Press, 1997.

[90] E. Timurdogan, Z. Su, K. T. Settaluri, S. Lin, S. Moazeni, C. Sun, G. Leake, D. D. Coolbaugh, B. R. Moss, M. Moresco, V. Stojanovic, and M. R. Watts, "An ultra low power 3D integrated intra-chip silicon electronic-photonic link," in *Opt. Fiber Commun. Conf. postdeadline Pap.*, 2015.

[91] K. T. Settaluri and V. Stojanovic, "Demonstration of an optical chip-to-chip link in a 3D integrated electronic-photonic platform," in *41st Eur. Solid State Circuits Conf.*, 2015, pp. 156–159.

[92] Y. Kang, H.-D. Liu, M. Morse, M. J. Paniccia, M. Zadka, S. Litski, G. Sarid, A. Pauchard, Y.-H. Kuo, H.-W. Chen, W. S. Zaoui, J. E. Bowers, A. Beling, D. C. McIntosh, X. Zheng, and J. C. Campbell, "Monolithic germanium/silicon avalanche photodiodes with 340 GHz gain-bandwidth product," *Nat Photonics*, vol. 3, no. 3, pp. 59–63, 2009.

[93] S. Assefa, F. Xia, and Y. A. Vlasov, "Reinventing germanium avalanche photodetector for nanophotonic on-chip optical interconnects," *Nature*, no. 464, pp. 80–84, 2010.

[94] J. C. Campbell, "Recent advances in avalanche photodiodes," *IEEE J Sel. Top. Quant.*, vol. 10, no. 4, pp. 777–787, 2004.

[95] M. Nada, Y. Muramoto, H. Yokoyama, T. Ishibashi, and S. Kodama, "InAlAs APD with high multipied responsivity-bandwidth product (MR-bandwidth) product of 168 A/W-GHz for 25 Gbit/s high-speed operation," *Electron Lett.*, vol. 48, no. 7, 2012.

[96] J. Wang, M. Yu, G. Lo, D.-L. Kwong, and S. Lee, "Silicon waveguide integrated germanium JFET photodetector with improved speed performance," *IEEE Photonic Tech. L.*, vol. 23, no. 12, pp. 765–767, 2011.

[97] S. Sahni, X. Luo, J. Liu, Y.-H. Xie, and E. Yablonovitch, "Junction field-effect-transistor-based germanium JFET photodetector with improved speed performance," *Opt. Lett.*, vol. 33, no. 10, pp. 1138–1140, 2008.

[98] S. Chandrashekhar, L. M. Lunardi, A. H. Gnauck, R. A. Hamm, and G. Qua, "High-speed monolithic p-i-n/HBT and HPT/HBT photoreceivers implemented with simple phototransistor structure," *IEEE Photonic Tech. L.*, vol. 5, no. 11, 1993.

[99] R. Going, T. J. Seok, J. Loo, K. Hsu, and M. C. Wu, "Germanium wrap-around photodetectors on Silicon photonics," *Opt. Express*, vol. 23, no. 9, p. 11 975, 2015.

[100] D. Wake, D. J. Newson, M. J. Harlow, and I. D. Henning, "Optically-biased, edge-coupled InP/InGaAs heterojunction phototransistors," *Electron Lett.*, vol. 29, no. 25, 1993.

[101] H. Fukano, Y. Takanashi, and M. Fujimoto, "High-speed InP/InGaAs heterojunction phototransistors employing a nonalloyed electrode metal as reflector," *IEEE J Quant Electron*, vol. 30, no. 12, 1994.

[102] J. Thuret, C. Gonzalez, J. L. Benchimol, M. Riet, and P. Berdaguer, "High speed InP/InGaAs heterojunction phototransistor for millimetre-wave fibre radio communications," in *11th Int. Conf. Indium Phosphide Relat. Mater.*, 1999.

[103] H. Kamitsuna, Y. Matsuoka, S. Yamahata, and N. A. Shikegawa, "An 82-GHz-Optical-Gain-Cutoff-Frequency InP/InGaAs double-heterostructure phototransistor (DHPT) and its application to a 40-GHz-band OEMMIC photoreceiver," in *30th Eur. Microw. Conf.*, 2000.

[104] A. Leven, V. Houtsma, R. Kopf, Y. Baeyens, and Y.-K. Chen, "InP-based double-heterostructure phototransistors with 135 GHz optical-gain cutoff frequency," *Electron Lett.*, vol. 40, no. 13, 2004.

[105] V. E. Houtsma, "High gain-bandwidth InP waveguide phototransistor," in *Indium Phosphide Relat. Mater.*, 2006.

[106] K.-W. Ang, M.-B. Yu, G.-Q. Lo, and D.-L. Kwong, "Low-voltage and high-responsivity germanium bipolar phototransistor for optical detection in the near-infrared regime," *IEEE Electr. Device L.*, vol. 29, no. 10, 2008.

[107] R. J. McIntyre, "Multiplication noise in uniform avalanche photodiodes," *IEEE T. Electron. Dev.*, vol. 13, no. 1, pp. 164–168, 1966.

[108] C. R. Crowell and S. M. Sze, "Temperature dependence of avalanche multiplication in semiconductors," *Appl. Phys. Lett.*, vol. 9, no. 6, pp. 242–244, 1966.

[109] C. L. F. Ma, M. J. Deen, L. E. Tarof, and J. C. H. Yu, "Temperature dependence of breakdown voltages in separate absorption, grading, charge, and multiplication InP/InGaAs avalanche photodiodes," *IEEE. T. Electron. Dev.*, vol. 42, no. 5, pp. 810–818, 1995.

[110] P. W. Casper and W. B. Ashley, *US Patent No. US4438348*, 1984.

[111] W. Y. Weng, S. J. Chang, C. L. Hsu, and T. J. Hsueh, "A ZnO-nanowire phototransistor prepared on glass substrates," *ACS Appl. Mater. Interfaces*, vol. 3, no. 2, pp. 162–166, 2011.

[112] C. Soci, A. Zhang, B. Xiang, S. A. Dayeh, D. P. R. Aplin, J. Park, X. Y. Bao, Y. H. Lo, and D. Wang, "ZnO nanowire UV photodetectors with high internal gain," *Nano Lett.*, vol. 7, no. 4, pp. 1003–1009, 2004.

[113] J. Lu, C. Sun, M. Zheng, Y. Wang, N. Mathews, J. A. van Kan, S. Mhaisalkar, and C. H. Sow, "Ultrasensitive phototransistor based on K-enriched MoO3 single nanowires," *J. Phys. Chem. C*, vol. 116, no. 41, pp. 22 015–22 020, 2012.

[114] C. Hu, *Modern semiconductor devices for integrated circuits*. Prentice Hall, 2010, pp. 259–289.

[115] J. C. Campbell and K. Ogawa, "Heterojunction phototransistors for long-wavelength optical receivers," *J. Appl. Phys.*, vol. 53, pp. 1203–1208, 1982.

[116] R. G. Smith and S. D. Personick, *Semiconductor devices for optical communication*. Springer, Berlin Heidelberg, 1982, pp. 89–160.

[117] S. M. Sze, *Physics of semiconductor devices*, 2nd ed. Wiley, New York, 1981, pp. 158–160.

[118] W. Hafez, W. Snodgrass, and M. Feng, "12.5 nm base pseudomorphic heterojunction bipolar transistor achieving fT = 710 GHz and fmax = 340 GHz," *Appl Phys Lett*, vol. 87, no. 252109, 2005.

[119] C. T. DeRose and M. Watts, "Ultra compact 45 GHz CMOS compatible Germanium waveguide photodiode with low dark current," *Opt Express*, vol. 19, no. 25, 2011.

[120] B. M. Kayes, H. A. Atwater, and N. S. Lewis, "Comparison of the device physics principles of planar and radial p-n junction nanorod solar cells," *J. Appl. Phys.*, vol. 97, no. 114302, 2005.

[121] S. M. Sze, *Physics of Semiconductor Devices*. John Wiley and Sons, New York, 1981, pp. 140–147.

[122] C. Hu, *Modern semiconductor devices for integrated circuits*. Prentice Hall, 2010, pp. 298–302.

[123] Y. Jia, M. Qiu, H. Wu, Y. Cui, S. Fan, and Z. Ruan, "Theory of half-space light absorption enhancement for leaky mode resonant nanowires," *Nano Lett*, vol. 15, no. 8, pp. 5513–5518, 2015.

[124] J. M. Early, "Effects of space-charge layer widening in junction transistors," *Proc. IRE*, vol. 40, no. 11, pp. 1401–1406, 1952.

[125] R. W. Going, J. Loo, T. J. K. Liu, and M. C. Wu, "Germanium Gate PhotoMOSFET Integrated to Silicon Photonics," *IEEE J. Sel. Top. Quantum Electron.*, vol. 20, no. 4, 2014.

[126] A. V. Krishnamoorthy, R. Ho, X. Zheng, H. Schwetman, J. Lexau, P. Koka, G. Li, I. Shubin, and J. E. Cunningham, "Computer systems based on silicon photonic interconnects," *Proc IEEE*, vol. 97, pp. 1337–1361, 2009.

[127] T. Wang, H. Liu, A. Lee, F. Pozzi, and A. Seeds, "1.3-um InAs/GaAs quantum-dot lasers monolithically grown on Si substrates," *Opt Express*, vol. 19, pp. 11 381–1186, 2011.

[128] J. Van Campenhout, P. Rojo-Romeo, P. Regreny, C. Seassal, D. Van Thourhout, S. Verstuyft, L. Di Coccio, J.-M. Fedeli, C. Lagahe, and R. Baets, "Electrically pumped InP-based microdisk lasers integrated with a nanophotonic silicon-on-insulator waveguide circuit," *Opt Express*, vol. 15, pp. 6744–6749, 2007.

[129] Y. H. Lo, R. Bhat, D. M. Hwang, C. Chua, and C.-H. Lin, "Semiconductor lasers on Si substrates using the technology of bonding by atomic rearrangement," *Appl Phys Lett*, vol. 62, pp. 1038–1040, 1993.

[130] T. Frost, A. Banerjee, K. Sun, S. L. Chuang, and P. Bhattacharya, "InGaN/GaN quantum dot red (lambda = 630 nm) laser," *IEEE J. Quant. Electron.*, vol. 49, pp. 923–931, 2013.

[131] A. Hazari, A. Aiello, T. Ng, B. S. Ooi, and P. Bhattacharya, "III-nitride disk-in-nanowire 1.2 um monolithic diode laser on (001)silicon," *Appl. Phys. Lett.*, vol. 107, 2015.

[132] R. Yan, D. Gargas, and P. Yang, "Nanowire photonics," *Nat. Photonics*, vol. 3, pp. 569–576, 2009.

[133] A. H. Chin, S. Vaddiraju, A. V. Maslov, C. Z. Ning, M. K. Sunkara, and M. Meyyappan, "Near-infrared semiconductor subwavelength-wire lasers," *Appl Phys Lett*, vol. 88, 2006.

[134] J. C. Johnson, H.-J. Choi, K. P. Knutsen, R. D. Schaller, P. Yang, and R. J. Saykally, "Single gallium nitride nanowire lasers," *Nat. Mater.*, vol. 1, pp. 106–110, 2002.

[135] R. Agarwal, C. J. Barrelet, and C. M. Lieber, "Lasing in single cadmium sulfide nanowire optical cavities," *Nano Lett*, vol. 5, pp. 917–920, 2005.

[136] F. Qian, Y. Li, S. Gradecak, H.-G. Park, Y. Dong, Y. Ding, Z. L. Wang, and C. M. Lieber, "Multi-quantum-well nanowire heterostructures for wavelength-controlled lasers," *Nat. Mater.*, vol. 7, pp. 701–706, 2008.

[137] Y. Xiao, C. Meng, P. Wang, Y. Ye, H. Yu, S. Wang, F. Gu, L. Dai, and L. Tong, "Single-nanowire single-mode laser," *Nano Lett*, vol. 11, pp. 1122–1126, 2011.

[138] A. Pan, W. Zhou, E. S. P. Leong, R. Liu, A. H. Chin, B. Zou, and C. Z. Ning, "Continuous alloy-composition spatial grading and superbroad wavelength-tunable nanowire lasers on a single chip," *Nano Lett*, vol. 9, pp. 784–788, 2009.

[139] M. A. Zimmler, J. Bao, F. Capasso, S. Mueller, and C. Ronning, "Laser action in nanowires: Observation of the transition from amplified spontaneous emission to laser oscillation," *Appl Phys Lett*, vol. 93, 2008.

[140] S. Chu, G. Wang, W. Zhou, Y. Lin, L. Chernyak, J. Zhao, J. Kong, L. Li, J. Ren, and J. Liu, "Electrically pumped waveguide lasing from ZnO nanowires," *Nat. Nanotech.*, vol. 6, pp. 506–510, 2011.

[141] B. Hua, J. Motohisa, Y. Kobayashi, S. Hara, and T. Fukui, "Single GaAs/AlGaAs core-shell nanowire lasers," *Nano Lett*, vol. 9, pp. 112–116, 2009.

[142] D. Saxena, S. Mokkapati, P. Parkinson, N. Jiang, Q. Gao, H. H. Tan, and C. Jagadish, "Optically pumped room-temperature GaAs nanowire laser," *Nat. Photonics*, vol. 7, pp. 963–968, 2013.

[143] B. Mayer, L. Janker, B. Loitsch, J. Treu, T. Kostenbader, S. Lichtmannecker, T. Reichert, S. Morkoetter, M. Kaniber, G. Abstreiter, C. Gies, G. Koblmueller, and J. J. Finley, "Monolithically integrated high-beta nanowire lasers on silicon," *Nano Lett*, vol. 16, pp. 152–156, 2016.

[144] M. V. Nazarenko, N. V. Sibirev, K. W. Ng, F. Ren, W. S. Ko, V. G. Dubroskii, and C. Chang-Hasnain, "Elastic energy relaxation and critical thickness for plastic deformation in the core-shell InGaAs/GaAs nanopillars," *J. Appl. Phys.*, vol. 113, p. 104 311, 2013.

[145] T. Trupke, R. A. Bardos, M. C. Schubert, and W. Warta, "Photoluminescence imaging of silicon wafers," *Appl Phys Lett*, vol. 89, p. 44 107, 2016.

[146] A. Delamarre, L. Lombez, and J. Guillemoles, "Contactless mapping of saturation currents of solar cells by photoluminescence," *Appl Phys Lett*, vol. 100, no. 131108, 2016.

[147] M. Rosenzweig, M. Moehrle, H. Dueser, and H. Venghaus, "Threshold-current analysis of InGaAs-InGaAsP multiquantum well separate-confinement lasers," *IEEE J. Quant. Electron.*, vol. 27, pp. 1804–1811, 1991.

[148] B. W. Hakki and T. L. Paoli, "Gain spectra in GaAs double-heterojunction injection lasers," *J Appl Phys*, vol. 46, no. 1299, 1975.

[149] Y. Arakawa and H. Sakaki, "Multidimensional quantum well laser and temperature dependence of its threshold current," *Appl Phys Lett*, vol. 40, pp. 939–941, 1982.

[150] Q. Gu, J. Shane, F. Vallini, B. Wingad, J. S. T. Smalley, N. C. Frateschi, and Y. Fainman, "Amorphous Al2O3 shield for thermal management in electrically pumped metallo-dielectric nanolasers," *IEEE J Quant Electron*, vol. 50, no. 7, pp. 499–509, 2014.

[151] H. Kim, A. C. Farrell, P. Senanayake, W. J. Lee, and D. L. Huffaker, "Monolithically Integrated InGaAs Nanowires on 3D Structured Silicon-on-Insulator as a New Platform for Full Optical Links," *Nano Lett.*, vol. 16, no. 3, pp. 1833–1839, 2016.

[152] H. Kim, W.-J. Lee, A. C. Farrell, J. S. D. Morales, P. Senanayake, S. V. Prikhodko, T. J. Ochalski, and D. L. Huffaker, "Monolithic InGaAs nanowire array lasers on silicon-on-insulator operating at room temperature," *Nano Lett*, vol. 17, no. 6, pp. 3465–3470, 2017.

[153] R. W. Boyd, *Nonlinear optics*, 3rd. Associated Press, 2007.

[154] J. F. Nye, *Physical properties of crystals*. New York: Oxford, 1957.

[155] R. Chen, S. Crankshaw, T. Tran, L. C. Chuang, M. Moewe, and C. Chang-Hasnain, "Second-harmonic generation from a single wurtzite GaAs nanoneedle," *Appl. Phys. Lett.*, vol. 96, no. 5, pp. 1–3, 2010.

[156] H. Fonseka, H. Tan, Y. Wong Leung, J. H. Kang, P. Parkinson, and C. Jagadish, "High vertical yield InP nanowire growth on Si (111) using a thin buffer layer," *Nanotechnology*, vol. 24, no. 46, 2013.

[157] Y. Watanabe, H. Hibino, S. Bhunia, K. Tateno, and T. Sekiguchi, "Site-controlled InP nanowires grown on patterned Si substrates," *Phys. E.*, vol. 24, pp. 133–137, 2004.

[158] P. Mohan, J. Motohisa, and T. Fukui, "Controlled growth of highly uniform axial/radial direction-defined, individually addressable InP nanowire arrays," *Nanotechnology*, vol. 16, no. 12, pp. 2903–2907, 2005.

[159] T.-T. D. Tran, R. Chen, K. W. Ng, W. S. Ko, F. Lu, and C. J. Chang-hasnain, "Three-dimensional whispering gallery modes in InGaAs nanoneedle lasers on silicon," *Appl. Phys. Lett.*, vol. 105, no. 11, p. 111 105, 2014.

[160] A. Maharjan, K. Pemasiri, P. Kumar, A. Wade, L. M. Smith, H. E. Jackson, J. M. Yarrison-Rice, A. Kogan, S. Paiman, Q. Gao, H. H. Tan, and C. Jagadish, "Room temperature photocurrent spectroscopy of single ZincBlende and Wurtzite InP nanowires," *Appl Phys Lett*, vol. 94, no. 193115, 2009.

[161] F. Lu, K. Li, K. W. Ng, W. S. Ko, and C. J. Chang-Hasnain, "Characteristics of InP nanoneedles grown on silicon by low-temperature MOCVD," in *Int. Symp. Compd. Semicond. Int. Conf. Indium Phosphide Relat. Mater.*, 2015.

[162] M. S. Eggleston, K. Messer, L. Zhang, E. Yablonovitch, and M. C. Wu, "Optical antenna enhanced spontaneous emission," *Proc. Natl. Acad. Sci.*, vol. 112, no. 1704-1709, 2015.

[163] A. T. M. Sarwar, B. Z. May, J. I. Deitz, T. J. Grassman, D. W. McComb, and R. C. Myers, "Tunnel junction enhanced nanowire ultraviolet light emitting diodes," *Appl Phys Lett*, vol. 107, no. 101103, 2015.

[164] E. D. Minot, F. Kelkensberg, M. Van Kouwen, J. A. van Dam, L. P. Kouwenhoven, V. Zwiller, M. T. Borgstrom, O. Wunnicke, M. Verheijen, and E. P. A. M. Bakkers, "Single quantum dot nanowire LEDs," *Nano Lett*, vol. 7, pp. 367–371, 2007.

[165] M. Eggleston, K. Messer, L. Zhang, E. Yablonovitch, and M. C. Wu, "Optical antenna enhanced spontaneous emission," *Proc. Natl. Acad. Sci. U. S. A.*, vol. 112, no. 6, 2014.